

DEVELOPMENT AND APPLICATIONS OF NEW PERIDYNAMIC MODELS

By

Tao Jia

A DISSERTATION

Submitted to
Michigan State University
in partial fulfillment of the requirements
for the degree of

DOCTOR OF PHILOSOPHY

Mechanical Engineering

2012

ABSTRACT

DEVELOPMENT AND APPLICATIONS OF NEW PERIDYNAMIC MODELS

By

Tao Jia

Studies of solid mechanics are traditionally based on continuum mechanics which utilizes differential equations. Differential equations, however, become troublesome when damage takes place. Instead of differential equations, this study presents a theory, so-called peridynamics, based on integral equations. Similar to molecular dynamics, peridynamics assumes that the domain of interest is organized by points. Each point interacts with every other point within a horizon through a bond. Damage at a point takes place when a critical amount of bonds associated with the point are broken. Besides the bond strength, peridynamics does not impose any additional damage theory such as fracture mechanics used in continuum mechanics. Peridynamics is still in its infant stage. New models need to be developed. In this study, a one-dimensional model was firstly proposed and verified by an associated solution based on continuum mechanics. The model was then used to simulate wave propagations in split Hopkinson's pressure bar (SHPB) and was validated by the experiment results. The peridynamic model was then used for designing required shapers in SHPB application and greatly improves the experiment efficiency. Secondly, a two-dimensional model was proposed and verified by an associated solution based on continuum mechanics. Two computational algorithms were then proposed and incorporated into peridynamic programming to significantly improve its computational efficiency. The uses of the two-dimensional peridynamic model for simulating dynamic damage progression were favorably validated by experiments. A four-parameter peridynamic model was finally presented for investigating orthotropic materials. The model was

verified by analyses involving uniaxial tension and vibration. It was also validated with single-edge-notch testing results.

ACKNOWLEDGEMENTS

I would like to thank my professor, Dr. Dahsin Liu, for both the financial support of my research and the directing of the research work. His insight allowed me to find suitable topics for research and complete this dissertation in a timely manner. I would also like to thank Dr. Ronald Averill, Dr. Thomas Pence and Dr. Zhengfang Zhou for agreeing to serve on my dissertation committee. Lastly, I would especially like to thank my parents for their love and support through the years.

TABLE OF CONTENTS

LIST OF TABLES	vii
LIST OF FIGURES.....	viii
Chapter 1 Introduction.....	1
1.1 Background.....	1
1.2 Literature review.....	2
1.3 Motivations and objectives.....	5
1.4 Outline of dissertation.....	6
References.....	8
Chapter 2 Basic Formulations.....	11
2.1 Peridynamic model of a continuum.....	11
2.2 Constitutive modeling.....	12
2.3 Failure criterion.....	13
2.4 Numerical method.....	14
Figures.....	15
References.....	19
Chapter 3 One-Dimensional Wave Propagation Analysis.....	21
3.1 Identification of stiffness.....	21
3.2 Definition of stress in peridynamics.....	22
3.3 Comparison with analytical solution.....	23
3.3.1 Analytical solution.....	23
3.3.2 Numerical studies.....	26
3.4 Comparison with experiment results.....	28
3.4.1 Square wave input.....	29
3.4.2 Using filter for computational results.....	33
3.4.3 Using the incidence wave as the computational input.....	35
3.5 Simulation with a striker.....	35
3.6 Validation with results in literature.....	39
3.7 Modeling shaper in SHPB.....	41
3.8 Conclusions.....	42
Figures.....	44
References.....	85
Chapter 4 Two-Dimensional Peridynamic Studies.....	87
4.1 Bar model.....	87
4.2 Definition of stress in peridynamics.....	89
4.3 Beam model.....	91
4.4 Computational efficiency.....	94

4.4.1 Using matrix computation.....	94
4.4.2 Using parallel computing.....	99
4.5 Comparison with vibration theory.....	101
4.5.1 Vibration theory.....	101
4.5.2 Numerical studies.....	102
4.6 Convergence to the one-dimensional results.....	104
4.7 Axisymmetric problems.....	105
4.8 Failure theory.....	107
4.9 Comparison of crack propagation velocity with experiments.....	108
4.10 Dynamic crack branching.....	109
4.11 Edge-cracked plate under impulsive loading.....	110
4.12 Conclusions.....	111
Figures.....	113
References.....	149
 Chapter 5 Orthotropic Model Analysis.....	152
5.1 Bar model for orthotropic materials.....	153
5.2 Beam model for orthotropic materials.....	160
5.3 Calculation of stress from peridynamics.....	161
5.4 Laminated plate under static loading.....	162
5.5 Free vibration of a laminated beam.....	164
5.6 Comparison of crack propagation velocity with experiments.....	167
5.7 Dynamic fracture mode in unidirectional composites.....	169
5.8 Conclusions.....	171
Figures.....	173
References.....	195
 Chapter 6 Conclusions and Recommendations.....	198
6.1 Conclusions.....	198
6.2 Recommendations.....	201
References.....	204

LIST OF TABLES

Table 3.1 Wave period (ms) based on various of m and δ	27
Table 3.2 Dimensions and material properties of the SHPB in Fig. 3.7.....	28
Table 3.3 Dimensions and material properties of the split bar in Fig. 3.28.....	36
Table 3.4 Dimensions and material properties of the SHPB in Fig. 3.33.....	40
Table 3.5 Dimensions and material properties of the SHPB used	41
Table 4.1 Twelve pairs of m and δ	103
Table 5.1 Simplified Eqn. 5.9 in terms of independent terms.....	155
Table 5.2 Simplified Eqn. 5.12 in terms of independent terms.....	157
Table 5.3 Material propteties of E-Glass/Epoxy.....	163
Table 5.4 Material propteties of Kevlar/Epoxy.....	164
Table 5.5 Material propteties of graphite/epoxy.....	168
Table 5.6 Material propteties of carbon/epoxy	170

LIST OF FIGURES

Figure 2.1 Horizon of point \mathbf{x}	15
Figure 2.2 Reference configuration and current configuration.....	16
Figure 2.3 Finite summation domain in numerical computation.....	17
Figure 2.4 Flow chart of a peridynamic program.....	18
Figure 3.1 Calculation of stress.....	44
Figure 3.2 Wave propagation in a one-dimensional bar	45
Figure 3.3 Analytical solution for wave propagation.....	46
Figure 3.4 Number of nodes within a horizon	47
Figure 3.5 Comparison between classical mechanics and peridynamics.....	48
Figure 3.6 Convergence of time step size.....	49
Figure 3.7 Set up of Split Hopkinson pressure bar (SHPB).....	50
Figure 3.8 Wave propagation in the SHPB.....	51
Figure 3.9 Square wave input for computational simulation	52
Figure 3.10 Comparison in Study One with a square wave input	53
Figure 3.11 Study Two: Two Bar	54
Figure 3.12 Study Two: comparison between experiment results and numerical solution, strain history in incidence bar (top) and strain history in transmission bar (bottom).....	55
Figure 3.13 Study Two: comparison between experiment results and numerical solution with grease, strain history in incidence bar (top) and strain history in transmission bar (bottom).....	56
Figure 3.14 A bond crossing an interface	57
Figure 3.15 Study Three: aluminum specimen with the same cross-section area as the split bars	58
Figure 3.16 Study Three: Aluminum specimen with the same-cross section area as the split bars, incidence bar strain history (top) and transmission bar strain history(bottom).....	59

Figure 3.17 Study Four: Steel specimen with a smaller cross-section area	60
Figure 3.18 Study Four: Steel specimen with a smaller cross-section area, incidence bar strain history (top) and transmission bar strain history (bottom).....	61
Figure 3.19 Study One: computational results with filter compared with experiment results.....	62
Figure 3.20 Study Two: Computational results with filter compared with experiment results ...	63
Figure 3.21 Study Three: Computational results with filter compared with experiment results...	64
Figure 3.22 Study Four: Computational results with filter compared with experiment results....	65
Figure 3.23 Incidence wave from Study Two	66
Figure 3.24 Study One: Incident wave as computational input	67
Figure 3.25 Study Two: Incident wave as computational input	68
Figure 3.26 Study Three: Incident wave as computational input	69
Figure 3.27 Study Four: Incident wave as computational input	70
Figure 3.28 Split bar system for validating impact process	71
Figure 3.29 Simulation of impact process.....	72
Figure 3.30 Comparison between experiment and simulation with velocity input.....	73
Figure 3.31 Impact of two cylindrical bars right before impact	74
Figure 3.32 Impact of two cylindrical bars after impact	75
Figure 3.33 SHPB system in [6].....	76
Figure 3.34 Stress-strain relation of the aluminum specimen from [6].....	77
Figure 3.35 Comparing computational results with experiment results from [6].....	78
Figure 3.36 Computational results with filter compared with experiment results.....	79
Figure 3.37 Incidence wave after filter from Ref. [8].....	80
Figure 3.38 SHPB with a shaper.....	81

Figure 3.39 Split bar system in Ref. [8].....	82
Figure 3.40 Stress-strain relation for the copper shaper given in Ref. [8].....	83
Figure 3.41 Simulation results compared with experiment results from Ref. [8].....	84
Figure 4.1 Two-dimensional domain under radial deformation.....	113
Figure 4.2 Definition of stress in peridynamics.....	114
Figure 4.3 Calculation of stress on point x.....	115
Figure 4.4 Bond force in beam model	116
Figure 4.5 Original configuration and current configuration.....	117
Figure 4.6 Flow chart of algorithm in peridynamic matrix calculation	118
Figure 4.7 Flow chart for parallel computing.....	119
Figure 4.8 Code before parallel modification and code after parallel modification.....	120
Figure 4.9 Vibration of a circular plate.....	121
Figure 4.10 Strain history on a circular plate.....	122
Figure 4.11 Convergence of numerical solution to analytical solution	123
Figure 4.12 Convergence of numerical solution to analytical solution	124
Figure 4.13 Convergence of numerical solution to vibration theory	125
Figure 4.14 Peridynamic calculation of strains at point A compared with results from vibration theory	126
Figure 4.15 Peridynamic calculation of strain at point B compared with results from vibration theory	127
Figure 4.16 Peridynamic calculation of strain at point C compared with results from vibration theory	128
Figure 4.17 Rectangular plate for free vibration study	129
Figure 4.18 One-dimensional result compared with two-dimensional result for aspect ratio of 0.2.....	130

Figure 4.19 One dimensional result compared with two-dimensional result for aspect ratio of 1.....	131
Figure 4.20 One-dimensional result compared with two-dimensional result for aspect ratio of 10.....	132
Figure 4. 21 One-dimensional result compared with two-dimensional result for aspect ratio of 50.....	133
Figure 4. 22 One-dimensional result compared with two-dimensional result for aspect ratio of 100.....	134
Figure 4.23 A two-dimensional axisymmetric model	135
Figure 4.24 Angular integration boundary of Eqn. 4.75.....	136
Figure 4.25 Comparison of peridynamic calculation of strain at Point A using axisymmetric model with results from the vibration theory	137
Figure 4.26 Comparison of peridynamic calculation of strain at Point B using axisymmetric model with results from the vibration theory	138
Figure 4.27 Comparison of peridynamic calculation of strain at Point C using axisymmetric model with results from the vibration theory	139
Figure 4.28 Calculation of the critical stretch.....	140
Figure 4.29 Schematic drawing of the sample for crack propagation test.....	141
Figure 4.30 Comparison of crack propagation simulated by peridynamics with experiment result	142
Figure 4.31 Comparison of crack propagation speed simulated by peridynamics with experiment result	143
Figure 4.32 A plate with single notch for crack branching study.....	144
Figure 4.33 Computational crack path (a) damage and (b) strain energy density simulated by peridynamics	145
Figure 4.34 A two-notch plate under impulsive loading.....	146
Figure 4.35 Computational crack path of the top notch	147
Figure 4.36 Horizontal displacement at 33.2 μ s from computational results.....	148

Figure 5.1 A composite plate with fiber in α° direction and a bond in θ° direction	173
Figure 5.2 Coordinate system for calculating strain energy density at point x	174
Figure 5.3 Beam model for orthotropic materials.....	175
Figure 5.4 Pulling test in a composite laminate	176
Figure 5.5 Comparison of u_x of 0° laminate calculated from peridynamics (top) and composite theory (bottom).....	177
Figure 5.6 Comparison of u_x of 45° laminate calculated from peridynamics (top) and the composite theory (bottom).....	178
Figure 5.7 Comparison of u_x of 60° laminate calculated from peridynamics (top) and the composite theory (bottom).....	179
Figure 5.8 Comparison of u_y of 0° laminate calculated from peridynamics (top) and the composite theory (bottom).....	180
Figure 5.9 Comparison of u_y of 45° laminate calculated from peridynamics (top) and the composite theory (bottom).....	181
Figure 5.10 Comparison of u_y of 60° laminate calculated from peridynamics (top) and the composite theory (bottom).....	182
Figure 5.11 Free vibration of a laminated beam with fibers in x direction.....	183
Figure 5.12 Peridynamic results compared with composite beam theory results with $a = 5$. Top: horizontal displacement u of point A. Bottom: vertical displacement w of point B	184
Figure 5.13 Peridynamic results compared with composite beam theory results with $a = 20$. Top: horizontal displacement u of point A. Bottom: vertical displacement w of point B	185
Figure 5.14 An unidirectional composite plate with single edge notch under three point bending.....	186
Figure 5.15 Comparison of crack propagation velocity between peridynamics and experiment.....	187
Figure 5.16 Compact tension test for a unidirectional composite plate	188

Figure 5.17 Simulation results for $t = 50 \mu s$ and $\alpha = 0^\circ$: (a) vertical displacement, (b) strain energy density, (c) local damage.....	189
Figure 5.18 Simulation results for $t = 70 \mu s$ and $\alpha = 30^\circ$: (a) vertical displacement, (b) strain energy density, (c) local damage.....	190
Figure 5.19 Simulation results for $t = 70 \mu s$ and $\alpha = 45^\circ$: (a) vertical displacement, (b) strain energy density, (c) local damage.....	191
Figure 5.20 Simulation results for $t = 90 \mu s$ and $\alpha = 60^\circ$: (a) vertical displacement, (b) strain energy density, (c) local damage.....	192
Figure 5.21 Simulation results for $t = 100.5 \mu s$ and $\alpha = 90^\circ$: (a) vertical displacement, (b) strain energy density, (c) local damage.....	193
Figure 5.22 Simulation results for $t = 40 \mu s$ and $\alpha = 30^\circ$: (a) vertical displacement, (b) strain energy density, (c) local damage.....	194

Chapter 1

Introduction

1.1 Background

The governing equation of continuum mechanics is a partial differential equation as given in the following equation

$$\rho \ddot{u} = \nabla \sigma + b \quad (1.1)$$

All solutions to solid mechanics problems, analytical as well as numerical, are based on this governing equation. The divergence of stresses in Eqn. 1.1 requires that the displacement field to be continuous. This requirement cannot be continuously satisfied when cracks occur since new cracks come with new boundaries which require new boundary conditions for solving the partial differential equation. Numerical techniques based on continuum mechanics such as finite element method are commonly used for investigating dynamic crack propagation in structures with complex geometry. However, prior knowledge of crack position and orientation is required. The simulation of dynamic crack propagation can become even more challenging, if not impossible, for fiber composites due to their high inhomogeneity and high anisotropy.

Silling [1] proposed an alternative formulation, so-called peridynamics. Its equation of motion can be expressed as follows

$$\rho \ddot{u} = \int f dV + b \quad (1.2)$$

where ρ is mass density, \ddot{u} is acceleration, f is bond force and b is body force. The bond force f is a function of displacements. The integration in Eqn. 1.2 is applied to the entire domain of

study. In peridynamics, the domain of study is assumed to be organized by points. Each point is connected to all points within its horizon. Eqn. 1.2 can be applied to continuous as well as discontinuous domains such as those with cracks. This ability renders peridynamics more useful for progressive damage analysis than commonly used finite element method which requires constant remeshing of the domain. Besides, peridynamics does not require any additional damage theory such as fracture mechanics since it is essentially based on the bond strength between points.

1.2 Literature review

The peridynamic theory proposed by Silling [1] assumes that all points in a domain of interest are connected by bond forces. A two-point bar model is used in Ref. [1] and the bond force f between the two points is dependent on the positions of the two points. The properties of the bar are related to the properties of the material of the domain. A shear crack propagation is also presented in Ref. [1] to show the benefit of the peridynamic theory. Silling [2] mentioned that peridynamics is similar to molecular dynamics in accounting of all points within a horizon of a point for calculating the internal forces of the point. However, the peridynamic domain is continuous and the grid can be of any size based on numerical consideration. This is a major difference from molecular dynamics in which the points can only be molecules or atoms. Hence, the molecular dynamics cannot be used to solve any solid mechanics problem in reasonable time due to the overwhelmingly large number of molecules involved in any structure. The bar-based peridynamic model is similar to the models proposed by Kunin [3] and Rogula [4] in the investigation of continuum properties of crystals based on interatomic interactions.

Several one-dimensional peridynamic solutions can be found in Refs. [5-8]. The studies include the effects of infinite horizon and comparisons of peridynamic solutions with those from continuum mechanics. Silling, Simmermann and Abeyaratne [5] studied an infinite long bar subject to two concentrated loads. They found the displacements away from the loading points are the same between peridynamic analysis and classical mechanics. However, the peridynamics-based displacements oscillate when points are close to the loading. Weckner and Abeyaratne [6] studied dynamic deformation of an infinite bar with various initial functions. They found the influence of horizon on the results. The displacements were discontinuous even though they started with continuous functions. However, the displacements converged to the classical mechanics solution when horizon approached zero. Silling [9,10] discussed the numerical implementations of peridynamics and EMU code [9]. Bobaru, Yang, Alvels, Silling, Askari and Xu [11] discussed the convergence issues in a one-dimensional static problem. They investigated an infinitely long bar with two concentrated forces by using analytical method and then compared the solution with that from numerical solution. In peridynamic solution, displacement was not continuous at points where forces were applied. There were singularity points (infinite jump). Three convergence techniques were studied in the paper: (1) fixing horizon and increasing the number of nodes in each horizon, (2) decreasing horizon and increasing the number of nodes per horizon and (3) decreasing the horizon and fixing the number of nodes per horizon. In case (1), the numerical solution converged to the analytical solution with a finite displacement jump. In case (2), the numerical solution converged to the peridynamic solution with singularity. In case (3), singularity disappeared when the horizon became zero. The peridynamic solution converged to the solution of classical mechanics when the horizon reduced to zero. However, it is almost impossible to have a zero horizon since the grid size will become

zero. Adaptive refinement of mesh was also discussed to improve the computational efficiency by Silling [12].

Applications of peridynamics for isotropic materials can be found in Refs. [2,9,12-15]. Silling and Bobaru [2] applied peridynamics to one-dimensional fiber structures and two-dimensional membrane structures. They investigated central crack propagation, burst of balloon, and tearing of rectangular sheet. They also simulated deformation of a fiber with different parts of the fiber interacting with each other through van der Waals force. Gerstle, Sau and Silling [13] studied dynamic crack propagation without initial crack in a two-dimensional plate. Silling [9] used EMU code to simulate crack propagation in a two-notch plate under drop weight. These studies showed the advantage of using long-range force in peridynamics for dealing with contact issues. Weckner, Askari and Xu [14] simulated three-dimensional crack branching in a unitized metal structure. Bobaru [15] studied a three-dimensional nano-fiber network using a similar method as that used in Ref. [2]. It was found that there was no need of a separate failure theory in peridynamic analysis.

The application of peridynamics on fiber-reinforced composite materials and the validation of peridynamics with experiments can be found in Refs. [16-18]. Silling, Xu and Askari [16,17] modeled fiber-reinforced composite materials by using two kinds of bonds, fiber bonds and matrix bonds. They then studied central crack and delamination problems. Xu, Askari and Weckner [19] compared the results from Refs. [16,17] with experiment results. Bobaru and Silling [18] modeled composite materials with micro-structure based on the method mentioned in Ref. [2].

The Poisson's ratio in the bar model introduced by Silling [1] and Zimmerman [20] was a fixed value. Gerstle, Sau and Silling [21], however, included pairwise moments in a model to account for various Poisson's ratios. A state-based peridynamic model was proposed in Refs. [22-26]. In this model, there were interactions between two points in two parts. The first part depended on the positions of the two points, similar to the bond-based model. The second part depended on all points in the horizon. Warren, Silling, Askari, Weckner, Epton and Xu [23] studied damage with state-based peridynamics. Silling and Lehoucq [25] defined a stress tensor in peridynamics. When the horizon goes to zero, the stress tensor converged to Piola-Kirchhoff stress tensor. Demmie and Silling [24] simulated gas using only the second part of the state-based peridynamic model.

1.3 Motivations and objectives

Computational methods, such as finite element method, based on Eqn. 1.1 require a continuous displacement field. The information concerning crack location and dimension also need to be known and included in the numerical model prior to computation to avoid imposing exhausted boundary conditions and crack surfaces everywhere in the domain of study. These prerequisites are almost impossible for problems involving dynamic crack propagation in fiber-reinforced composite materials which can have very complex damage configurations. The integral equation based peridynamic theory, on the contrary, does not have any prerequisite since it is essentially based bond force between points. The modeling of the damage process of fiber composites can be benefited from peridynamics since crack can occur whenever bonds break and there is no need of any additional damage theory other than the bond strength.

As a novel theory, peridynamics is still in its infant stage. More advanced models are needed. Analytical verifications and experiment validations are also required for justifying the models. Silling's bar model [10] assumes that two points are linked by a bar and there is only one material property – the modulus - and the Poisson's ratio is limited to be $\frac{1}{4}$ in three-dimensional problems. Silling, Xu and Askari's fiber-reinforced composite material model [16,17] is also based on the bar model. There are only two independent material properties in their models although there are four independent material properties for two-dimensional orthotropic materials and six independent material properties for three-dimensional orthotropic materials.

A new beam model for two-dimensional problems with two independent material properties will be presented in this dissertation research. This model should be capable of simulating isotropic materials with various Poisson's ratios. An orthotropic material model will also be proposed based on the new beam model. There will be four independent material properties in this model to accommodate the four independent material properties in orthotropic materials. With this material model and bond failure criterion, it should be sufficient to simulate dynamic damage crack propagation in fiber composite materials.

1.4 Outline of dissertation

The basic formulation of peridynamics is introduced in Chapter 2. In Chapter 3, one-dimensional equation of motion is investigated. A simple bar model is proposed and the associated material property is identified from energy method. The convergence of the numerical method is then studied. The one-dimensional model can be used to study split Hopkinson's pressure bar (SHPB)

for verification and validation of the bar model. The bar model can also be used for studying two-dimensional problems with a fixed Poisson's ratio. In Chapter 4, a beam model is proposed to simulate two-dimensional isotropic materials. The beam model is able to capture various Poisson's ratios. The verification of numerical studies requires a comparison with an analytical solution based on classical mechanics. A failure theory is then established with the use of energy method. The failure theory is subsequently used for investigating three problems concerning dynamic damage propagation. The results are validated by experiment results from literature. A model for anisotropic materials is proposed in Chapter 5, in which there are four independent material properties. This model is verified by a static problem and a dynamic vibration problem. The dynamic damage propagation in composites is then simulated by the proposed four-parameter model and the results are validated by experiment results from published works.

REFERENCES

References

- [1] Silling, S. A., Reformulation of elasticity theory for discontinuities and long-range forces, *J. Mech. Phys. Solids*, **48**, 175-209 (2000)
- [2] Siling. S. A., Bobaru, F., Peridynamic modeling of membranes and fibers. *Int. J. Non-linear Mech.*, **40**, 395-409 (2005)
- [3] Kunin, I. A., *Elastic Media with Microstructure I: One-dimensional Models*, pp. 27. Springer, Berlin (1982)
- [4] Rogula, D., *Nonlocal Theory of Material Media*, pp. 137-149 and 243-278. Springer, Berlin (1982)
- [5] Siling, S. A., Simmermann, M., Abeyaratne, R., Deformation of a peridynamic bar. *J. Elast.*, **73**, 173-190 (2003)
- [6] Weckner, O., Abeyaratne, R., The effect of long-range forces on the dynamics of a bar. *J. Mech. Phys. Solids*, **53**, 705-728 (2005)
- [7] Weckner, O., Emmrich, E., Numerical simulation of the dynamics of a nonlocal, inhomogeneous, infinite bar. *J. Comput. Appl. Mech.*, **6**, 311–319 (2005)
- [8] Meerich, E., Weckner, O. Analysis and Numerical Approximation of an Integro-differential Equation Modeling Non-local Effects in Linear Elasticity, *Mathematics and Mechanics of Solids*, **12**, 363-384, 2007
- [9] Silling, S.A., Dynamic fracture modeling with a meshfree peridynamic code, *Computational Fluid and Solid Mechanics*, 641–644, Elsevier, Amsterdam (2003)
- [10] Silling, S.A., Askari, E., A meshfree method based on the peridynamic model of solid mechanics. *Comput. Struct.*, **83**, 1526–1535 (2005)
- [11] Bobaru, F., Yang, M., Alvels, L. F., Silling, S. A., Askari, E. Xu, J., Convergence, Adaptive Refinement, and Scaling in 1D Peridynamics, *International Journal for Numerical Methods in Engineering*, **77**, 852-877 (2009)
- [12] Bobaru, F., Alves, L., Silling, S., Askari, A., Dynamic Crack Branching and Adaptive Refinement in Peridynamics, 8th World Congress on Computational Mechanics, June 30-July 5, 2008, Venice, Italy
- [13] Gerstl, W., Sau, N., Silling, S., Peridynamic modeling of plain and reinforced concrete structures. In: 18th International Conference on Structural Mechanics and Reactor Technology (SMiRT 18), Beijing, China, SMiRT18-B01-2(2005)

- [14] Weckner, O., Askari, A., Xu, J., Damage and Failure Analysis Based on Peridynamics-Theory and Applications, 48th AIAA/ASME/ASCE/AHA/ASC Structures, Structural Dynamics, and Materials Conference, April 23-26, 2007, Honolulu, Hawaii
- [15] Bobaru, F., Influence of van der Waals Forces on Increasing the Strength and Toughness in Dynamic Fracture of nanofiber Networks: a Peridynamic Approach, Modeling and Simulation in Materials Science and Engineering, **15**, 397-417 (2007)
- [16] Silling, S. A., Xu, J. Askari, E., Peridynamic modeling of impact damage. In: Moody, F.J. Problems Involving Thermal-Hydraulics, Liquid Sloshing, and Extreme Loads on Structures, **489**, 197-205, American Society of Mechanical Engineers, New York (2004)
- [17] Askari, A., Xu, J., Silling, S., Peridynamic analysis of damage and failure in composite. In: 44th AIAA Aerospace Sciences Meeting and Exhibit, Reno, Nevada, AIAA-2006-88 (2006)
- [18] Bobaru, F., Silling, S.A., Peridynamic 3D models of nanofiber networks and carbon nanotub-reinforced composites. In: Materials Processing and Design: Modeling, Simulation, and Applications– NUMIFORM 2004 – American Institute of Physics Conference Proceedings, **712**, 1565–1570 (2004)
- [19] Xu, J., Askari, A., Weckner, O., Damage and Failure Analysis of Composite laminates under Biaxial Loads, 48th AIAA/ASME/ASCE/AHA/ASC Structures, Structural Dynamics, and Materials Conference, April 23-26, 2007, Honolulu, Hawaii
- [20] Zimmermann, M., A Continuum Theory with Long-Range Forces for Solids, PhD dissertation, Massachusetts Institute of Technology (2005)
- [21] Gerstle, W., Sau, N., Silling, S., Peridynamic modeling of concrete structures, Nucl. Eng. Des., **237**, 1250-1258 (2007)
- [22] Silling, S., Epton, M., Weckner, O., Xu, J., Askari, E., Peridynamic States and Constitutive Modeling, Journal Elasticity, **88**, 151-184 (2007)
- [23] Warren, T., Silling, A. S., Askari, Weckner, O., Epton, A., Xu, J., A Non-ordinary State-based Peridynamic Method to Model Solid Material Deformation and Fracture, International Journal of Solids and Structures, **46**, 1186-1195 (2009)
- [24] Demmie, P., Silling, A., An Approach to Modeling Extreme Loading of Structures Using Peridynamics, Journal of Mechanics of Materials and Structures, **2**, No. 10 (2007)
- [25] Bobaru, F., Yang, M., Alvels, L. F., Silling, S. A., Askari, E. Xu, J., Convergence, Adaptive Refinement, and Scaling in 1D Peridynamics, International Journal for Numerical Methods in Engineering, **77**, 852-877 (2009)
- [26] Lehoucq, R., Silling, S., Force Flux and the Peridynamic Stress Tensor, Journal of the Mechanics and Physics of Solids, **56**, 1566-1577 (2008)

Chapter 2

Basic Formulations

2.1 Peridynamic model of a continuum

The acceleration of any particle at \mathbf{x} in the reference configuration at time t can be expressed by the following equation [1]

$$\rho \ddot{\mathbf{u}}(\mathbf{x}, t) = \int \mathbf{f}(\mathbf{u}(\mathbf{x}', t) - \mathbf{u}(\mathbf{x}, t), \mathbf{x}' - \mathbf{x}) dV_{\mathbf{x}'} + \mathbf{b}(\mathbf{x}, t) \quad (2.1)$$

where \mathbf{u} is displacement, \mathbf{b} is body force density, ρ is mass density and \mathbf{f} is force per volume square which exerts on particle \mathbf{x} by particle \mathbf{x}' . Fig. 2.1 shows the relation.

The relative position of these two particles in the reference configuration is denoted by $\boldsymbol{\xi}$, i.e.

$$\boldsymbol{\xi} = \mathbf{x}' - \mathbf{x} \quad (2.2)$$

while the relative displacement is denoted by $\boldsymbol{\eta}$, i.e.

$$\boldsymbol{\eta} = \mathbf{u}(\mathbf{x}', t) - \mathbf{u}(\mathbf{x}, t) \quad (2.3)$$

Accordingly, $\boldsymbol{\xi} + \boldsymbol{\eta}$ represents the current relative position vector between the two particles in the current configuration as shown in Fig. 2.2.

It is convenient to assume that there exists a positive number δ , called horizon, also shown in Fig. 2.1, such that the force \mathbf{f} vanishes when $|\boldsymbol{\xi}|$ is greater than δ , i.e.

$$|\boldsymbol{\xi}| > \delta \Rightarrow \mathbf{f}(\boldsymbol{\eta}, \boldsymbol{\xi}) = 0 \quad \forall \boldsymbol{\eta} \quad (2.4)$$

The domain of the integration in Eqn. 2.1 should be the spherical neighborhood of \mathbf{x} with a

radius equal to δ .

Bases on the conservation of angular momentum, the following equation should hold

$$(\xi + \eta) \times f(\eta, \xi) = 0 \quad \forall \xi, \eta \quad (2.5)$$

That is

$$f(\eta, \xi) = \hat{f}(\eta, \xi) \cdot (\xi + \eta) / |\xi + \eta| \quad (2.6)$$

where $\hat{f}(\eta, \xi)$ is a scalar function. This is to say, the force vector between the two particles is parallel to their current relative position vector.

The natural boundary condition and external forces are applied through the body force density \mathbf{b} . They can be made nonzero within a boundary layer. The thickness of the boundary layer is commonly assumed to be equal to the horizon δ .

2.2 Constitutive modeling

If the material of interest is isotropic, \hat{f} from Eqn. 2.6 does not depend on the direction of ξ . For simplicity, it can be assumed that the scalar bond force \hat{f} depends only on the bond stretch, s , defined by

$$s = \frac{|\xi + \eta| - |\xi|}{|\xi|} \quad (2.7)$$

where s is positive when the bond is in tension and negative when the bond is in compression.

Accordingly,

$$\hat{f} = c \cdot s \quad (2.8)$$

where c is stiffness which depends on both material and the geometrical property of the material.

A material is said to be micro-elastic [1] if the force function is derivable from a scalar micro-potential w_b :

$$f(\boldsymbol{\eta}, \boldsymbol{\xi}) = \frac{\partial w_b(\boldsymbol{\eta}, \boldsymbol{\xi})}{\partial \boldsymbol{\eta}} \quad \forall \boldsymbol{\xi}, \boldsymbol{\eta} \quad (2.9)$$

The micro-potential is the energy in a single bond and has the dimension of energy per unit volume square. The energy per unit volume at a given point, i.e. the strain energy density, then becomes

$$W = \frac{1}{2} \int w_b(\boldsymbol{\eta}, \boldsymbol{\xi}) dV_{\boldsymbol{\xi}} \quad (2.10)$$

The domain of integration is the same as that of Eqn. 2.1. The factor of $\frac{1}{2}$ is imposed because each point of a bond owns only half the energy in the bond.

2.3 Failure criterion

The bond between two particles will break if they are stretched beyond a critical value s_0 defined as the critical stretch. Once the bond fails, there is no tensile force between the two points. The force function $\hat{f}(\boldsymbol{\eta}, \boldsymbol{\xi})$ can be modified as history dependent:

$$\hat{f}(\boldsymbol{\eta}, \boldsymbol{\xi}) = c \cdot s \cdot \mu(t, \boldsymbol{\xi}) \quad (2.11)$$

where μ is a history-dependent scalar function, i.e.

$$\mu(t, \boldsymbol{\xi}) = \begin{cases} 1 & \text{if } s(t', \boldsymbol{\xi}) < s_0 \text{ for all } 0 \leq t' \leq t \\ 0 & \text{if } s(t', \boldsymbol{\xi}) \geq s_0 \text{ for any } 0 \leq t' \leq t \end{cases} \quad (2.12)$$

The damage at a point can be defined by a function $\varphi(\boldsymbol{x}, t)$, where

$$\varphi(\boldsymbol{x}, t) = 1 - \frac{\int \mu(t, \boldsymbol{\xi}) dV_{\boldsymbol{\xi}}}{\int dV_{\boldsymbol{\xi}}} \quad (2.13)$$

The domain of integration is the same as that of Eqn. 2.1. Note that $0 \leq \varphi \leq 1$, where 0 represents virgin material and 1 represents complete disconnection of the point from all points with which it initially interacted. A value of φ should be defined as the criterion of the beginning of the crack (discontinuity in displacement). A value of 0.3 is used in [2].

2.4 Numerical method

The force function f is usually very complex for integration. Numerical integration hence should be used. To begin with, the integral form of Eqn. 2.1 is replaced by a finite summation

$$\rho \ddot{u}_i^n = \sum_p f(u_p^n - u_i^n, x_p - x_i) V_p + b_i^n \quad (2.14)$$

where superscript n is the integration step number, V_p is the volume of node p and subscripts i denotes the node number as shown in Fig. 2.3. The summation is taken over all nodes p such that

$$|x_p - x_i| \leq \delta \quad (2.15)$$

After obtaining \ddot{u}_i^n at each point, the displacement of the next integration step u_i^{n+1} can be found from the formula for finite difference, i.e.

$$\ddot{u}_i^n = \frac{\frac{u_i^{n+1} - u_i^n}{\Delta t} - \frac{u_i^n - u_i^{n-1}}{\Delta t}}{\Delta t} = \frac{u_i^{n+1} - 2u_i^n + u_i^{n-1}}{(\Delta t)^2} \quad (2.16)$$

Fig. 2.4 shows the flow chart of the numerical program.

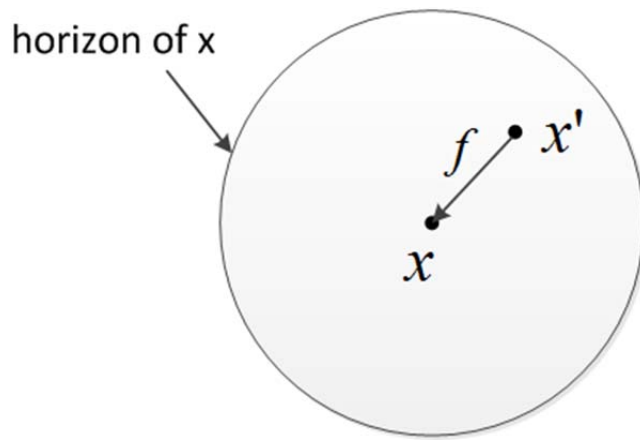


Figure 2.1 Horizon of point x .

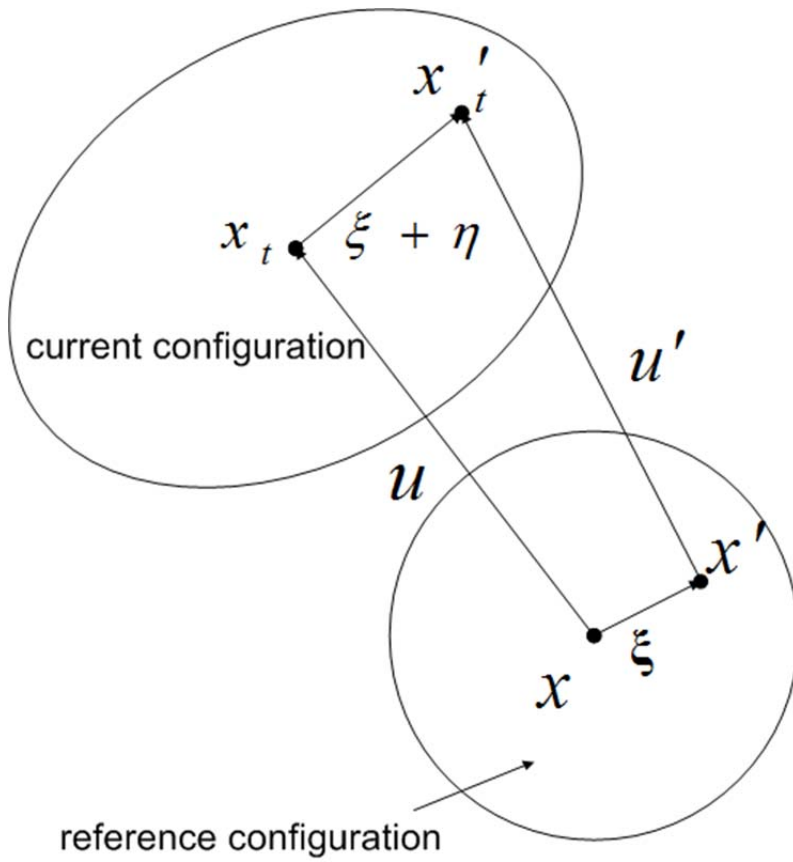


Figure 2.2 Reference configuration and current configuration.

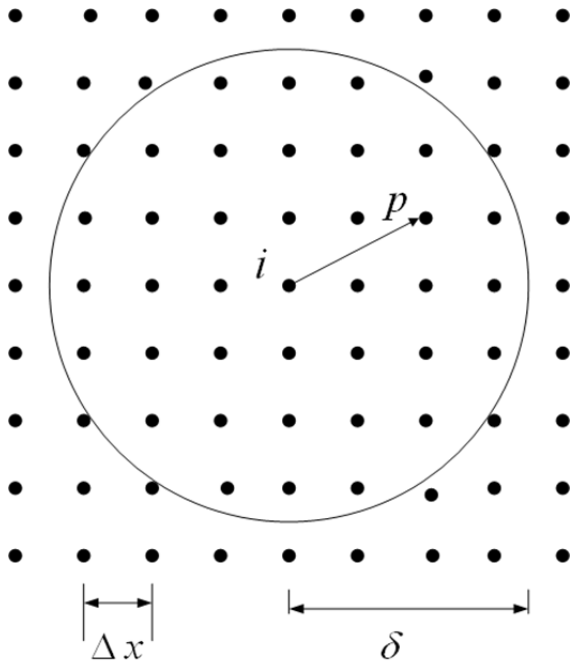


Figure 2.3 Finite summation domain in numerical computation.

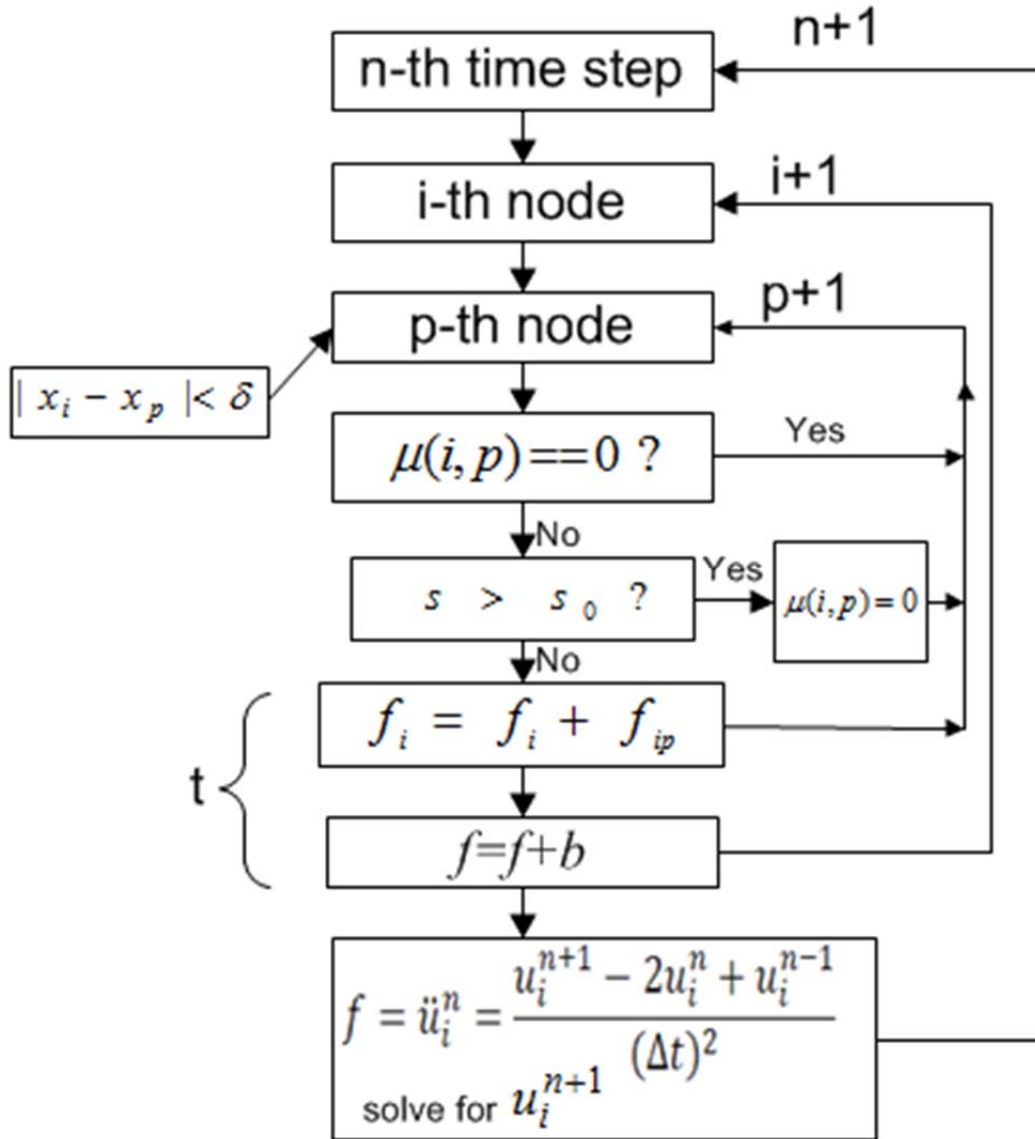


Figure 2.4 Flow chart of a peridynamic program.

REFERENCES

References

- [1] Silling, S. A., Reformulation of elasticity theory for discontinuities and long-range forces, *J. Mech. Phys. Solids*, **48**, 175-209 (2000)
- [2] Silling, S.A., Askari, E., A meshfree method based on the peridynamic model of solid mechanics. *Comput. Struct*, **83**, 1526–1535 (2005)

Chapter 3

One-Dimensional Wave Propagation Analysis

3.1 Identification of stiffness

Based on the peridynamic theory established in Chapter 2, this chapter investigates one-dimensional wave propagation. To obtain the peridynamic equation of motion for the one-dimensional problem, consider a bar with a length L and a constant cross-sectional area A . Eqn. 2.1 is integrated over the cross-section and divided by A , resulting in

$$\rho \ddot{u}(x, t) = \int f(x, x', t) dx' + b \quad (3.1)$$

$$u(x_1, t) = \frac{1}{A} \int u_1(x, t) dA \quad (3.2)$$

$$b(x_1, t) = \frac{1}{A} \int b_1(x, t) dA \quad (3.3)$$

$$f(x_1, x'_1, t) = \frac{1}{A} \iint f_1(x, x', t) dA' dA \quad (3.4)$$

where $x \equiv x_1$ and $dV' = dA' \cdot dx'$ are used. The bond force f is expressed in terms of force per unit length per unit volume, e.g. N/m^4 .

A simple model of the bond force can be expressed as

$$f = c \cdot s \quad (3.5)$$

where c is stiffness and s is stretch. To find c , it is necessary to find the strain energy density from peridynamics and set it equal to that used in classical mechanics.

Consider a bar under a uniform stretch of s . Based on the bond micro-potential of Eqn. 2.9, integrate f to find

$$w_b = \frac{c \cdot |\eta|^2}{2 \cdot |\xi|} = \frac{c \cdot s^2 \cdot |\xi|}{2} \quad (3.6)$$

This is the energy in one bond. From Eqn. 2.10, the strain energy density based on peridynamic analysis becomes

$$W = \frac{1}{2} \int_{-\delta}^{+\delta} w_b d\xi = \frac{1}{2} \int_{-\delta}^{+\delta} \frac{c \cdot s^2 \cdot |\xi|}{2} d\xi = \frac{c \cdot s^2 \cdot \delta^2}{4} \quad (3.7)$$

The strain energy density from classical mechanics is $\frac{1}{2}Es^2$. Setting it equal to that obtained from peridynamic analysis, i.e. Eqn. 3.7, the stiffness c in Eqn. 3.5 can be found to be

$$c = \frac{2E}{\delta^2} \quad (3.8)$$

3.2 Definition of stress in peridynamics

One way to verify a peridynamic model is to compare it with the associated term in classical mechanics. Most classical mechanics results are presented by stresses. Therefore, to verify peridynamics, it is useful to define stress in peridynamics and compare it with the classical mechanics counterpart. This definition is for comparison purpose only since stress is not commonly used in peridynamics. As shown in Fig. 3.1, the stress at a point x is defined as the force connecting the two half-domains together at point x , i.e. the summation of all positive bond forces crossing the point x .

$$\sigma = \int_0^\delta \int_0^{\delta-h} c \cdot s dx dh = \frac{cs\delta^2}{2} = E \cdot s \quad (3.9)$$

where stiffness c is defined in Eqn. 3.8. Hence, the stress in peridynamics, shown in Eqn. 3.9, is exactly the same as that in classical mechanics.

3.3 Comparison with analytical solution

Consider the wave propagation in a one-dimensional bar due to an initial uniform strain ε_0 , as depicted in Fig. 3.2. Both ends of the bar are assumed to be free of load.

3.3.1 Analytical solution

The equation of motion for the bar [1] is

$$\frac{\partial^2 u}{\partial t^2} - \frac{E}{\rho} \frac{\partial^2 u}{\partial x^2} = 0 \quad (3.10)$$

where u is displacement, t is time, E is Young's modulus, ρ is density and x is position.

The boundary conditions are

$$\frac{\partial u}{\partial x}(0, t) = 0 \quad (3.11)$$

$$\frac{\partial u}{\partial x}(L, t) = 0 \quad (3.12)$$

where L is the length of the bar.

The initial conditions are

$$u(x, 0) = \varepsilon_0 x \quad (3.13)$$

$$\dot{u}(x, 0) = 0 \quad (3.14)$$

Using the method of separation of variables, the displacement can be expressed as a product of position x and time t , i.e.

$$u(x, t) = X(x)T(t) \quad (3.15)$$

Substituting Eqn. 3.15 into Eqn. 3.10, it yields

$$\frac{T''}{T} = \frac{E}{\rho} \frac{X''}{X} \quad (3.16)$$

Since the left-hand side of the equation is dependent on t only and the right-hand side of the equation is dependent on x only, both sides of Eqn. 3.16 then must be equal to a constant, such as $-\omega^2$.

Rewrite Eqn. 3.16 as

$$T'' + \omega^2 T = 0 \quad (3.17)$$

$$X'' + \lambda^2 X = 0 \quad (3.18)$$

where $\lambda^2 = \frac{\rho}{E} \omega^2$.

A general solution of Eqn. 3.17 is

$$T = A \sin \omega t + B \cos \omega t \quad (3.19)$$

In order to satisfy the initial condition of Eqn. 3.14, $A = 0$. Similarly, a general solution of Eqn. 3.18 is

$$X = C \sin \lambda x + D \cos \lambda x \quad (3.20)$$

In order to satisfy the boundary condition given in Eqn. 3.11, $C = 0$. Similarly, in order to satisfy the boundary condition given in Eqn. 3.12, $\sin \lambda L = 0$. Hence,

$$\lambda L = i\pi, i = 0, 1, 2, 3, \dots$$

Redefine

$$\lambda_i = \frac{i\pi}{L}, i = 0, 1, 2, 3, \dots \quad (3.21)$$

The solution to Eqn. 3.10 can be expressed as

$$u(x, t) = \sum_{i=0}^{\infty} A_i \cos \lambda_i x \cos \omega_i t \quad (3.22)$$

where ω in Eqn. 3.19 has been replaced by ω_i ($i = 0, 1, 2, 3, \dots$) and a new coefficient A_i has been installed.

Eqn. 3.13 can be rewritten as

$$\sum_{i=0}^{\infty} A_i \cos \lambda_i x = \varepsilon_0 x \quad (3.23)$$

In order to find A_i in Eqn. 3.23, multiply both sides of the equation with $\cos \lambda_k x$ and integrate them from 0 to L , i.e.

$$A_k \int_0^L \cos \lambda_k x \cdot \cos \lambda_k x \, dx = \int_0^L \varepsilon_0 x \cos \lambda_k x \, dx \quad (3.24)$$

Hence,

$$A_k = \frac{2\varepsilon_0}{L\lambda_k^2} [(-1)^k - 1] \quad (3.25)$$

$$u = \frac{2}{L} \varepsilon_0 \sum_{i=0}^{\infty} [(-1)^i - 1] \frac{1}{\lambda_i^2} \cos \lambda_i x \cdot \cos \omega_i t \quad (3.26)$$

$$\varepsilon = \frac{\partial u}{\partial x} = \frac{2}{L} \varepsilon_0 \sum_{i=0}^{\infty} [1 - (-1)^i] \frac{1}{\lambda_i} \sin \lambda_i x \cdot \cos \omega_i t \quad (3.27)$$

in which $\lambda_i = \frac{i\pi}{L}$ and $\omega_i = \sqrt{\frac{E}{\rho}} \lambda_i$.

This analytical solution will be used to justify numerical solutions based on peridynamics. It will also be used to study the convergence of parameters used in peridynamic analysis. Fig. 3.3 shows the strain history of a bar under an initial strain of 0.0001. The bar is made of a material with Young's modulus $E = 193 \text{ GPa}$ and density $\rho = 8027 \text{ kg/m}^3$. The ripples at the corners are due to Gibbs phenomenon [2], which states that the truncated Fourier series of a discontinuous signal will exhibit high frequency ripples and overshoot near the discontinuities. The overshoot does not die out as the frequency increases, but approaches a finite limit.

3.3.2 Numerical studies

Three parameters are involved in the peridynamic numerical analysis. They are the time step dt , the size of horizon δ and the number of nodes within the horizon m . Fig. 3.4 shows a one-dimensional peridynamic model and the associated horizon. When solving the peridynamic problem and comparing its results with those obtained from classical mechanics analysis, it is found that the magnitudes of waves from both analyses are always the same. However, the wave speed and wave period vary with m and δ . Table 3.1 shows the wave periods based on nine combinations of m and δ .

Based on theory of vibration, the wave period in the bar is equal to

$$2 \times \frac{L}{\sqrt{E/\rho}} = 0.41 \text{ ms} \quad (3.28)$$

where L is the bar length and $\sqrt{E/\rho}$ is wave speed.

Table 3.1 Wave period (*ms*) based on various of *m* and δ

$\delta \backslash m$	1 mm	5 mm	10mm
1	0.2912	0.2893	0.2873
5	0.3761	0.3747	0.3732
10	0.3827	0.3915	0.3903

Comparing the peridynamic results given in Table 3.1 with that from vibration theory, the numerical solution becomes closer to the analytical solution when the number of nodes within the horizon (*m*) increases, i.e., the distance between nodes decreases. Besides, when *m* is fixed, the peridynamic solution becomes closer to the classical mechanics solution if the horizon δ decreases. This result is thought to be due to the fact that classical mechanics is based on contact force. When δ decreases, the bond force in peridynamics becomes closer to the contact force in classical mechanics and the peridynamics solution converges to the classical mechanics solution. It then seems to be ideal to use small δ and large *m* in peridynamic analysis. However, this will pose a significant increase in computational time. Fig. 3.5 shows comparison between classical mechanics and peridynamic analysis. Numerical studies based on $\delta = 2.2 \text{ mm}$ and $dx = 0.5 \text{ mm}$ (with *m* = 4) give peridynamic results within 1.2% of discrepancy from that of classical mechanics. The convergence of time step based on these parameters is also shown in Fig. 3.6. As long as *m* and δ are fixed, the result does not vary too much with the change of time step. Consequently, $dt = 1 \times 10^{-7} \text{ s}$, $dx = 0.5 \text{ mm}$ and $\delta = 2.2 \text{ mm}$ will be used in subsequent numerical investigations.

3.4 Comparison with experiment results

For studying one-dimensional wave propagation, the commonly used split Hopkinson's pressure bar (SHPB) [3] is taken as an example in this study. SHPB consists of three bars, a striker bar, an incidence bar and a transmission bar as shown in Fig. 3.7. It is commonly used for characterizing material constitutive relations. Table 3.2 shows an example of dimensions and material properties of bars used in SHPB. The results from the experiments based on SHPB can be used to justify the peridynamic analysis.

Table 3.2 Dimensions and material properties of the SHPB in Fig. 3.7

	Striker	Incidence bar	Transmission bar
Length	191 mm	991 mm	724 mm
Diameter	13 mm	13 mm	13 mm
Young's modulus	193 GPa	193 GPa	193 GPa
Mass density	8027 kg/m^3	8027 kg/m^3	8027 kg/m^3

In performing the SHPB test, a specimen is placed in between the incidence bar and the transmission bar. The striker is then accelerated to collide with the incidence bar, creating a strain wave. The strain wave will propagate through the two bars and rebound from any surface between any two bars. A pair of strain gages are installed on each of the incidence bar and transmission bar to record the strain wave history. From the strain wave, the dynamic stress-strain curve of the specimen can be identified.

When the striker bar is fired onto the incidence bar, it creates a constant pressure over a period of

time. The strain wave then propagates toward the specimen with partial transmission into the specimen and partial reflection from the specimen, which has different material properties and cross-sectional areas than the split bars as shown in Fig. 3.8. The reflected strain ε_r is related to the strain in the specimen ε by the following relation

$$\frac{d\varepsilon}{dt} = -\frac{2\sqrt{E/\rho}}{L}\varepsilon_r \quad (3.29)$$

where E , ρ and L are Young's modulus, mass density and length of the incidence bar, respectively. The transmitted strain ε_t is related to the stress in the specimen σ by the following relation

$$\sigma = E \frac{A_0}{A} \varepsilon_t \quad (3.30)$$

where E and A are Young's modulus and cross-sectional area of the transmission bar and A_0 is the original cross-sectional area of the specimen. The stress-strain relation of the material can then be found from Eqn. 3.29 and Eqn. 3.30.

The goal of this study is to validate peridynamic models and associated computational results with experiment results from SHPB tests, i.e. validation of theory by experiment. Hence, materials with known properties will be used as input for peridynamic analysis. The strain history in the incidence bar and the transmission bar will be computed based on peridynamics and the results will be compared with the experiment results.

3.4.1 Square wave input

A perfect impact between a striker bar and an incidence bar can result in a square-shaped pulse with a stress magnitude $\sigma = \frac{V\rho C_0}{2}$ and a duration $T = 2\frac{L_s}{C_0}$, where V , ρ , C_0 and L_s are velocity

before impact, mass density, wave velocity and length of the striker bar. In peridynamic analysis, the constant pressure $\sigma = \frac{V\rho C_0}{2}$ and duration $T = 2\frac{L_s}{C_0}$, shown in Fig. 3.9, are used as input in the computational program.

Study One - one bar

In this study, no specimen is used and the transmission bar is isolated from the incidence bar, resulting in only wave propagation in the incidence bar. Experiment results and computational results are shown in Fig. 3.10 for comparison.

Study Two - two bars

In this study, no specimen is used and the incidence bar and the transmission bar are put in contact with each other as shown in Fig. 3.11. The testing results are compared with peridynamic simulation as shown in Fig.3.12. They are the strain histories of the incidence bar and the transmission bar. One obvious observation is that the majority of the wave enters the transmission bar with only a small portion of approximately 12% reflected. At the end of wave propagation, the two bars separate from each other.

Based on theoretical analysis, the wave period in the transmission bar is

$$2 \times \frac{L_t}{v_c} = 2.95 \times 10^{-4} s \quad (3.31)$$

where L_t is the length of transmission bar and v_c is the wave velocity. The experiment measurement gives an average wave period of $2.99 \times 10^{-4} s$, which is 1.4% higher than the theoretical value, while the peridynamic simulation gives an average of $3 \times 10^{-4} s$, which is

1.7% higher than the theoretical value.

In the peridynamic simulation of SHPB, the bond force crossing the interface between two bars can only be negative, otherwise the two bars will separate. At each time step of calculation, the stretch of the bond between the two bars is calculated. If the stretch is greater than zero, it implies there is a separation between two bars. Hence, the bond force is set to zero. When the bond stretch is negative, the bond force can then be calculated by Eqn. 3.5. Using this technique, there will be no interaction between the incidence bar and the transmission bar when they are separated. The comparison between the simulation and experiment for the transmission bar shows good agreement. The periods also match well even after several periods. However, the comparison for the incidence bar shows a discrepancy. Oscillations on the incidence bar do not look like reflection waves. They are smaller than the reflection wave shown in Fig. 3.12.

In the experiment of SHPB, a layer of grease may be applied to the interface between two bars to promote the continuity of wave propagation. The effect of the grease layer on the wave propagation should then be considered in the investigation. The testing result given in Fig. 3.13 shows almost no reflection in the incidence bar, implying the complete wave transmission through the grease layer to the transmission bar.

Study Three – specimen with different property

The wave propagation through an interface can be affected by the material change and the cross-sectional area change across the interface. Both the changes can cause wave reflection on the interface. This study investigates the effect of material change on the wave propagation. A study

model given in Fig. 3.14 is used for the study. In identifying the interfacial bond force, it is necessary to determine a composite stiffness c , given in Eqn. 3.5 and a composite cross-sectional area A , given in Eqn. 3.2. The composite stiffness c can be expressed in terms of the individual stiffness on c_1 and c_2 on both sides of the interface with the coordinate x_3 and the displacement u_3 of the interface.

The bond force for material with stiffness equal to c_1 is defined as

$$f_1 = c_1 \frac{u_3 - u_1}{x_3 - x_1} \quad (3.32)$$

while that for material with stiffness c_2 is defined as

$$f_2 = c_2 \frac{u_2 - u_3}{x_2 - x_3} \quad (3.33)$$

Both of them should be equal to the composite bond force, i.e.

$$f = f_1 = f_2 = c \frac{u_2 - u_1}{x_2 - x_1} \quad (3.34)$$

Solving for c , it yields

$$c = \frac{1}{\frac{x_3 - x_1}{c_1(x_2 - x_1)} + \frac{x_2 - x_3}{c_2(x_2 - x_1)}} \quad (3.35)$$

In order to demonstrate the effect due to the change of material across an interface, an aluminum specimen with a cross-sectional area identical to that of SHPB (Fig. 3.15) is used. The specimen is made of AL6061 with a Young's modulus of 69 GPa and a mass density of 2700 kg/m^3 .

Results are shown in Fig. 3.16 for comparison. The simulation results match reasonably well with the experiment counterparts. The technique for modeling an interfacial bond joining different materials is thus validated.

Study Four – specimen with smaller cross-sectional area

This study investigates the effect of different cross-sectional areas across an interface on the wave propagation. A specimen made of Steel 347, identical to that used for the SHPB is used. The diameter of the specimen is 10 *mm* and the length of it is 26 *mm*. Since the specimen diameter is smaller than the incidence bar diameter, the bond stiffness of the specimen should be modified with the area ratio between them, i.e.

$$c = \frac{2E}{\delta^2} \times \frac{A_{specimen}}{A_{incident}} \quad (3.37)$$

Once the specimen bond stiffness is defined, the composite bond stiffness can be found from Eqn. 3.35. The result is given in Fig. 3.18.

3.4.2 Using filter for computational results

All the four computational results given above match reasonably well with their experiment counterparts. However, it is necessary to point out that the computational results always show square waves with overshoots around the corners when a square wave as shown Fig. 3.9 is used as input. The experiment results, however, show trapezoidal waves with smooth, low shoulders. The overshoots are likely due to numerical process while the low shoulders are likely due to the bandwidth limit of data acquisition system. The sharp rise of the square wave is of a very high frequency signal. It is almost impossible to have a perfectly square wave in experiment since all

electrical devices work as low-pass filters and they have a limited bandwidth. Based on this reality, a filter is added to the following computational investigations.

The Fourier transform for a discrete-time function [2] is

$$X(\omega) = \sum_{n=-\infty}^{+\infty} x[n]e^{-j\omega n} \quad (3.38)$$

The inverse Fourier transform, back to time domain, is

$$x[n] = \frac{1}{2\pi} \int_{2\pi} X(\omega) e^{j\omega n} d\omega \quad (3.39)$$

where ω is the frequency. If the high frequency part of function $X(\omega)$ is cut off and Eqn. 3.39 is added to transform back to the time domain, a low-pass filter can be achieved. In computation, Matlab function *fft* [4] shown below may be used

$$Y = \text{fft}(\text{strain}) \quad (3.40)$$

where *strain* is the strain history vector and $Y(j)$ is the magnitude of the j -th frequency term.

Once a cutoff value is set, the first k components of Y can be used to find a new strain history by inverse Fourier transform function *ifft* [5], i.e

$$\text{newStrain} = \text{ifft}(Y, k) \quad (3.41)$$

Simulation results for Study One, Study Two, Study Three and Study Four with filters are compared with experiment results. Fig. 3.19, Fig. 3.20, Fig. 3.21 and Fig. 3.22 show the comparisons. The cut-off frequency used is 100 MHz. As can be seen from the four sets of comparison, the computational results with filters are of trapezoidal shape and the overshoots are smaller. The numerical solutions match more favorably with the experiment results with the use

of filter.

3.4.3 Using the incidence wave as the computational input

Another source to cause the discrepancies between the computational simulations and the experiment results is likely due to the imperfect impact between the striker bar and the incidence bar. The computational study is based on a perfect impact while the experiment study is not. One way to eliminate the discrepancy is to use the incidence wave from experiment as input for computation. Take Study Two as an example, the incidence wave can be extracted from the experiment shown in Fig. 3.23. It then can be used as the input wave for the computational study. The computational result is given in Fig. 3.25. The computational result is almost the same as the experiment result. With the incidence waves from experiments as the computational inputs, computational simulations for Study One, Study Two, Study Three and Study Four are shown in Fig. 3.24, Fig. 3.25, Fig. 3.26 and Fig. 3.27, respectively. The results between experiments and computations match very well.

3.5 Simulation with a striker

All simulations given above use a mathematical stress function as the input pressure. The function is either a perfect square function or an incidence wave from an experiment. The simulations do not model the impact process between the striker bar and the incidence bar. To simulate and validate the true impact process, an impact bar system shown in Fig. 3.28 is considered. Only a striker bar and an incidence bar are needed for investigating the incident wave created by the impact. Their dimensions and material properties are listed in Table 3.3. A velocity sensor is installed right before the incidence bar to monitor the striker velocity right

before the impact.

Table 3.3 Dimensions and material properties of the split bar in Fig. 3.28

	Striker	Incidence bar
Length	491 <i>mm</i>	2743 <i>mm</i>
Diameter	25.4 <i>mm</i>	25.4 <i>mm</i>
Young's modulus	227.26 <i>GPa</i>	227.26 <i>GPa</i>
Mass density	7610.5 <i>kg/m³</i>	7610.5 <i>kg/m³</i>

The simulation begins when the striker just touches the incidence bar without causing any deformation to the incidence bar. It is a two-bar problem with the striker bar having an initial velocity while the incidence bar stays static.

From the velocity sensor, the striker has a velocity of 4.12 *m/s* right before impact. The strain history in the incidence bar after the impact is recorded by the strain gages mounted on it. In simulation, the velocity of 4.12 *m/s* is the only input for the computation, i.e. all nodes within the striker bar (491 *mm*) have an initial velocity of 4.12 *m/s*. Fig. 3.30 shows the comparison between the experiment and the simulation. Results from simulation with a stress input, similar to Study One, is also presented in Fig. 3.30. The two simulation results are exactly the same.

Another way to verify the aforementioned results is to study the impact of two bars using classical mechanics. Consider a short cylindrical bar, with a length L_s , a cross-sectional area of A_s and a mass density of ρ_s , is travelling to a long cylindrical bar with a cross-sectional area of

A_i and a mass density of ρ_i . Right before the impact, the short bar has a velocity of V_0 and both bars are stress free as shown in Fig. 3.31. After impact (Fig. 3.32), a compressive wave travels in both bars. Two conditions must be satisfied at the interface between the two bars. The first condition is the continuity of velocity. If the interface velocity after the impact is V , the particle velocity at the interface of the short bar is V_s . The following relation holds for V , V_0 and V_s .

$$V = V_0 - V_s \quad (3.42)$$

The particle velocity at the interface of the long bar is V_i , i.e.

$$V = V_i \quad (3.43)$$

Combining Eqn. 3.42 and Eqn. 3.43, it yields

$$V_i = V_0 - V_s \quad (3.44)$$

Another condition which must be satisfied is the balance of forces at the interface, i.e.

$$F_s = F_i \quad (3.45)$$

where F_s and F_i are axial forces on the short bar and long bar, respectively. The relation between the particle velocity and the axial force can be derived from wave theory as follows

$$\sigma_s = \rho_s c_s \frac{\partial u_s}{\partial t} \quad (3.46)$$

where $\sigma_s = \frac{F_s}{A_s}$, $V_s = \frac{\partial u_s}{\partial t}$ and $c_s = \sqrt{\frac{E_s}{\rho_s}}$.

$$\sigma_i = \rho_i c_i \frac{\partial u_i}{\partial t} \quad (3.47)$$

where $\sigma_i = \frac{F_i}{A_i}$ and $V_i = \frac{\partial u_i}{\partial t}$ and $c_i = \sqrt{\frac{E_i}{\rho_i}}$.

Combining Eqn. 3.44, Eqn. 3.45, Eqn. 3.46 and Eqn. 3.47, the following relations can be concluded

$$V_i = \frac{\rho_s A_s c_s V_0}{\rho_i A_i c_i + \rho_s A_s c_s} \quad (3.48)$$

$$V_s = \frac{\rho_i A_i c_i V_0}{\rho_i A_i c_i + \rho_s A_s c_s} \quad (3.49)$$

In SHPB, the striker bar is the short bar while the incidence bar is the long bar. The two bars have identical mass density, Young's modulus and cross-sectional area. From Eqn. 3.44, Eqn. 3.48 and Eqn. 3.49, it yields

$$V_i = V_s = \frac{1}{2} V_0 \quad (3.50)$$

Combining Eqn. 3.46, Eqn. 3.47 and Eqn. 3.50, the following stresses can be obtained

$$\sigma_s = \sigma_i = \frac{1}{2} \rho_0 c_0 V_0 \quad (3.51)$$

where $\rho_0 = \rho_i = \rho_s$ and $c_0 = c_i = c_s$. Then the strain on the incidence bar becomes

$$\varepsilon_i = \frac{1}{2} \rho_0 c_0 V_0 / E \quad (3.52)$$

Consider an SHPB system of $E = 227.26 \text{ GPa}$, $\rho_0 = 7610.5 \text{ kg/m}^3$ and the diameter of the bars $d_0 = 25.4 \text{ mm}$. Also, from the velocity sensor, the striker velocity before the impact is 4.12 m/s . Substituting these values into Eqn. 3.52, the magnitude of strain is found to be 3.77×10^{-4} . The magnitude of strain wave from computation is 3.79×10^{-4} . A difference of only 0.5% exists.

In conclusion, based on the assumption of perfect impact and perfect signal acquisition, the study based on striker impact is the same as the square function input as shown in Fig. 3.9. Therefore, there is no need to include the striker impact in the simulation, hence significant computational effort can be save. Another observation is that peridynamics is convenient for simulating the impact process without using the complex theory involved in contact mechanics. The long range force covers the contact between two bodies automatically.

3.6 Validation with results in literature

The purpose of the previous study is to validate the elastic model of peridynamics. The initial velocity of the striker bar is controlled to be small so the deformation of the specimen is always within elastic range. In SHPB experiment, the deformations of the bars are always within elastic range.

Most of the existing work on SHPB is to find material properties of a specimen, i.e. stress-strain curve, in elastic as well as in plastic range. To simulate an SHPB test from the existing works, a plastic or nonlinear bond function must be used for the specimen.

An SHPB system is given in Fig. 3.33. The dimensions and material properties are listed in Table 3.4. An aluminum specimen with a length of 25.38 mm and a diameter of 12.6 mm is used in the SHPB study. From the reflection wave and the transmission wave, the stress-strain relation of the specimen can be identified and is shown in Fig. 3.35.

Table 3.4 Dimensions and material properties of the SHPB in Fig. 3.33

	Striker	Incidence bar	Al Specimen	Transmission bar
Length	203 mm	838 mm	25.38 mm	419 mm
Diameter	19 mm	19 mm	12.6 mm	19 mm
Young's modulus	191.4 GPa	191.4 GPa	Fig. 3.35	191.4 GPa
Mass density	7858 kg/m^3	7858 kg/m^3	2700 kg/m^3	7858 kg/m^3

Fig. 3.35 is then used as the input material property for peridynamic simulations. The computational results are then compared with the experiment results from Ref. [6]. Matlab curve-fitting toolbox [7] is used to convert the curve in Fig. 3.34 for a piece-wise linear function. For every strain, the corresponding stress calculated from the fitted function is divided by the strain to obtain an equivalent Young's modulus which is subsequently used to find the bond stiffness. Fig. 3.35 compares experiment results with computational results. They show a good correlation except some discrepancies around the corner. Fig. 3.36 shows the filtered computational results with the experiment results. The agreement between the two is significantly improved. This study demonstrates the capability of peridynamics in modeling plastic materials.

3.7 Modeling shaper in SHPB

In performing SHPB tests, it is necessary to maintain constant strain rate during the loading process. This requires a slow loading process such as a triangular incidence wave as shown in Fig. 3.37. A square incidence wave, as shown previously for computational purpose, can cause a

rapid loading in the beginning of testing and hence is not suitable since it can damage the specimen prematurely. A so-called shaper must be installed between the striker bar and the incidence bar as shown in Fig. 3.38 to slow down the initial loading rate.

The selection of the shaper materials and its dimensions, however, requires significant experience and trial and error. A computer simulation based peridynamics may help to ease the selection process.

Frew [8] used a copper shaper in SHPB tests. To study the shaping effect, only the striker and the incidence bar are needed. Table 3.5 shows dimensions and material properties of the individual bars. The strain wave propagated into the incidence bar is altered due to the plastic deformation of the shaper during impact. Frew [8] proposed the following stress-strain model for the copper shaper while Fig. 3.40 shows the plot of it, i.e. Eqn. 3.53,

$$\sigma = \frac{\sigma_0 \varepsilon^n}{1 - \varepsilon^m} \quad (3.53)$$

where $\sigma_0 = 625 \text{ MPa}$, $n = 0.32$ and $m = 4.25$. The unloading process is elastic and the Young's modulus is 117 GPa .

Table 3.5 Dimensions and material properties of the SHPB used

	striker	shaper	incidence bar
length	152mm	1.6mm	2130mm
diameter	12.7mm	4.8mm	12.7mm
Young's modulus	200 GPa	Fig. 3.40	200 GPa
Mass density	8100 kg/m^3	8910 kg/m^3	8100 kg/m^3

Similar to those presented in Section 3.6, the stresses from Fig. 3.40 are divided by the strain to gain an equivalent Young's modulus E_{eq} . The deformed cross-sectional area of the shaper, A , is calculated from the following equation

$$A = \frac{A_0 L_0}{L} \quad (3.54)$$

where L is the deformed shaper length, A_0 is the original shaper area and L_0 is the original shaper length. The equivalent strain E_{eq} is modified by the change of the cross-sectional area as shown below

$$E'_{eq} = E_{eq} \frac{A}{A_0} \quad (3.55)$$

The bond stiffness involved in the shaper can then be calculated by using Eqn. 3.35. It should be pointed out that the significant change of area should be considered in Eqn. 3.53 because the deformation of the shaper can be quite large, deviating from one-dimensional assumption.

Simulation of the shaped incidence wave is compared with the experiment results in Fig. 3.41. They agree with each other very well. Overall, this study shows that peridynamics is able to simulate the shaping effect required for SHPB operations. It provides an efficient way to select a shaper material with associated dimensions without numerous trial-and-errors.

3.8 Conclusions

A one-dimensional peridynamic model is proposed and its engineering applications are evaluated. The numerical solutions from peridynamic analyses are well compared with the associated analytical solutions in both convergence and accuracy studies. The feasibility of using

peridynamics in modeling Split Hopkinson Pressure Bar (SHPB) is also validated by the experiments. Since SHPB tests performed in this dissertation are essentially focused on validating the peridynamic theory, the tests are specifically designed for comparison purpose, some assumptions and requirements of SHPB technique are not be completely satisfied. For example, it is required in SHPB tests that the specimen diameter be smaller than that of the striker, incidence and transmission bars. Study Three, however, does not follow this guideline. The experiment data from Study Three is able to validate Eqn. 3.35 but may be not able to get the accurate material properties from Eqn. 3.29 and Eqn. 3.30. Peridynamics is convenient for simulating impact process with its long range force. All fundamental elements for mechanical analysis are included in the formulation of peridynamics. No additional theory, such as contact mechanics, is required. Because of its numerical nature, peridynamic method can be used to simulate the shaper of the SHPB. This can help accelerate the use SHBP in dynamic material characterizations significantly.

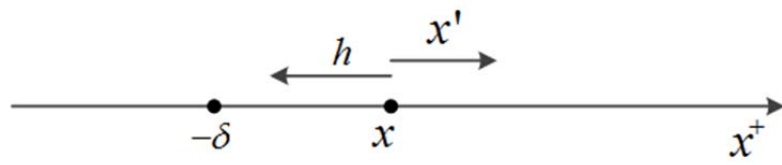


Figure 3.1 Calculation of stress.

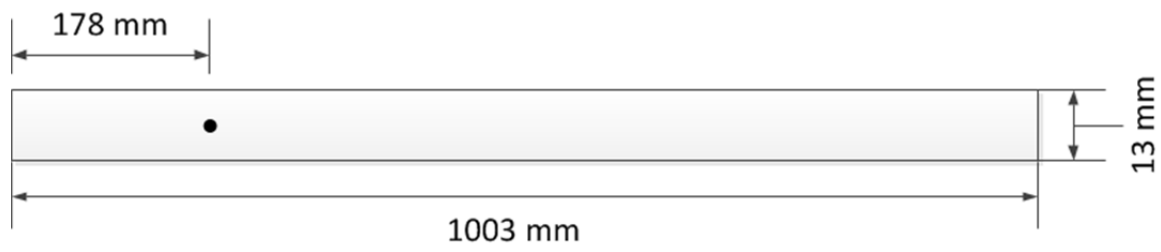


Figure 3.2 Wave propagation in a one-dimensional bar.

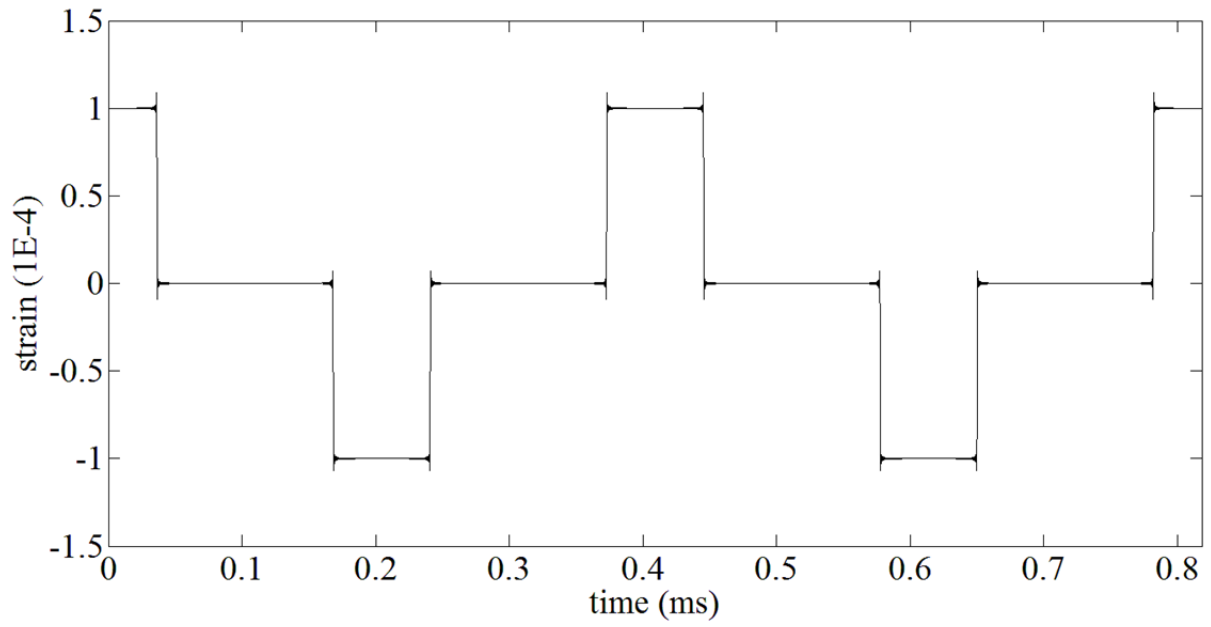


Figure 3.3 Analytical solution for wave propagation.

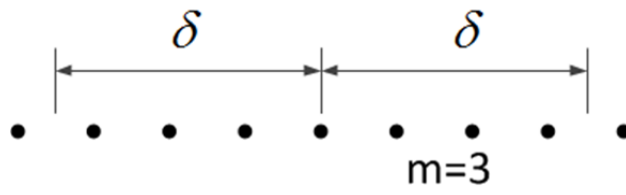


Figure 3.4 Number of nodes within a horizon.

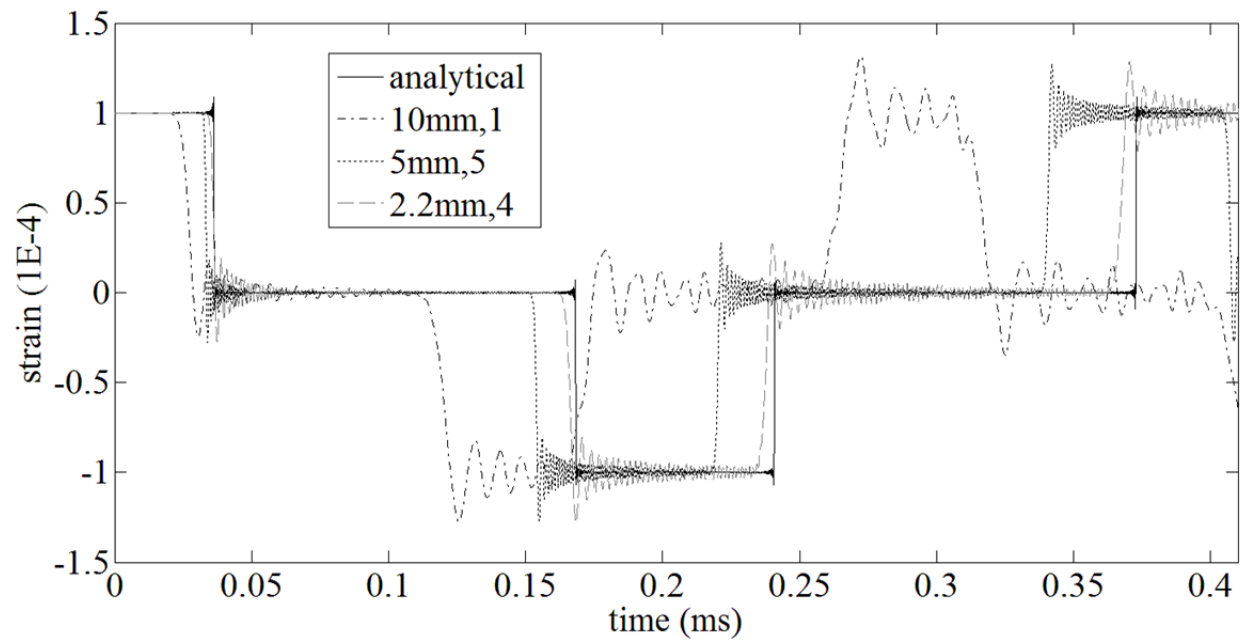


Figure 3.5 Comparison between classical mechanics and peridynamics.

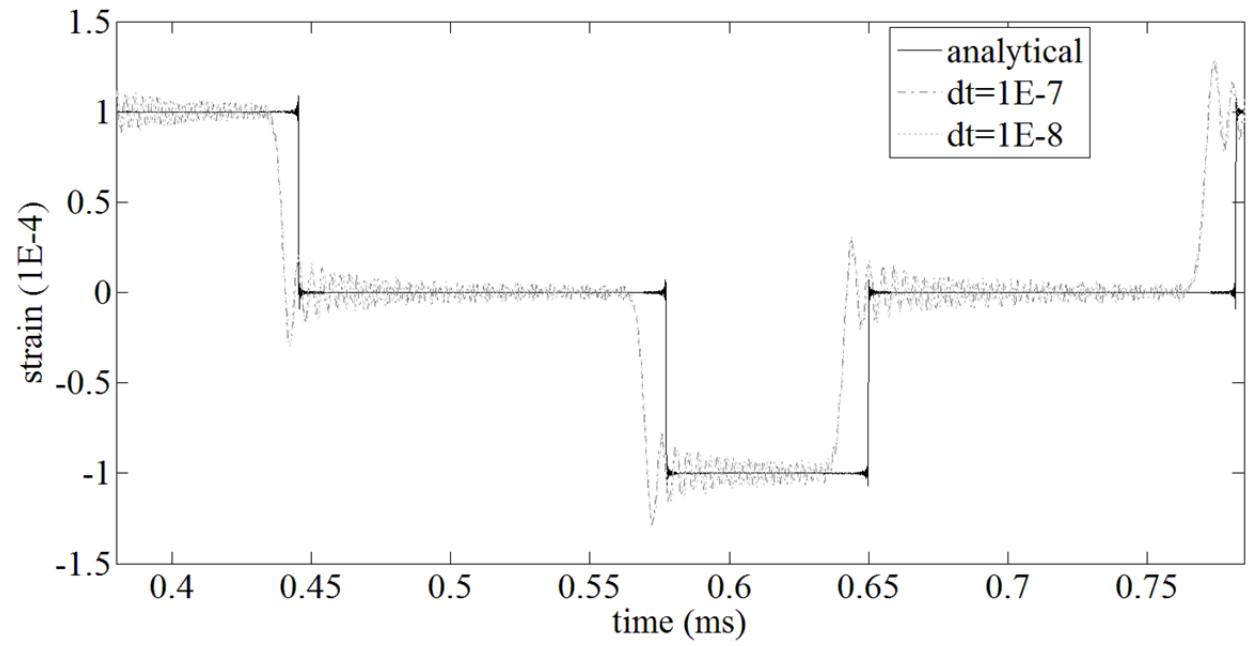


Figure 3.6 Convergence of time step size.

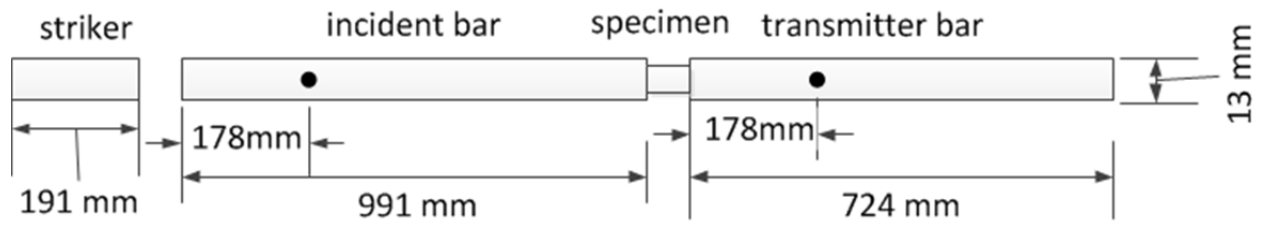


Figure 3.7 Set up of Split Hopkinson pressure bar (SHPB).

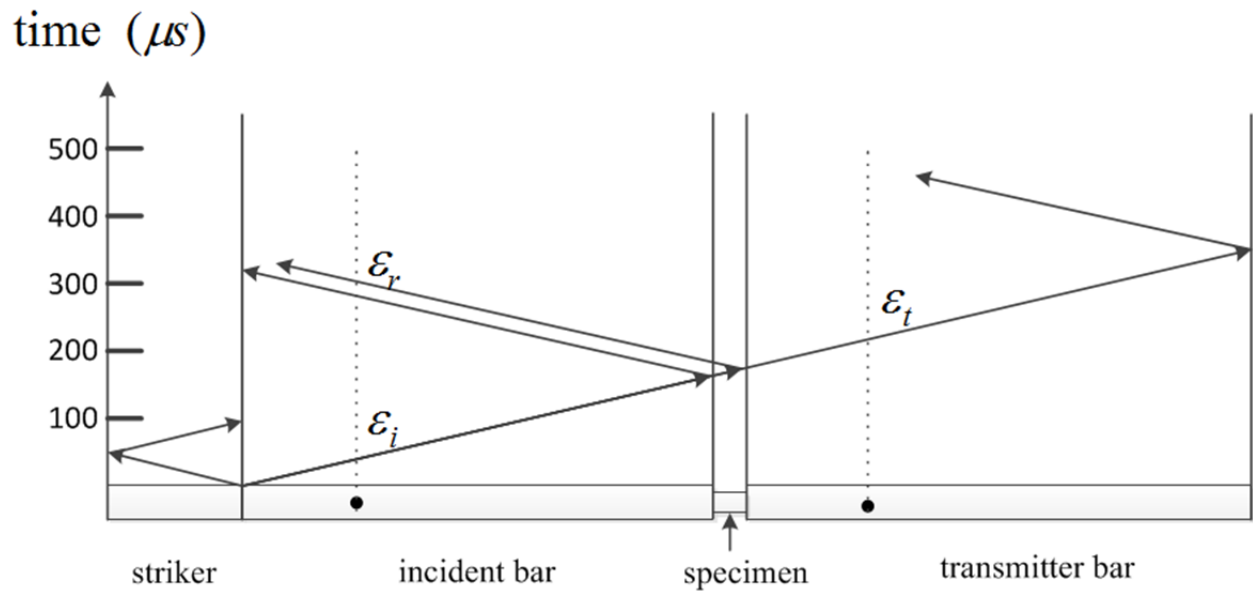


Figure 3.8 Wave propagation in SHPB.

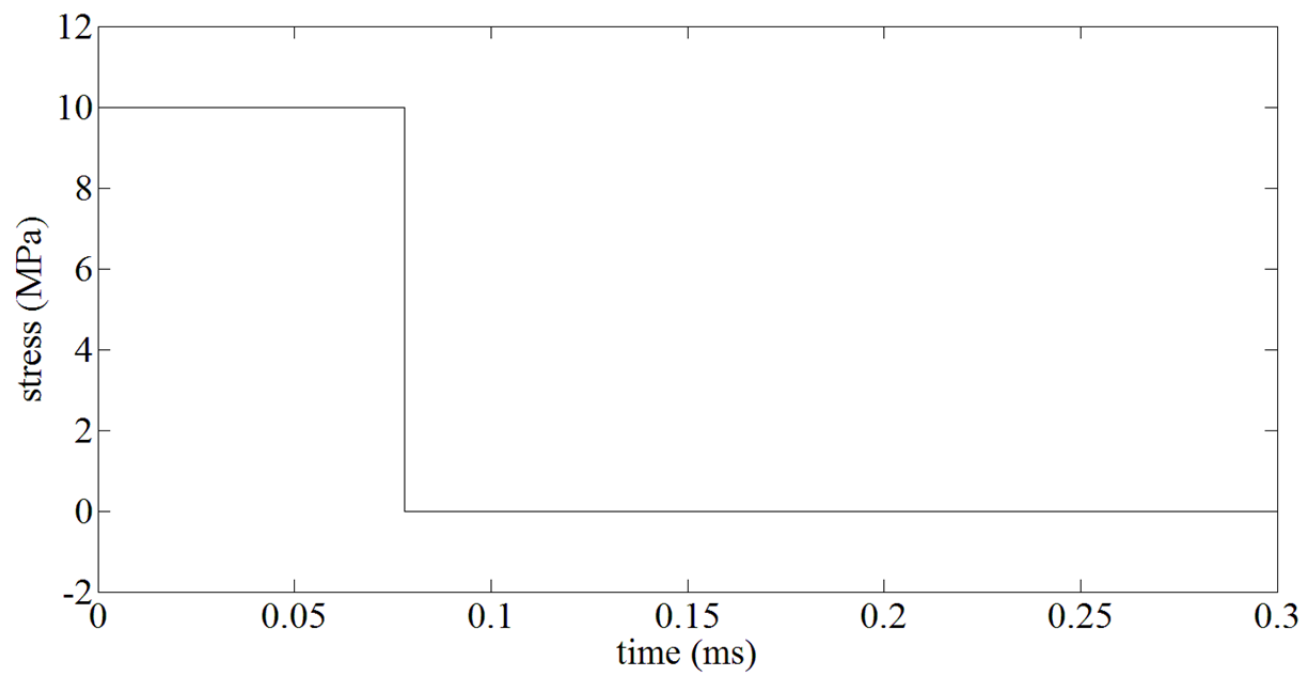


Figure 3.9 Square wave input for computational simulation.

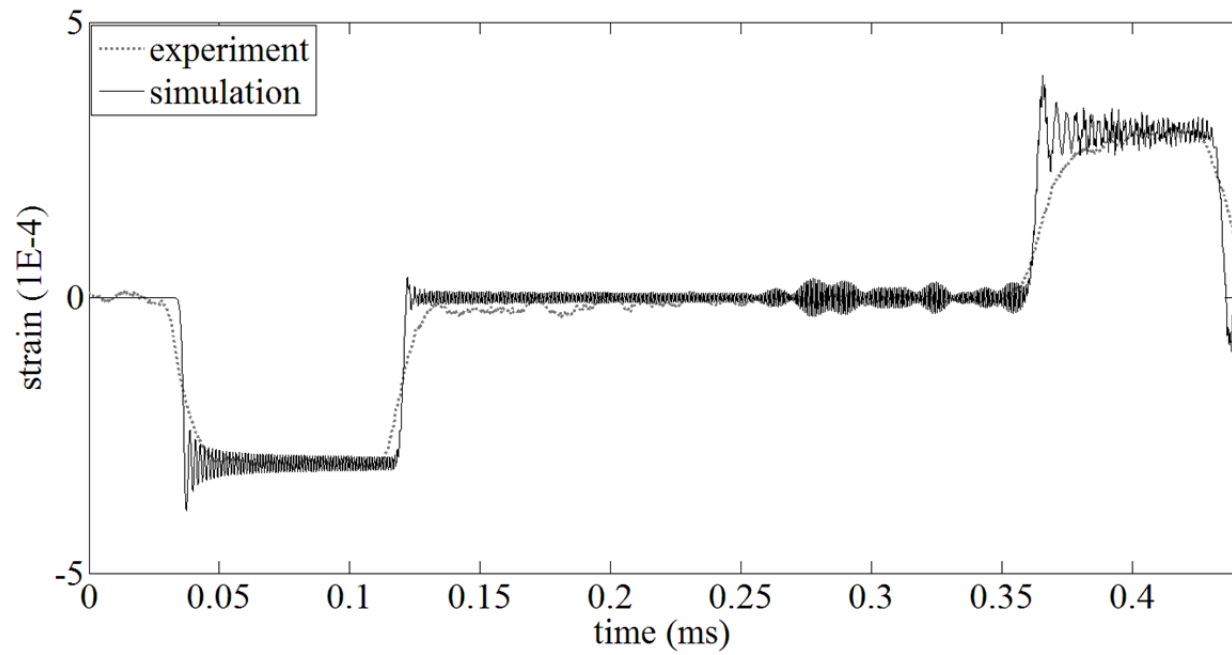


Figure 3.10 Comparison in Study One with a square wave input.

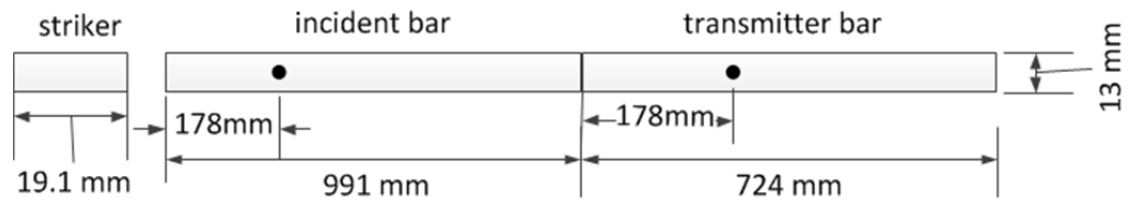


Figure 3.11 Study Two: Two Bar.

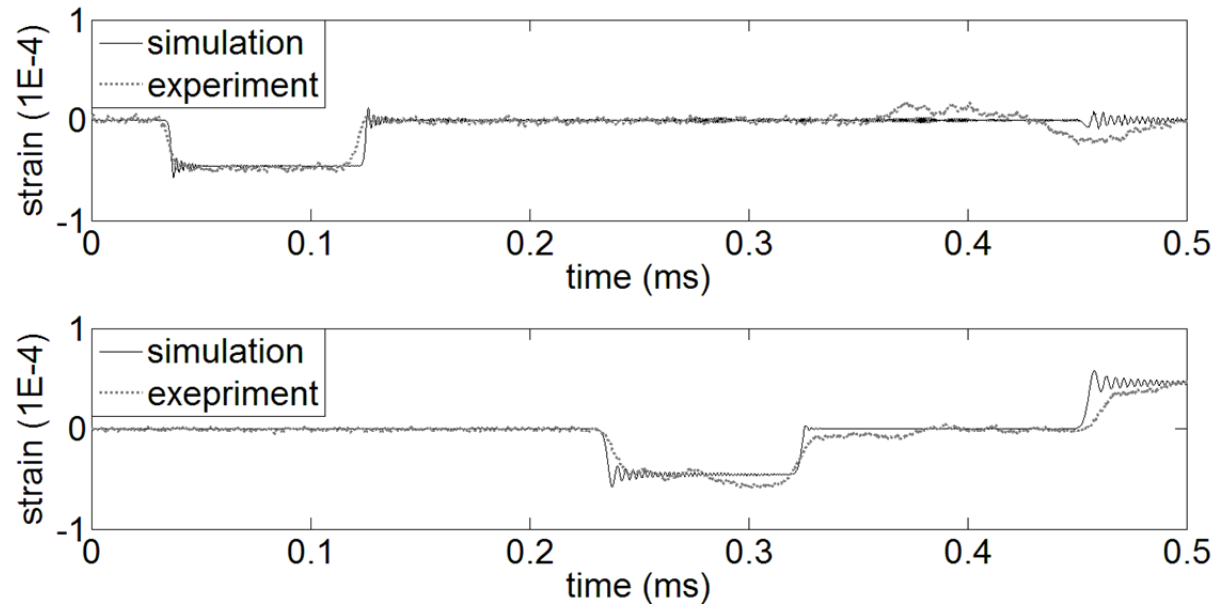


Figure 3.12 Study Two: comparison between experiment results and numerical solution, strain history in incidence bar (top) and strain history in transmission bar (bottom).

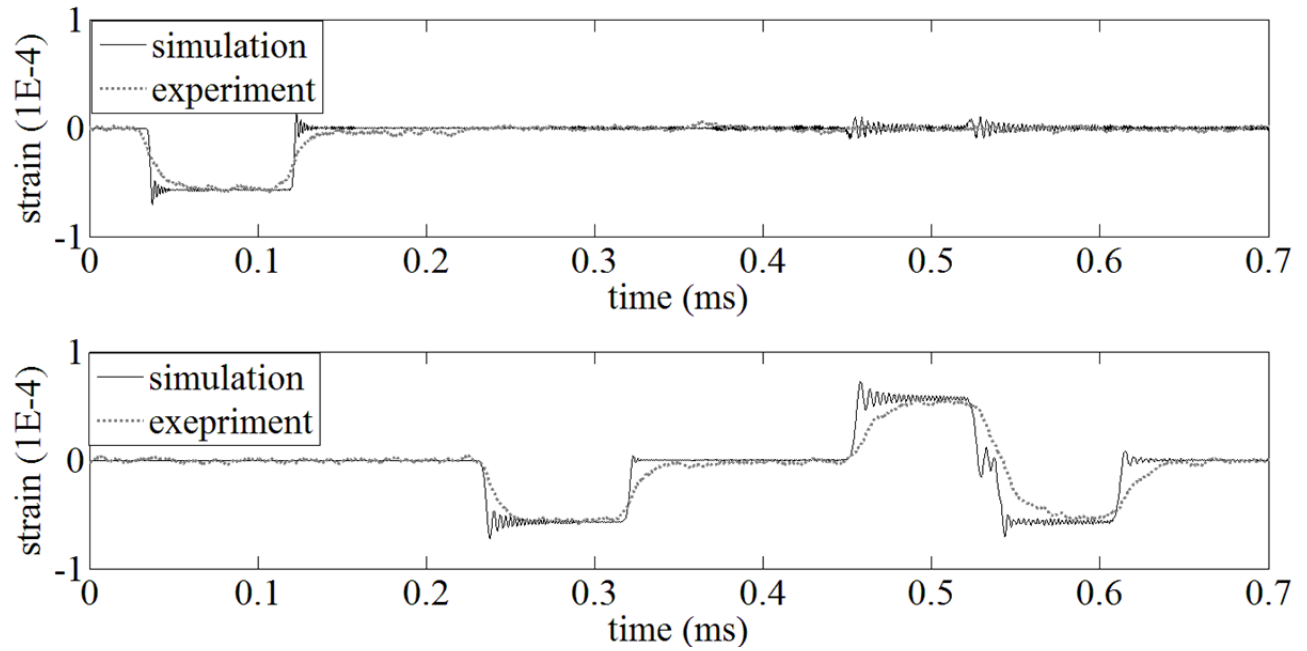


Figure 3.13 Study Two: comparison between experiment results and numerical solution with grease, strain history in incidence bar (top) and strain history in transmission bar (bottom).

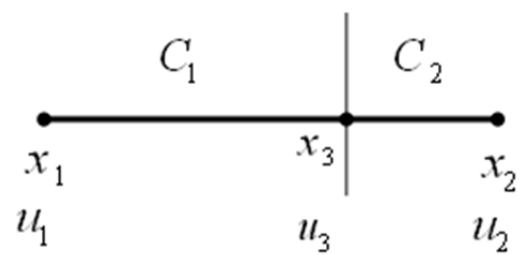


Figure 3.14 A bond crossing an interface.

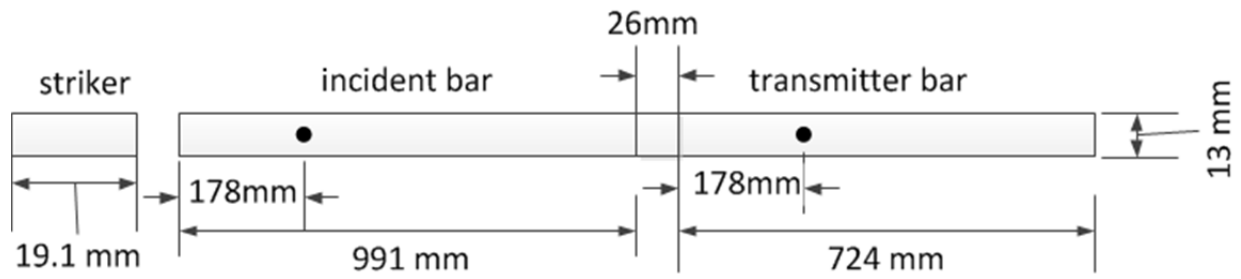


Figure 3.15 Study Three: aluminum specimen with the same cross-section area as the split bars.

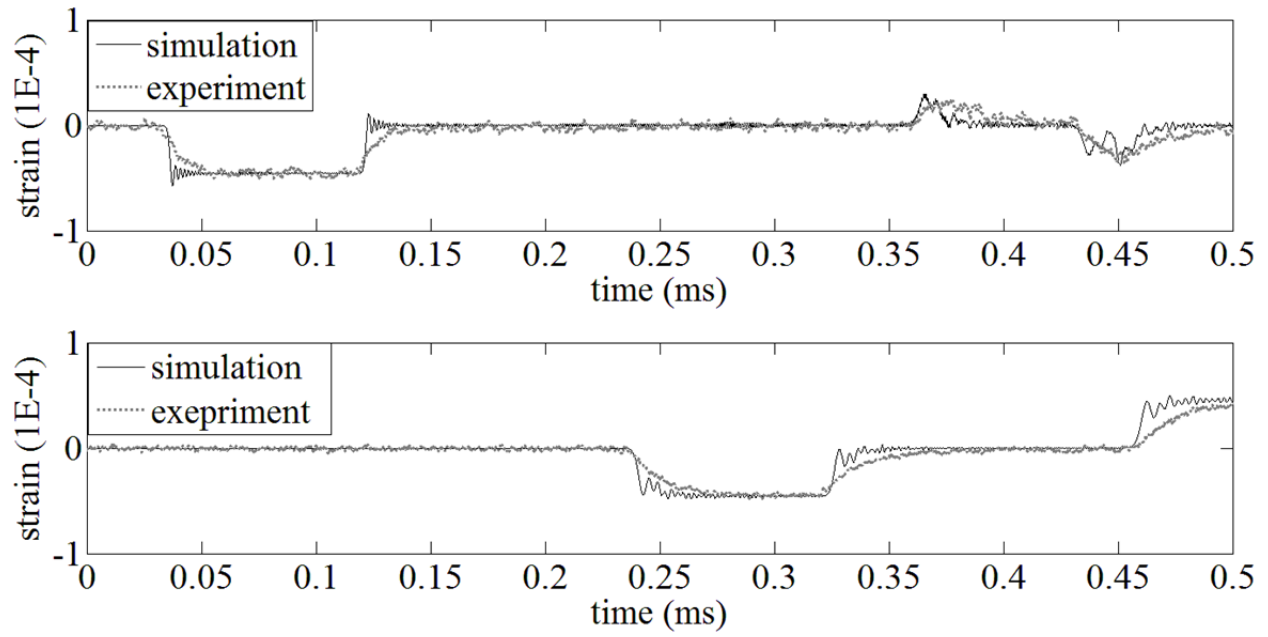


Figure 3.16 Study Three: Aluminum specimen with the same-cross section area as the split bars, incidence bar strain history (top) and transmission bar strain history(bottom).

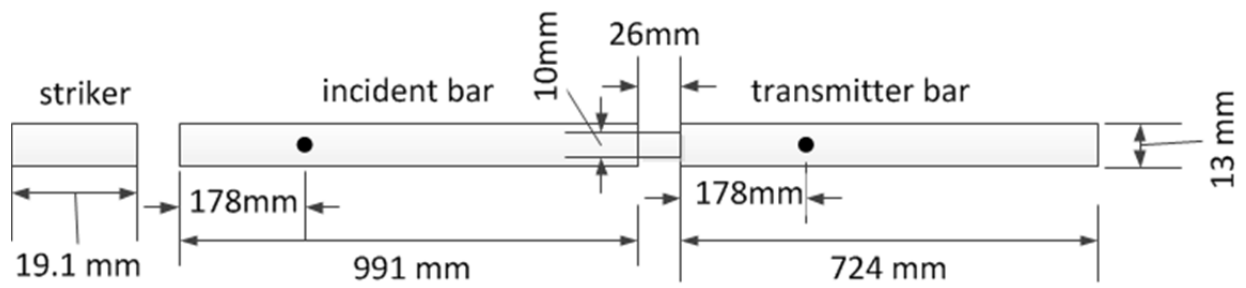


Figure 3.17 Study Four: Steel specimen with a smaller cross-section area.

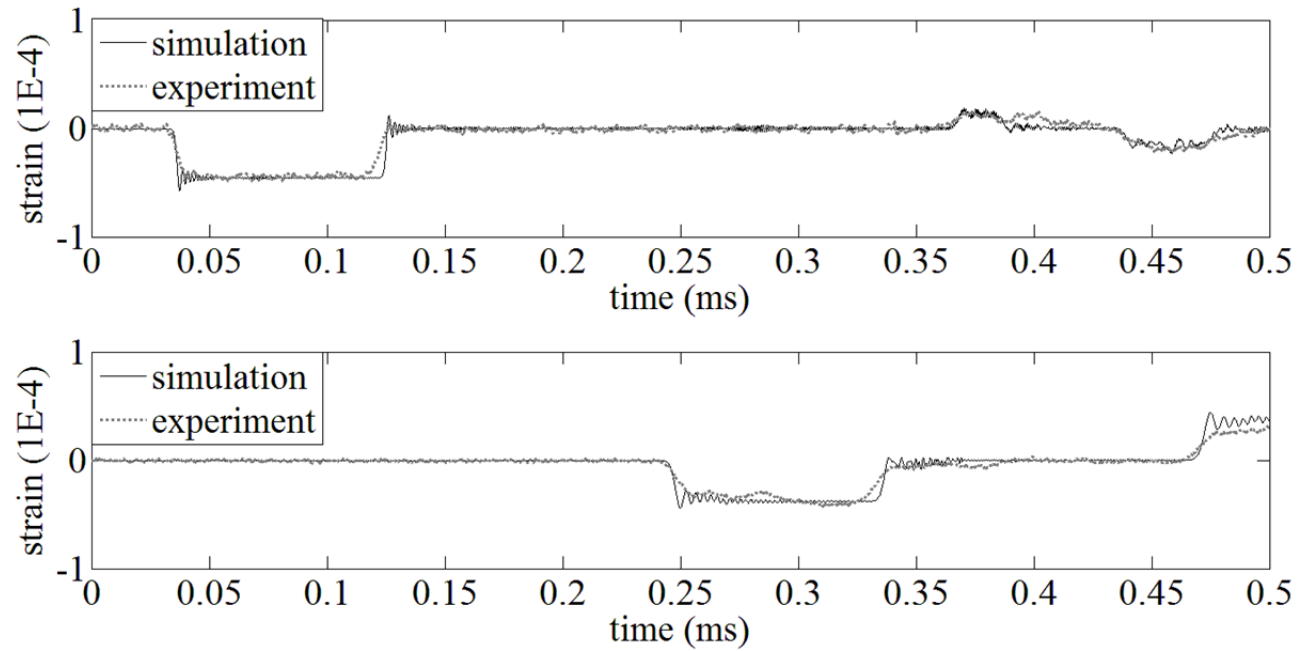


Figure 3.18 Study Four: Steel specimen with a smaller cross-section area, incidence bar strain history (top) and transmission bar strain history (bottom).

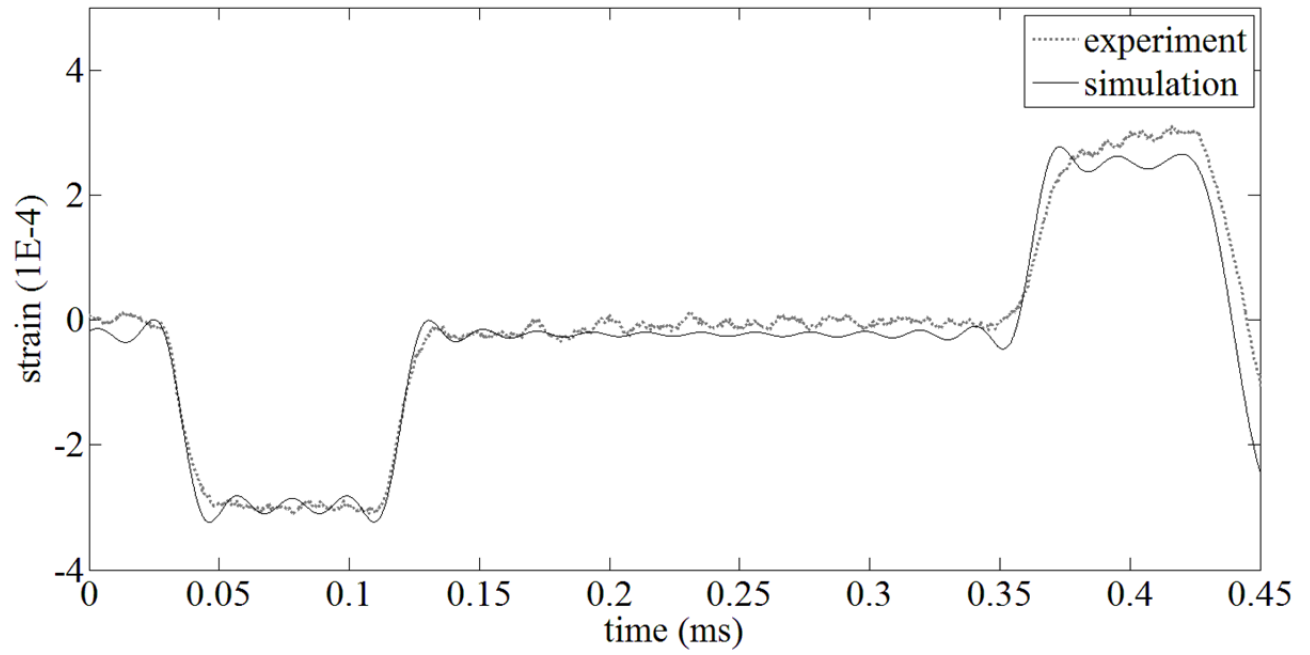


Figure 3.19 Study One: computational results with filter compared with experiment results.

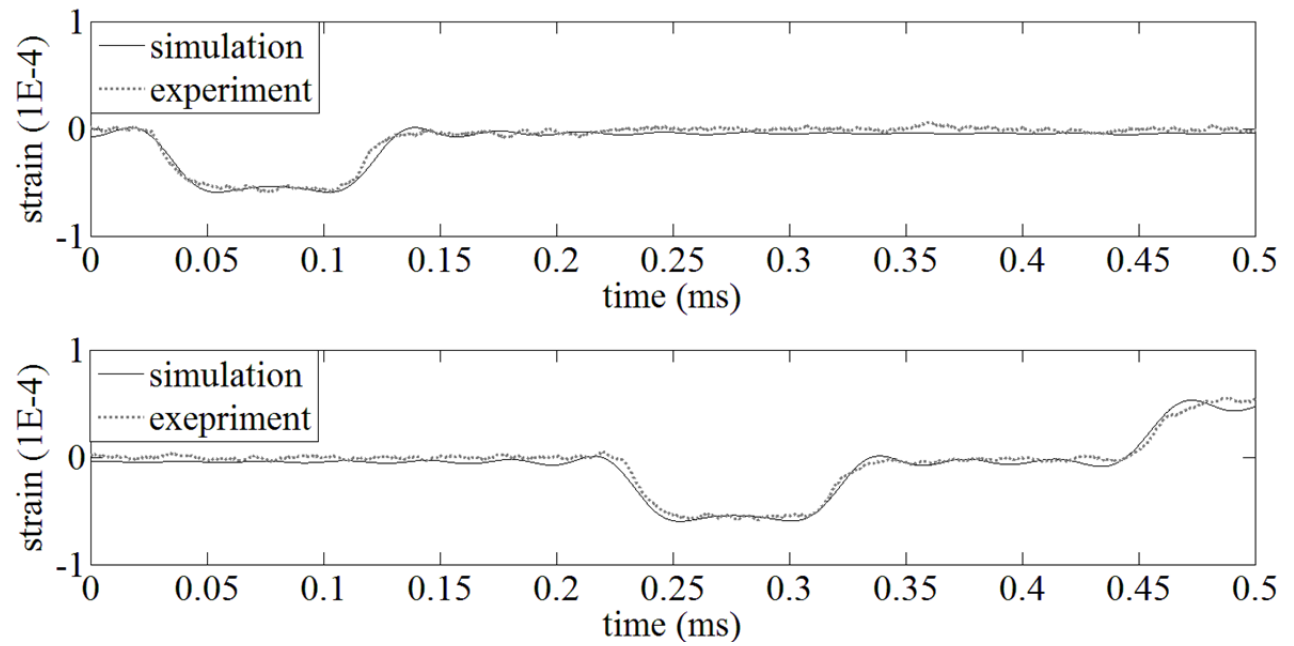


Figure 3.20 Study Two: Computational results with filter compared with experiment results.

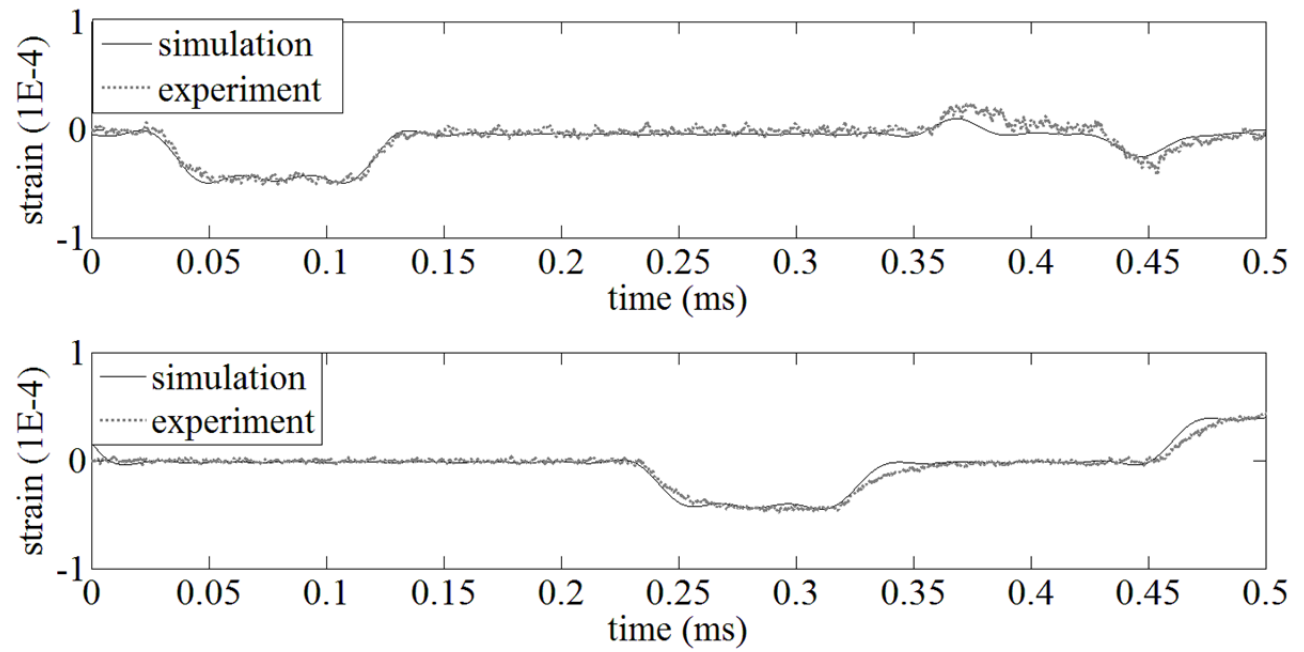


Figure 3.21 Study Three: Computational results with filter compared with experiment results.

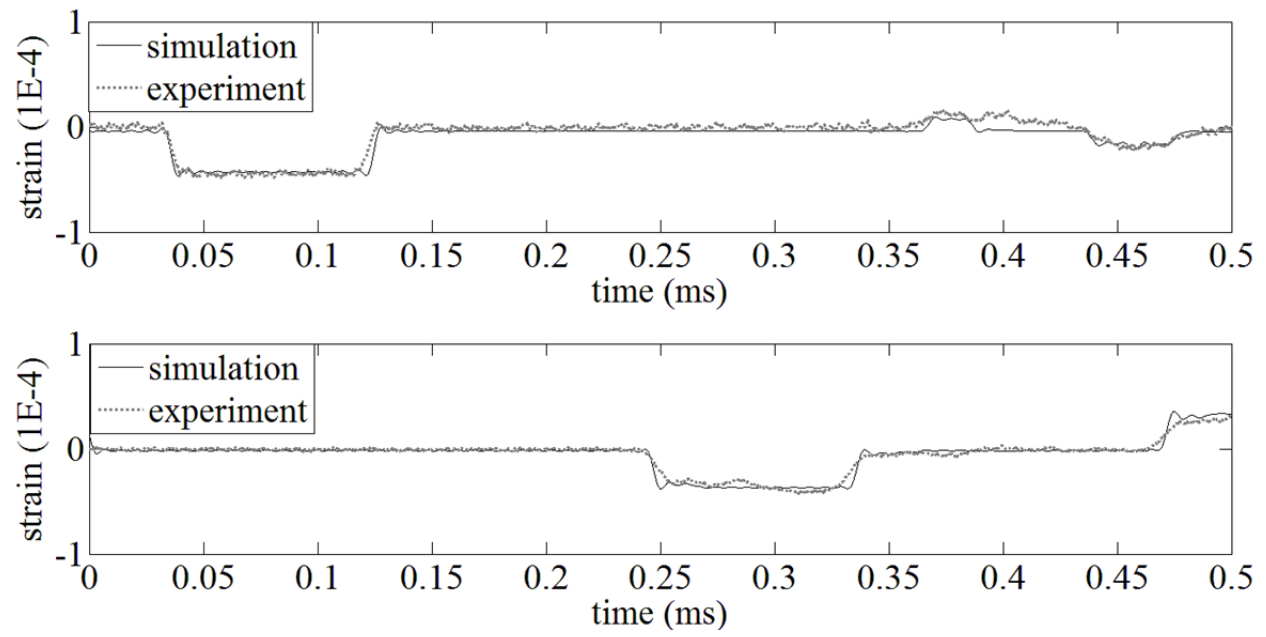


Figure 3.22 Study Four: Computational results with filter compared with experiment results.

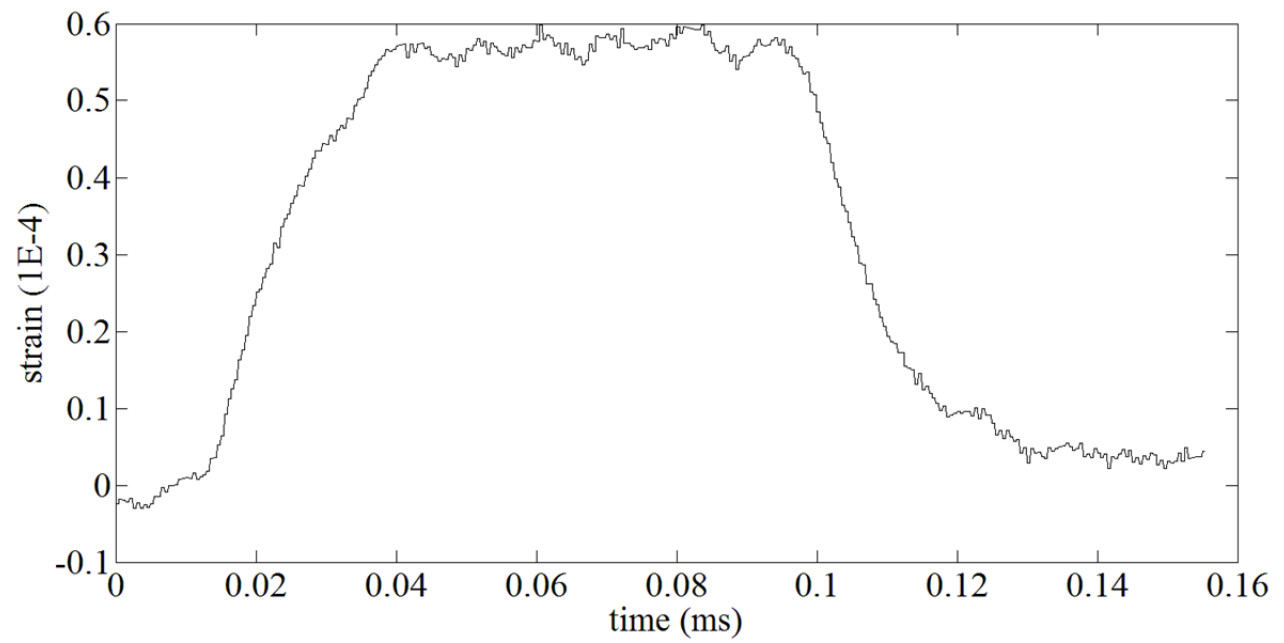


Figure 3.23 Incidence wave from Study Two.

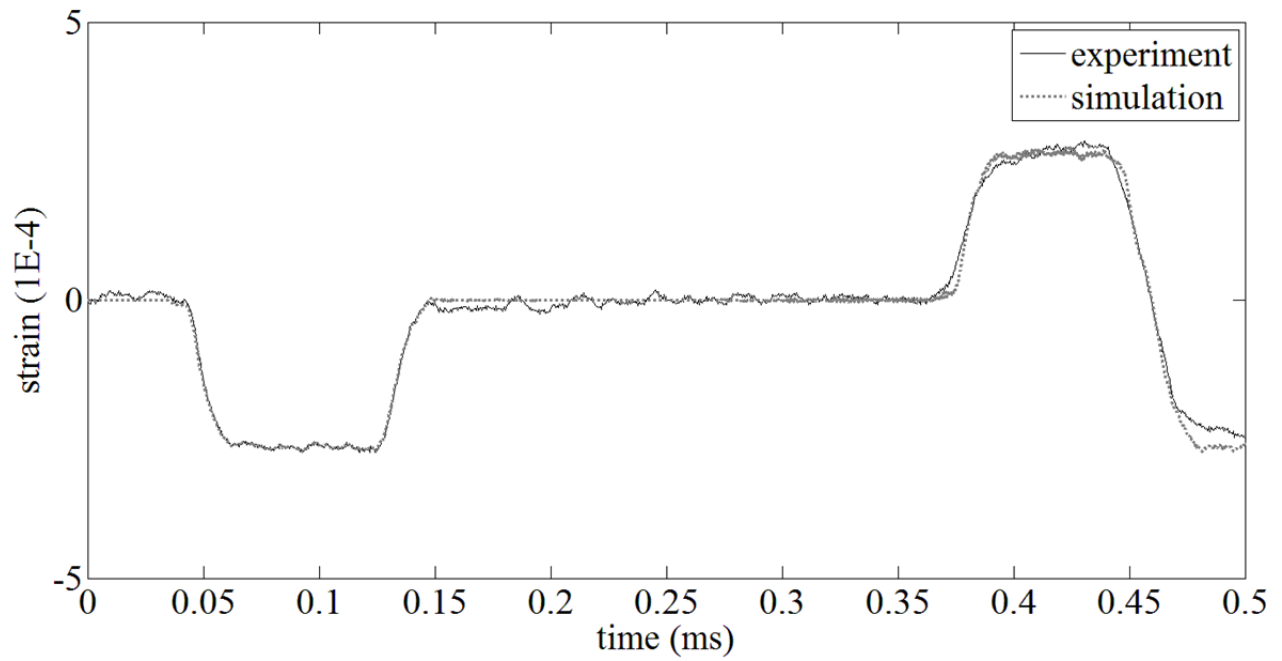


Figure 3.24 Study One: Incident wave as computational input.

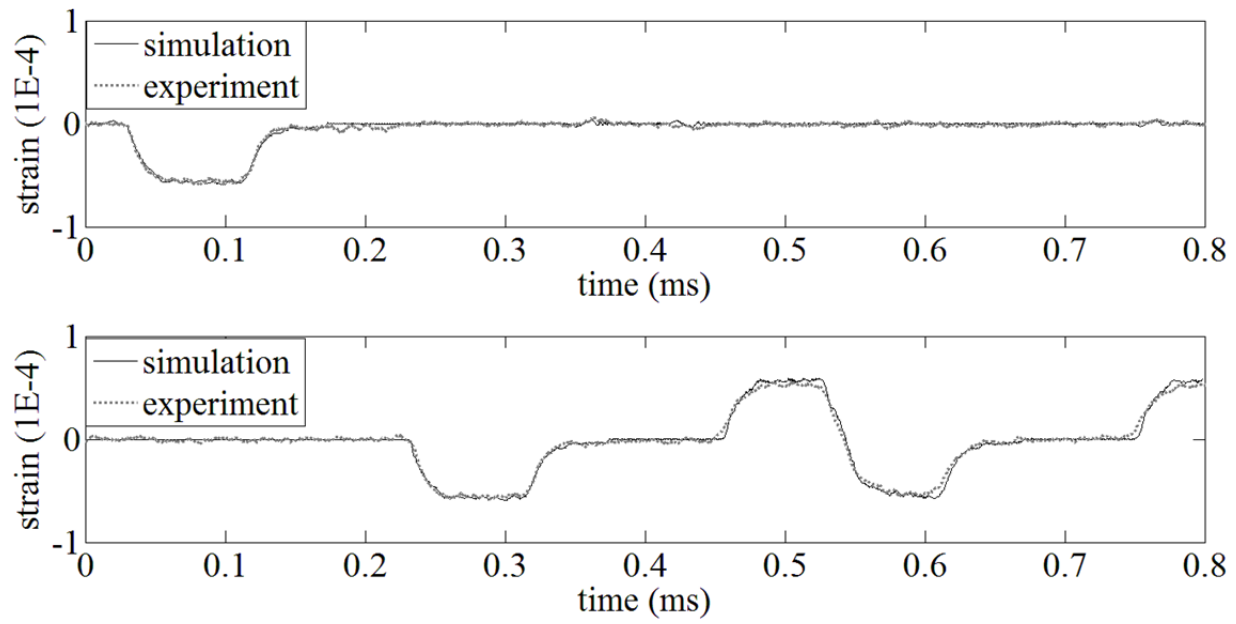


Figure 3.25 Study Two: Incident wave as computational input.

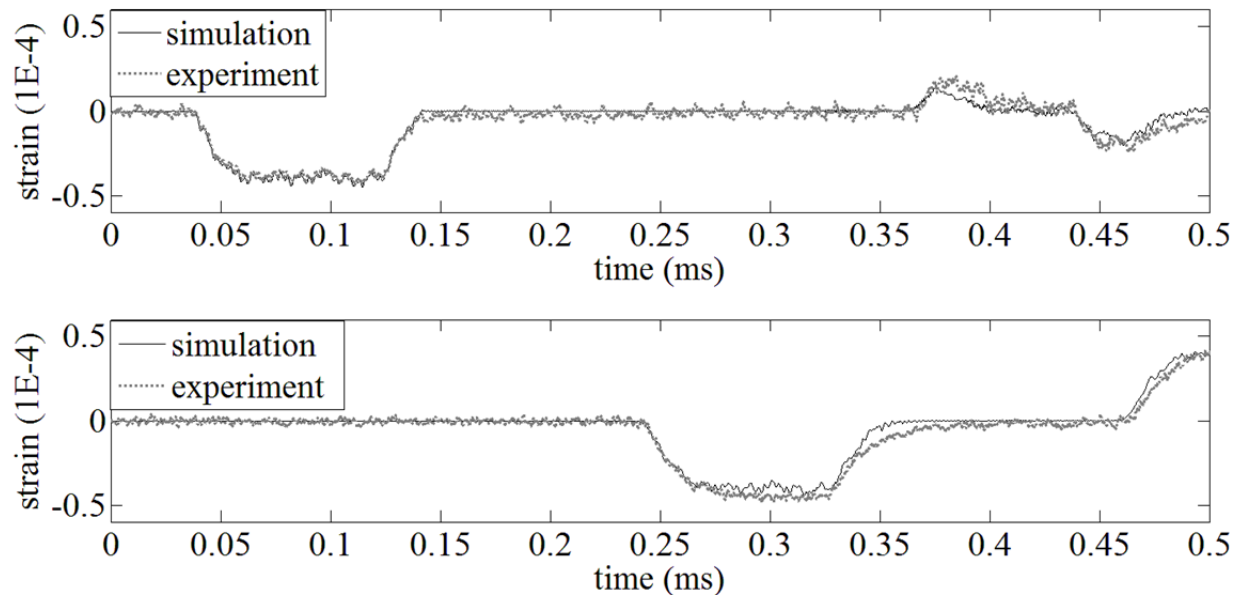


Figure 3.26 Study Three: Incident wave as computational input.

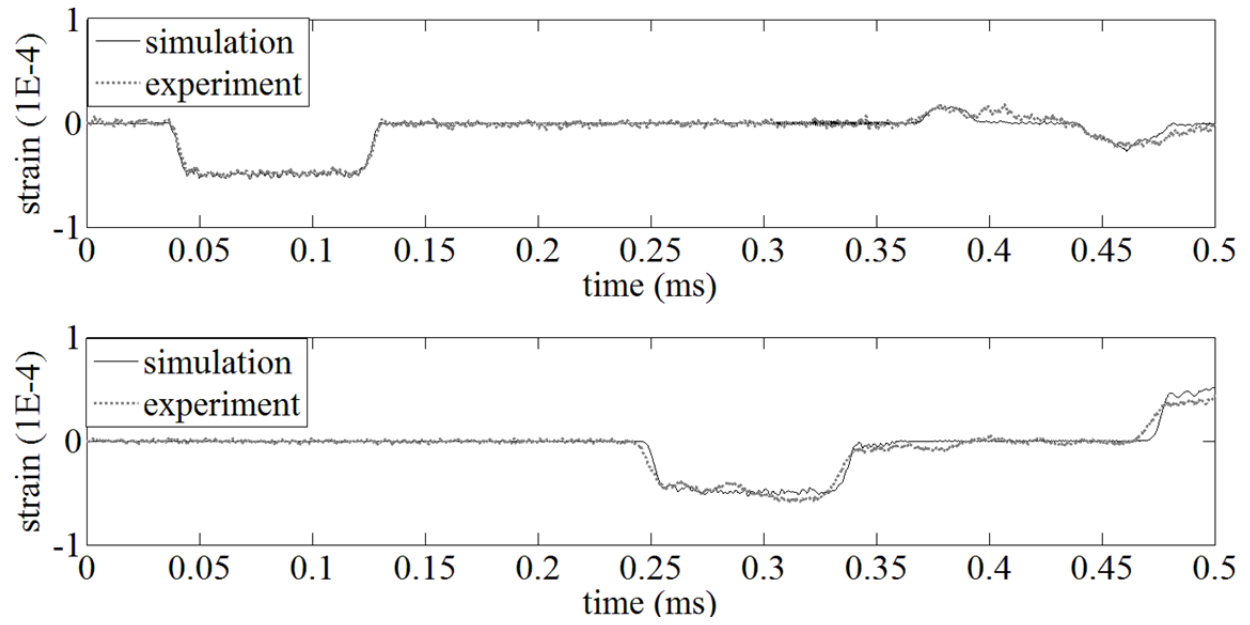


Figure 3.27 Study Four: Incident wave as computational input.

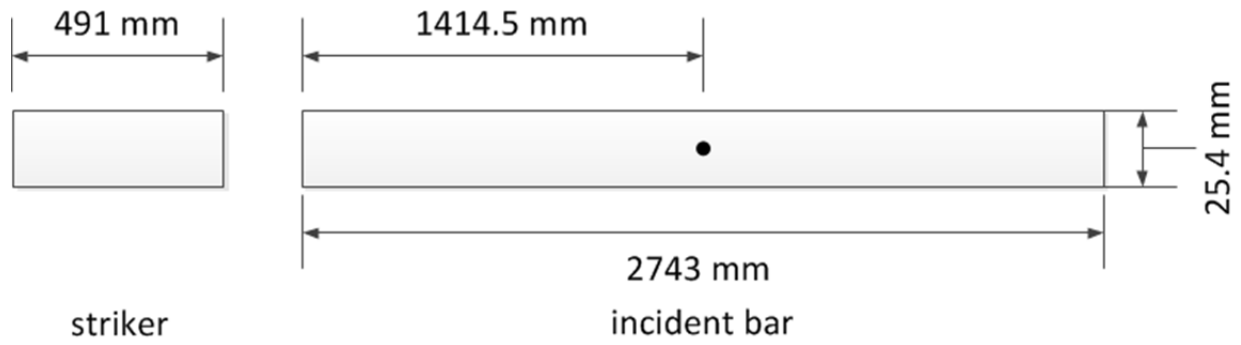


Figure 3.28 Split bar system for validating impact process.

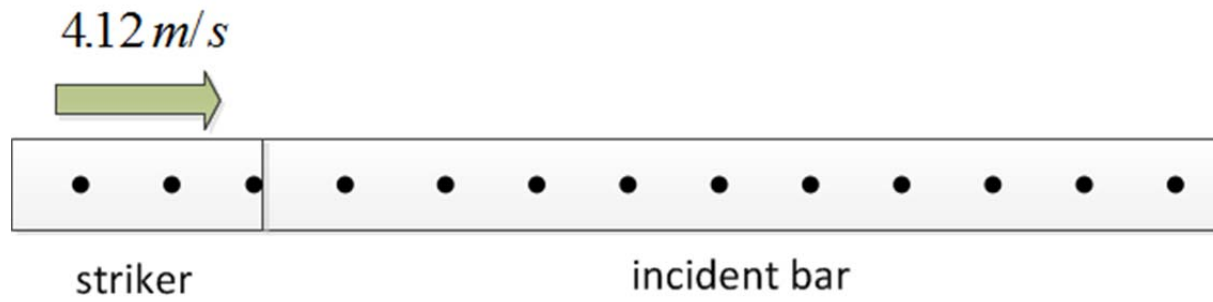


Figure 3.29 Simulation of impact process.

For interpretation of the references to color in this and all other figures, the reader is referred to the electronic version of this dissertation.

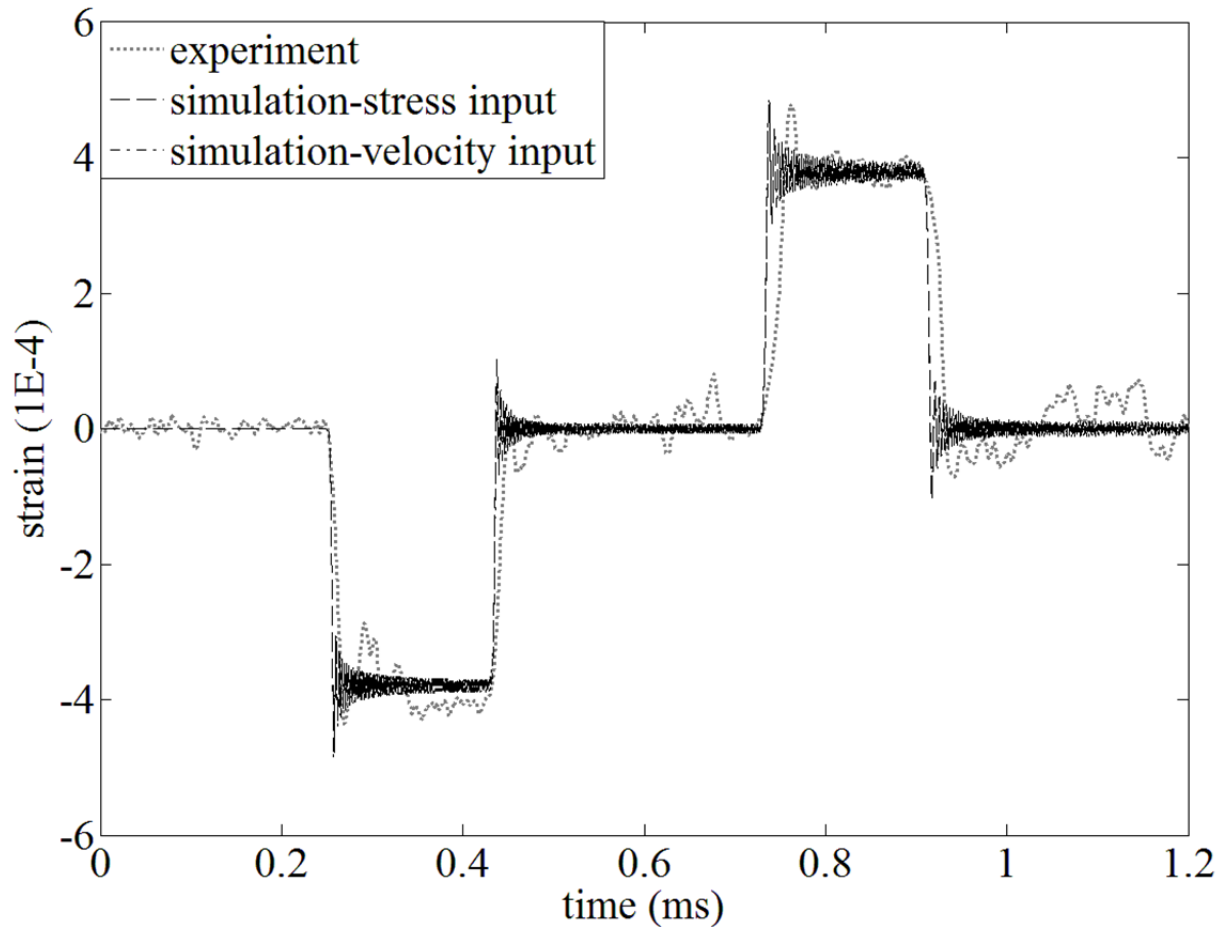


Figure 3.30 Comparison between experiment and simulation with velocity input.

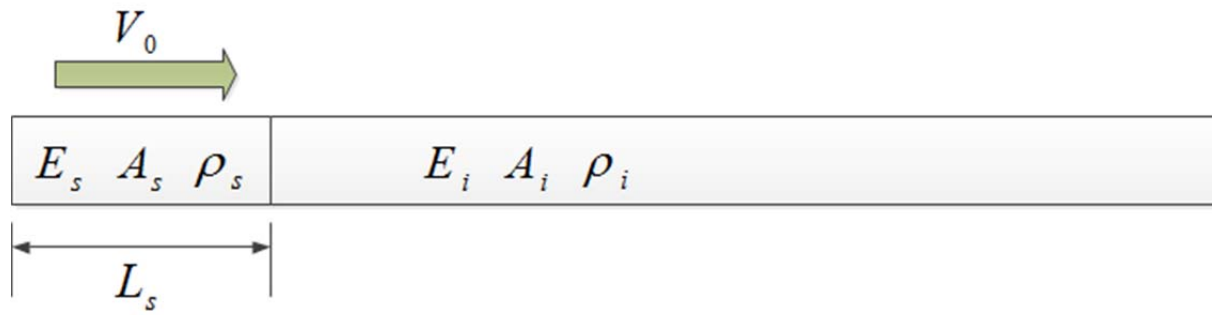


Figure 3.31 Impact of two cylindrical bars right before impact.



Figure 3.32 Impact of two cylindrical bars after impact.

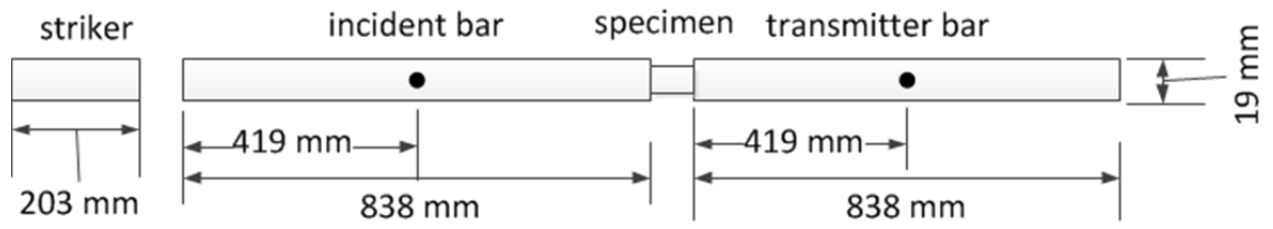


Figure 3.33 SHPB system [6].

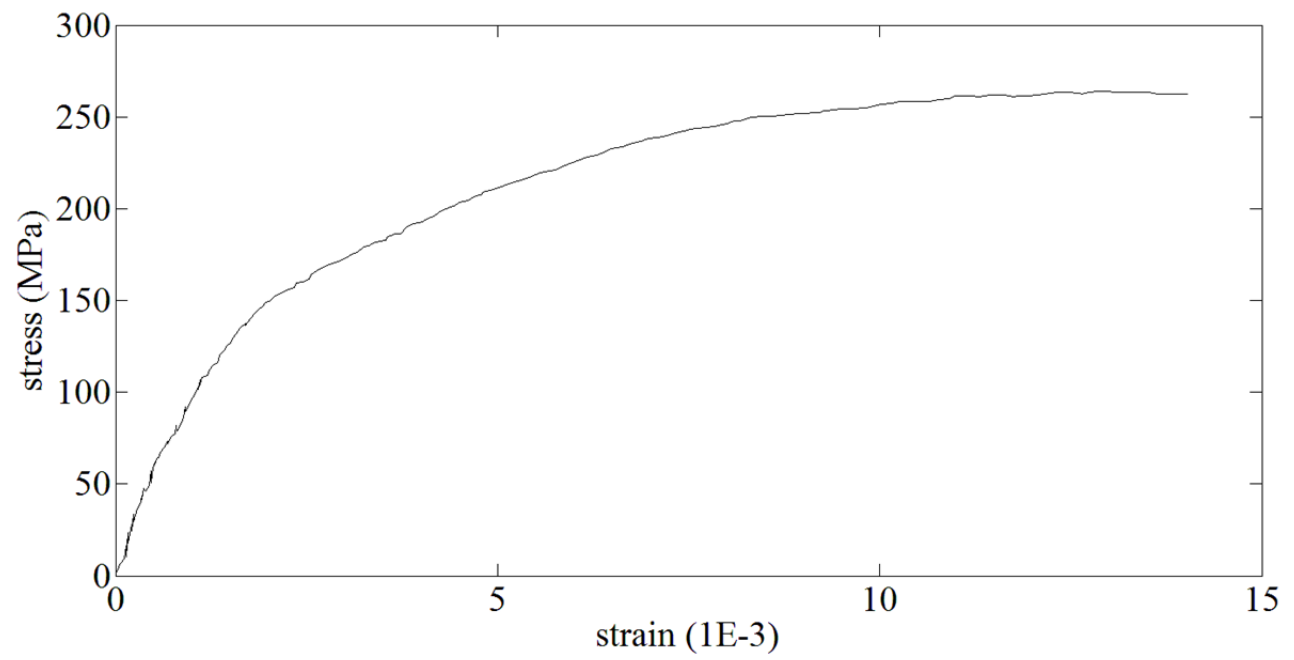


Figure 3.34 Stress-strain relation of the aluminum specimen from [6].

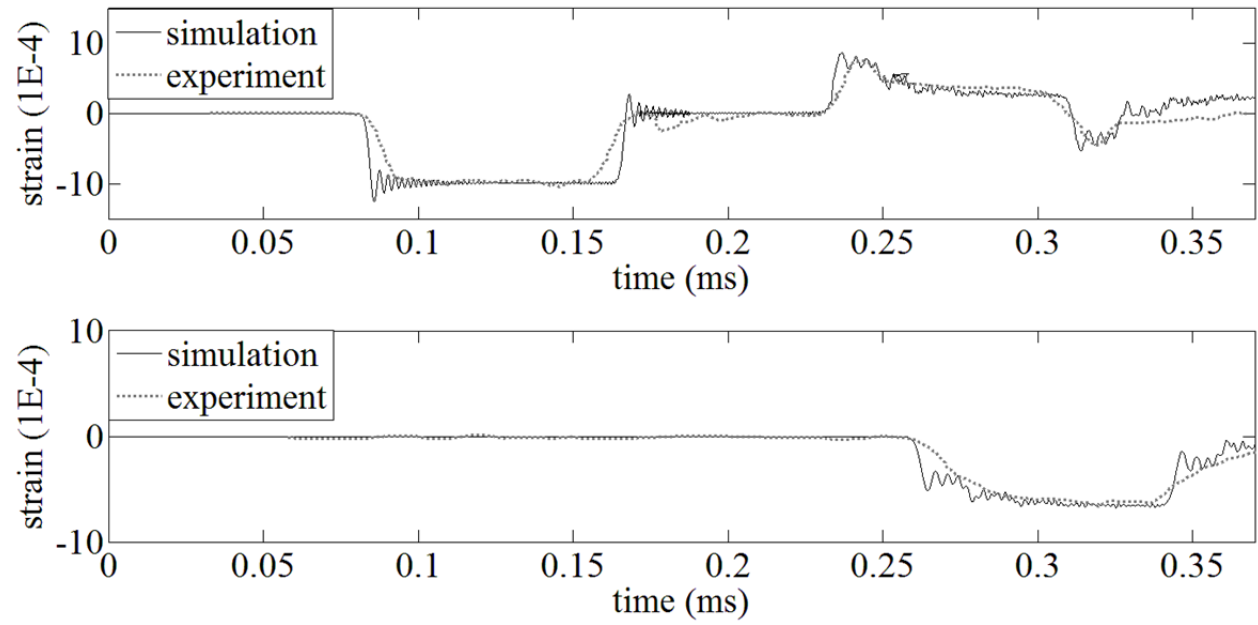


Figure 3.35 Comparing computational results with experiment results from [6].

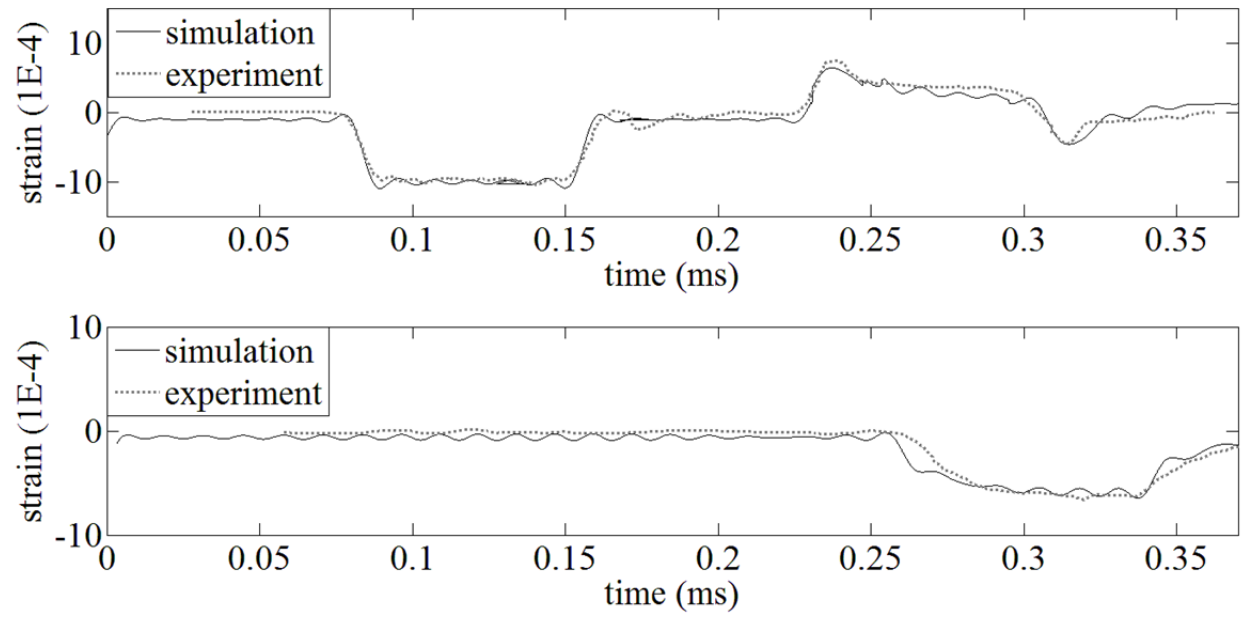


Figure 3.36 Computational results with filter compared with experiment results.

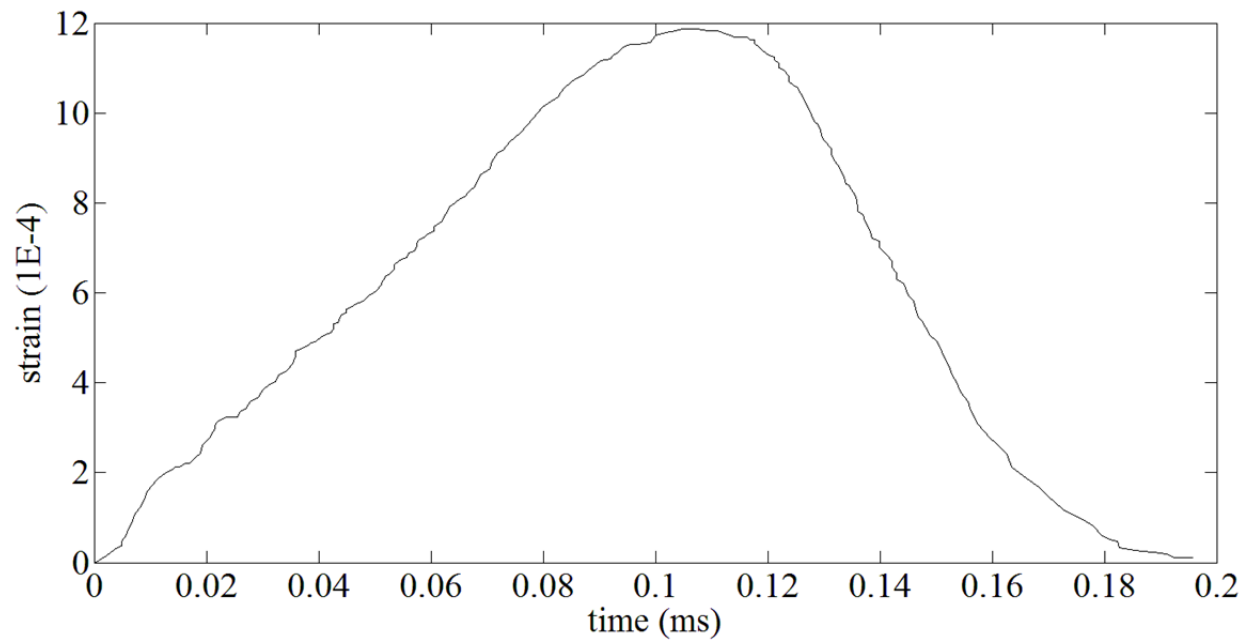


Figure 3.37 Incidence wave after filter from Ref. [8].

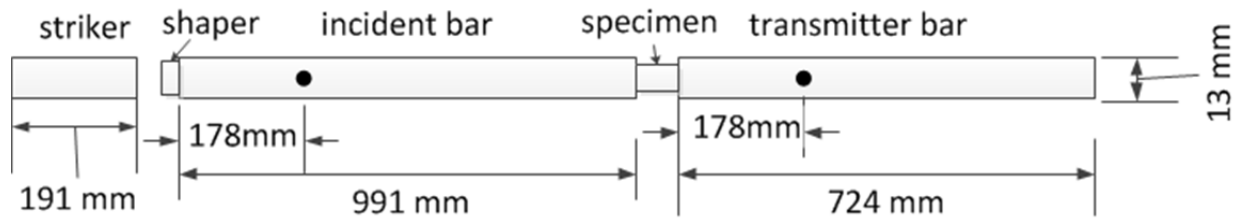


Figure 3.38 SHPB with a shaper.

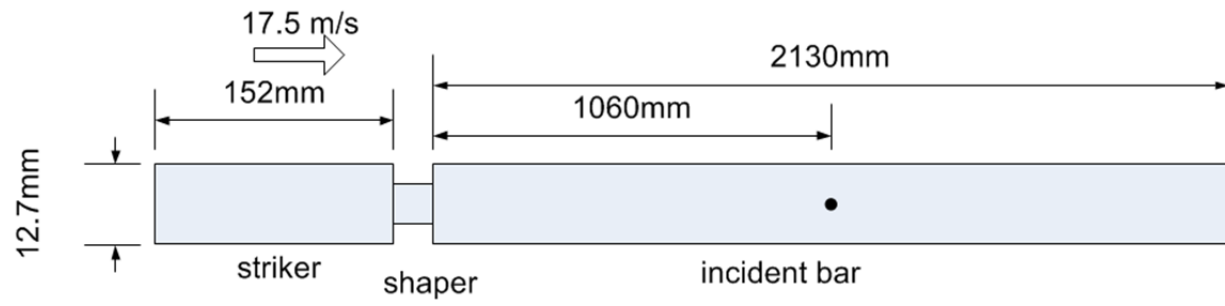


Figure 3.39 Split bar system in Ref. [8].

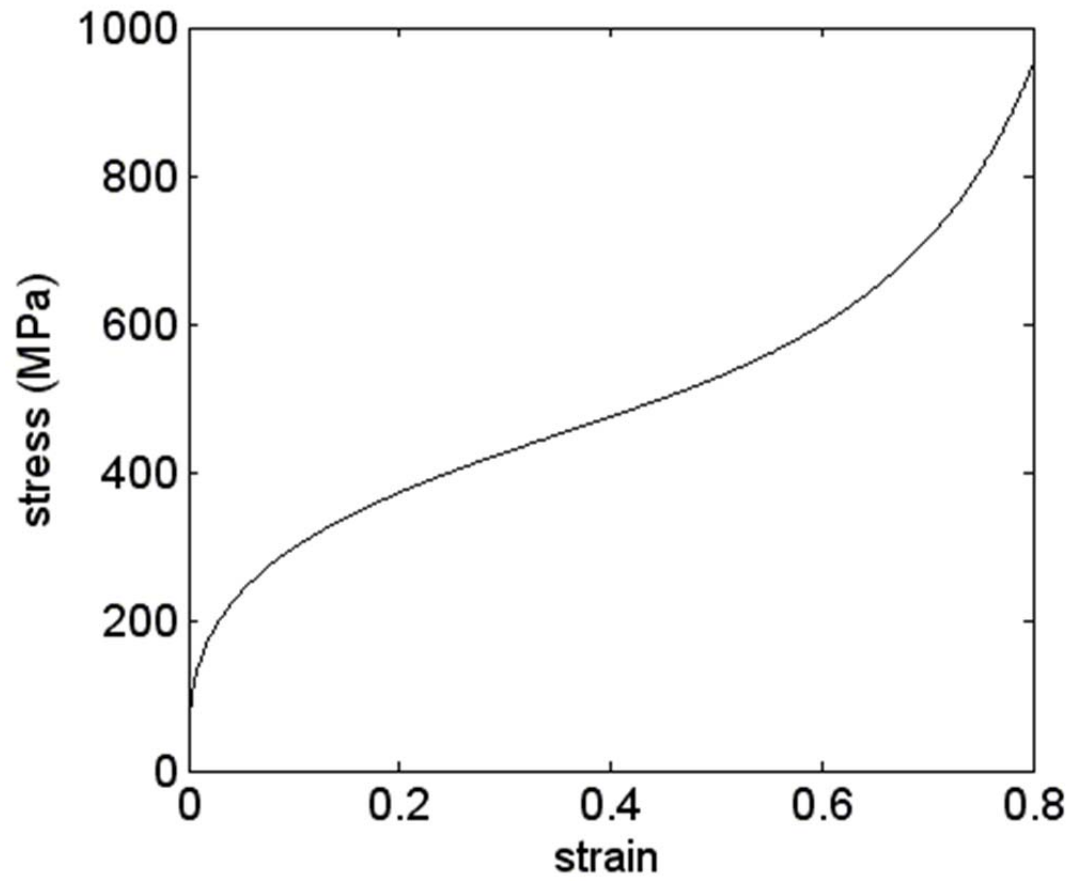


Figure 3.40 Stress-strain relation for the copper shaper given in Ref. [8].

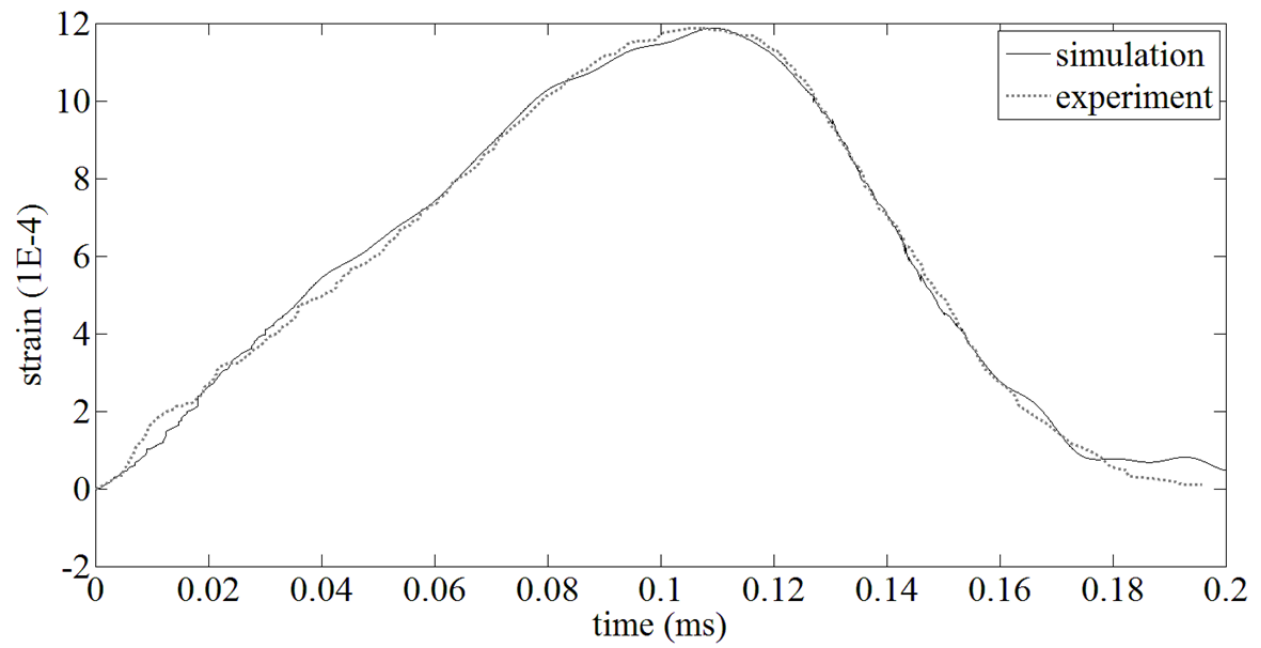


Figure 3.41 Simulation results compared with experiment results from Ref. [8].

REFERENCES

References

- [1] Thomson, W. T., Dahleh, M. D., Theory of Vibration and Applications, 5th edition, Prentice Hall (1997)
- [2] Oppenheim, A. V., Willsky, A. S., Nawab, S. H., Signals and Systems, 2nd edition, Prentice Hall (1996)
- [3] Chen, W. W., Song, B., Split Hopkinson (Kolsky) Bar: Design, Testing and Applications (Mechanical Engineering Series), 1st edition, Springer (2010)
- [4] <http://www.mathworks.com/help/techdoc/ref/fft.html>
- [5] <http://www.mathworks.com/help/techdoc/ref/fft.html>
- [6] Li, G., Construction, calibration and applications of a Split Hopkinson Pressure Bar, thesis for the Degree of M. S., Michigan State University (2002)
- [7] <http://www.mathworks.com/products/curvefitting/>
- [8] Frew, D. J., Forrestal, M. J. and Chen, W., Pulse shaping techniques for testing brittle materials with a split Hopkinson pressure bar, Experimental Mechanics, **42**, 93-106 (2002)

Chapter 4

Two-Dimensional Peridynamic Studies

The one-dimensional bar-like model presented in the previous chapter is excellent for one-dimensional analysis. This chapter investigates a beam-like model for two-dimensional analysis.

The two-dimensional governing equation of peridynamics [1] is

$$\rho \ddot{\mathbf{u}} = \int f \, dA \quad (4.1)$$

where the integration domain is horizon δ .

4.1 Bar model

Similar to the bar model given in section 3.1, a simple model of bond force can be expressed as

$$f = c \cdot s \quad (4.2)$$

where c is a material property, such as stiffness. To identify c , it is necessary to find strain energy density based on peridynamics and set it equal to that based on classical mechanics.

Consider a plane stress problem with the following displacement field

$$\begin{aligned} u_r &= \varepsilon_0 r \\ u_\theta &= 0 \end{aligned} \quad (4.3)$$

as shown in Fig. 4.1.

For the point at the origin \mathbf{x} , the bond stretch is

$$s = \varepsilon_{rr} = \varepsilon_0 \quad (4.4)$$

From Eqn. 2.7, it is defined that

$$\eta = s\xi \quad (4.5)$$

Substituting Eqn. 4.5 into Eqn. 4.2, it yields

$$f = c \cdot s = c \cdot \eta / \xi \quad (4.6)$$

Based on the definition of the micro-potential (Eqn. 2.9), it follows that

$$w_b = \frac{c\eta^2}{2\xi} = cs^2\xi/2 \quad (4.7)$$

This is the strain energy in one bond. Integrating w_b over the horizon of \mathbf{x} , the strain energy density becomes

$$W = \frac{1}{2} \int w_b dA = \frac{1}{2} \int_0^\delta \int_0^{2\pi} \frac{cs^2\xi}{2} \xi d\theta d\xi = \frac{c\pi s^2\delta^3}{6} \quad (4.8)$$

The strain energy density can also be calculated from theory of elasticity. From Eqn. 4.3, the strain components [2] are

$$\varepsilon_{rr} = \frac{\partial u_r}{\partial r} = \varepsilon_0 \quad (4.9)$$

$$\varepsilon_{\theta\theta} = \frac{u_r}{r} = \varepsilon_0 \quad (4.10)$$

$$\gamma_{r\theta} = 0 \quad (4.11)$$

Using Hook's law [2], the stress elements are found to be

$$\sigma_{rr} = \frac{E}{1-\nu^2} \varepsilon_{rr} + \frac{E\nu}{1-\nu^2} \varepsilon_{\theta\theta} \quad (4.12)$$

$$\sigma_{\theta\theta} = \frac{E\nu}{1-\nu^2} \varepsilon_{rr} + \frac{E}{1-\nu^2} \varepsilon_{\theta\theta} \quad (4.13)$$

The strain energy density from classical mechanics then becomes

$$W = \frac{1}{2}(\sigma_{rr}\varepsilon_{rr} + \sigma_{\theta\theta}\varepsilon_{\theta\theta}) = \frac{E\varepsilon_0^2}{1-\nu} \quad (4.14)$$

Setting the two strain energy densities, i.e. Eqn. 4.8 and Eqn. 4.14, equal to each other, it yields

$$\frac{Es^2}{1-\nu} = \frac{c\pi s^2\delta^3}{6} \quad (4.15)$$

Rearranging Eqn. 4.15, the material property c can be found as follows

$$c = \frac{6E}{\pi\delta^3(1-\nu)} \quad (4.16)$$

4.2 Definition of stress in peridynamics

Similar to Section 3.2, the definition of stress is only sought for comparison purposes since there is no need of stress in peridynamic simulations. In two-dimensional analysis, the traction [3] at point \mathbf{x} is defined as the total internal force applied on the segment $[-\delta, 0]$ by the domain on the right-hand side of \mathbf{x} as shown in Fig. 4.2 and can be expressed by the following equation

$$\boldsymbol{\tau}(\mathbf{x}) = \int_0^\delta \int_{R^+} \mathbf{f} dA_{x'} dh \quad (4.17)$$

where R^+ is the domain on the right-hand side of point \mathbf{x} , x' is a point in R^+ , $dA_{x'}$ is the integration element area of x' and \mathbf{f} is the bond force applied on dh by x' . It should be noted that all points on the R^+ apply forces not only on point \mathbf{x} but also beyond \mathbf{x} along a layer of thickness δ , which is the horizon. The x component of $\boldsymbol{\tau}(\mathbf{x})$ is σ_{xx} and is defined as

$$\sigma_{xx} = \int_0^\delta \int_{R^+} f_x dA_{x'} dh \quad (4.18)$$

Consider a deformation with strains $\varepsilon_{xx} = \varepsilon_1$ and $\varepsilon_{yy} = \varepsilon_2$, the bond stretch should become

$$s = \varepsilon_1 \cos^2 \theta + \varepsilon_2 \sin^2 \theta \quad (4.19)$$

Then the x component of the bond force is

$$f_x = c \cdot s \cdot \cos \theta \quad (4.20)$$

Substituting Eqn. 4.20 into Eqn. 4.18, it arrives

$$\begin{aligned} \sigma_{xx} &= \int_0^\delta \int_h^\delta \int_{-\cos^{-1}\frac{h}{r}}^{\cos^{-1}\frac{h}{r}} f_x r d\theta dr dh = \int_0^\delta \int_h^\delta \int_{-\cos^{-1}\frac{h}{r}}^{\cos^{-1}\frac{h}{r}} c \cdot \varepsilon_0 \cdot \sin^2 \theta \cdot \cos \theta r d\theta dr dh \\ &= \frac{3E\varepsilon_1}{4(1-\nu)} + \frac{E\varepsilon_2}{4(1-\nu)} \end{aligned} \quad (4.21)$$

The integration domain shown in Fig. 4.3 can be explained as that f_x is the x component of the force applied by R^+ on point A. The distance from point \mathbf{x} to point A is h which covers from 0 to δ because R^+ has no interaction with points beyond δ . For point A, which is located a distance h from \mathbf{x} , the distance between a point in R^+ and point A is r . The smallest value of r is h and the largest value of r is δ . For every r , only points from $\theta = -\cos^{-1}\frac{h}{r}$ to $\theta = \cos^{-1}\frac{h}{r}$ are in R^+ domain. Points outside this range are not in R^+ domain. The symbolic integration can be calculated by Mathematica [4].

In classical mechanics, σ_{xx} is defined as follows

$$\sigma_{xx} = \frac{E}{1-\nu^2} \varepsilon_1 + \frac{E\nu}{1-\nu^2} \varepsilon_2 \quad (4.22)$$

Eqn. 4.21 and Eqn. 4.22 are equal to each other when $\nu = 1/3$. There is only one material property defined in the bar model based on peridynamic analysis as opposed to two independent properties used in classical mechanics. Hence, the Poisson's ratio for the peridynamic bar model has to be $1/3$.

4.3 Beam model

In order to accommodate two material properties, an upgraded peridynamic model resembling a beam is proposed here. The interaction force between two points depends not only on the deformation along the axial direction but also along the transverse direction as depicted in Fig. 4.4.

Consider a point x_2 located away from x_1 , with an angle θ . The bond forces between x_1 and x_2 , based on the local coordinate on x_1 , are

$$f'_x = c_1(u'_2 - u'_1)/r \quad (4.23)$$

$$f'_y = c_2(v'_2 - v'_1)/r^3 \quad (4.24)$$

where f'_x is the axial force applied on x_1 by x_2 , f'_y is the transverse force applied on x_1 by x_2 and r is the original length of the bond x_1 - x_2 . The transformation equations between the local coordinate and the global coordinate are

$$u' = u \cos \theta + v \sin \theta \quad (4.25)$$

$$v' = -u \sin \theta + v \cos \theta \quad (4.26)$$

Consider a case with strains in x and y directions are ε_1 and ε_2 , i.e. $\varepsilon_1 = \frac{u_2 - u_1}{r \cos \theta}$ and $\varepsilon_2 = \frac{v_2 - v_1}{r \sin \theta}$.

Eqn. 4.23 and Eqn. 4.24 become

$$f'_x = \frac{c_1(u_2 \cos \theta + v_2 \sin \theta - u_1 \cos \theta - v_1 \sin \theta)}{r} = c_1 (\varepsilon_1 r \cos \theta^2 + \varepsilon_2 r \sin \theta^2) / r \quad (4.27)$$

$$f'_y = \frac{c_2(-u_2 \sin \theta + v_2 \cos \theta + u_1 \sin \theta - v_1 \cos \theta)}{r^3} = (-\varepsilon_1 r \cos \theta \sin \theta + \varepsilon_2 r \cos \theta \sin \theta) / r^3 \quad (4.28)$$

The strain energy of this bond becomes

$$w_b = \frac{c_1(\varepsilon_1 r \cos \theta^2 + \varepsilon_2 r \sin \theta^2)^2}{2r} + \frac{c_2(-\varepsilon_1 r \cos \theta \sin \theta + \varepsilon_2 r \cos \theta \sin \theta)^2}{2r^3} \quad (4.29)$$

Integrating Eqn. 4.29, the strain energy density at x_1 becomes

$$\begin{aligned} W &= \frac{1}{2} \int w_b dA = \frac{1}{2} \int_0^\delta \int_0^{2\pi} w_b r d\theta dr \\ &= \frac{1}{48} \pi \delta [3c_2(\varepsilon_1 - \varepsilon_2)^2 + c_1(3\varepsilon_1^2 + 2\varepsilon_1\varepsilon_2 + 3\varepsilon_2^2)\delta^2] \end{aligned} \quad (4.30)$$

where δ is the horizon.

On the other hand, from classical mechanics, the stresses are defined as

$$\sigma_1 = \frac{E}{1-v^2} (\varepsilon_1 + v\varepsilon_2) \quad (4.31)$$

$$\sigma_2 = \frac{E}{1-v^2} (\varepsilon_2 + v\varepsilon_1) \quad (4.32)$$

The strain energy density is

$$W = \frac{1}{2} \sigma_1 \varepsilon_1 + \frac{1}{2} \sigma_2 \varepsilon_2 = \frac{E}{2(1-v^2)} \varepsilon_1^2 + \frac{Ev}{(1-v^2)} \varepsilon_1 \varepsilon_2 + \frac{E}{2(1-v^2)} \varepsilon_2^2 \quad (4.33)$$

Set Eqn. 4.30 and Eqn. 4.33 equal to each other, the following solutions can be obtained

$$c_1 = -\frac{6E}{\pi\delta^3(\nu-1)} \quad (4.34)$$

$$c_2 = -\frac{2E(1-3\nu)}{\pi\delta(\nu^2-1)} \quad (4.35)$$

where c_1 and c_2 are the two independent material properties of the beam model. When $\nu = 1/3$ and $c_2 = 0$, the beam model can be reduced to the bar model presented in Section 4.1.

From Eqn. 4.34 and Eqn. 4.35, Young's modulus E and Poisson's ratio ν can also be expressed by c_1 and c_2

$$E = \frac{c_1(3c_2+c_1\delta^2)\pi\delta^3}{9(c_2+c_1\delta^2)} \quad (4.36)$$

$$\nu = -1 + \frac{4\delta^2}{3(c_2/c_1+\delta^2)} \quad (4.37)$$

From Eqn. 4.37, it can be concluded that ν can vary from -1 to infinity. This implies that the peridynamic beam model is capable of modeling any isotropic material which has ν ranging from -1 to 0.5.

Similar to Section 4.2, the stresses can be calculated from the peridynamic beam model and compared with those given in classical mechanics. Consider a deformation with strains $\varepsilon_{xx} = \varepsilon_1$ and $\varepsilon_{yy} = \varepsilon_2$. In the beam model, the x component of bond force is

$$f_x = f'_x \cdot \cos \theta - f'_y \cdot \sin \theta \quad (4.38)$$

This is different from the bar model which gives $f_x = f'_x \cdot \cos \theta$. Eqn. 4.18 can then be expressed as

$$\begin{aligned}
\sigma_{xx} &= \int_0^\delta \int_h^\delta \int_{-\cos^{-1}\frac{h}{r}}^{\cos^{-1}\frac{h}{r}} (fx' \cdot \cos \theta - fy' \cdot \sin \theta) r d\theta dr dh \\
&= \frac{\pi\delta}{24} [c_1 \delta^2 (3\varepsilon_1 + \varepsilon_2) + 3c_2 (\varepsilon_1 - \varepsilon_2)]
\end{aligned} \tag{4.39}$$

Substituting Eqn. 4.34 and Eqn. 4.35 into Eqn. 3.39, it yields

$$\sigma_{xx} = \frac{E}{1-\nu^2} \varepsilon_1 + \frac{E\nu}{1-\nu^2} \varepsilon_2 \tag{4.40}$$

The interpretation of Eqn. 4.39 is similar to that of Eqn. 4.21. As can be seen, Eqn. 4.40 is exactly the same as σ_{xx} in Eqn. 4.22 obtained from classical mechanics analysis.

4.4 Computational efficiency

From Fig. 2.4, it can be seen that there are three loops in peridynamic calculations, namely time loop, domain loop and neighbor loop. With the loops, small time step and small distance between nodes, peridynamic calculations will become very time consuming. For example, Study Three in Chapter 3 has about 3500 nodes in the one-dimensional domain. It takes about two hours to complete the calculation using the serial computational algorithm shown in Fig. 2.4. Hence, it can be expected that two-dimensional peridynamic problems containing more nodes will further slow down the calculation process if the serial computational algorithm shown in Fig. 2.4 is used. This section studies methods to improve the computational efficiency of peridynamics.

4.4.1 Using matrix computation

For problems involving infinitesimal deformation, the relationships between nodes may be

considered unchanged during the deformation process. The calculation of these relationships in each time step shown in the flowchart given in Fig. 2.4 may be disregarded. For computational efficiency, it is desired to calculate these relationships before the beginning of computation and store them in a matrix like the stiffness matrix practiced in finite element analysis. Therefore, only matrix multiplication is required in each time step.

For two-dimensional analysis, the peridynamic equation of motion can be rewritten in the following discrete form based on node i

$$\rho \ddot{\mathbf{u}}_i = \sum_{is} \mathbf{f} \Delta A + \mathbf{b}_i \quad (4.41)$$

where is is any node in the horizon of point i shown in Fig. 4.5. Other notations are mass density ρ , acceleration (of node i) $\ddot{\mathbf{u}}_i$, force (between node i and node is) \mathbf{f} , area (of node is) ΔA and body force (of node i) \mathbf{b}_i . The following notations are also defined below:

nodal positions: $[x_1, x_2]$ for node i and $[x_{1s}, x_{2s}]$ for node is

node displacements: $[u_1, u_2]$ for node i and $[u_{1s}, u_{2s}]$ for node is

relative displacement: $\boldsymbol{\eta} = [(u_{1s} - u_1), (u_{2s} - u_2)]$

relative position: $\boldsymbol{\xi} = [(x_{1s} - x_1), (x_{2s} - x_2)]$

bond stretch: $s = \frac{|\boldsymbol{\eta} + \boldsymbol{\xi}|}{|\boldsymbol{\xi}|} - 1$

force between node i and node is : $\mathbf{f} = c \cdot s \cdot \frac{\boldsymbol{\eta} + \boldsymbol{\xi}}{|\boldsymbol{\eta} + \boldsymbol{\xi}|}$ (4.42)

The x_1 component of \mathbf{f} is

$$f_1(u_1, u_2, u_{1s}, u_{2s}) = c \cdot s \cdot \frac{(u_{1s} - u_1 + x_{1s} - x_1)}{|\boldsymbol{\eta} + \boldsymbol{\xi}|} \quad (4.43)$$

To express f_1 in a matrix form, the following truncated Taylor's series may be used

$$\begin{aligned}
f_1(u_1, u_2, u_{1s}, u_{2s}) = & f_1(0,0,0,0) + \frac{\partial f_1}{\partial u_1}(0,0,0,0) \cdot u_1 + \frac{\partial f_1}{\partial u_2}(0,0,0,0) \cdot u_2 + \frac{\partial f_1}{\partial u_{1s}}(0,0,0,0) \cdot u_{1s} + \\
& \frac{\partial f_1}{\partial u_{2s}}(0,0,0,0) \cdot u_{2s} + \frac{1}{2} \left(\frac{\partial^2 f_1}{\partial u_1^2}(0,0,0,0) \cdot u_1^2 + 2 \frac{\partial^2 f_1}{\partial u_1 \partial u_2}(0,0,0,0) \cdot u_1 u_2 + 2 \frac{\partial^2 f_1}{\partial u_1 \partial u_{1s}}(0,0,0,0) \cdot \right. \\
& u_1 u_{1s} + 2 \frac{\partial^2 f_1}{\partial u_1 \partial u_{2s}}(0,0,0,0) \cdot u_1 u_{2s} + \frac{\partial^2 f_1}{\partial u_2^2}(0,0,0,0) \cdot u_2^2 + 2 \frac{\partial^2 f_1}{\partial u_2 \partial u_{1s}}(0,0,0,0) \cdot u_2 u_{1s} + \\
& 2 \frac{\partial^2 f_1}{\partial u_2 \partial u_{2s}}(0,0,0,0) \cdot u_2 u_{2s} + \frac{\partial^2 f_1}{\partial u_{1s}^2}(0,0,0,0) \cdot u_{1s}^2 + 2 \frac{\partial^2 f_1}{\partial u_{1s} \partial u_{2s}}(0,0,0,0) \cdot u_{1s} u_{2s} + \\
& \left. \frac{\partial^2 f_1}{\partial u_{2s}^2}(0,0,0,0) \cdot u_{2s}^2 \right) + \dots
\end{aligned} \tag{4.44}$$

The x_2 component of \mathbf{f} is

$$f_2 = c \cdot s \cdot \frac{(u_{2s} - u_2 + x_{2s} - x_2)}{|\boldsymbol{\eta} + \boldsymbol{\xi}|} \tag{4.45}$$

Similarly, to express f_2 in a matrix form, the following truncated Taylor's series may be used

$$\begin{aligned}
f_2(u_1, u_2, u_{1s}, u_{2s}) = & f_2(0,0,0,0) + \frac{\partial f_2}{\partial u_1}(0,0,0,0) \cdot u_1 + \frac{\partial f_2}{\partial u_2}(0,0,0,0) \cdot u_2 + \frac{\partial f_2}{\partial u_{1s}}(0,0,0,0) \cdot \\
& u_{1s} + \frac{\partial f_2}{\partial u_{2s}}(0,0,0,0) \cdot u_{2s} + \\
& \frac{1}{2} \left(\frac{\partial^2 f_2}{\partial u_1^2}(0,0,0,0) \cdot u_1^2 + 2 \frac{\partial^2 f_2}{\partial u_1 \partial u_2}(0,0,0,0) \cdot u_1 u_2 + 2 \frac{\partial^2 f_2}{\partial u_1 \partial u_{1s}}(0,0,0,0) \cdot u_1 u_{1s} + \right. \\
& 2 \frac{\partial^2 f_2}{\partial u_1 \partial u_{2s}}(0,0,0,0) \cdot u_1 u_{2s} + \frac{\partial^2 f_2}{\partial u_2^2}(0,0,0,0) \cdot u_2^2 + 2 \frac{\partial^2 f_2}{\partial u_2 \partial u_{1s}}(0,0,0,0) \cdot u_2 u_{1s} + \\
& 2 \frac{\partial^2 f_2}{\partial u_2 \partial u_{2s}}(0,0,0,0) \cdot u_2 u_{2s} + \frac{\partial^2 f_2}{\partial u_{1s}^2}(0,0,0,0) \cdot u_{1s}^2 + 2 \frac{\partial^2 f_2}{\partial u_{1s} \partial u_{2s}}(0,0,0,0) \cdot u_{1s} u_{2s} + \\
& \left. \frac{\partial^2 f_2}{\partial u_{2s}^2}(0,0,0,0) \cdot u_{2s}^2 \right) + \dots
\end{aligned} \tag{4.46}$$

The equation of motion can then be written in a matrix form

$$\rho \cdot \ddot{\mathbf{d}} = \mathbf{K} \cdot \mathbf{d} + \mathbf{d}^T \cdot \mathbf{M} \cdot \mathbf{d} + \mathbf{b} \quad (4.47)$$

where \mathbf{d} is a displacement vector and is defined as

$$\begin{aligned} d_{2i-1} &= u_1 \\ d_{2i} &= u_2 \\ d_{2is-1} &= u_{1s} \\ d_{2is} &= u_{2s} \end{aligned} \quad (4.48)$$

\mathbf{K} is the first-order term matrix (two-dimensional symmetric matrix) and is defined as

$$\begin{aligned} K_{2i-1,2i-1} &= \frac{\partial f_1}{\partial u_1}(0,0,0,0) \\ K_{2i-1,2i} &= \frac{\partial f_1}{\partial u_2}(0,0,0,0) \\ K_{2i-1,2is-1} &= \frac{\partial f_1}{\partial u_{1s}}(0,0,0,0) \\ K_{2i-1,2is} &= \frac{\partial f_1}{\partial u_{2s}}(0,0,0,0) \\ K_{2i,2i-1} &= \frac{\partial f_2}{\partial u_1}(0,0,0,0) \\ K_{2i,2i} &= \frac{\partial f_2}{\partial u_2}(0,0,0,0) \\ K_{2i,2is-1} &= \frac{\partial f_2}{\partial u_{1s}}(0,0,0,0) \\ K_{2i,2is} &= \frac{\partial f_2}{\partial u_{2s}}(0,0,0,0) \end{aligned} \quad (4.49)$$

\mathbf{M} is the second-order term matrix (three-dimensional matrix) and is defined as

$$M_{2i-1,2i-1,2i-1} = \frac{1}{2} \frac{\partial^2 f_1}{\partial u_1^2} (0,0,0,0)$$

$$M_{2i-1,2i,2i-1} = \frac{\partial^2 f_1}{\partial u_1 \partial u_2} (0,0,0,0)$$

$$M_{2i-1,2is-1,2i-1} = \frac{\partial^2 f_1}{\partial u_1 \partial u_{1s}} (0,0,0,0)$$

$$M_{2i-1,2is,2i-1} = \frac{\partial^2 f_1}{\partial u_1 \partial u_{2s}} (0,0,0,0)$$

$$M_{2i,2i,2i-1} = \frac{1}{2} \frac{\partial^2 f_1}{\partial u_2^2} (0,0,0,0)$$

$$M_{2i,2is-1,2i-1} = \frac{\partial^2 f_1}{\partial u_2 \partial u_{1s}} (0,0,0,0)$$

$$M_{2i,2is,2i-1} = \frac{\partial^2 f_1}{\partial u_2 \partial u_{2s}} (0,0,0,0)$$

$$M_{2is-1,2is-1,2i-1} = \frac{1}{2} \frac{\partial^2 f_1}{\partial u_{1s}^2} (0,0,0,0)$$

$$M_{2is-1,2is,2i-1} = \frac{\partial^2 f_1}{\partial u_{1s} \partial u_{2s}} (0,0,0,0)$$

$$M_{2is,2is,2i-1} = \frac{1}{2} \frac{\partial^2 f_1}{\partial u_{2s}^2} (0,0,0,0)$$

$$M_{2i-1,2i-1,2i} = \frac{1}{2} \frac{\partial^2 f_2}{\partial u_1^2} (0,0,0,0)$$

$$M_{2i-1,2i,2i} = \frac{\partial^2 f_2}{\partial u_1 \partial u_2} (0,0,0,0)$$

$$M_{2i-1,2is-1,2i} = \frac{\partial^2 f_2}{\partial u_1 \partial u_{1s}} (0,0,0,0)$$

$$M_{2i-1,2is,2i} = \frac{\partial^2 f_2}{\partial u_1 \partial u_{2s}} (0,0,0,0)$$

$$\begin{aligned}
M_{2i,2i,2i} &= \frac{1}{2} \frac{\partial^2 f_2}{\partial u_2^2} (0,0,0,0) \\
M_{2i,2is-1,2i} &= \frac{\partial^2 f_2}{\partial u_2 \partial u_{1s}} (0,0,0,0) \\
M_{2i,2is,2i} &= \frac{\partial^2 f_2}{\partial u_2 \partial u_{2s}} (0,0,0,0) \\
M_{2is-1,2is-1,2i} &= \frac{1}{2} \frac{\partial^2 f_2}{\partial u_{1s}^2} (0,0,0,0) \\
M_{2is-1,2is,2i} &= \frac{\partial^2 f_2}{\partial u_{1s} \partial u_{2s}} (0,0,0,0) \\
M_{2is,2is,2i} &= \frac{1}{2} \frac{\partial^2 f_2}{\partial u_{2s}^2} (0,0,0,0)
\end{aligned} \tag{4.50}$$

Eqn. 4.49 and Eqn. 4.50 are calculated before the first time step. Once the \mathbf{K} matrix and the \mathbf{M} matrix are built, each step can be carried out by Eqn. 4.47. The computational flowchart is shown in Fig. 4.6. As compared with that shown in Fig. 2.4, two layers of loop in each time step are eliminated. A significant amount of time can then be saved. For a one-dimensional problem with about 3500 nodes as used in Study Three of Chapter 3, it takes about two hours to complete the simulation on a PC with an Intel(R) Core(TM) i7-2860QM CPU based on the algorithm showing in Fig. 2.4. However, it only requires approximately five seconds to complete the simulation on the same PC using the matrix computation algorithm.

4.4.2 Using parallel computing

Another problem continues to hinder the computational process in the matrix computation is associated with damage process. When damage takes place, bond stretches still have to be calculated and checked one by one to identify the locations and directions of the damage. Once

damage is identified, the corresponding elements of \mathbf{K} and \mathbf{M} will have to be nulled to represent the loss of bond stiffness due to the broken bonds. This process will also slow down the peridynamic computation and hinders the convenience of the peridynamic method in damage problems.

Since the computation of peridynamic nodes is independent of one another, there is a great advantage to use parallel computing in peridynamic simulations. Therefore, the algorithm shown in Fig. 2.4 is modified for parallel computing. As shown in Fig. 4.7, the computation of individual nodes are carried out independently.

In this study, the Matlab parallel computing toolbox [5] is used to implement the parallel computing. The program is modified as shown in Fig. 4.8. As can be seen from Fig. 4.7, the neighboring loop is also eliminated by using matrix computation in Matlab. Instead of processing one neighboring node to another, it is possible to use Matlab matrix computation to manipulate all neighboring nodes at the same time. The facility located at High Performance Computing Center (HPCC) at MSU [6] is used to run the modified program. However, due to the limited resources at the HPCC, eight workers are considered as a balanced choice between queue time and computation time. When solving a two-dimensional problem with 10,201 nodes, it takes 215 seconds to compute 100 time steps based on serial computing while it only takes 27 seconds to complete the same task based on eight-worker parallel computing. Ideally, if resource is available, it is possible to use the same number of workers as the number of nodes to significantly reduce the computational time.

4.5 Comparison with vibration theory

4.5.1 Vibration theory

In a two-dimensional polar coordinate system (r, θ, t) , consider the free vibration of a circular plate, shown in Fig. 4.9, under the following initial conditions

$$u_r(r, \theta, 0) = \varepsilon_0 r \quad (4.51)$$

$$u_\theta(r, \theta, 0) = 0 \quad (4.52)$$

Since the circumference of the circle, $r = R$, is a free boundary, the boundary condition should be

$$\sigma_{rr}(R, \theta, t) = 0 \quad (4.53)$$

Apparently, this is an axisymmetric problem and the displacements can be redefined as

$$u_r(r, \theta, t) = u(r, t) \quad (4.54)$$

$$u_\theta(r, \theta, t) = 0 \quad (4.55)$$

Hence, the strains are [2]

$$\varepsilon_{rr} = \frac{\partial u}{\partial r} \quad (4.56)$$

$$\varepsilon_{\theta\theta} = \frac{u}{r} \quad (4.57)$$

$$\gamma_{r\theta} = 0 \quad (4.58)$$

By substituting Eqn. 4.56, Eqn. 4.57 and Eqn. 4.58 into Hook's law, the following stresses can be found

$$\sigma_{rr} = \frac{E}{1-\nu^2} \varepsilon_{rr} + \frac{E\nu}{1-\nu^2} \varepsilon_{\theta\theta} = \frac{E}{1-\nu^2} \frac{\partial u}{\partial r} + \frac{E\nu}{1-\nu^2} \frac{u}{r} \quad (4.59)$$

$$\sigma_{\theta\theta} = \frac{E}{1-\nu^2} \varepsilon_{\theta\theta} + \frac{E}{1-\nu^2} \varepsilon_{rr} = \frac{E}{1-\nu^2} \frac{u}{r} + \frac{E}{1-\nu^2} \frac{\partial u}{\partial r} \quad (4.60)$$

$$\sigma_{r\theta} = 0 \quad (4.61)$$

The polar coordinates based equation of motion in r -direction is defined as

$$\rho \ddot{u} = \frac{\partial \sigma_{rr}}{\partial r} + \frac{1}{r} \frac{\partial \sigma_{\theta\theta}}{\partial \theta} + \frac{\sigma_{rr} - \sigma_{\theta\theta}}{r} = \frac{E}{1-\nu^2} \frac{\partial^2 u}{\partial r^2} + \frac{E}{r(1-\nu^2)} \frac{\partial u}{\partial r} - \frac{E}{1-\nu^2} \frac{u}{r^2} \quad (4.62)$$

The equation of motion can be solved using numerical method. With $E = 75 \text{ GPa}$, $\nu = 0.3$, $\rho = 2800 \text{ kg/m}^3$ and $R = 0.1 \text{ m}$, the strain history of point B on the circular plate is shown in Fig. 4.10.

4.5.2 Numerical studies

There are three parameters in numerical calculation. They are time step dt , number of nodes in horizon m and the size of horizon δ . As discussed in Chapter 3, the smaller the horizon, the closer the solution will be to that of classical mechanics. When the horizon is fixed, more nodes within the horizon, i.e. smaller node size, will give higher solution accuracy. However, smaller node size and higher node number in the horizon will require higher computational time. A practical computation should have a balance between computational efficiency and numerical accuracy.

Twelve pairs of m and δ are investigated for comparison. They are shown in Table 4.1. Fig. 4.11 shows the computational results of case 10, case 11 and case 12 along with their analytical

solution. Although $\delta = 10mm$ is a large horizon, it still can be seen that the increase of the node number in the horizon, i.e. the decrease of node size, improves the accuracy of the peridynamic solution to the theoretical solution. Fig. 4.12 compares case 5 and case 6 with the solution from vibration theory. When the number of nodes in a horizon is fixed at 4, two different horizons, $\delta = 2.2 mm$ and $\delta = 2.5 mm$, are used. As shown in Fig. 4.12, the smaller the horizon, the closer the peridynamic solution becomes to the solution from vibration theory solution.

Table 4.1 Twelve pairs of m and δ

	$m = 1$	$m = 3$	$m = 4$	$m = 5$	$m = 10$
$\delta = 1$	1			2	3
$\delta = 1.6 mm$		4			
$\delta = 2.2 mm$			5		
$\delta = 2.5 mm$			6		
$\delta = 5 mm$	7			8	9
$\delta = 10 mm$	10			11	12

When $m = 4$ and $\delta = 2.2 mm$, the size of time step dt is studied. As shown in Fig. 4.13, two different time steps, $dt = 1 \times 10^{-7}s$ and $dt = 1 \times 10^{-8}s$, are used and the results are compared with the results from the vibration theory. The result with $dt = 1 \times 10^{-8}s$ is slightly better than that from $dt = 1 \times 10^{-7}s$ at the rising time of the radial strain. Other than that, the two results are almost the same. However, the case with $dt = 1 \times 10^{-8}s$ is about ten times slower than the case with $dt = 1 \times 10^{-7}s$.

Based on these results, $dx = 0.5mm$, $\delta = 2.2 mm$ and $dt = 1 \times 10^{-7}s$ are used and the strain histories of point A, point B and point C, as shown in Fig. 4.9, are compared with the vibration theory results in Fig. 4.14, Fig. 4.15 and Fig. 4.16 respectively. They agree well.

4.6 Convergence to the one-dimensional results

To further verify the two-dimensional peridynamic model, it is also of interest to compare the results from the two-dimensional peridynamic simulations with those from the one-dimensional peridynamic simulations.

The free vibration of a rectangular plate as shown in Fig. 4.17 is considered. The length of the plate is $L_1 = 0.4 m$ and the aspect ratio is $a = L_1/L_2$. The material properties are $E = 75 GPa$, $\nu = 0.3$ and $\rho = 2800 kg/m^3$. The boundaries are all free and the initial conditions are

$$u_1(x_1, x_2) = \varepsilon_1 \cdot x_1 \quad (4.63)$$

$$u_2(x_1, x_2) = -\nu\varepsilon_1 \cdot x_2 \quad (4.64)$$

The vibration process is simulated by the two-dimensional peridynamic method and the strain history of point A, shown in Fig. 4.17, is recorded and compared with the results from the one-dimensional peridynamic analysis.

Figs. 4.18, 4.19, 4.20, 4.21 and 4.22 show the comparison for $a = 0.2$, $a = 1$, $a = 10$, $a = 50$ and $a = 100$, respectively. As can be seen, the results based on the two-dimensional theory converge to those based on the one-dimensional theory when the aspect ratio becomes larger.

4.7 Axisymmetric problems

In this section, an axisymmetric model of peridynamics is proposed. Similar to classical mechanics, the calculation of an axisymmetric problem can be simplified and the dimension can be reduced. A two-dimensional axisymmetric problem can be reduced to a one-dimensional problem. This will simplify the calculation and reduce the computational time significantly.

For a two-dimensional axisymmetric problem, as shown in Fig. 4.23, consider a point $P(R_0)$.

The governing equation of point P using local radial coordinate (r, θ) is expressed as follows

$$\rho \ddot{u}(R_0) = \int_0^\delta \int_0^{2\pi} f_R r d\theta dr \quad (4.65)$$

where δ is horizon and f_R is the force applied on point P by point Q in global radial direction R .

The R component of bond force f_R is

$$f_R = c \cdot s \cdot \sin \theta \quad (4.66)$$

and s is the stretch between the two points, which can be defined as

$$s = \frac{|x_Q + u_Q - x_P - u_P|}{|x_Q - x_P|} - 1 \quad (4.67)$$

where

$$x_P = R_0 \hat{e}_j \quad (4.68)$$

$$x_Q = r \cos \theta \hat{e}_i + (R_0 + r \sin \theta) \hat{e}_j \quad (4.69)$$

$$u_P = u(R_0) \hat{e}_j \quad (4.70)$$

$$u_Q = u(R) \cos \theta \hat{e}_i + u(R) \sin \theta \hat{e}_j \quad (4.71)$$

Substituting Eqn. 4.67, Eqn. 4.68, Eqn. 4.69 and Eqn. 4.70 into Eqn. 4.71, it yields

$$S = \frac{\sqrt{[r \cos \theta + u(R) \cos \theta]^2 + [r \sin \theta + u(R) \sin \theta - u(R_0)]^2}}{r} - 1 \quad (4.72)$$

The two radial coordinate systems are used for convenience. They are local coordinate (r, θ) and global coordinate (R, θ) . The relationship between them, as shown in Fig. 4.22, is

$$r = \sqrt{R^2 + R_0^2 - 2RR_0 \sin \theta} \quad (4.73)$$

$$\theta = \tan^{-1} \frac{R \sin \theta - R_0}{R \cos \theta} \quad (4.74)$$

After substituting Eqn. 4.73 and Eqn. 4.74 into Eqn. 4.72, the governing equation at point P in global coordinate can be found as

$$\rho \ddot{u}(R_0) = \int_{R-\delta}^{R+\delta} \int_{\frac{\pi}{2} - \cos^{-1} \frac{R_0^2 + R^2 - \delta^2}{2R_0R}}^{\frac{\pi}{2} + \frac{R_0^2 + R^2 - \delta^2}{2R_0R}} f_R(R, \theta) R d\theta dR \quad (4.75)$$

where the integration bound can be found from the triangle shown in Fig. 4.24.

The innermost integration of Eqn. 4.75 is a function of R only. Let

$$F(R) = \int_{\frac{\pi}{2} - \cos^{-1} \frac{R_0^2 + R^2 - \delta^2}{2R_0R}}^{\frac{\pi}{2} + \frac{R_0^2 + R^2 - \delta^2}{2R_0R}} f_R(R, \theta) R d\theta \quad (4.76)$$

Eqn. 4.75 then becomes

$$\rho \ddot{u}(R_0) = \int_{R-\delta}^{R+\delta} F(R) dR \quad (4.77)$$

A two-dimensional problem is therefore reduced to a one-dimensional problem with the

assumption of axisymmetry.

The same problem solved in Section 4.5.1 is simulated using the axisymmetric peridynamic model proposed above and the strains at points A, B and C are compared with the results from Section 4.5.1 in Fig. 4.25, Fig. 4.26 and Fig. 4.27. Good matches are shown between the two results.

4.8 Failure theory

The critical stretch s_0 in Eqn. 2.12 can be found from the energy method similar to Eqn. 4.7. Consider a fracture surface in a large homogeneous body. In order to completely separate the body into two halves, it will require breaking all the bonds crossing the two halves. Let w_{b0} denote the work required to break a single bond,

$$w_{b0} = \int_0^{s_0} \hat{f}(s) d\eta \quad (4.78)$$

where $d\eta = \xi ds$.

Using Eqn. 4.2, Eqn. 4.78 becomes

$$w_{b0} = \frac{1}{2} c s_0^2 \xi \quad (4.79)$$

The work G_0 required to break all the bonds per unit fracture surface area shown in Fig. 4.28 can then be expected as follows

$$G_0 = \int_0^\delta \int_h^\delta \int_{-\cos^{-1} h/r}^{\cos^{-1} h/r} w_{b0} \cdot r d\theta dr dh = \frac{1}{4} c s_0^2 \delta^4 \quad (4.80)$$

The calculation of this integration is similar to that of Eqn. 4.21.

Solving for s_0 , the critical bond stretch can be related to the energy per unit fracture area for completely separating the two halves of the body, i. e.

$$s_0 = \sqrt{\frac{4G_0}{c\delta^4}} \quad (4.81)$$

4.9 Comparisons of crack propagation velocity with experiments

It is challenging to validate the dynamic crack propagation obtained from numerical simulation since there is no analytical solution which can be readily compared with the numerical solution [7]. Therefore, experiment results are often used to compare and validate the numerical models.

Many crack propagation problems were simulated by finite element method. Song [7] compared three different finite element analysis (FEA) techniques with experiment results. The three methods are the extended finite element method (XFEM), element deletion method and interelement crack method. The element deletion method is unable to predict crack branching. The XFEM and the interelement method showed similar crack velocity and crack paths but both failed to predict a benchmark experiment without an adjustment of the energy release rate.

Crack tip propagation from peridynamic analysis are compared with experimental study here. Boudet [8] studied the crack propagation in a PMMA plate which has a mass density $\rho = 1200 \text{ kg/m}^3$ and a Young's modulus $E = 2.5 \text{ GPa}$. The experiments were conducted on a $100\text{mm} \times 290\text{mm}$ plate with a 10mm notch in the middle of a boundary, as shown in Fig. 4.29. The velocity of the crack propagation was measured using several equally spaced conductive strips deposited on one of the surfaces of the sample.

In the experiment, the specimen was first loaded by displacement control and the applied displacement was slowly increased every 10 seconds. Because 10 seconds is too long for computational method, an initial strain just below what is needed to trigger crack propagation is applied as the initial condition. The starter crack is made by releasing all bonds crossing the 10mm notch.

Fig. 4.30 shows the predicted crack length as a function of time. Using the predicted crack length, crack propagation velocity can be calculated and is shown in Fig. 4.31. The maximum crack propagation velocity is about 600 m/s, which is less than the Rayleigh wave speed of the PMMA material, 930 m/s. The predicted crack propagation velocity is within the theoretical limit for steady mode-I fracture [9]. The peridynamic results are compared with the experiment results given in Ref. [8]. Both Fig. 4.30 and Fig. 4.31 show good agreements between the two results.

4.10 Dynamic crack branching

Experiments on crack branching were reported in literature [10-14]. In these experiments, a crack starts to propagate from a notch. At a certain point, the crack branches into at least two cracks. The angle of the branches, however, varies from one experiment to another. Sharon and Fineberg [13] showed that the branching angles were in Gaussian distribution with an average of 30° . Numerical methods to predict crack branching were studied. The Yoffe calculation [15] predicted an angle of 60° while molecular simulations [16] predicted an angle of 30° . An angle of 18° was also predicted using an energy criterion with consideration of nonsingular terms in the stress field [17].

The qualitative comparison between peridynamic prediction of crack branching and associated experiment study is to be examined. The goal is to see if peridynamics is able to predict crack branching without requiring additional theories.

Consider a pre-notched glass plate with $\rho = 2450 \text{ kg/m}^3$, $E = 32 \text{ GPa}$ and $\nu = 0.2$. The dimensions of the plate is $100 \text{ mm} \times 100 \text{ mm}$ with a 10 mm notch located in the middle of the left boundary as shown in Fig. 4.32. A tensile stress $\sigma = 2 \text{ MPa}$ is applied at both top and bottom boundaries. The initial displacement and the initial velocity is zero. Fig. 4.33(a) shows the crack path at different times calculated by peridynamics. Fig. 4.33(b) is strain energy density of the corresponding steps. Crack branching can be clearly seen in Fig. 4.33(a) and Fig. 4.33(b) and there is always stress concentration at the crack tips.

4.11 Edge-cracked plate under impulsive loading

Kalthoff and Winkler [18] studied crack propagation of an edge-cracked plate under impulsive loading and found that the crack propagated in a direction approximately 70° from the original crack. In this section, the same problem is simulated by the proposed peridynamic model and the results are to be compared with the experiment results from [18].

Consider a $100 \text{ mm} \times 200 \text{ mm}$ maraging steel 18Ni1900 plate as shown in Fig. 4.34. There are two parallel notches along the left edge of the plate. The material properties [19] are $\rho = 8000 \text{ kg/m}^3$, $E = 190 \text{ GPa}$ and $\nu = 0.3$. The two edge notches are impacted by a projectile with an initial velocity of 36 m/s . This impact results in a compressive wave propagating to the interior of the plate. Once the compressive wave arrives at the notch tips, a mode-II brittle failure

occurs. The crack do not propagate in the same direction as the original crack but in a direction that is about 70° away from the original direction.

In numerical simulation based on peridynamics, it is assumed that the projectile has the same material properties as the specimen. Hence, one half of the initial velocity, 18 m/s , is used as the initial condition at the left edge [20, 21] and all boundaries are free. Fig 4.35 shows the simulated crack path from peridynamic computation. The crack path is about 68° from the original notch. Fig. 4.36 shows the horizontal displacement of the plate at $t = 33.2\text{ }\mu\text{s}$. The displacement discontinuity shows the crack path which is 68° from the original notch. The peridynamic computation successfully predicts the experimentlly observed crack propagation angle.

4.12 Conclusion

A novel two-parameter beam model for peridynamic analysis is proposed in this chapter. The numerical solution of peridynamics has been verified by an analytical solution and it converges to the analytical solution. To improve the computational efficiency in two-dimensional simulations, two computational techniques are implimented in this work. One uses matrix computation and the other parallel computation. The first method works well for elastic problems without damage while the second method is proved to be excellent for simulating dynamic damage propagation. Failure theory of peridynamics is also studied and applied to simulate several dynamic damage propagation problems. Three experiment studies from literature [8, 10,18] are used to validate the two-dimensional peridynamic model and algorithm.

Being a reformulation of continuum mechanics, peridynamics covers fracture mechanics

automatically. This poses a great potential for peridynamics since it is convenient for simulating dynamic damage propagation. Compared with the commonly used finite element method, there is no need of remeshing in peridynamics since peridynamics is mesh free. Peridynamics does not require additional external theories for crack growth since it is controlled by bond strength. Besides, peridynamics does not require tracking individual cracks since cracks occur when the bonds are damaged. As shown in this work, peridynamics is also capable of simulating elastic deformations without damage.

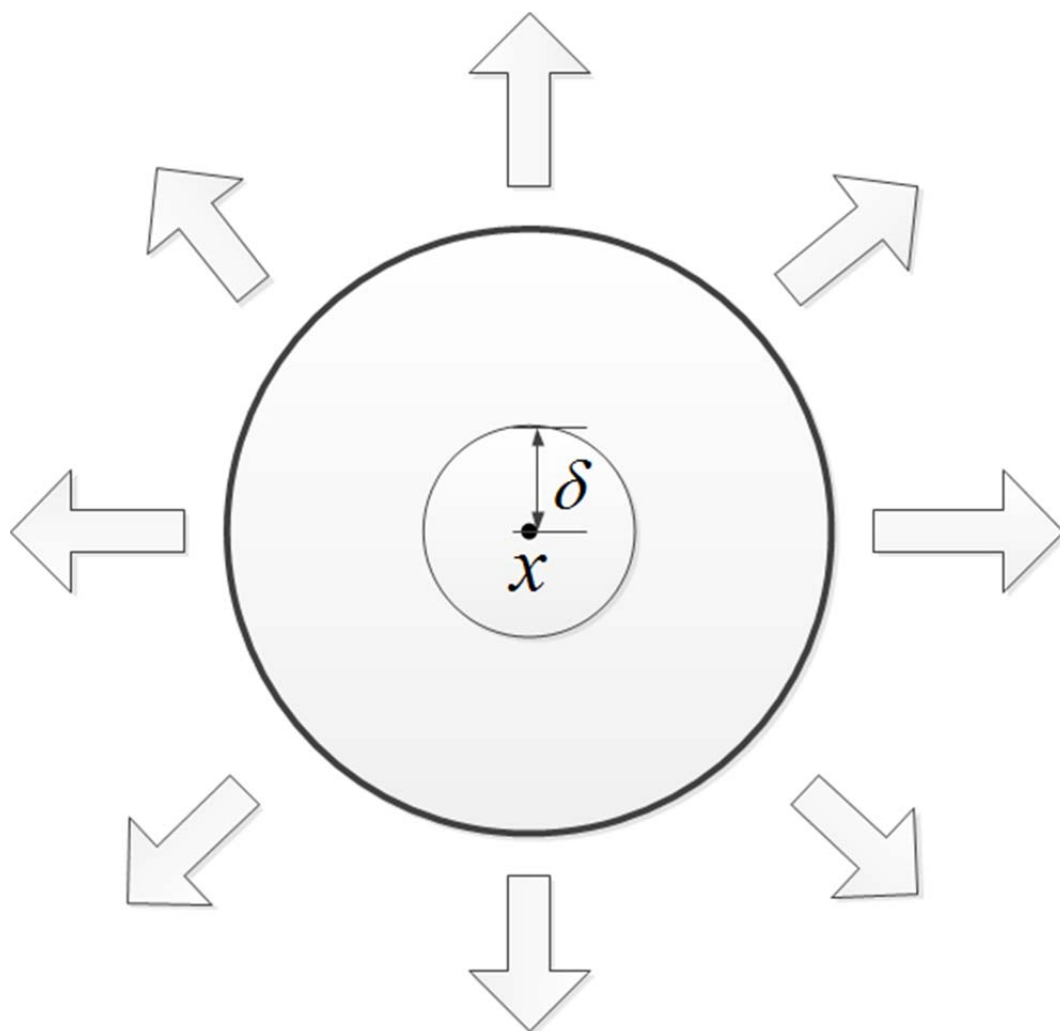


Figure 4.1 Two-dimensional domain under radial deformation.

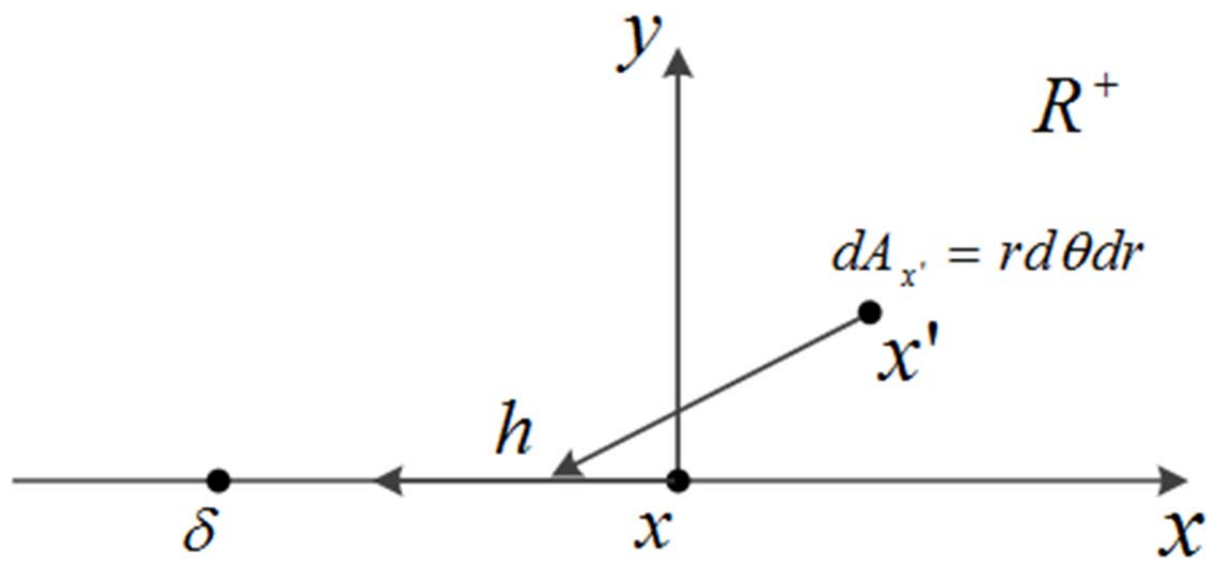


Figure 4.2 Definition of stress in peridynamics.

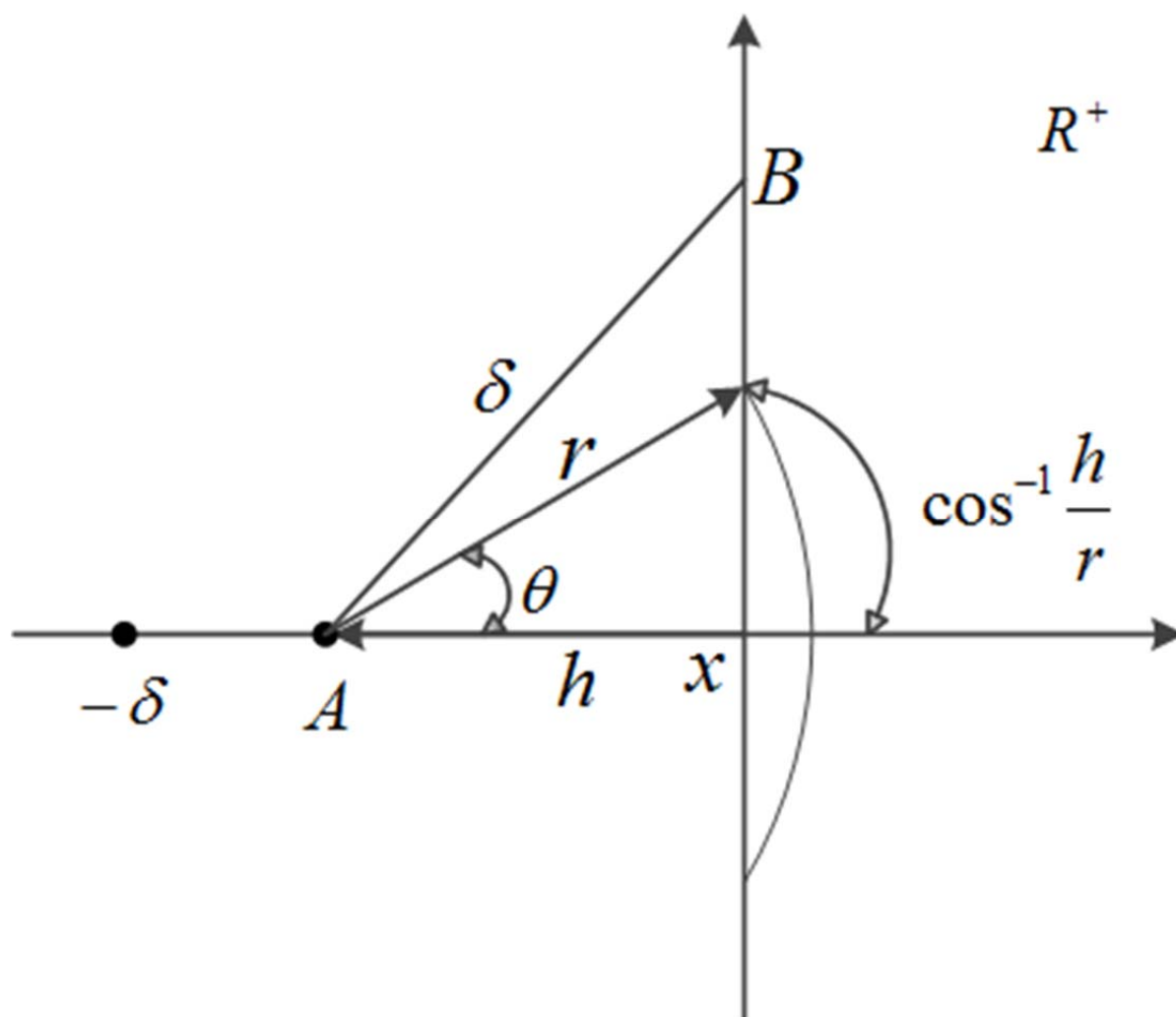


Figure 4.3 Calculation of stress at point x .

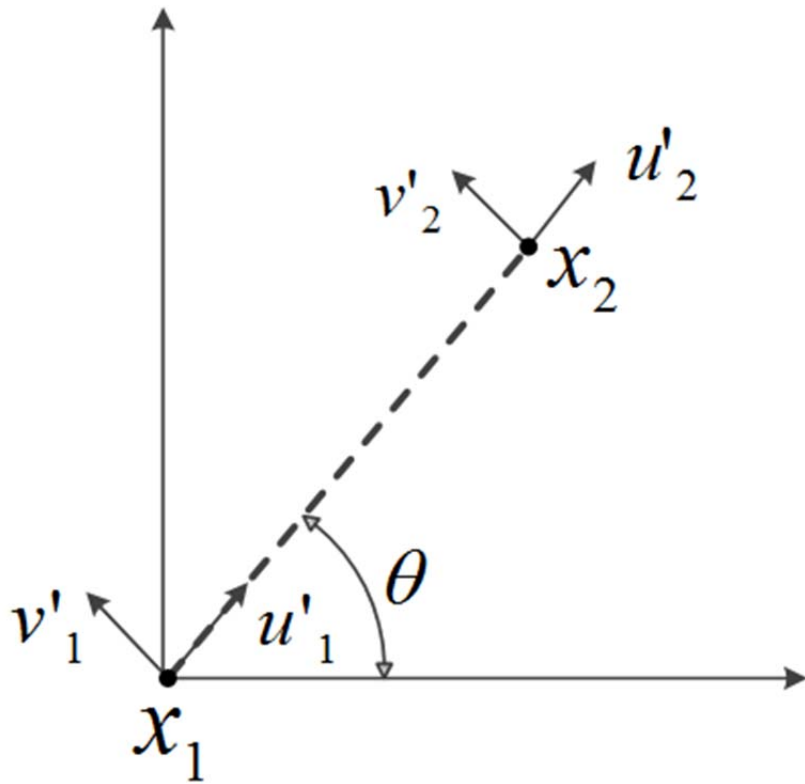


Figure 4.4 Bond force in beam model.

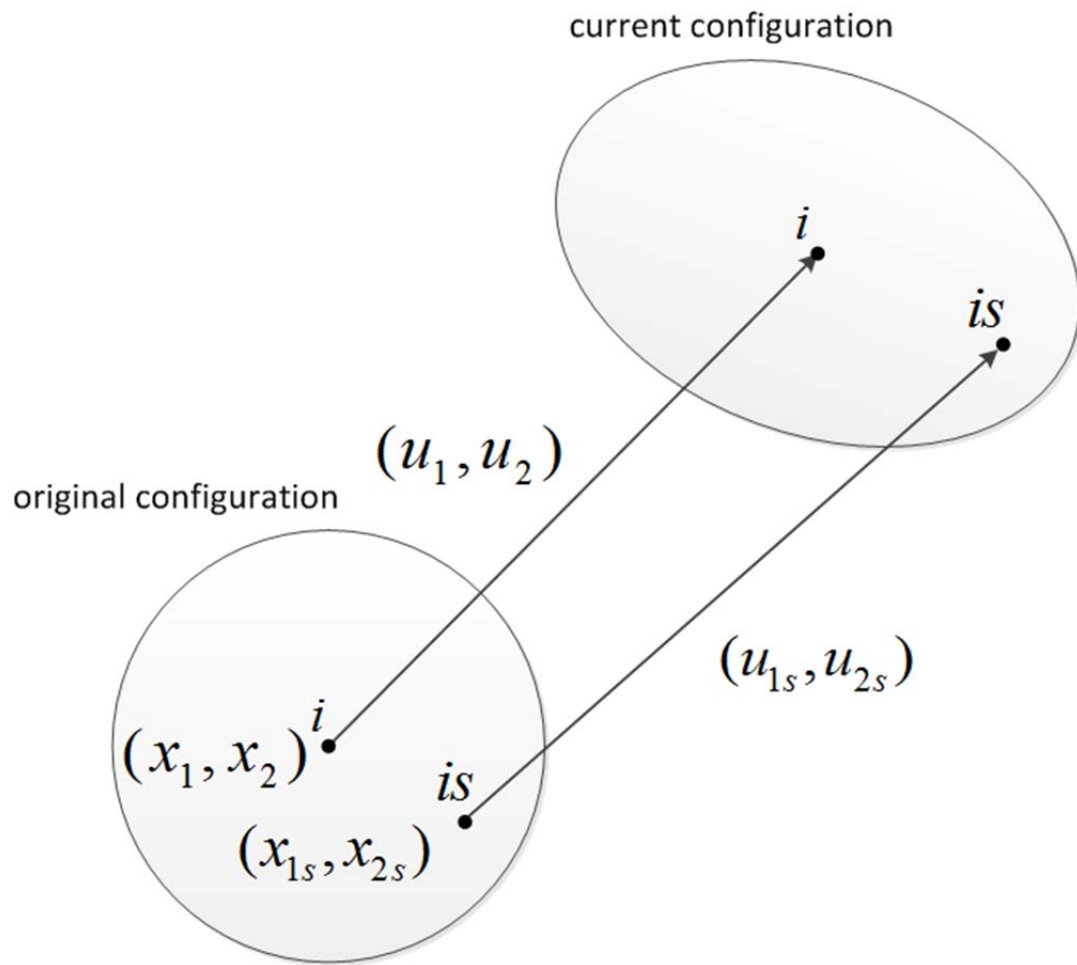


Figure 4.5 Original configuration and current configuration.

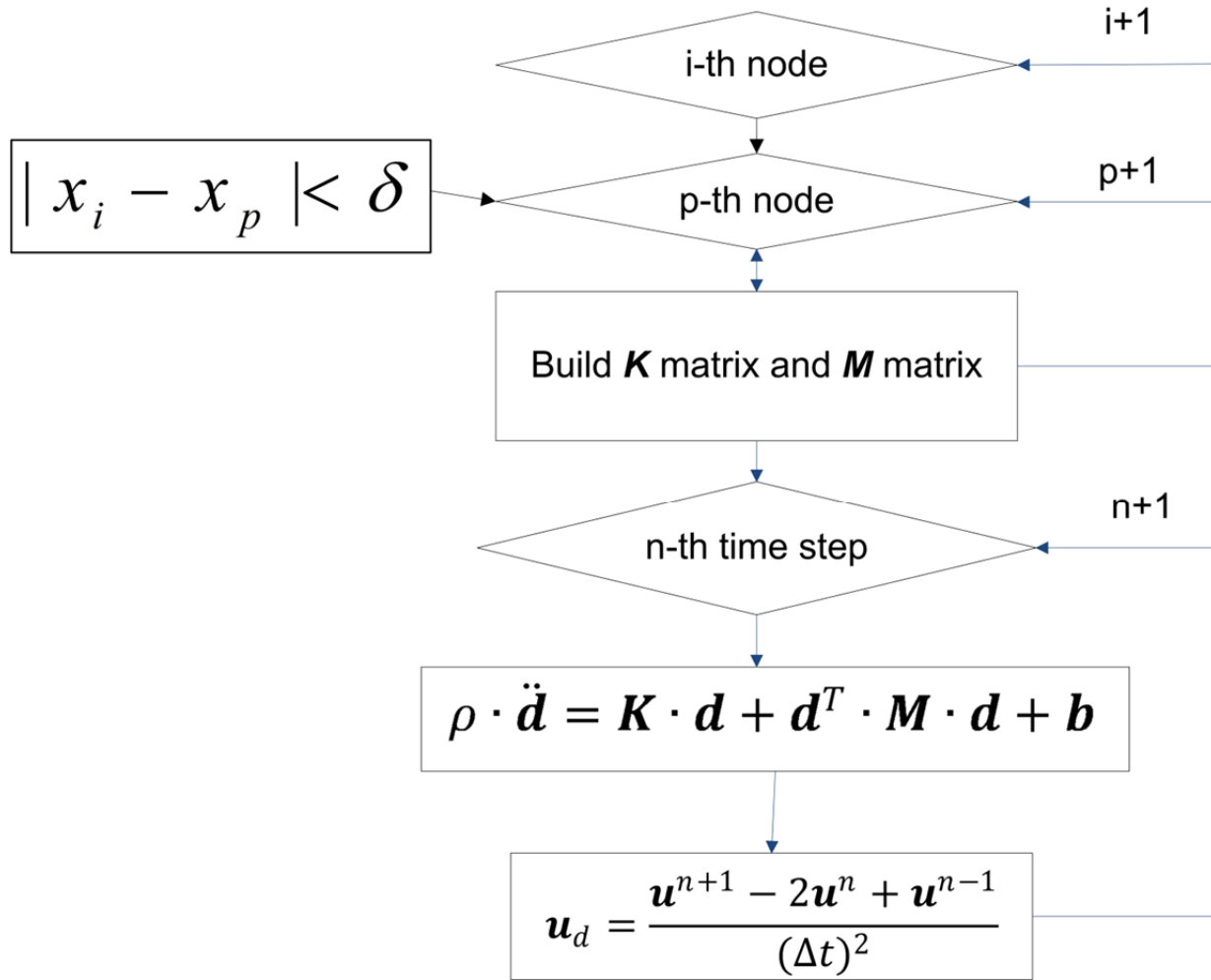


Figure 4.6 Flow chart of algorithm in peridynamic matrix calculation.

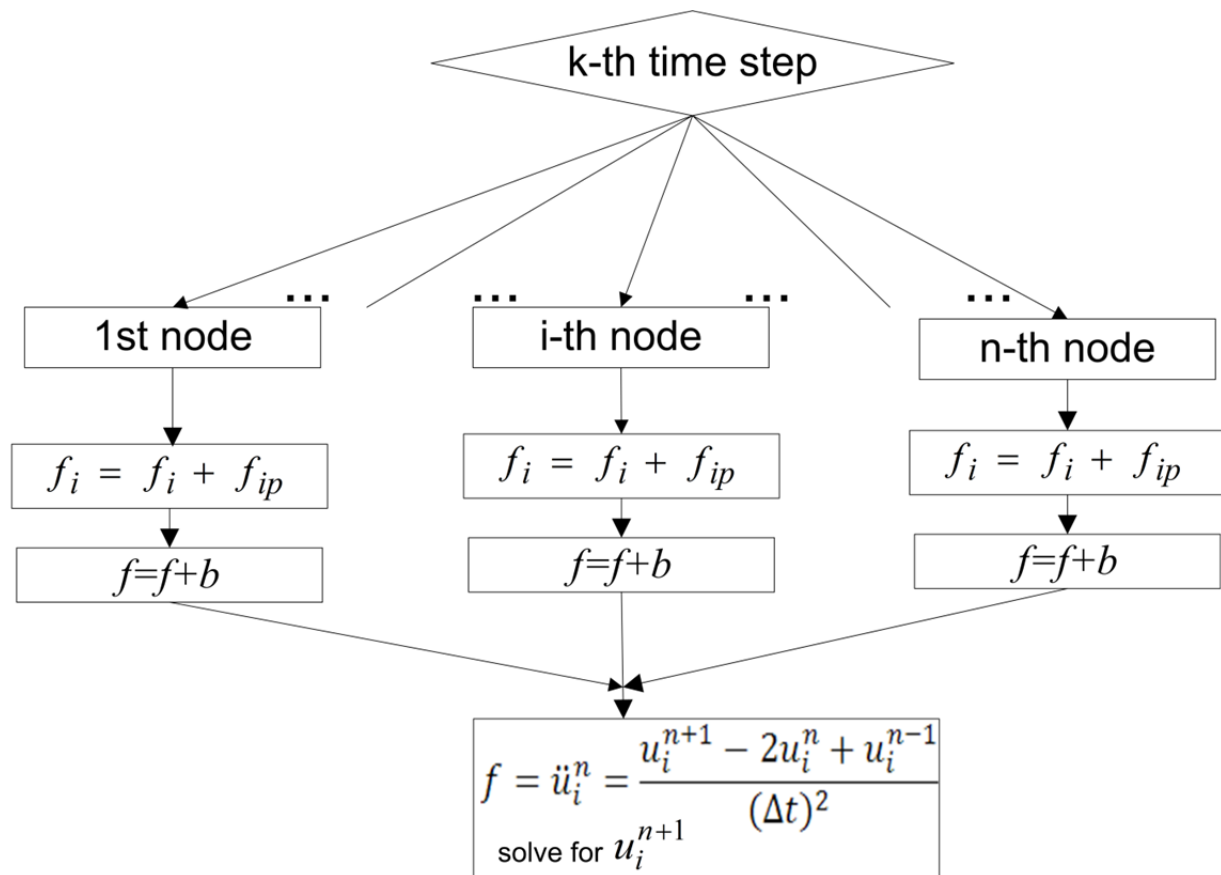


Figure 4.7 Flow chart for parallel computing.

<p>Original program:</p> <pre>... for k=1:nt % time loop for i=1:n % domain loop ... end end ...</pre>	<p>Current program:</p> <pre>... matlabpool(8) %open matlab pool: 8 workers for k=1:nt % time loop parfor i=1:n % domain loop ... end end ...</pre>
--	--

Figure 4.8 Code before parallel modification and code after parallel modification.

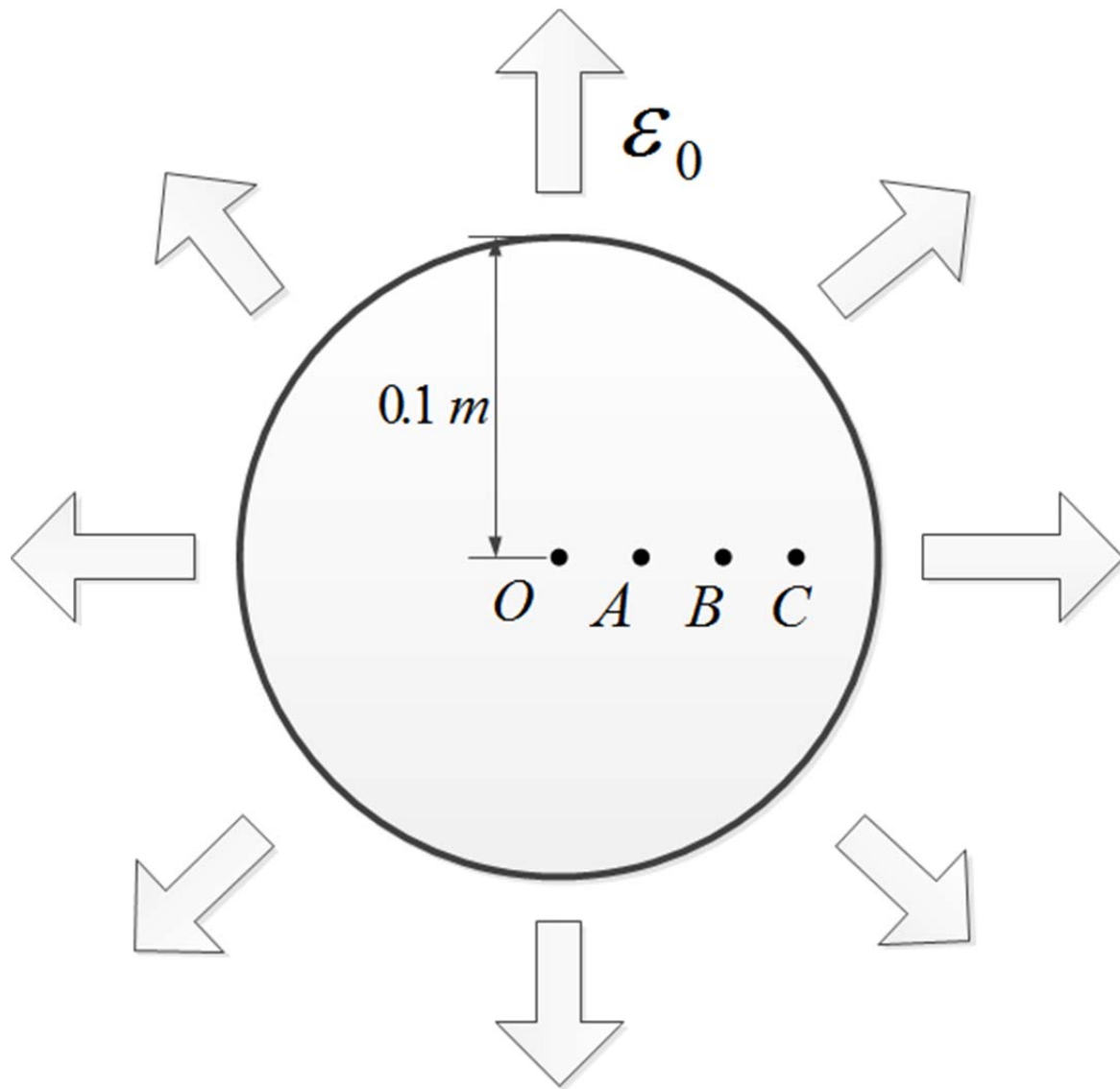


Figure 4.9 Vibration of a circular plate.

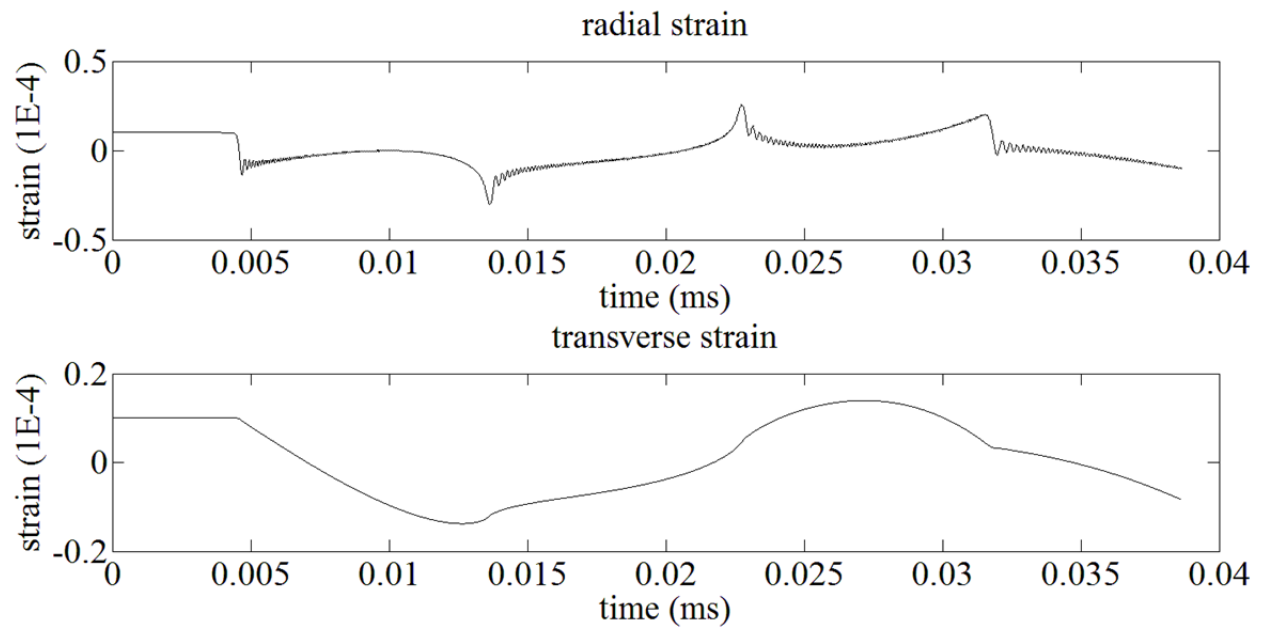


Figure 4.10 Strain history on a circular plate.

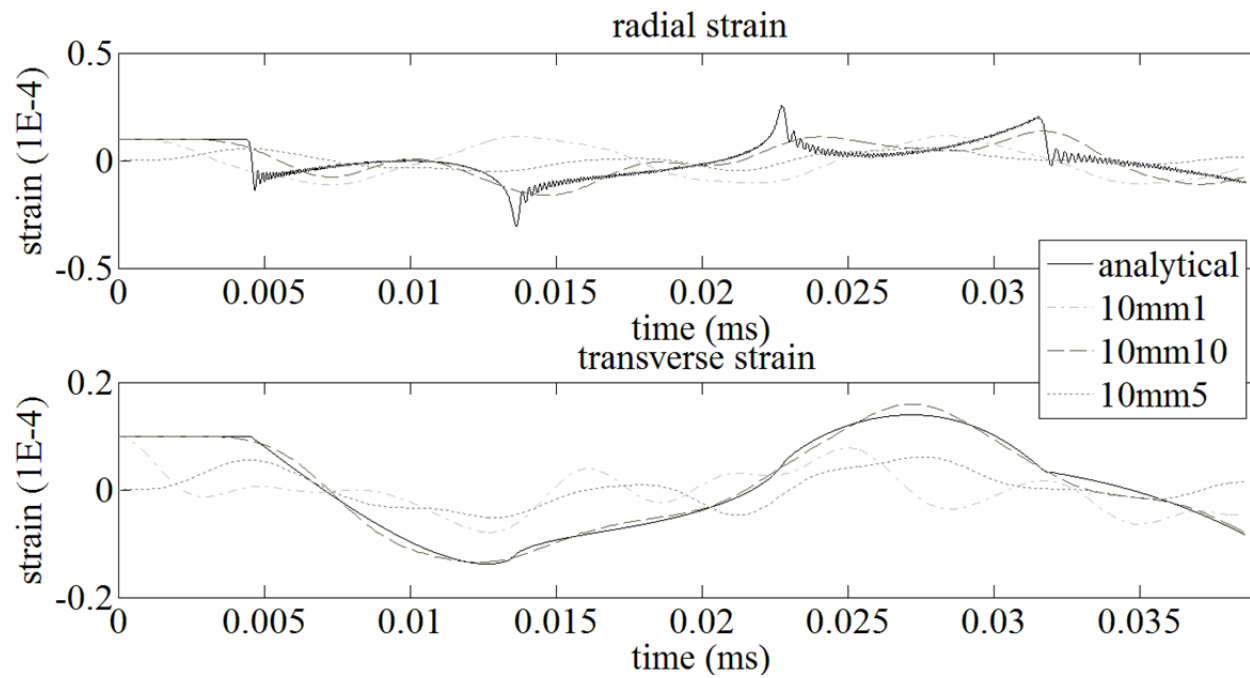


Figure 4.11 Convergence of numerical solution to analytical solution.

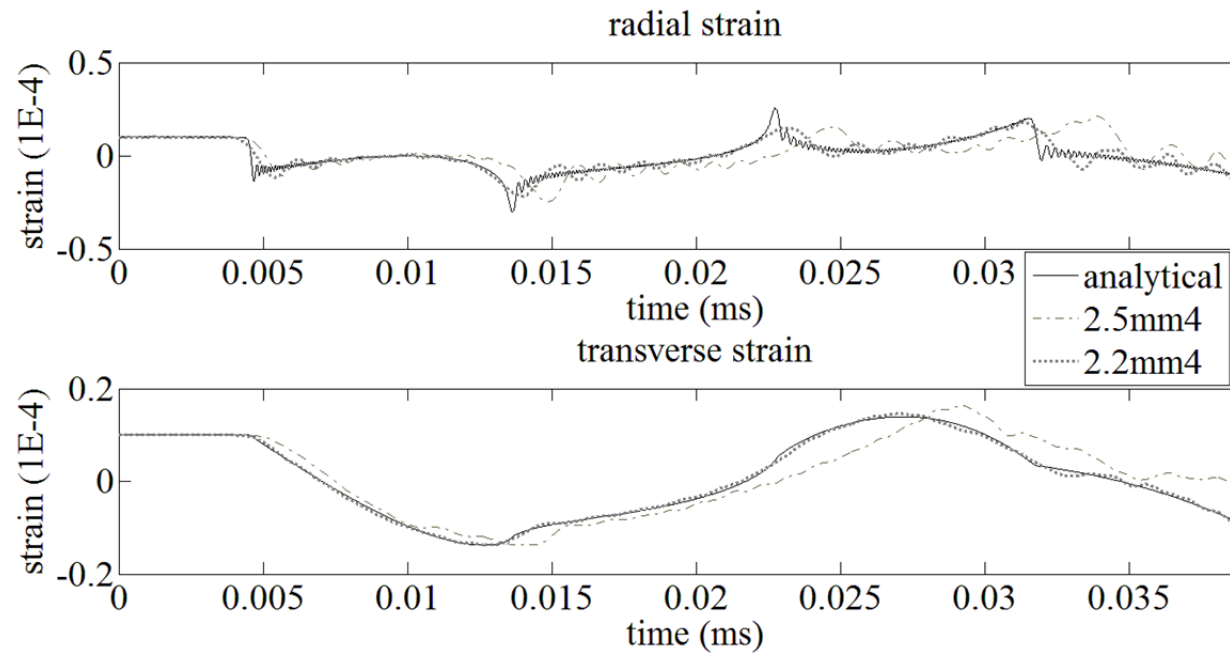


Figure 4.12 Convergence of numerical solution to analytical solution.

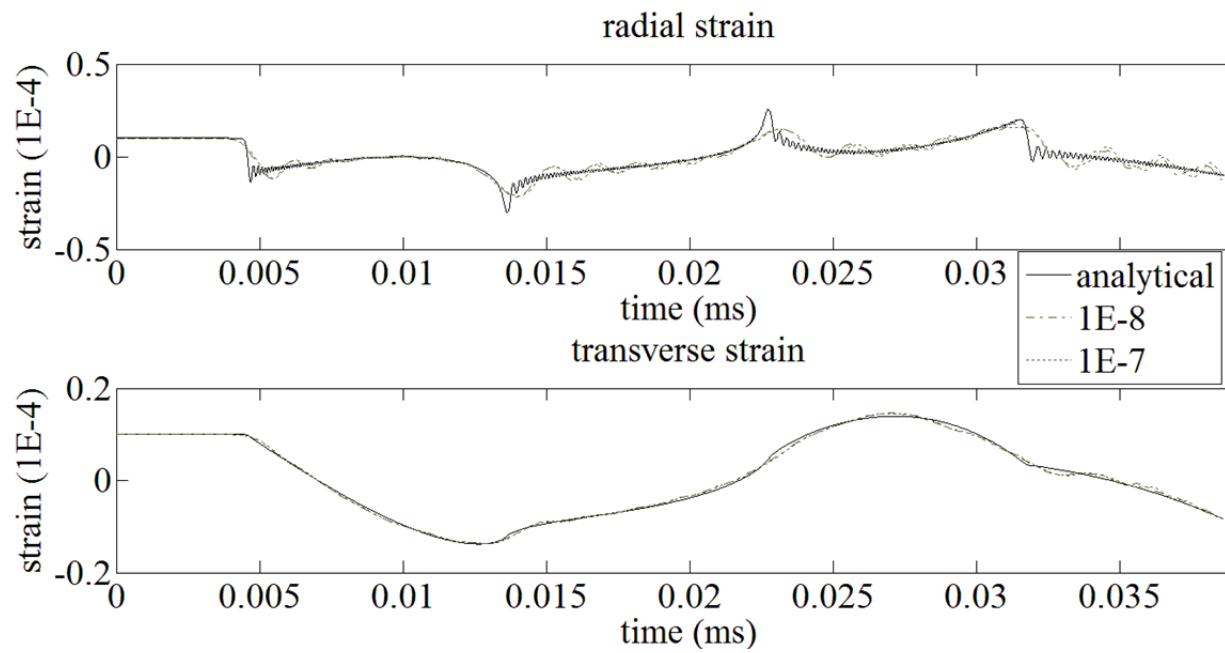


Figure 4.13 Convergence of numerical solution to vibration theory.

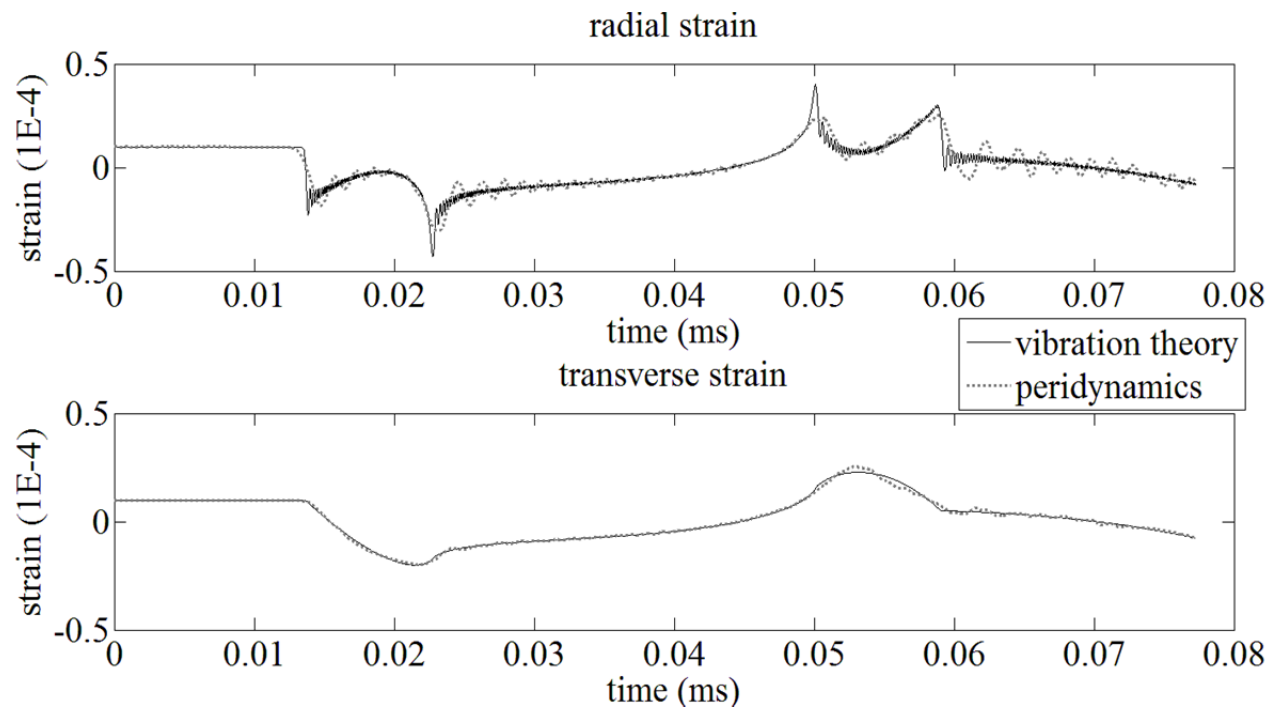


Figure 4.14 Peridynamic calculation of strains at point A compared with results from vibration theory.

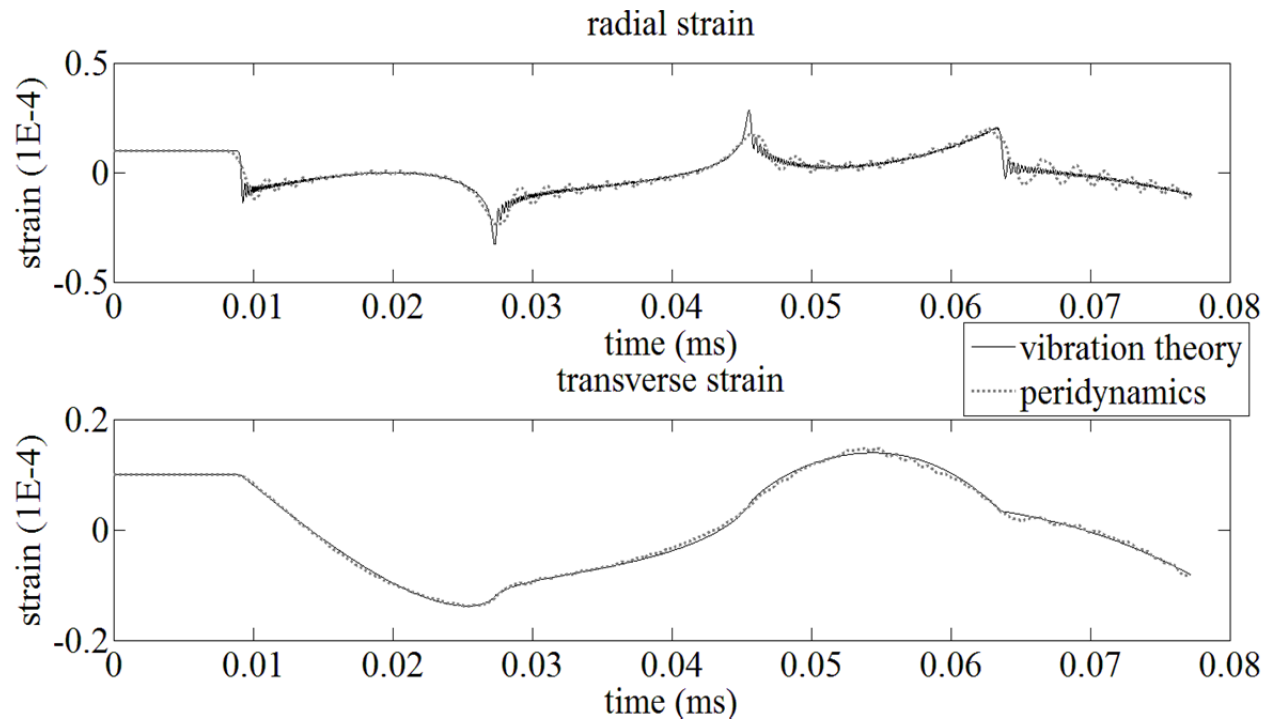


Figure 4.15 Peridynamic calculation of strain at point B compared with results from vibration theory.

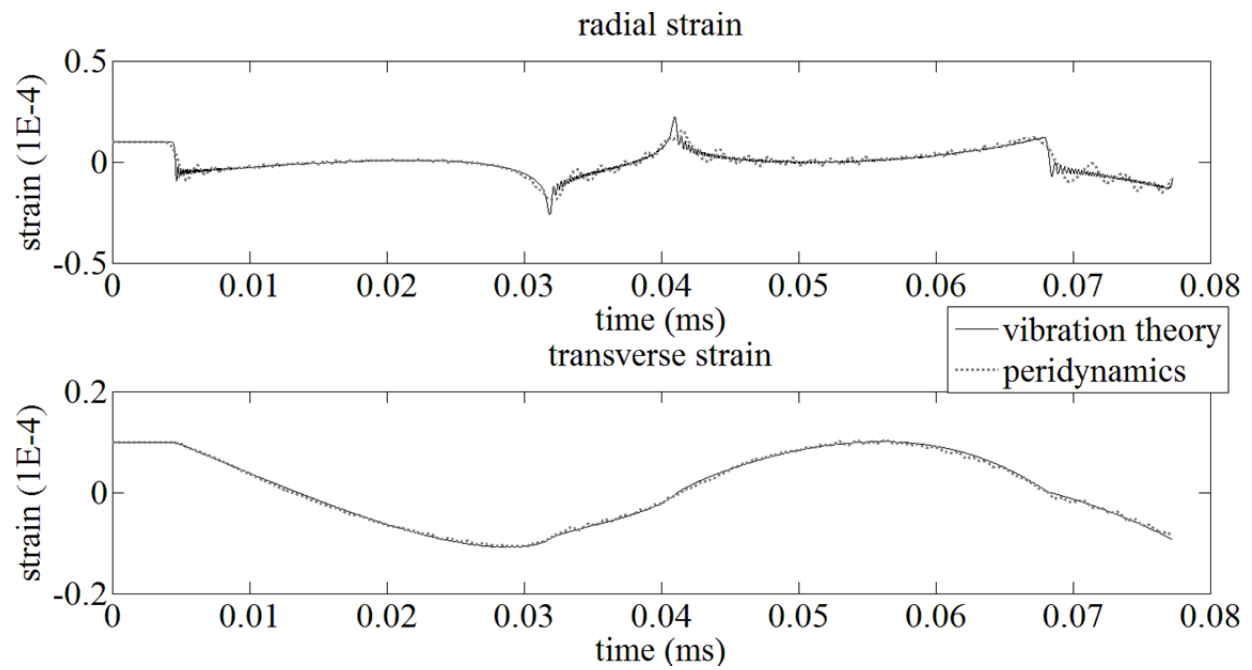


Figure 4.16 Peridynamic calculation of strain at point C compared with results from vibration theory.

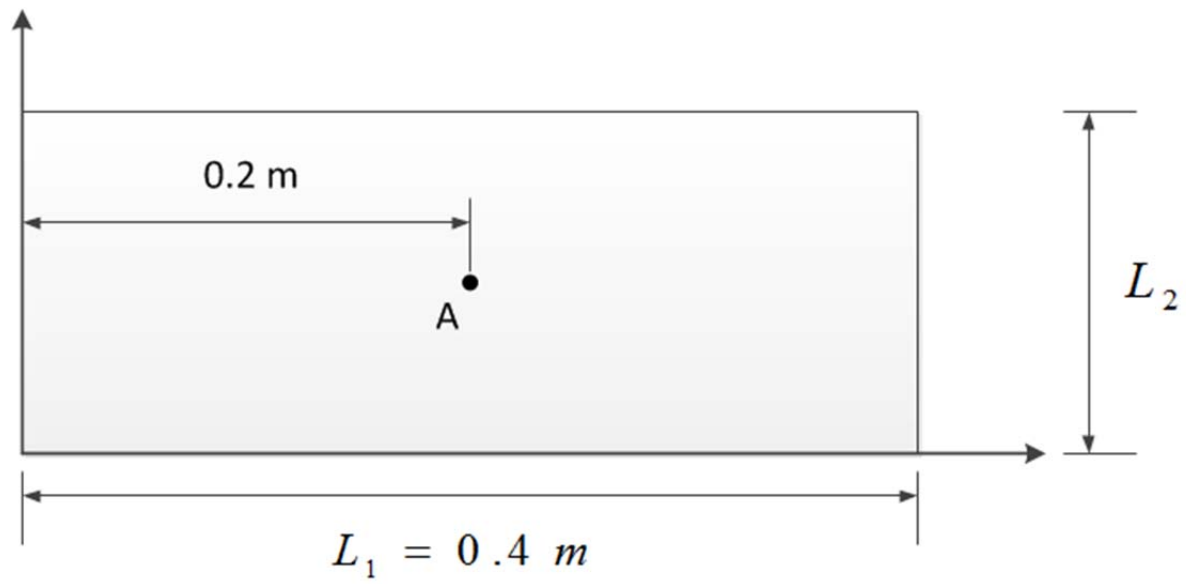


Figure 4.17 Rectangular plate for free vibration study

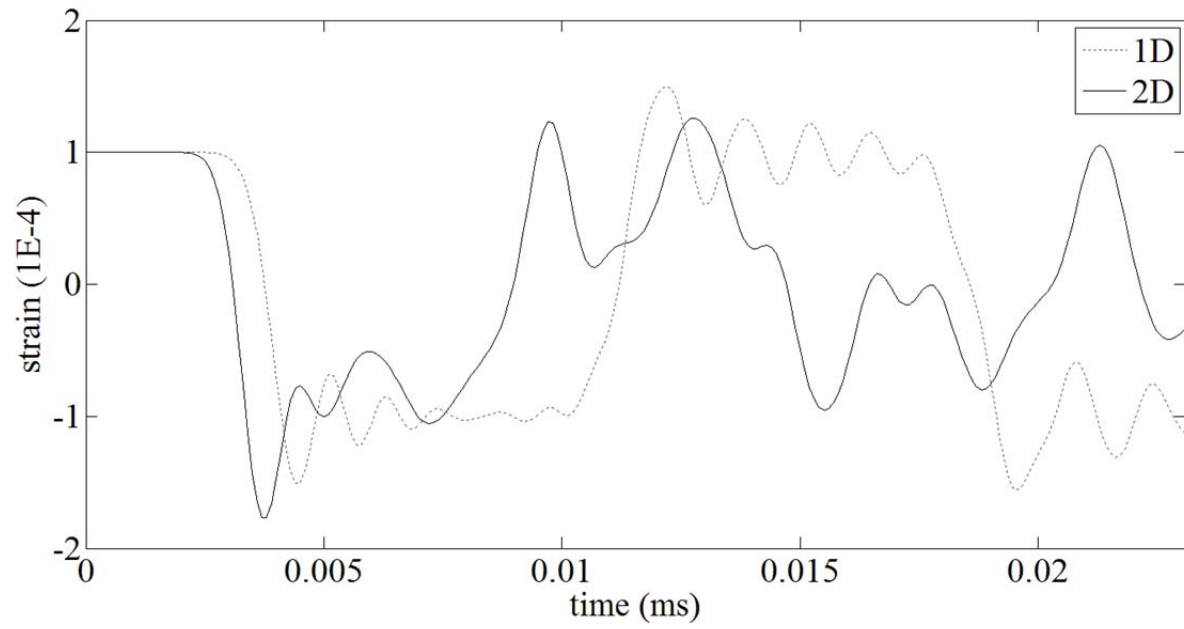


Figure 4.18 One-dimensional result compared with two-dimensional result for aspect ratio of 0.2.

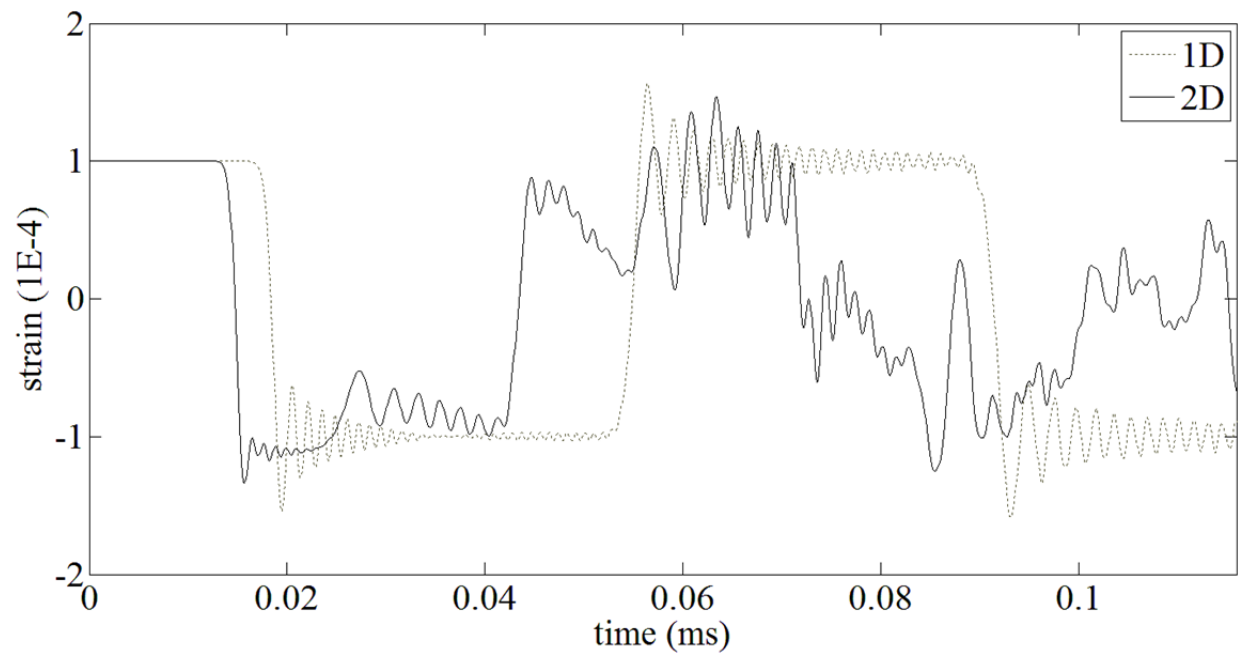


Figure 4.19 One dimensional result compared with two-dimensional result for aspect ratio of 1.

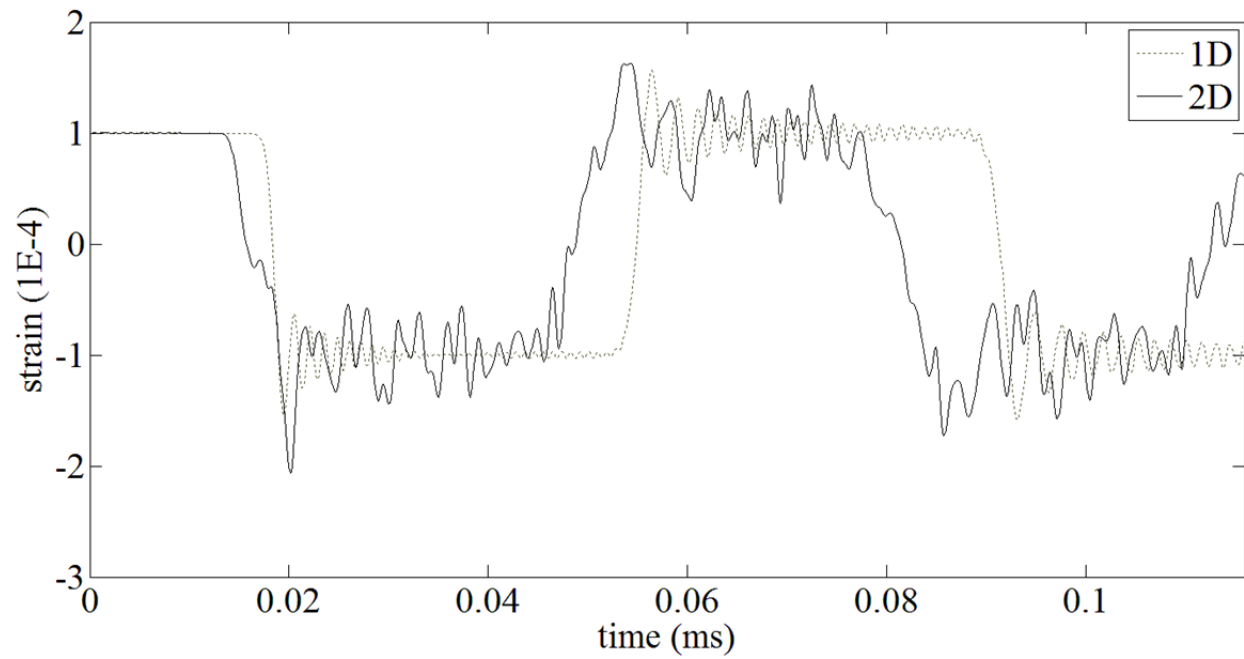


Figure 4.20 One-dimensional result compared with two-dimensional result for aspect ratio of 10.

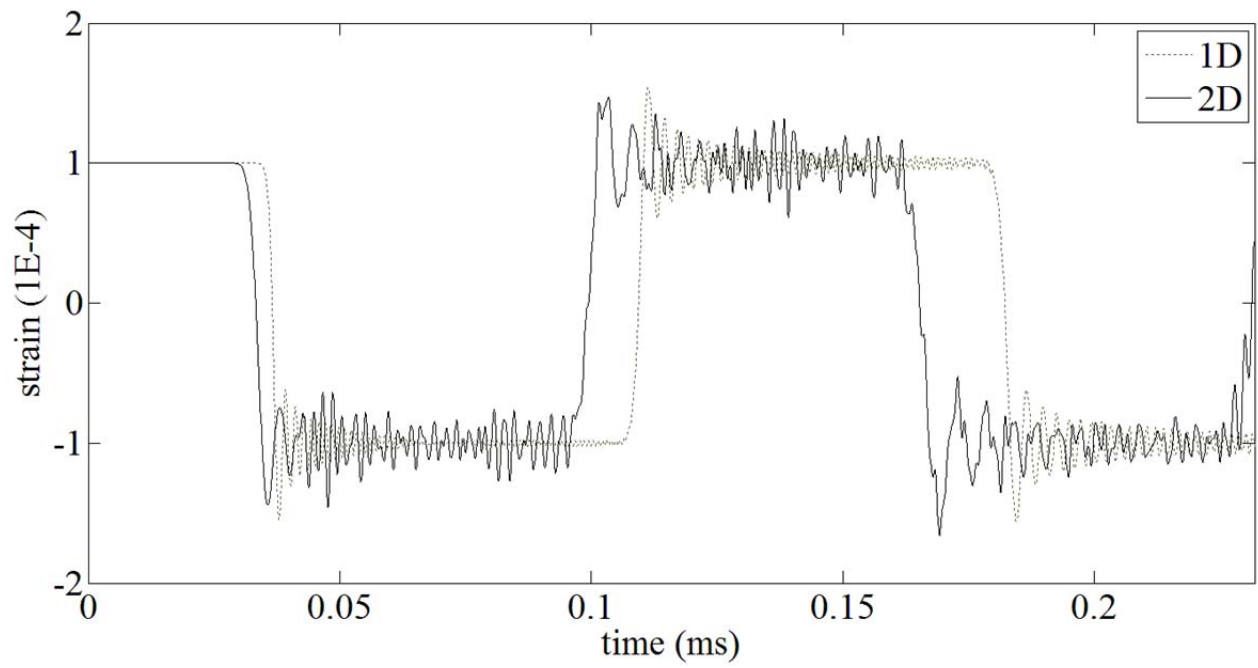


Figure 4. 21 One-dimensional result compared with two-dimensional result for aspect ratio of 50.

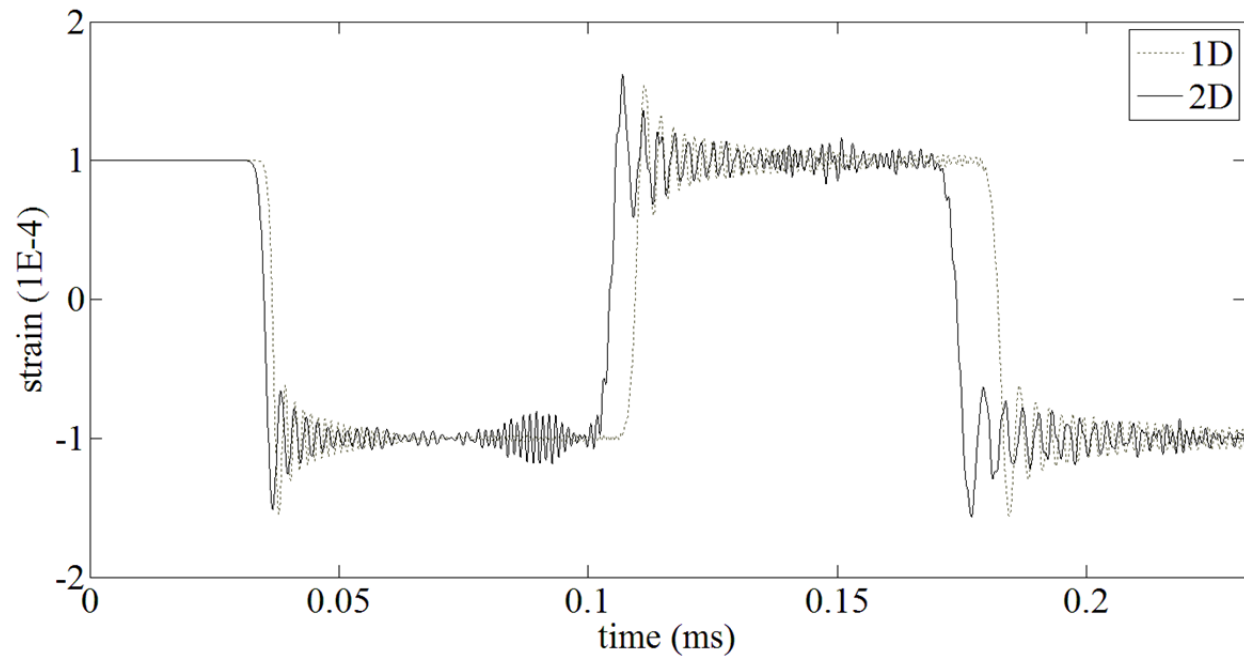


Figure 4. 22 One-dimensional result compared with two-dimensional result for aspect ratio of 100.

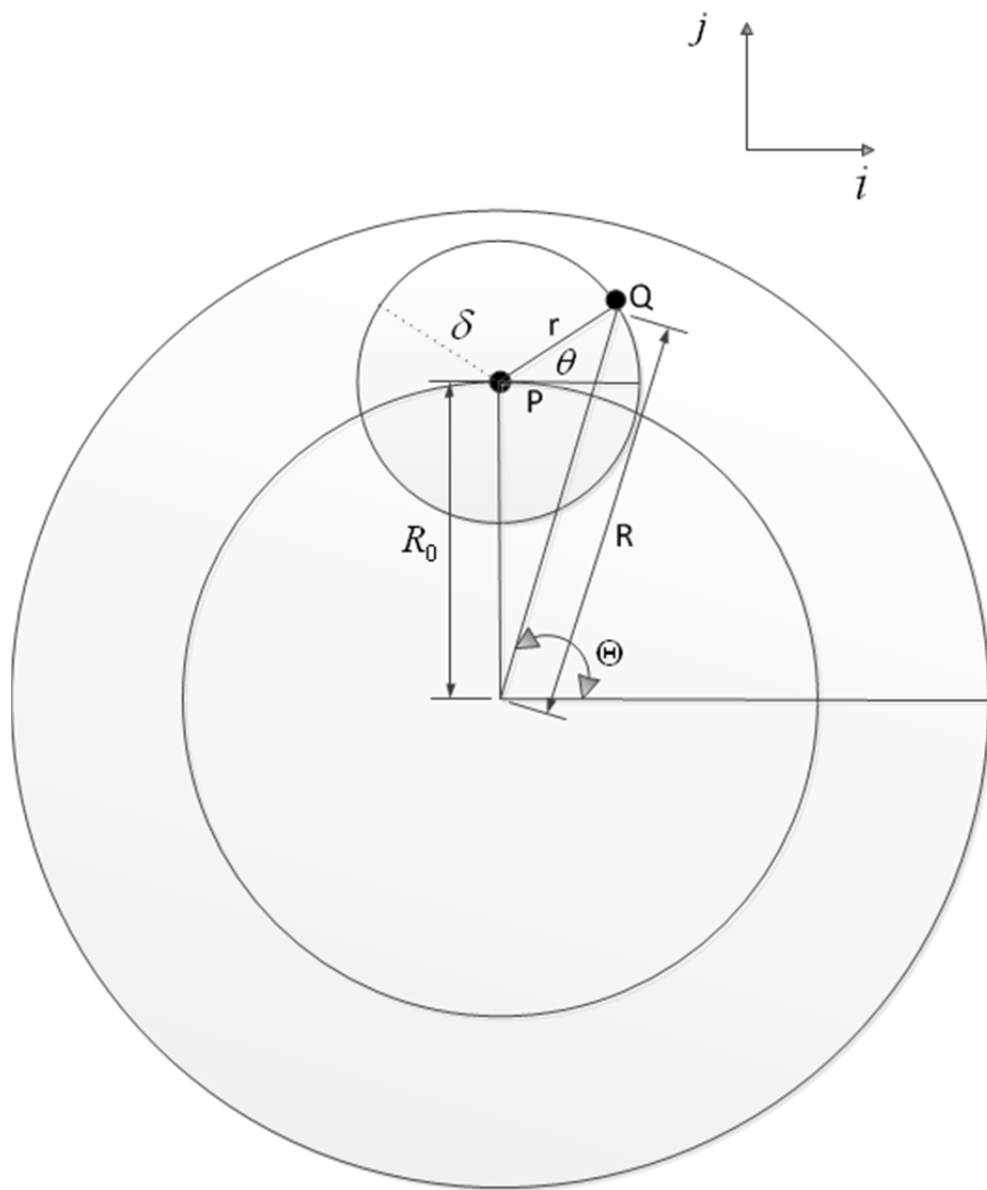


Figure 4.23 A two-dimensional axisymmetric model.

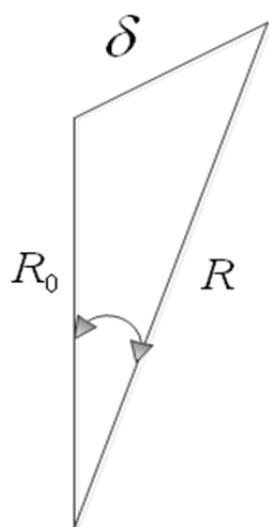


Figure 4.24 Angular integration boundary of Eqn. 4.75.

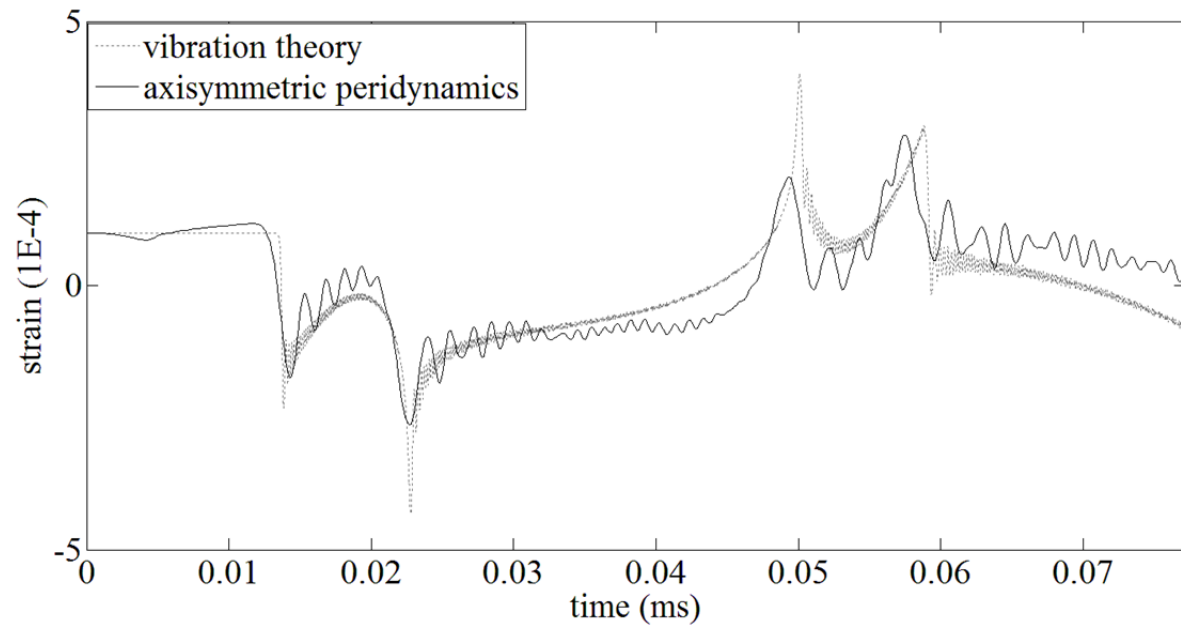


Figure 4.25 Comparison of peridynamic calculation of strain at Point A using axisymmetric model with results from the vibration theory.

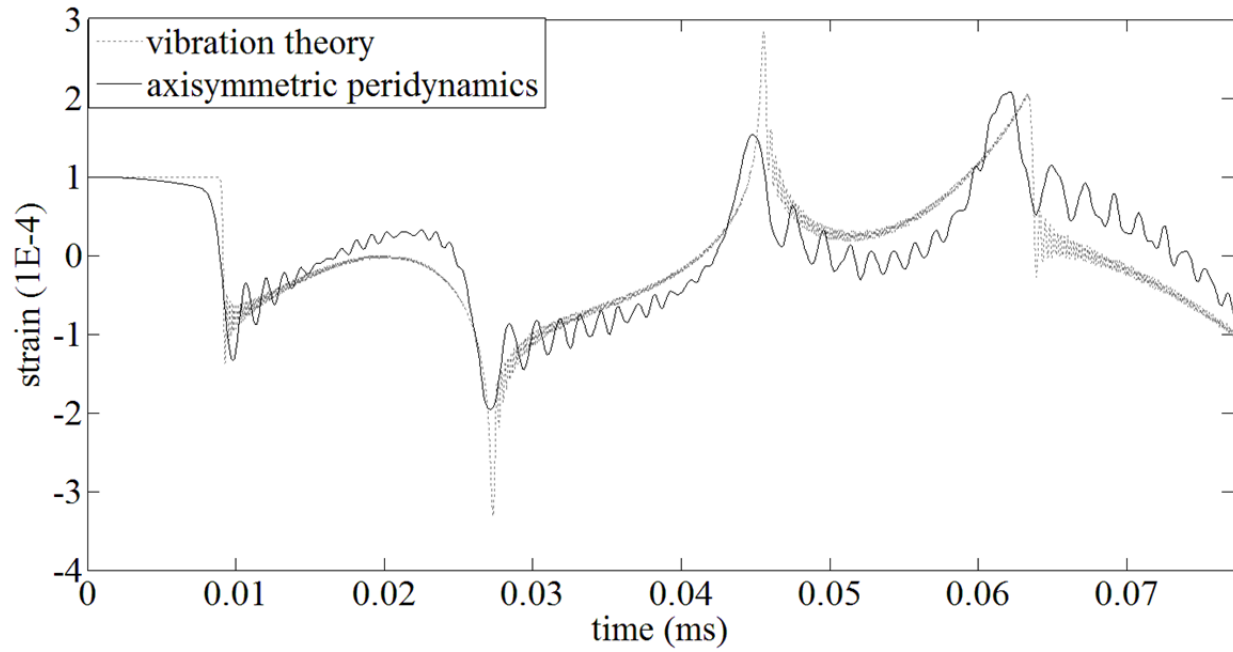


Figure 4.26 Comparison of peridynamic calculation of strain at Point B using axisymmetric model with results from the vibration theory.

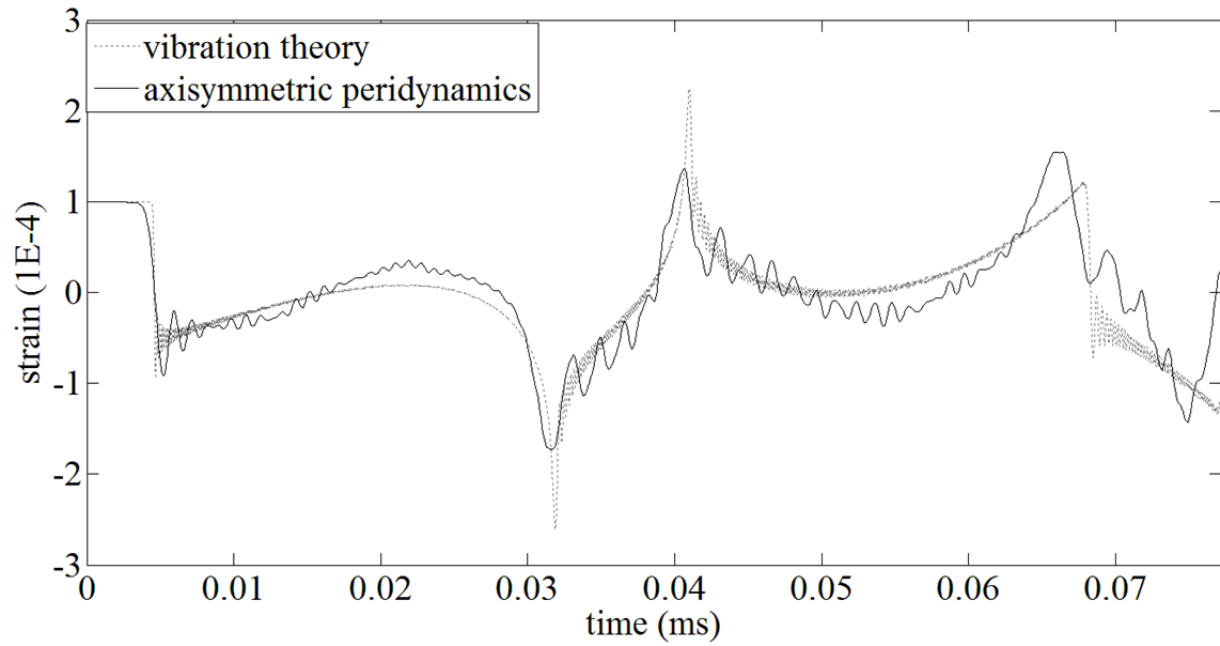


Figure 4.27 Comparison of peridynamic calculation of strain at Point C using axisymmetric model with results from the vibration theory.

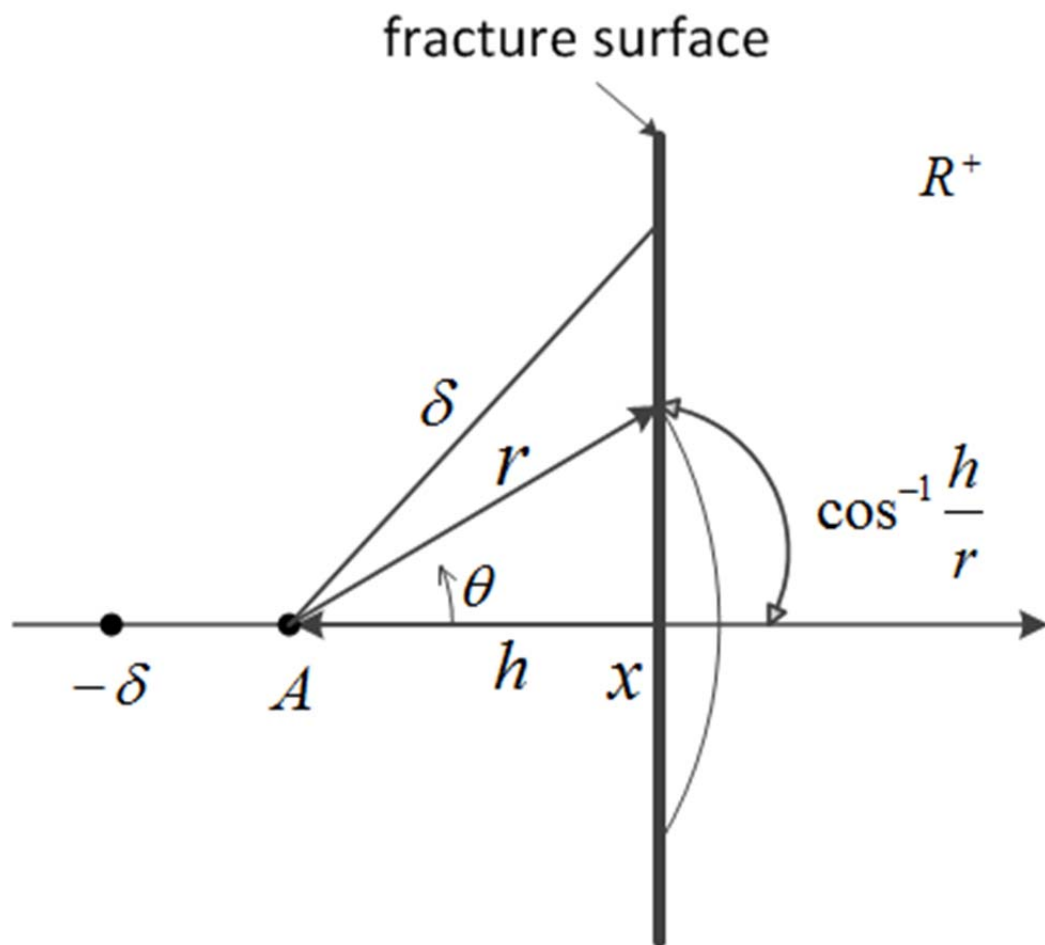


Figure 4.28 Calculation of the critical stretch.

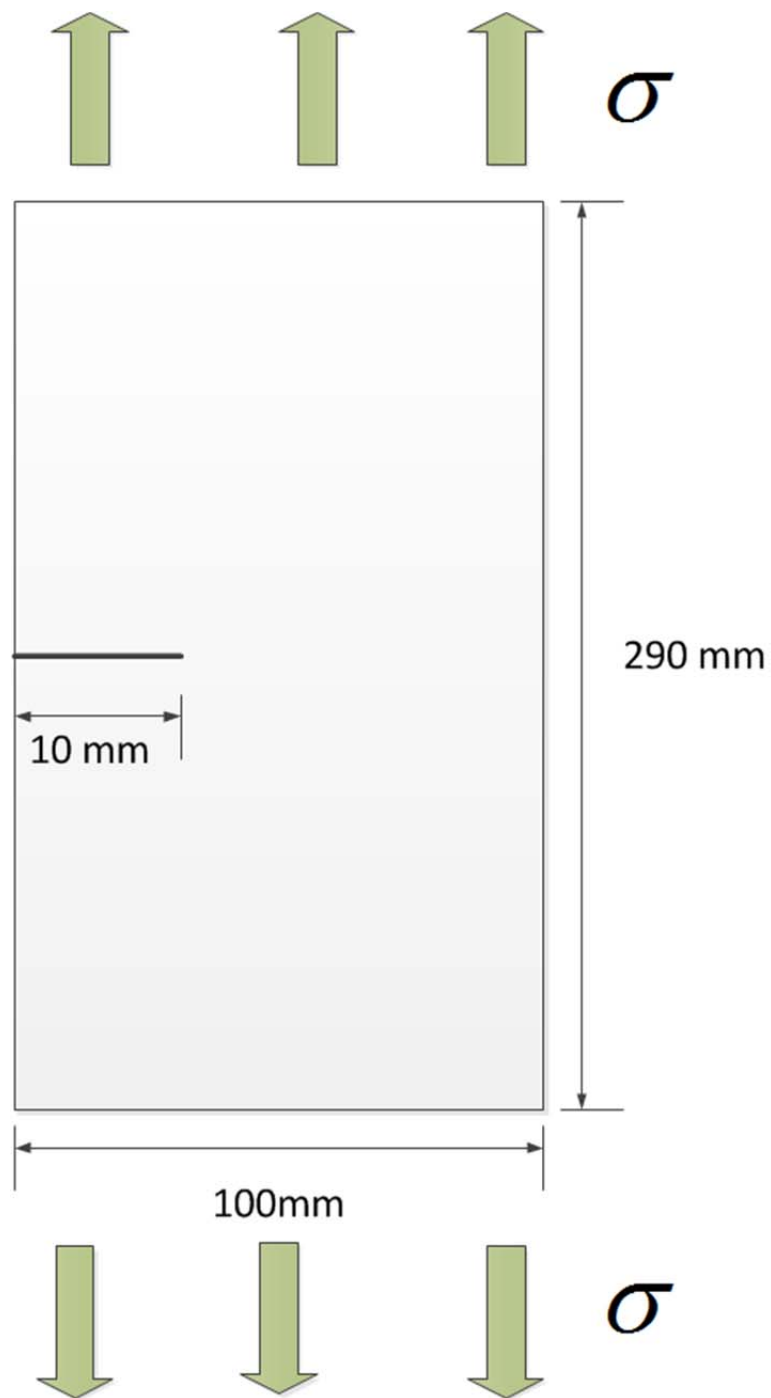


Figure 4.29 Schematic drawing of the sample for crack propagation test.

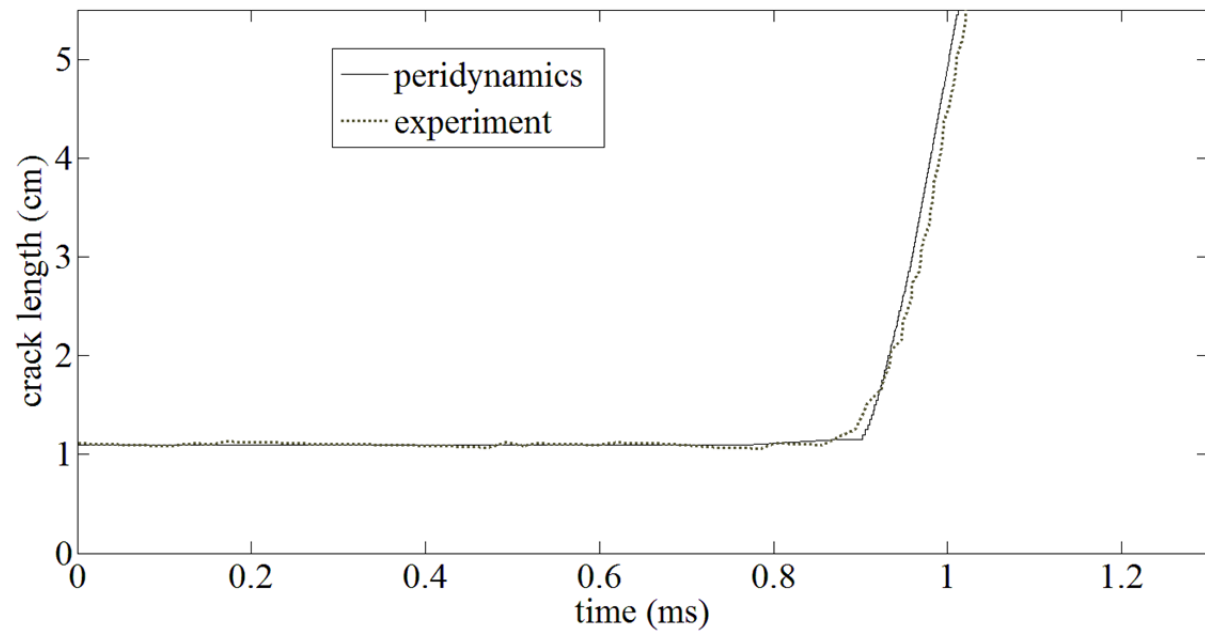


Figure 4.30 Comparison of crack propagation simulated by peridynamics with experiment result.

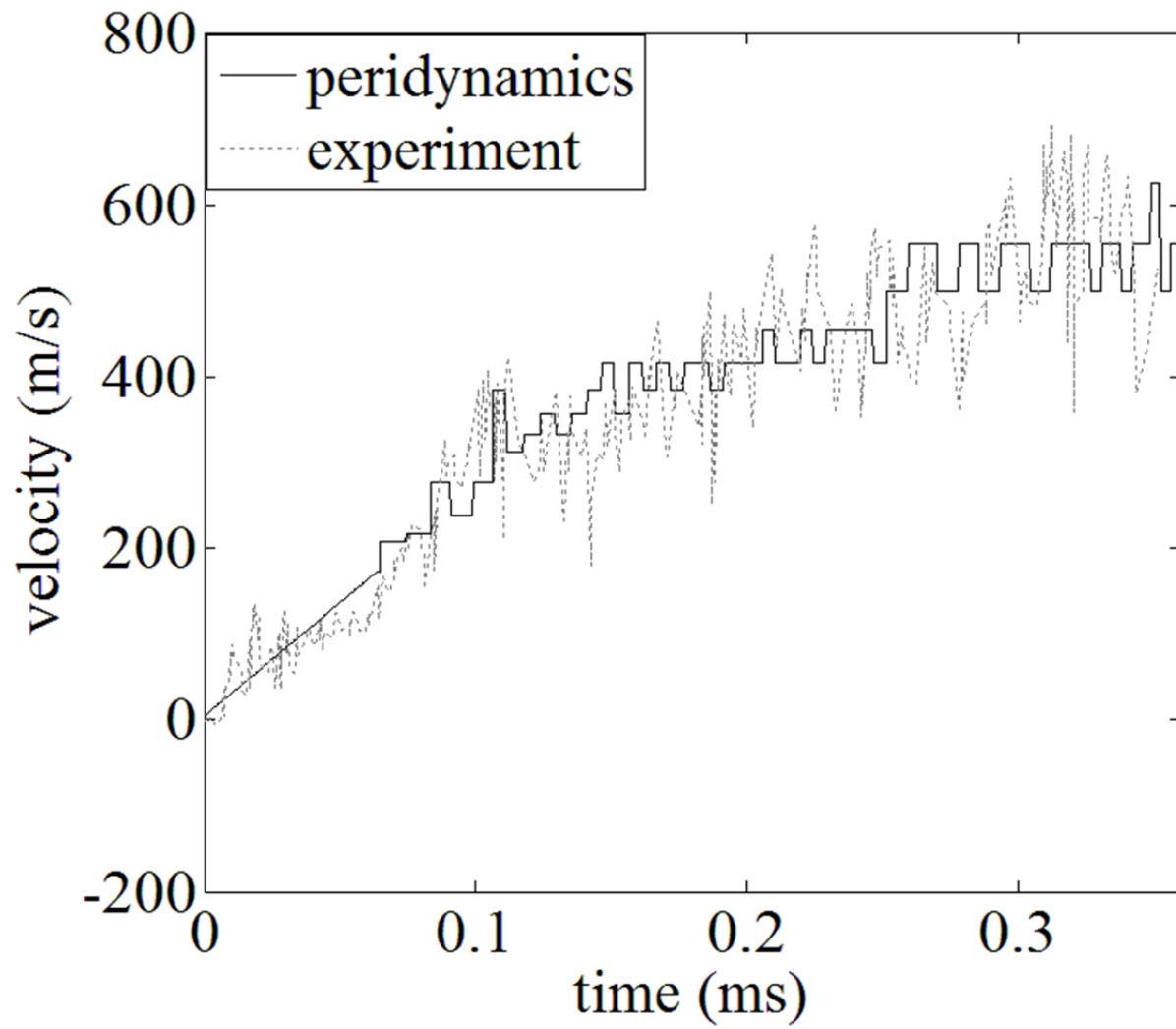


Figure 4.31 Comparison of crack propagation speed simulated by peridynamics with experiment result.

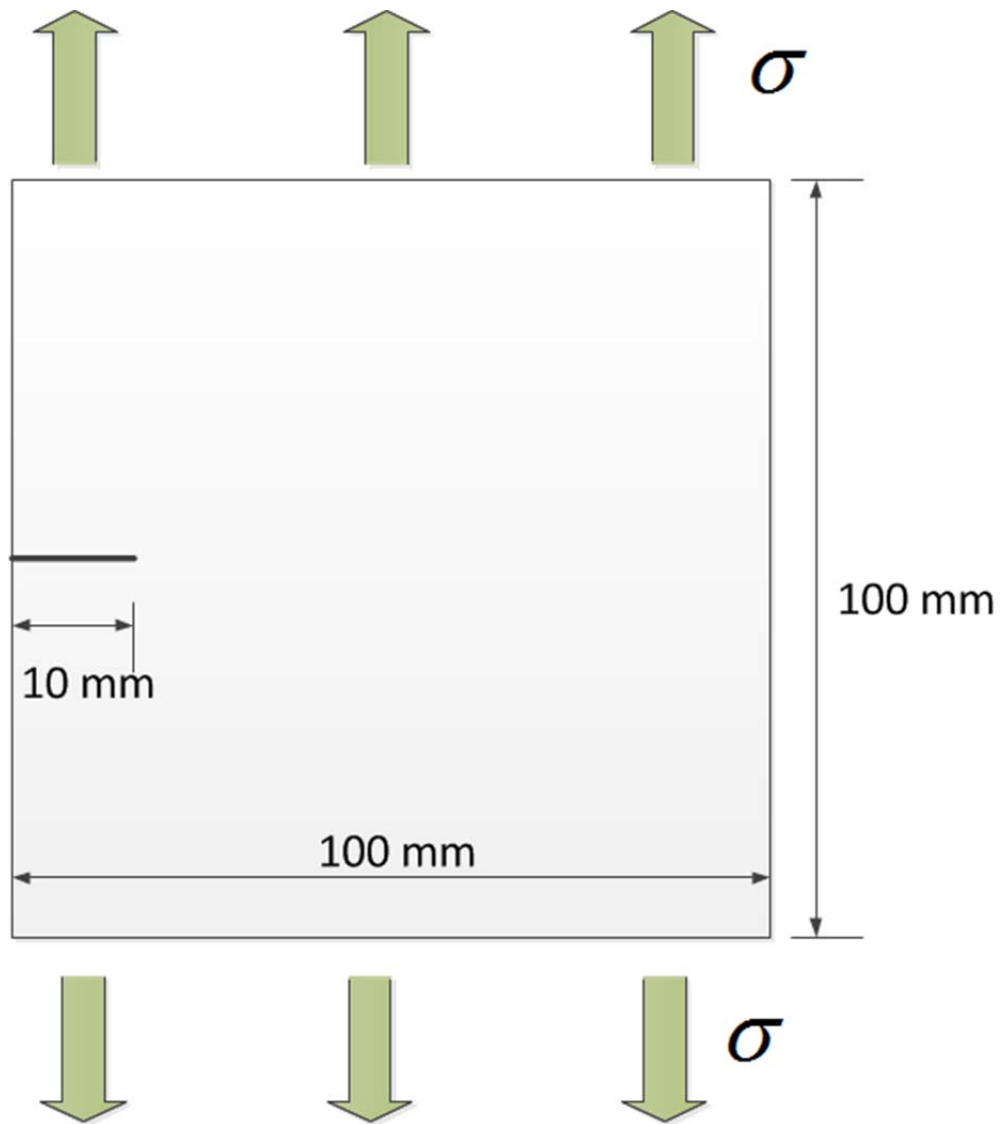


Figure 4.32 A plate with single notch for crack branching study.

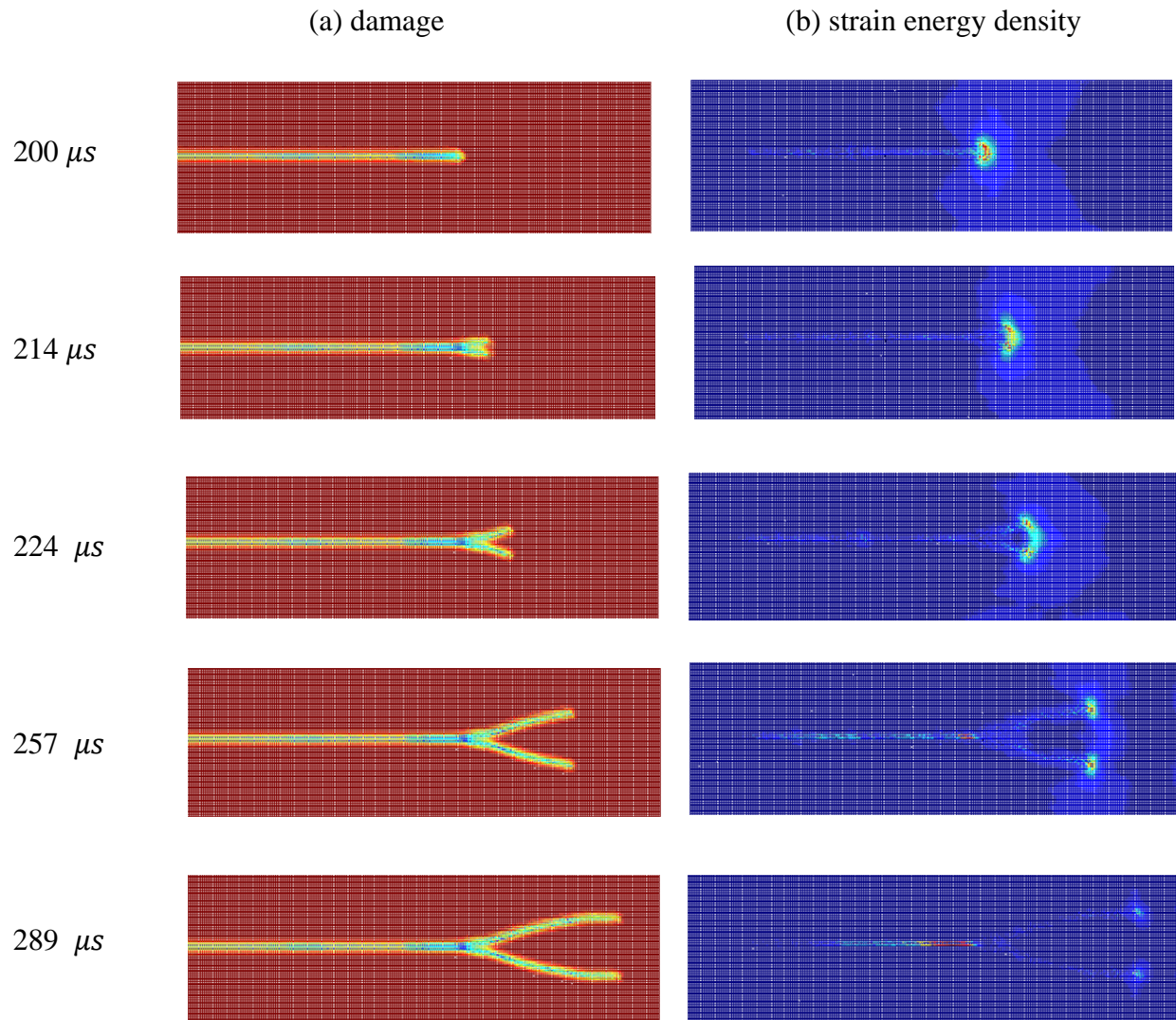


Figure 4.33 Computational crack path (a) damage and (b) strain energy density simulated by peridynamics.

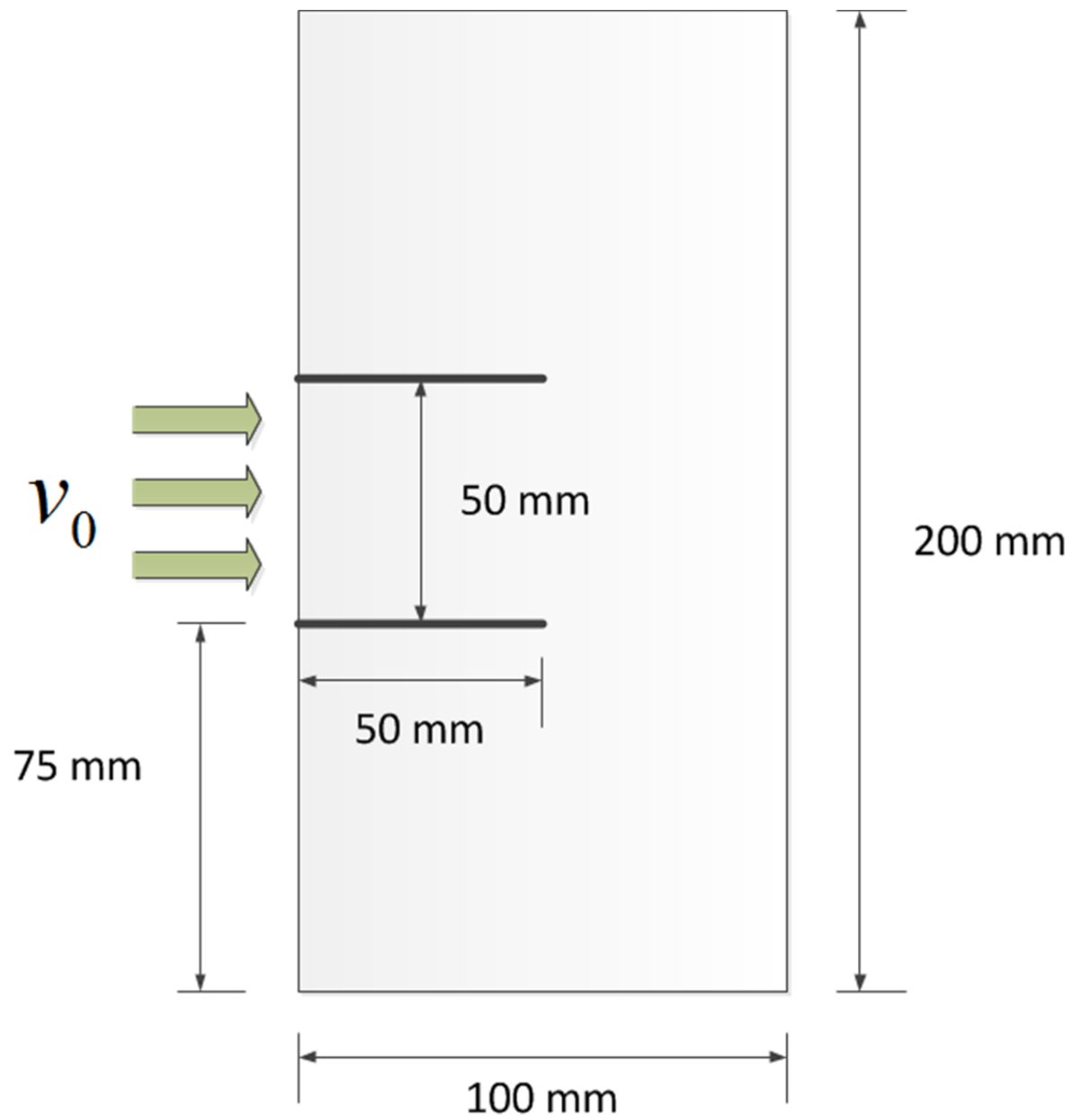


Figure 4.34 A two-notch plate under impulsive loading.

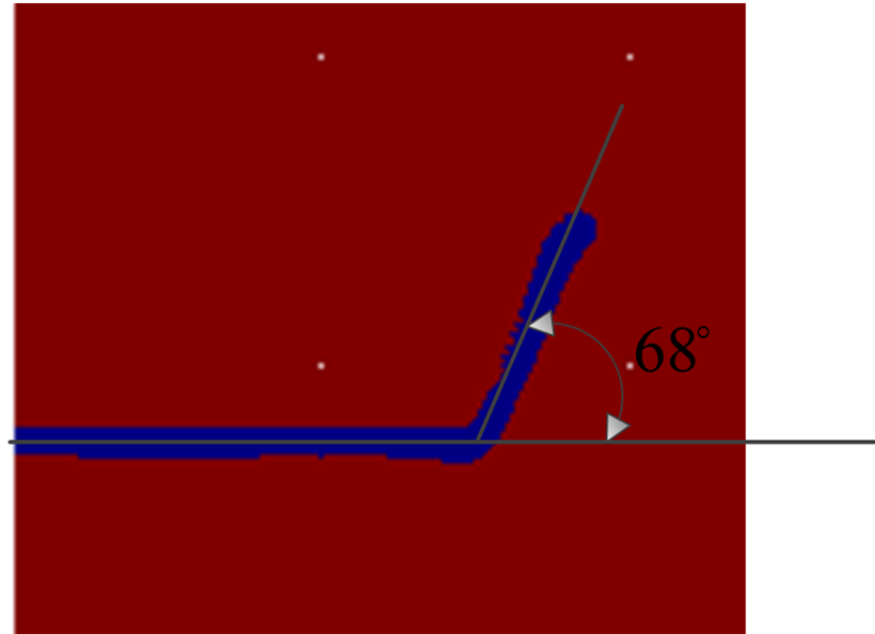


Figure 4.35 Computational crack path of the top notch.

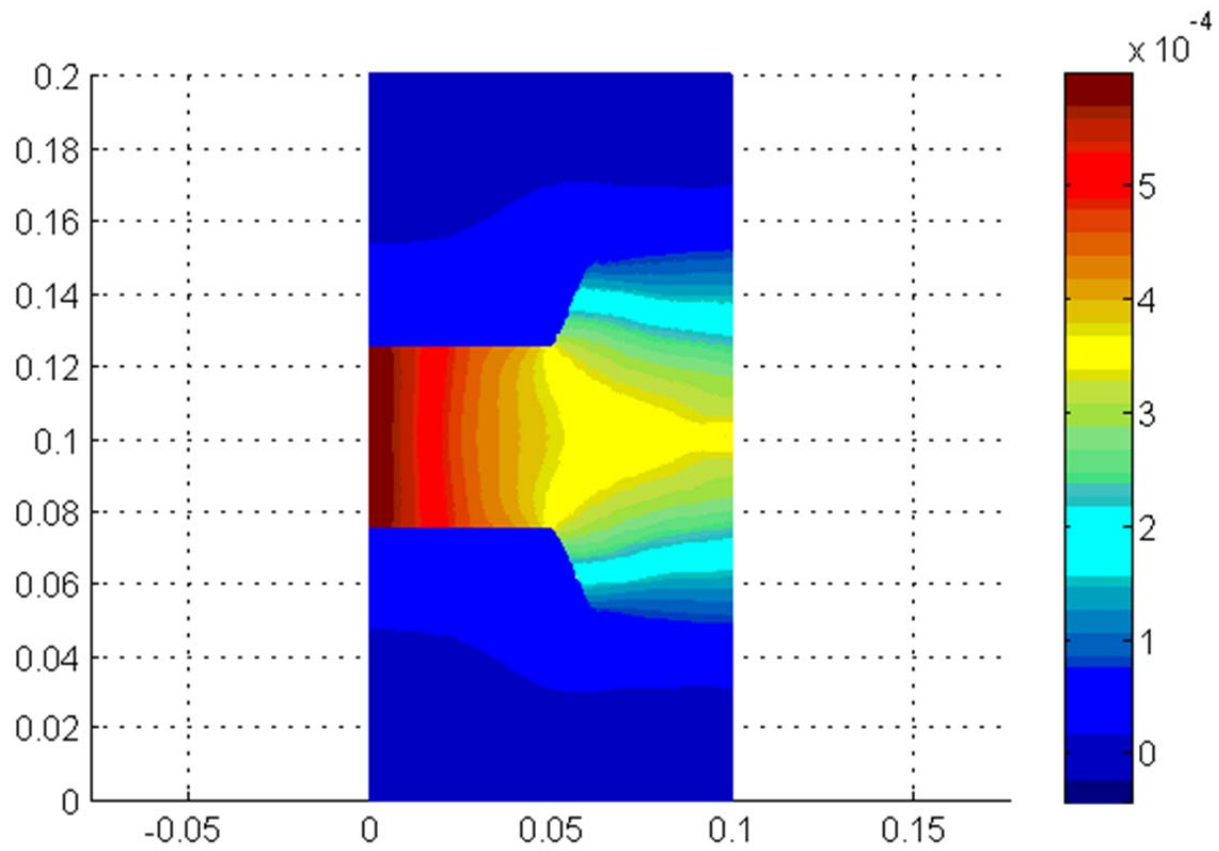


Figure 4.36 Horizontal displacement at $33.2 \mu s$ from computational study.

REFERENCES

References

- [1] Silling, S. A., Reformulation of elasticity theory for discontinuities and long-range forces, *J. Mech. Phys. Solids*, **48**, 175-209 (2000)
- [2] Timoshenko, S. P. Goodier, J. N., *Theory of Elasticity*, Third edition, McGraw-Hill Publishing Company (1970)
- [3] Silling, S.A., Askari, E., A meshfree method based on the peridynamic model of solid mechanics. *Comput. Struct*, **83**, 1526–1535 (2005)
- [4] <http://www.wolfram.com/mathematica/>
- [5] <http://www.mathworks.com/products/parallel-computing/>
- [6] <http://www.icer.msu.edu/?q=hpc>
- [7] Song, J. H., Wang, H., Belytschko, T., A comparative study on finite element methods for dynamic fracture, *Computational Mechanics*, **42**, 239-250 (2008)
- [8] Boudet, J. F., Ciliberto, S., Steinberg, V., Dynamics of Crack Propagation in Brittle Materials, *J. Phys.*, **6**, 1493-1516 (1996)
- [9] Yoffe, E. H., The moving Griffith crack, *Philosophical Magazine*, **42**, 739-750 (1951)
- [10] Ramulu, M., Kobayashi A. S., Mechanics of crack curving and branching-a dynamic fracture analysis, *Int. J. Fract.*, **27**, 187-201 (1985)
- [11] Ravi-Chandar, K., Dynamic fracture of nominally brittle materials, *Int. J. Fract.*, **90**, 83-102 (1998)
- [12] Sharon, E., Gross, S. P., Fineberg J., Local crack branching as a mechanism for instability in dynamic fracture, *Phys. Rev. Lett.*, **74**, 5096-5099 (1995)
- [13] Sharon, E., Fineberg, J., Microbranching instability and the dynamic fracture of brittle materials, *Phys. Rev. B*, **54**, 7128-7139 (1996)
- [14] Fineberg, J., Sharon, E., Cohen, G., Crack front waves in dynamic fracture, *Int. J. Fract.*, **119**, 247-261 (2003)
- [15] Marder, M., Liu, X., Instability in lattice fracture, *Phys. Rev. Lett.*, **71**, 2417 (1993)
- [16] Abraham, F. F., Brodbeck, D., Rafey, R. A., Rudge, W. E., Instability dynamics of fracture: A computer simulation investigation, *Phys. Rev. Lett.*, **73**, 272 (1994)

- [17] Michopoulos, J. G., Theocaris, P. S., The Directional Instability of the Running Crack: A Deterministic and Stochastic Approach, *Int. J. Engng. Sci.*, **29**, 13-36 (1991)
- [18] Kalthoff, J. F., Winkler, S., Failure mode transition at high rates of shear loading, *International conference on impact loading and dynamic behavior of materials*, **1**, 185-195 (1987)
- [19] Decker, R.F., *Source book on maraging steels*, American Society for Metals (1979)
- [20] Lee, Y.J., Freund, L.B., Fracture initiation due to asymmetric impact loading of an edge cracked plate, *J. Appl. Mech*, **57**, 104-111 (1990)
- [21] Kalthoff, J.F., Modes of dynamic shear failure in solids, *Int. J., Fract.*, **101**, 1-31 (2000)

Chapter 5

Orthotropic Model Analysis

It has been shown in Chapter 4 that peridynamic simulation of damage process does not require any knowledge of the damage location and orientation prior to the simulation. This is fundamentally different from finite element analysis which requires knowledge of damage location and orientation in advance to impose special finite element mesh, such as initial damage elements and cohesive zone layers [1], for damage simulations. This prerequisite becomes even more challenging when inhomogeneous and anisotropic composite materials are of interest. In addition, peridynamic simulation does not require remeshing at the end of each damage processing step since it is a mesh free method. On the contrary, finite element analysis does. Based on these difference, peridynamics should be more suitable for simulating dynamic damage process in composite materials which have different properties in different locations and different orientations.

Quite some simulations of composite damage process have been available in the literatures. Dwivedi [1] modeled the propagation of single-edge notch (SEN) in 0° laminated plate using cohesive zone method. Xu [2] and Hu [3] proposed a two-parameter discrete peridynamic model for composite damage simulations, in which there were two kinds of bonds: fiber bond and matrix bond. Two material properties, a_1 and a_2 , were associated with the two types of bonds. Only the bonds along the fiber direction were associated with the material property a_1 while all other bonds with the material property a_2 . This model required remeshing for different fiber directions. For example, a 0° - 90° grid mesh could only be used for a 0° or 90° laminae. For

a 45° lamina, a grid mesh consisting of 45° and 135° was required. The two-parameter model was an approximation of the four material properties involved in orthotropic materials. They were mainly associated with two Young's moduli, E_1 and E_2 . Its capability of modeling shear behavior is unknown.

In this study, a continuous orthotropic material model is proposed. It is based on continuous trigonometric functions. With the continuous material property functions, it is not necessary to have bond in fiber direction and therefore, this model is mesh independent.

5.1 Bar model for orthotropic materials

This model is based on the bar model presented in Section 4.1. The peridynamic equation of motion [4] in two-dimensional domain can be expressed as

$$\rho \ddot{\mathbf{u}} = \int \mathbf{f} dA + \mathbf{b} \quad (5.1)$$

where \mathbf{b} is external force. The force boundary condition can be included in the external force.

For bar model, the bond function f is

$$f = c \cdot s \quad (5.2)$$

where s is bond stretch. Contrary to the isotropic material model, bond material property c is assumed to be a trigonometric function

$$c = d_1 \cos(\theta - \alpha)^4 + d_2 \cos(\theta - \alpha)^2 + d_3 \quad (5.3)$$

where d_1 , d_2 and d_3 are constants and can be identified from composite material properties. θ is bond direction and α is the fiber direction as shown in Fig. 5.1.

Similar to the analysis in the previous chapters, d_1 , d_2 and d_3 can be identified from comparing the strain energy densities based on peridynamic analysis and those based on classical mechanics.

Consider a composite plate with the fibers oriented in α° direction and subjected to the following strain field

$$\varepsilon_{xx} = \varepsilon_1 \quad (5.4)$$

$$\varepsilon_{yy} = \varepsilon_2 \quad (5.5)$$

$$\gamma_{xy} = \gamma_{12} \quad (5.6)$$

The three components are independent of one another.

For a bond in θ direction, and connected to a point \mathbf{x} in the domain, the bond force should be

$$f = c \cdot (\varepsilon_1 \cos \theta^2 + \varepsilon_2 \sin \theta^2 + \gamma_{12} \sin \theta \cos \theta) \quad (5.7)$$

From Eqn. 4.7, the strain energy in the bond becomes

$$w_b = \frac{c\eta^2}{2\xi} = cs^2\xi/2 \quad (5.8)$$

Substituting Eqn. 5.3 and Eqn. 5.7 into Eqn. 5.8 and integrating w_b over the horizon, the strain energy density at the point \mathbf{x} should be

$$\begin{aligned} W = \frac{1}{2} \int w_b dA = \frac{1}{2} \int_0^\delta \int_0^{2\pi} \frac{cs^2\xi}{2} \xi d\theta d\xi = \delta^3 \pi \{ & 16(d_1 + d_2)(\varepsilon_1 - \varepsilon_2)(\varepsilon_1 + \\ & \varepsilon_2) \cos 2\alpha + d_1[(\varepsilon_1 - \varepsilon_2)^2 - \gamma_{12}^2] \cos 4\alpha + 2[(3d_1 + 4d_2 + 8d_3)(3\varepsilon_1^2 + 2\varepsilon_1\varepsilon_2 + 3\varepsilon_2^2 + \gamma_{12}^2) + \\ & 8(d_1 + d_2)(\varepsilon_1 + \varepsilon_2)\gamma_{12} \sin 2\alpha + d_1(\varepsilon_1 - \varepsilon_2)\gamma_{12} \sin 4\alpha] \} / 768 \end{aligned} \quad (5.9)$$

Eqn. 5.9 can be simplified to find the coefficient of each independent term, as shown in Table 5.1. The simplification is achieved based on Mathematica [5].

Table 5.1 Simplified Eqn. 5.9 in terms of independent terms

Coefficients	Independent terms
$d_1 \delta^3 \pi / 96$	$\cos \alpha^4 \varepsilon_1^2$
$d_1 \delta^3 \pi / 96$	$\cos \alpha^4 \varepsilon_2^2$
$-d_1 \delta^3 \pi / 48$	$\cos \alpha^4 \varepsilon_1 \varepsilon_2$
$-d_1 \delta^3 \pi / 96$	$\cos \alpha^4 \gamma_{12}^2$
$(3d_1 + 4d_2) \delta^3 \pi / 96$	$\cos \alpha^2 \varepsilon_1^2$
$(-5d_1 - 4d_2) \delta^3 \pi / 96$	$\cos \alpha^2 \varepsilon_2^2$
$d_1 \delta^3 \pi / 48$	$\cos \alpha^2 \varepsilon_1 \varepsilon_2$
$d_1 \delta^3 \pi / 96$	$\cos \alpha^2 \gamma_{12}^2$
$(3d_1 + 8d_2 + 48d_3) \delta^3 \pi / 768$	ε_1^2
$(35d_1 + 40d_2 + 48d_3) \delta^3 \pi / 768$	ε_2^2
$(5d_1 + 8d_2 + 16d_3) \delta^3 \pi / 384$	$\varepsilon_1 \varepsilon_2$
$(5d_1 + 8d_2 + 16d_3) \delta^3 \pi / 768$	γ_{12}^2
$(3d_1 + 4d_2) \delta^3 \pi / 96$	$\sin \alpha \cos \alpha \gamma_{12} \varepsilon_1$
$(5d_1 + 4d_2) \delta^3 \pi / 96$	$\sin \alpha \cos \alpha \gamma_{12} \varepsilon_2$
$d_1 \delta^3 \pi / 48$	$\sin \alpha \cos \alpha^3 \gamma_{12} \varepsilon_1$
$-d_1 \delta^3 \pi / 48$	$\sin \alpha \cos \alpha^3 \gamma_{12} \varepsilon_2$

On the other hand, from the theory of composite materials [6], the strain energy density under

$\varepsilon_{xx} = \varepsilon_1$, $\varepsilon_{yy} = \varepsilon_2$ and $\gamma_{xy} = \gamma_{12}$ is

$$W = \frac{1}{2}\sigma_{xx}\varepsilon_1 + \frac{1}{2}\sigma_{yy}\varepsilon_2 + \frac{1}{2}\sigma_{xy}\gamma_{12} \quad (5.10)$$

The stresses in Eqn. 5.10 can be calculated by

$$\begin{bmatrix} \sigma_{xx} \\ \sigma_{yy} \\ \sigma_{xy} \end{bmatrix} = \begin{bmatrix} Q_{xx} & Q_{xy} & Q_{xs} \\ Q_{xy} & Q_{yy} & Q_{ys} \\ Q_{xs} & Q_{ys} & Q_{ss} \end{bmatrix} \begin{bmatrix} \varepsilon_{xx} \\ \varepsilon_{yy} \\ \gamma_{xy} \end{bmatrix} \quad (5.11)$$

where,

$$Q_{xx} = Q_{11}m^4 + Q_{22}n^4 + 2m^2n^2Q_{12} + 4m^2n^2Q_{66} \quad (5.12)$$

$$Q_{yy} = Q_{11}n^4 + Q_{22}m^4 + 2m^2n^2Q_{12} + 4m^2n^2Q_{66} \quad (5.13)$$

$$Q_{xy} = Q_{11}m^2n^2 + Q_{22}m^2n^2 + (m^4 + n^4)Q_{12} - 4m^2n^2Q_{66} \quad (5.14)$$

$$Q_{xs} = m^3nQ_{11} - mn^3Q_{22} - mn(m^2 - n^2)Q_{12} - 2mn(m^2 - n^2)Q_{66} \quad (5.15)$$

$$Q_{ys} = mn^3Q_{11} - m^3nQ_{22} + mn(m^2 - n^2)Q_{12} + 2mn(m^2 - n^2)Q_{66} \quad (5.16)$$

$$Q_{ss} = m^2n^2Q_{11} + m^2n^2Q_{22} - 2m^2n^2Q_{12} + (m^2 - n^2)^2Q_{66} \quad (5.17)$$

$$m = \cos \alpha \quad (5.18)$$

$$n = \sin \alpha \quad (5.19)$$

$$Q_{11} = \frac{E_1}{1 - \nu_{12}\nu_{21}} \quad (5.20)$$

$$Q_{22} = \frac{E_2}{1 - \nu_{12}\nu_{21}} \quad (5.21)$$

$$Q_{12} = \frac{E_2\nu_{12}}{1 - \nu_{12}\nu_{21}} \quad (5.22)$$

$$Q_{66} = G_{12} \quad (5.23)$$

E_1, E_2, ν_{12} and G_{12} are the four material properties of orthotropic materials. Substituting Eqns. 5.11 - 5.23 into Eqn. 5.10, it yields

$$\begin{aligned} W = & \frac{1}{2(E_1 - E_2\nu_{12}^2)} \{ (\varepsilon_1^2 E_1^2 + E_1 \varepsilon_2^2 E_2 + E_1 G_{12} \gamma_{12}^2 + 2\varepsilon_1 E_1 \varepsilon_2 E_2 \nu_{12} - E_2 G_{12} \gamma_{12}^2 \nu_{12}^2) \cos \alpha^4 + \\ & 2\gamma_{12} [\varepsilon_2 (E_1 (2G_{12} + E_2(-1 + \nu_{12})) - 2E_2 G_{12} \nu_{12}^2) + \varepsilon_1 (E_1^2 + 2E_2 G_{12} \nu_{12}^2 - E_1 (2G_{12} + \\ & E_2 \nu_{12}))] \cos \alpha^3 \sin \alpha + [2\varepsilon_1 E_1 \varepsilon_2 (E_1 + E_2) + E_1^2 \gamma_{12}^2 + 2\varepsilon_1^2 E_1 E_2 \nu_{12} + 2E_2 G_{12} \gamma_{12}^2 \nu_{12}^2 + \\ & E_1 (-2G_{12} \gamma_{12}^2 + E_2 (\gamma_{12}^2 + 2\varepsilon_2^2 \nu_{12} - 2\gamma_{12}^2 \nu_{12}))] \cos \alpha^2 \sin \alpha^2 + 2\gamma_{12} [E_1^2 \varepsilon_2 + 2(-\varepsilon_1 + \\ & \varepsilon_2) E_2 G_{12} \nu_{12}^2 + E_1 (\varepsilon_1 (2G_{12} + E_2(-1 + \nu_{12})) - \varepsilon_2 (2G_{12} + E_2 \nu_{12}))] \cos \alpha \sin \alpha^3 + [E_1^2 \varepsilon_2^2 - \\ & E_2 G_{12} \gamma_{12}^2 \nu_{12}^2 + E_1 (\varepsilon_1^2 E_2 + G_{12} \gamma_{12}^2 + 2\varepsilon_1 \varepsilon_2 E_2 \nu_{12})] \sin \alpha^4 + (\varepsilon_1 - \varepsilon_2)^2 G_{12} (E_1 - E_2 \nu_{12}^2) \sin 2\alpha^2 \} \end{aligned} \quad (5.24)$$

After simplification processes, the coefficient of each independent terms can be found. They are listed in Table 5.2.

Table 5.2 Simplified Eqn. 5.12 in terms of independent terms

Coefficients	Independent terms
$\frac{E_1^2 + 4E_2 G_{12} \nu_{12}^2 + E_1 (E_2 - 4G_{12} - 2E_2 \nu_{12})}{2(E_1 - E_2 \nu_{12}^2)}$	$\cos \alpha^4 \varepsilon_1^2$
$\frac{E_1^2 + 4E_2 G_{12} \nu_{12}^2 + E_1 (E_2 - 4G_{12} - 2E_2 \nu_{12})}{2(E_1 - E_2 \nu_{12}^2)}$	$\cos \alpha^4 \varepsilon_2^2$
$-\frac{E_1^2 + 4E_2 G_{12} \nu_{12}^2 + E_1 (E_2 - 4G_{12} - 2E_2 \nu_{12})}{(E_1 - E_2 \nu_{12}^2)}$	$\cos \alpha^4 \varepsilon_1 \varepsilon_2$

Table 5.2 (cont'd)	
$-\frac{E_1^2 + 4E_2G_{12}v_{12}^2 + E_1(E_2 - 4G_{12} - 2E_2v_{12})}{2(E_1 - E_2v_{12}^2)}$	$\cos \alpha^4 \gamma_{12}^2$
$\frac{E_1(2G_{12} + E_2(-1 + v_{12})) - 2E_2G_{12}v_{12}^2}{E_1 - E_2v_{12}^2}$	$\cos \alpha^2 \varepsilon_1^2$
$\frac{-E_1^2 + 2E_1G_{12} + E_1E_2v_{12} - 2E_2G_{12}v_{12}^2}{E_1 - E_2v_{12}^2}$	$\cos \alpha^2 \varepsilon_2^2$
$\frac{E_1^2 + 4E_2G_{12}v_{12}^2 + E_1(E_2 - 4G_{12} - 2E_2v_{12})}{E_1 - E_2v_{12}^2}$	$\cos \alpha^2 \varepsilon_1\varepsilon_2$
$\frac{E_1^2 + 4E_2G_{12}v_{12}^2 + E_1(E_2 - 4G_{12} - 2E_2v_{12})}{2(E_1 - E_2v_{12}^2)}$	$\cos \alpha^2 \gamma_{12}^2$
$\frac{E_1E_2}{2(E_1 - E_2v_{12}^2)}$	ε_1^2
$\frac{E_1^2}{2(E_1 - E_2v_{12}^2)}$	ε_2^2
$\frac{E_1E_2v_{12}}{E_1 - E_2v_{12}^2}$	$\varepsilon_1\varepsilon_2$
$\frac{E_1G_{12} - E_2G_{12}v_{12}^2}{2(E_1 - E_2v_{12}^2)}$	γ_{12}^2
$\frac{E_1(2G_{12} + E_2(-1 + v_{12})) - 2E_2G_{12}v_{12}^2}{E_1 - E_2v_{12}^2}$	$\sin \alpha \cos \alpha \gamma_{12}\varepsilon_1$
$\frac{E_1^2 + 2E_2G_{12}v_{12}^2 + E_1(-2G_{12} - E_2v_{12})}{E_1 - E_2v_{12}^2}$	$\sin \alpha \cos \alpha \gamma_{12}\varepsilon_2$
$\frac{E_1^2 + 4E_2G_{12}v_{12}^2 + E_1(E_2 - 4G_{12} - 2E_2v_{12})}{(E_1 - E_2v_{12}^2)}$	$\sin \alpha \cos \alpha^3 \gamma_{12}\varepsilon_1$
$-\frac{E_1^2 + 4E_2G_{12}v_{12}^2 + E_1(E_2 - 4G_{12} - 2E_2v_{12})}{(E_1 - E_2v_{12}^2)}$	$\sin \alpha \cos \alpha^3 \gamma_{12}\varepsilon_2$

Eqn. 5.9 should be equal to Eqn. 5.24. Hence, it is possible to set the coefficients of identical terms equal to each other and identify d_1 , d_2 and d_3 .

$$d_1 = \frac{24}{\delta^3 E_1 \pi} \left(E_1^2 + E_1 E_2 - 12 E_1 G_{12} + \frac{E_1 \sqrt{E_1 E_2 + 4 G_{12}^2}}{\sqrt{E_2/E_1}} + \sqrt{E_1 E_2} \sqrt{E_1 E_2 + 4 G_{12}^2} \right) \quad (5.25)$$

$$d_2 =$$

$$\frac{6}{\delta^3 E_1 \pi} \left(-3 E_1^2 - 5 E_1 E_2 + 48 E_1 G_{12} - \frac{3 E_1 \sqrt{E_1 E_2 + 4 G_{12}^2}}{\sqrt{E_2/E_1}} - 5 \sqrt{E_1 E_2} \sqrt{E_1 E_2 + 4 G_{12}^2} \right) \quad (5.26)$$

$$d_3 = \frac{3}{2 \delta^3 E_1 \pi} (E_1^2 + 5 E_1 E_2 - 20 E_1 G_{12} + \frac{E_1 \sqrt{E_1 E_2 + 4 G_{12}^2}}{\sqrt{E_2/E_1}} + 5 \sqrt{E_1 E_2} \sqrt{E_1 E_2 + 4 G_{12}^2}) \quad (5.27)$$

$$v_{12} = \frac{-E_1 E_2 + \sqrt{E_1 E_2} \sqrt{E_1 E_2 + 4 G_{12}^2}}{2 E_2 G_{12}} \quad (5.28)$$

The composite model has three parameters and it can model shearing deformation. The bond stiffness is a continuous function so the stiffness at any direction can be calculated. It can be found that the bond becomes stronger as the angle between the bond and the fiber becomes smaller. Similar to the bar model in Section 4.1, the Poisson's ratio of this model is fixed and is related to the remaining three independent material properties. For example, the Poisson's ratio of Kevlar/Epoxy is 0.34 while the Poisson's ratio calculated from this model is 0.39.

5.2 Beam model for orthotropic materials

To accomodate the four material properties of orthotropic materials, a beam model based on Section 4.2 is proposed here.

From the composite theory, there are four independent material properties, E_1, E_2, ν_{12} and G_{12} .

The composite stiffness varies with fiber orientation. Bond functions are

$$f'_x = \frac{c_1(u'_2 - u'_1)}{r} \quad (5.29)$$

$$f'_y = \frac{c_2(v'_2 - v'_1)}{r^3} \quad (5.30)$$

They are identical to Eqn. 4.23 and Eqn. 4.24. However, c_1 and c_2 for a bond in θ direction will be dependent on fiber orientations as follows,

$$c_1 = d_1 \cos(\theta - \alpha)^4 + d_2 \cos(\theta - \alpha)^2 + d_3 \quad (5.31)$$

$$c_2 = d_4 \quad (5.32)$$

where α is the orientation of the fiber, as shown in Fig. 5.3. The coefficients d_1, d_2, d_3 and d_4 are four independent material properties. They are related to the four material properties defined in the composite theory.

Consider a composite plate with fiber in α direction and subject to the following strain field

$$\varepsilon_{xx} = \varepsilon_1 \quad (5.33)$$

$$\varepsilon_{yy} = \varepsilon_2 \quad (5.34)$$

$$\gamma_{xy} = \gamma_{12} \quad (5.35)$$

The three strains are independent from each other.

Similar to Eqn. 4.29, the strain energy in one bond becomes

$$w_b = \frac{c_1(\varepsilon_1 r \cos \theta^2 + \varepsilon_2 r \sin \theta^2)^2}{2r} + \frac{c_2(-\varepsilon_1 r \cos \theta \sin \theta + \varepsilon_2 r \cos \theta \sin \theta)^2}{2r^3} \quad (5.36)$$

Integrate Eqn. 5.36 to find the strain energy density for a point

$$\begin{aligned} W = \frac{1}{2} \int w_b dA = \frac{1}{2} \int_0^\delta \int_0^{2\pi} w_b r d\theta dr = \frac{1}{768} \pi \delta \{ & 16(d_1 + d_2) \delta^2 (\varepsilon_1^2 - \varepsilon_2^2) \cos 2\alpha + \\ & d_1 \delta^2 (\varepsilon_1^2 - 2\varepsilon_1 \varepsilon_2 + \varepsilon_2^2 - \gamma_{12}^2) \cos 4\alpha + 2[24d_4(\varepsilon_1 - \varepsilon_2)^2 + 9d_1 \delta^2 \varepsilon_1^2 + 12d_2 \delta^2 \varepsilon_1^2 + \\ & 24d_3 \delta^2 \varepsilon_1^2 + 6d_1 \delta^2 \varepsilon_1 \varepsilon_2 + 8d_2 \delta^2 \varepsilon_1 \varepsilon_2 + 16d_3 \delta^2 \varepsilon_1 \varepsilon_2 + 9d_1 \delta^2 \varepsilon_2^2 + 12d_2 \delta^2 \varepsilon_2^2 + 24d_3 \delta^2 \varepsilon_2^2 + \\ & 24d_4 \gamma_{12}^2 + 3d_1 \delta^2 \gamma_{12}^2 + 4d_2 \delta^2 \gamma_{12}^2 + 8d_3 \delta^2 \gamma_{12}^2 + 8(d_1 + d_2) \delta^2 (\varepsilon_1 + \varepsilon_2) \gamma_{12} \sin 2\alpha + \\ & d_1 \delta^2 (\varepsilon_1 - \varepsilon_2) \gamma_{12} \sin 4\alpha] \} \end{aligned} \quad (5.37)$$

The Strain energy density based on the composite theory is the same as Eqn. 5.24. Similar to Section 5.1, by setting Eqn. 5.24 equal to Eqn. 5.37 and comparing the coefficients of the independent terms, the following equations are obtained

$$d_1 = \frac{48(E_1^2 + E_1 E_2 - 4E_1 G_{12} - 2E_1 E_2 v_{12} + 4E_2 G_{12} v_{12}^2)}{\pi(E_1 - E_2 v_{12}^2) \delta^3} \quad (5.38)$$

$$d_2 = - \frac{12(3E_1^2 + 5E_1 E_2 - 16E_1 G_{12} - 8E_1 E_2 v_{12} + 16E_2 G_{12} v_{12}^2)}{\pi(E_1 - E_2 v_{12}^2) \delta^3} \quad (5.39)$$

$$d_3 = \frac{3(E_1^2 + 5E_1 E_2 - 8E_1 G_{12} - 2E_1 E_2 v_{12} + 8E_2 G_{12} v_{12}^2)}{\pi(E_1 - E_2 v_{12}^2) \delta^3} \quad (5.40)$$

$$d_4 = - \frac{4(-E_1 G_{12} + E_1 E_2 v_{12} + E_2 G_{12} v_{12}^2)}{\pi(E_1 - E_2 v_{12}^2) \delta} \quad (5.41)$$

5.3 Calculation of stresses from peridynamics

Similar to Section 4.2, stresses can be defined and calculated from peridynamics. They can be used for some special comparison but not necessary in peridynamic simulations.

Consider a case with $\varepsilon_{xx} = \varepsilon_1$ and $\varepsilon_{yy} = \varepsilon_2$. The stress σ_{xx} can be calculated by using Eqn. 4.39 and is given below

$$\sigma_{xx} = \int_0^\delta \int_h^\delta \int_{-\cos^{-1}\frac{h}{r}}^{\cos^{-1}\frac{h}{r}} (fx' \cdot \cos \theta - fy' \cdot \sin \theta) r d\theta dr dh = \frac{1}{384} \pi \delta \{48d_4(\varepsilon_1 - \varepsilon_2) + 2(3d_1 + 4d_2 + 8d_3)(3\varepsilon_1 + \varepsilon_2)\delta^2 + \delta^2[16\varepsilon_1 \cos 2\alpha (d_1 + d_2) + d_1(\varepsilon_1 - \varepsilon_2) \cos 4\alpha]\} \quad (5.42)$$

Substituting Eqns. 5.38 - 5.41 into Eqn. 5.42, it yields

$$\begin{aligned} \sigma_{xx} = & \frac{1}{8(E_1 - E_2 v_{12}^2)} \{3\varepsilon_1 E_1^2 + \varepsilon_2 E_1^2 + 3\varepsilon_1 E_1 E_2 + \varepsilon_2 E_1 E_2 + 4\varepsilon_1 E_1 G_{12} - 4\varepsilon_2 E_1 G_{12} + 2\varepsilon_1 E_1 E_2 v_{12} + \\ & 6\varepsilon_2 E_1 E_2 v_{12} - 4\varepsilon_1 E_2 G_{12} v_{12}^2 + 4\varepsilon_2 E_2 G_{12} v_{12}^2 + 4\varepsilon_1 E_1 (E_1 - E_2) \cos 2\alpha + (\varepsilon_1 - \varepsilon_2)(E_1^2 + \\ & 4E_2 G_{12} v_{12}^2 + E_1(E_2 - 4G_{12} - 2E_2 v_{12})) \cos 4\alpha\} \end{aligned} \quad (5.43)$$

While from the composite theory, σ_{xx} can be expressed as

$$\begin{aligned} \sigma_{xx} = Q_{xx}\varepsilon_1 + Q_{xy}\varepsilon_2 = & \frac{1}{(E_1 - E_2 v_{12}^2)} \{E_1(\varepsilon_1 E_1 + \varepsilon_2 E_2 v_{12}) \cos a^4 + [E_1^2 \varepsilon_2 + 4(-\varepsilon_1 + \\ & \varepsilon_2)E_2 G_{12} v_{12}^2 + E_1(\varepsilon_2 E_2 + 4\varepsilon_1 G_{12} - 4\varepsilon_2 G_{12} + 2\varepsilon_1 E_2 v_{12})] \cos a^2 \sin a^2 + E_1 E_2 (\varepsilon_1 + \\ & \varepsilon_2 v_{12}) \sin a^4\} \end{aligned} \quad (5.44)$$

With further simplification, it can be found that Eqn. 5.43 is identical to Eqn. 5.44.

5.4 Laminated plate under static loading

In this section, it is to verify the proposed peridynamic model with an analytical solution. A simple tensile test is performed on a laminated plate. The peridynamic results will be compared with the results obtained from the composite theory.

Consider a $100\text{ mm} \times 100\text{ mm}$ laminated plate with fibers in α direction as shown in Fig. 5.4. A tensile pressure of 10 MPa is applied at the bottom and the top of the plate. The plate is made of E-Glass/Epoxy and the material properties are shown in Table 5.3.

Table 5.3 Material properties of E-Glass/Epoxy

Longitudinal Young's modulus, E_1	41 GPa
Transverse Young's modulus, E_2	10.4 GPa
Poisson's ratio, ν_{12}	0.28
Shear modulus, G_{12}	4.3 GPa
Mass density, ρ	1970 kg/m^3

Based on the composite theory [6], the components of the compliance matrix are

$$S_{11} = 1/E_1 \quad (5.45)$$

$$S_{22} = 1/E_2 \quad (5.46)$$

$$S_{12} = -\nu_{12}/E_1 \quad (5.47)$$

$$S_{66} = 1/G_{12} \quad (5.48)$$

Strains from the composite theory can be calculated as follows

$$\begin{bmatrix} \varepsilon_{xx} \\ \varepsilon_{yy} \\ \gamma_{xy} \end{bmatrix} = \begin{bmatrix} S_{xx} & S_{xy} & S_{xs} \\ S_{xy} & S_{yy} & S_{ys} \\ S_{xs} & S_{ys} & S_{ss} \end{bmatrix} \begin{bmatrix} \sigma_{xx} \\ \sigma_{yy} \\ \sigma_{xy} \end{bmatrix} \quad (5.49)$$

The transformed compliance matrix is caculated as

$$\begin{bmatrix} S_{xx} & S_{xy} & S_{xs} \\ S_{xy} & S_{yy} & S_{ys} \\ \frac{1}{2}S_{xs} & \frac{1}{2}S_{ys} & \frac{1}{2}S_{ss} \end{bmatrix} = T^{-1} \begin{bmatrix} S_{11} & S_{12} & 0 \\ S_{12} & S_{22} & 0 \\ 0 & 0 & \frac{1}{2}S_{66} \end{bmatrix} T \quad (5.50)$$

where

$$T = \begin{bmatrix} m^2 & n^2 & 2mn \\ n^2 & m^2 & -2mn \\ -mn & mn & m^2 - n^2 \end{bmatrix} \quad (5.51)$$

and $m = \cos \alpha$ and $n = \sin \alpha$.

From Eqn. 5.49, the displacement field can be obtained from the composite theory. Displacements from peridynamics are compared with those from the composite theory in Fig. 5.5-Fig. 5.10 with $\alpha = 0^\circ, 45^\circ$ and 60° . As can be seen, the results from peridynamics and those from composite theory are identical to each other.

5.5 Free vibration of a laminated beam

The free vibration of a laminated beam is investigated in this section by the Classical Laminated Beam Theory and the solution will be used to verify that obtained from peridynamic model.

Consider a simply supported beam as shown Fig. 5.11. The length of the beam is $L = a \cdot h$ and the thickness of the beam is $h = 10 \text{ mm}$, where a is the aspect ratio of the beam. The beam is made of Kevlar/Epoxy with fibers oriented in x direction. The material properties are shown in

Table 5.4.

Table 5.4 Material properties of Kevlar/Epoxy

Longitudinal Young's modulus, E_1	80 <i>GPa</i>
Transverse Young's modulus, E_2	5.5 <i>GPa</i>
Poisson's ratio, ν_{12}	0.34
Shear modulus, G_{12}	2.2 <i>GPa</i>
Mass density, ρ	1380 <i>kg/m³</i>

From [7], the governing equations of the beam are

$$A_{11} \frac{d^2 u^\circ}{dx^2} - B_{11} \frac{d^3 w}{dx^3} - \rho \omega^2 u^\circ = 0 \quad (5.52)$$

$$D_{11} \frac{d^4 w}{dx^4} - B_{11} \frac{d^3 u^\circ}{dx^3} - \rho \omega^2 w = 0 \quad (5.53)$$

where

$$A_{11} = \int_{-h/2}^{h/2} Q_{11} dz = Q_{11} h \quad (5.54)$$

$$B_{11} = \int_{-h/2}^{h/2} Q_{11} z dz = 0 \quad (5.55)$$

$$D_{11} = \int_{-h/2}^{h/2} Q_{11} z^2 dz = Q_{11} h^3 / 12 \quad (5.56)$$

A solution satisfying the governing equations is

$$u_0 = U \cos px \quad (5.57)$$

$$w = W \sin px \quad (5.58)$$

Eqn. 5.57 and Eqn. 5.58 satisfy the simply supported boundary conditions automatically.

Substituting Eqn. 5.57 and Eqn. 5.58 into Eqn. 5.52 and Eqn. 5.53, it yields

$$-A_{11}p^2U - \rho\omega^2U = 0 \quad (5.59)$$

$$D_{11}p^4W - \rho\omega^2W = 0 \quad (5.60)$$

Solving Eqn. 5.59 and Eqn. 5.60, it can be concluded that

$$\omega^2 = \frac{Q_{11}p^4h^3}{12\rho} \quad (5.61)$$

$$U = 0 \quad (5.62)$$

If the initial condition of the beam is

$$w(t = 0) = 1 \times 10^{-5} \sin \frac{\pi}{L}x \quad (5.63)$$

then

$$W = 1 \times 10^{-5} \quad (5.64)$$

$$p = \frac{\pi}{L} \quad (5.65)$$

The solution of the problem should have the following forms

$$w'(x, t) = W \sin px \cos \omega t \quad (5.66)$$

$$u'(x, z, t) = -zpW \cos px \cos \omega t \quad (5.67)$$

where W , p and ω can be found from Eqn. 5.64, Eqn. 5.65 and Eqn. 5.61, respectively.

The same problem can be simulated by peridynamics. The displacement history of point A and point B (Fig. 5.11) are recorded. Fig. 5.12 compares the peridynamic results with those from the

composite beam theory for the aspect ratio $a = 5$. Fig. 5.13 compares the peridynamic results with those from the composite beam theory for the aspect ratio $a = 20$. Results from the two methods show good match in vertical displacement w of point B. For horizontal displacement u of point A, peridynamic result is almost the same as the beam theory result when the aspect ratio $a = 20$. However, there is difference between the peridynamic result and the beam theory result when the aspect ratio $a = 5$. This is because the beam theory assumes no variation of vertical displacement when the beam is slender. With a small aspect ratio, such as $a = 5$, this variation is not negligible and the beam theory does not provide a good approximation.

5.6 Comparisons of crack propagation velocity with experiments

Experiment studies on dynamic crack propagation in fiber-reinforced composite materials have been conducted by Zheng[9], Rosakis[8], Stout[10] and Coker[11,12]. It has been shown that a weak fracture plane usually occurs between fiber and matrix in unidirectional fiber-reinforced composites. Due to material anisotropy, the wave speed along the fiber direction is very different from that along the perpendicular direction. Dynamic crack propagation has been commonly investigated by finite element method. A limited number of computational studies have been reported by Huang [13], Hwang [14], Kumar [15], Stout [10], Lo [16], Sun [17] and Pandey[18]. The limit of computational works is likely due to the requirement of remeshing and the complexity of handling elements once crack starts. In this section, dynamic crack propagation in a unidirectional graphite/epoxy composite is studied with the use of peridynamics. The computational results are validated by the experiment results given in reference [8].

Consider a $76\text{ mm} \times 152\text{ mm}$ unidirectional graphite/epoxy fiber-reinforced composite plates

under three-point bending [8] as shown in Fig. 5.14. The fiber is in 90° direction. The material properties are shown in Table 5.5 [8, 22]. There is a notch with a length of 15.2 mm , i.e. 20% of the plate width, at the left boundary of the plate. This crack length is used because it was used in the past to produce reliable results in dynamic fracture experiments [19]. To minimize residual stresses due to machining, a low-speed diamond saw was used to produce the initial notch with a width of approximately 1.5 mm .

Table 5.5 Material properties of graphite/epoxy

Longitudinal Young's modulus, E_1	150 GPa
Transverse Young's modulus, E_2	11.6 GPa
Poisson's ratio, ν_{12}	0.36
Shear modulus, G_{12}	3.5 GPa
Mode I intralaminar fracture energy for longitudinal loading, G_{10}	77.9 J/m ²
Mode I intralaminar fracture energy for transverse loading, G_{20}	5 J/m ²
Mass density, ρ	1590 kg/m ³

A drop-weight tower is used to introduce impact on the opposite side of the notch with an impacting speed of $v_0 = 4\text{ m/s}$. After the impact, stress waves propagate to the interior of the plate and then reflect from the boundaries. Because of the anisotropy of the material, stress waves travel in different directions at different velocities. Experiments show that the crack starts to propagate at about $25\mu\text{s}$ after the impact so the effects of dispersion are not very important since the applied stress pulse is very long (about $120\mu\text{s}$) compared with the time of crack initiation. Therefore, loading is continuously applied throughout the entire event.

The real-time visualization of dynamic fracture is produced by an optical method of coherent gradient sensing (CGS) in reflection [20, 21]. Imaging is performed with a rotating-mirror high-speed camera. Details of the CGS system can be found in [8, 20, 21].

Fig. 5.15 shows the crack propagation velocity from the peridynamic simulation. The initial time $t = 0$ is used to denote the beginning of the crack propagation. For negative time, $v = 0 \text{ m/s}$. The crack starts from about 700 m/s and accelerates to 900 m/s within about $10 \mu\text{s}$. It then decelerates to less than 500 m/s in $40 \mu\text{s}$ after the initiation. This deceleration is believed to be due to the fact that the growing crack tip enters a region of high compressive stress zone as it approaches the loading area. The peridynamic computational results are compared with the experiment results from Ref. [8]. As shown in Fig. 5.15, they agree each other reasonably well.

5.7 Dynamic fracture mode in unidirectional composites

In order to investigate the behavior of cracks, Wu [24] conducted experiments with unidirectional, fiberglass-reinforced Scotch composites with a centered precrack in the direction of fibers. The composites were loaded with tension, pure shear and combined tension and shear. In all three cases, it was observed that the crack propagated in the same direction as the fiber direction. Finite element analysis were also used to study the damage path and failure initiation of pre-notched composites by Boger [25] and Satyanarayana [26]. They predicted damage in composite plates notched in the center for different layups under tension. Both experiment results and simulation results showed that the crack path and failure initiation depends on fiber orientation.

In this section, the crack propagation path and dynamic fracture mode of unidirectional fiber-reinforced composites are studied using the proposed peridynamic model. The qualitative comparison of the peridynamic results with those from experiments are of interest.

Consider the compact tension test on a $100\text{ mm} \times 200\text{ mm}$ carbon/epoxy unidirectional composite plate with a 20 mm pre-notch at the center as shown in Fig. 5.16. The plate is loaded at the top and the bottom boundary by a uniform stress σ . The fiber orientation is α . The material properties of the carbon/epoxy plate are shown in Table 5.6 [23].

Table 5.6 Material properties of carbon/epoxy

Longitudinal Young's modulus, E_1	329 GPa
Transverse Young's modulus, E_2	6 GPa
Poisson's ratio, ν_{12}	0.346
Shear modulus, G_{12}	4.4 GPa
Mode I intralamina fracture energy for longitudinal loading, G_{10}	15.49 kJ/m ²
Mode I intralamina fracture energy for transverse loading, G_{20}	0.168 kJ/m ²
Mass density, ρ	1630 kg/m ³

Fig. 5.17, Fig. 5.18, Fig. 5.19, Fig. 5.20 and Fig. 5.21 show the peridynamic simulation results for $\alpha = 0^\circ$, $\alpha = 30^\circ$, $\alpha = 45^\circ$, $\alpha = 60^\circ$ and $\alpha = 90^\circ$, respectively. In each figure, there are three contour plots with (a) vertical displacement of the plate, (b) strain energy density distribution and (c) local damage of the plate. Different color bars are associated with different plots with red

indicating the highest value while blue the lowest value. Crack paths can be clearly seen from the strain energy density contour plot as there are always strain energy concentrations at the crack tips. The local damage is defined by Eqn. 2.12 and Enq. 2.13, which show different levels of damage. A proper cutoff value can be defined to judge if there is a crack. In all cases, the crack propagates in the same direction as the fibers, which is consistent with the experiment observations from Wu [24]. The damage is due to the separation between matrix and fiber. There is no fiber breakage.

As expected, in the $\alpha = 0^\circ$ case, the crack propagates in the same direction as the pre-notch. This also matches with the computational and experiment results in Section 5.6. In the smaller angle case $\alpha = 30^\circ$, aside from the major crack, which propagates in 30° , there is matrix shattering at the sides of the plate in 0° direction. The matrix shattering happens before the crack starts to propagate as shown in Fig. 5.22. It starts at the lateral of the plate and propagates to the interior of the plate. From Fig. 5.18 (c), the matrix shattering is not as severe as the major crack since only 20% of the bonds are broken. However, in the major crack, more than 70% of the bonds are broken. This is why matrix shattering is only a material softening and may not be seen from experiment observation as reported in [24]. For the $\alpha = 90^\circ$ case, the composite plate fails due to splitting caused by shear stress in the matrix. It which matches with the findings of Boger [25].

5.8 Conclusions

A peridynamic orthotropic material model based on the beam model is proposed in this chapter. There are four independent material parameters in this model and it matches with the four

material properties for two-dimensional orthotropic materials. The bond material properties depend on these four material parameters and the angle between the bond orientation and fiber orientation. This results in the continuity of the bond stiffness function with no need of remeshing for different fiber orientations. This model is verified by a static tensile test and a vibration problem of a laminated beam.

Dynamic damage propagation problems in composite materials can be greatly benefited from peridynamics. The prediction of damage initiation and crack propagation of composite materials is complex using traditional methods, such as finite element analysis, due to its anisotropy. As investigated in peridynamic simulations, there is no need of tracking each crack propagation, finding different damage modes and applying different damage rules. Damage happens automatically. A single edge notch test is simulated in this chapter and the results match with the experiment results. Crack path and failure initiation of a center notch plate is predicted successfully by peridynamics when comparing with the experiment results.

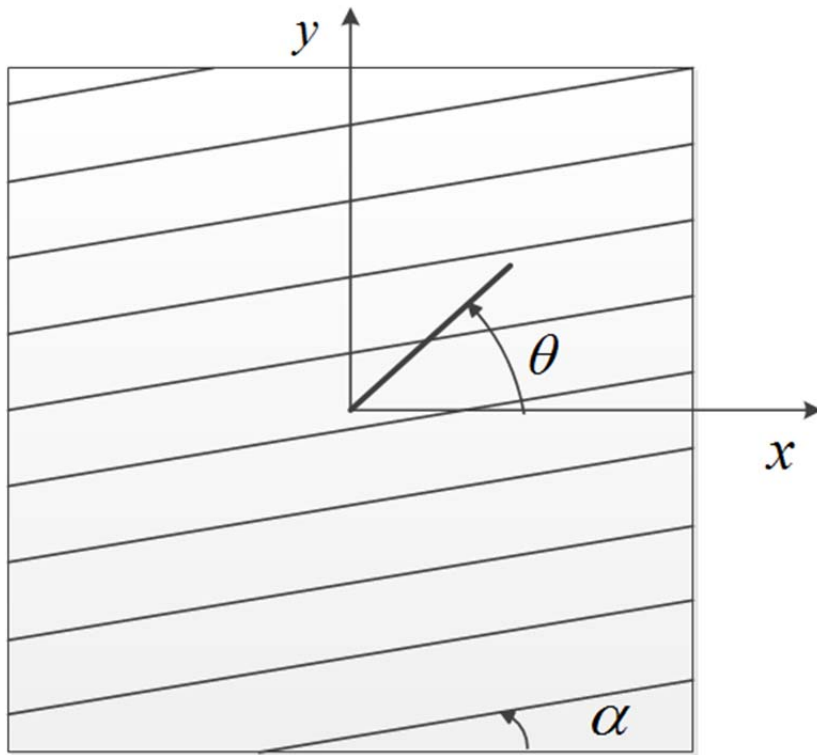


Figure 5.1 A composite plate with fiber in α° direction and a bond in θ° direction.

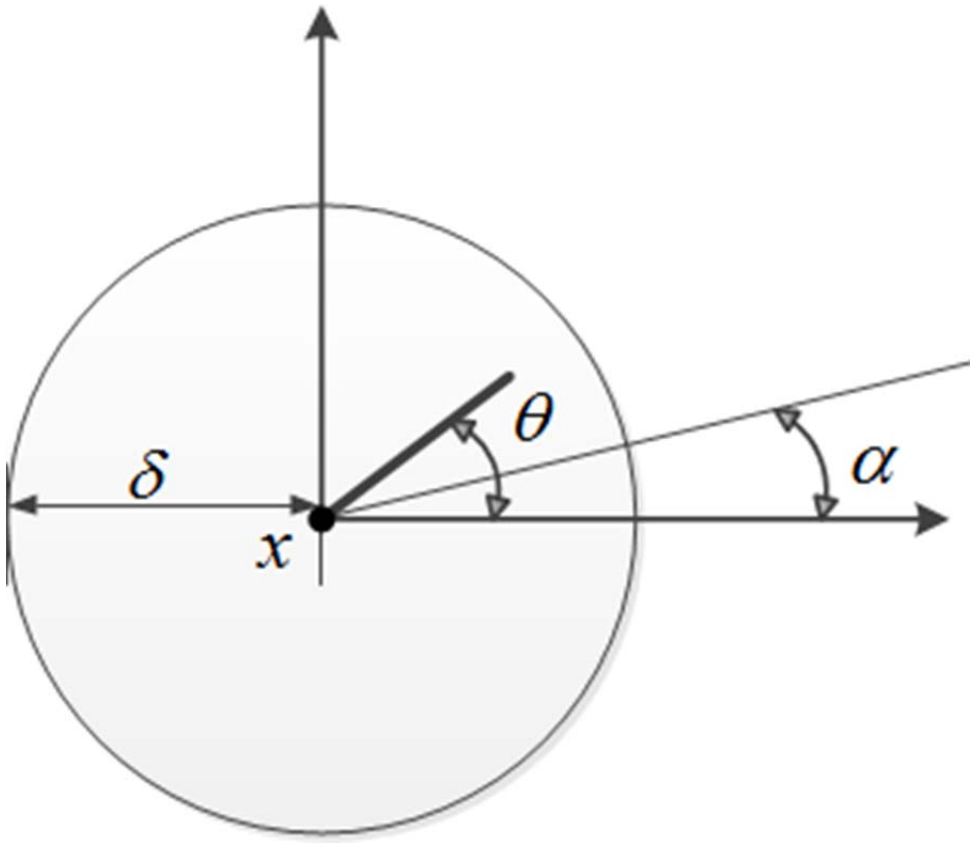


Figure 5.2 Coordinate system for calculating strain energy density at point x .

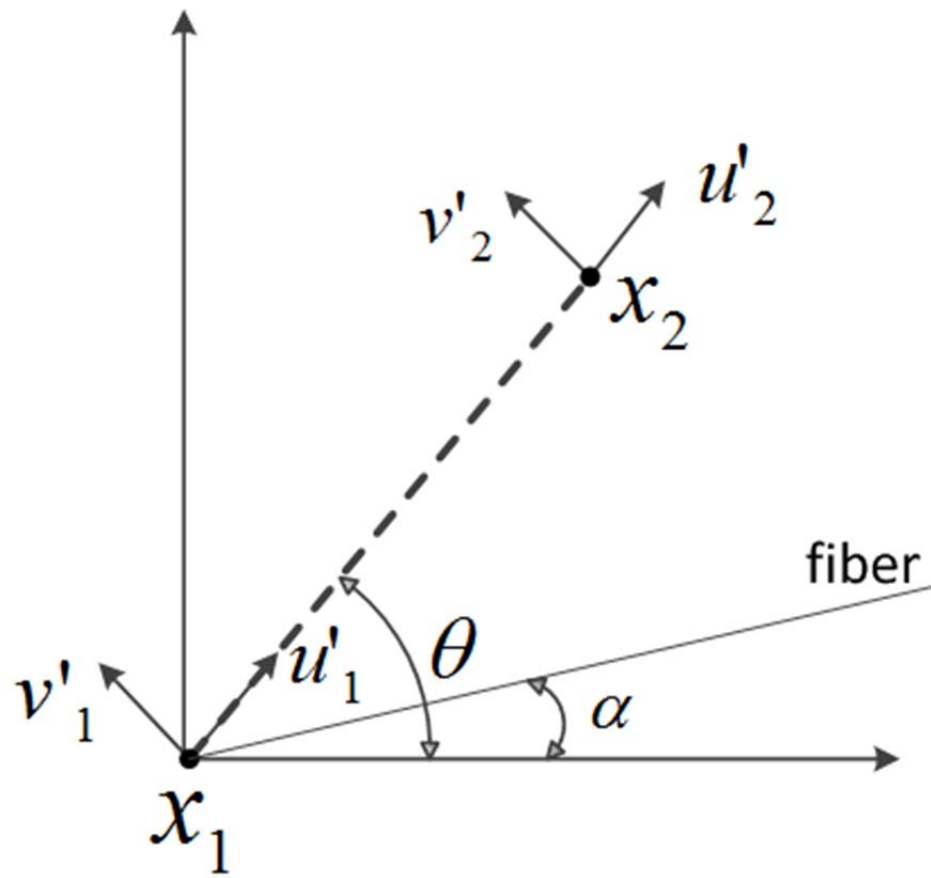


Figure 5.3 Beam model for orthotropic materials.

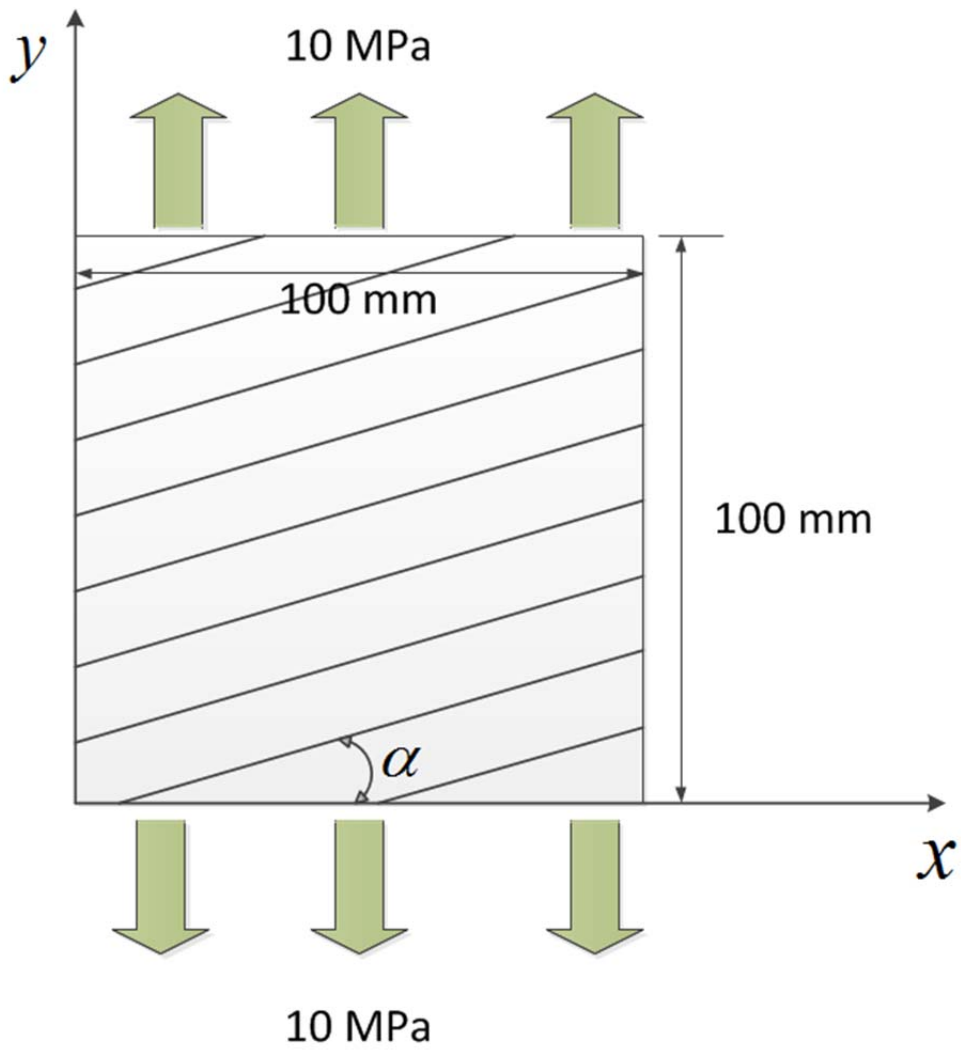


Figure 5.4 Pulling test in a composite laminate.

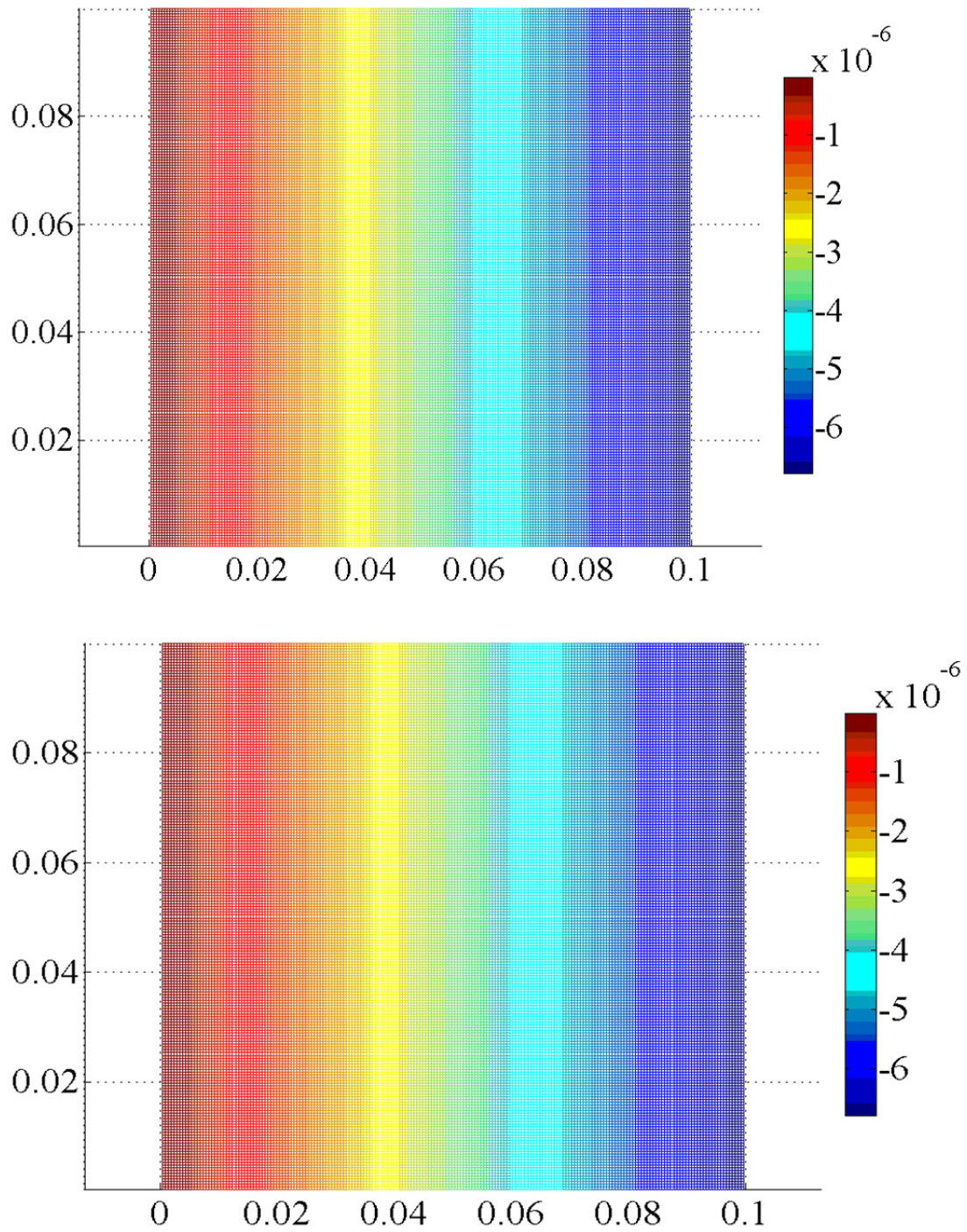


Figure 5.5 Comparison of u_x of 0° laminate calculated from peridynamics (top) and composite theory (bottom).

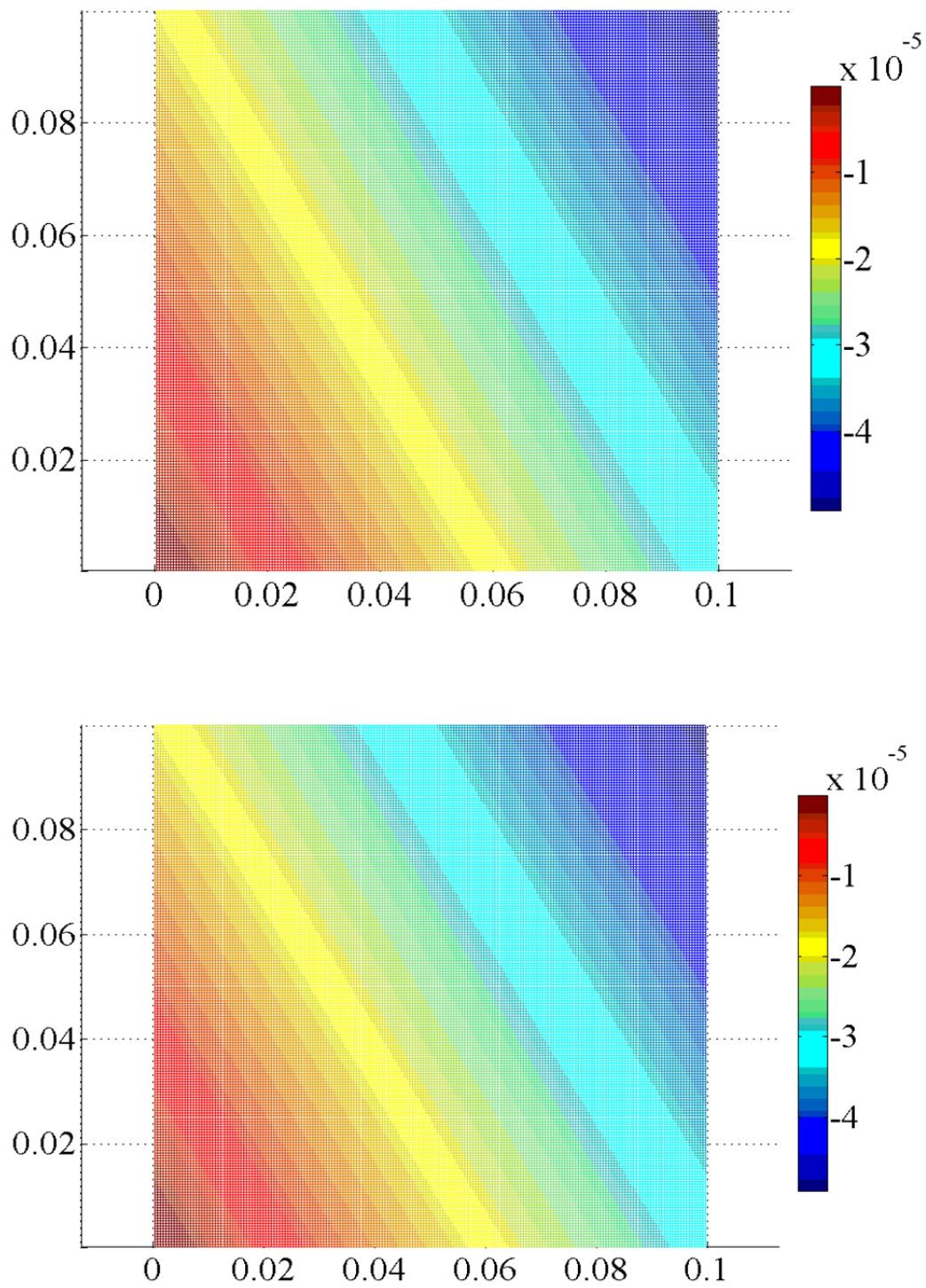


Figure 5.6 Comparison of u_x of 45° laminate calculated from peridynamics (top) and the composite theory (bottom).

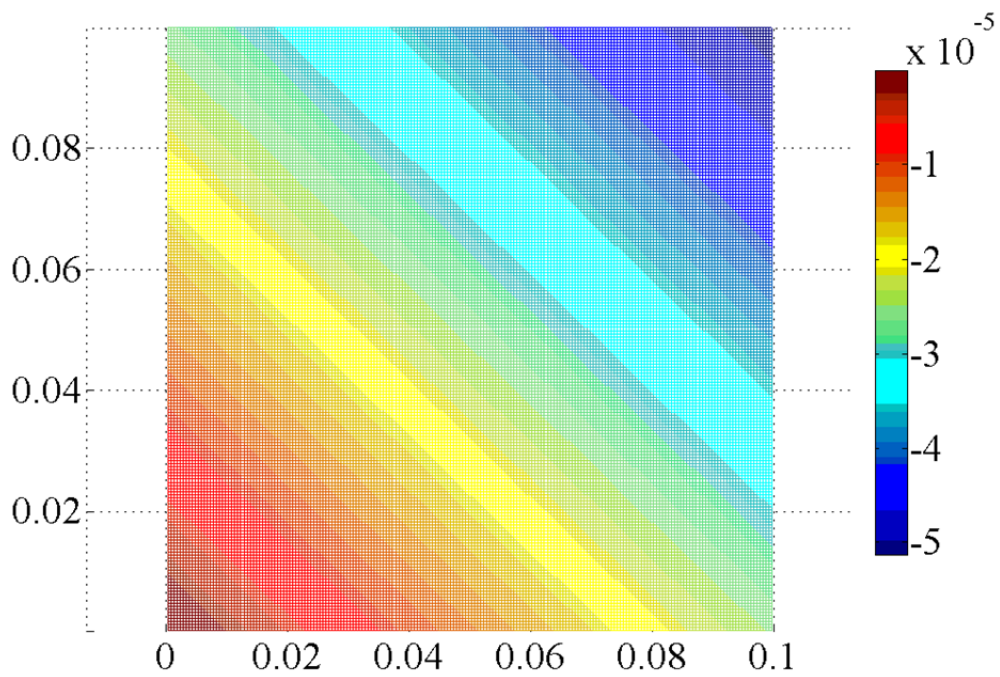
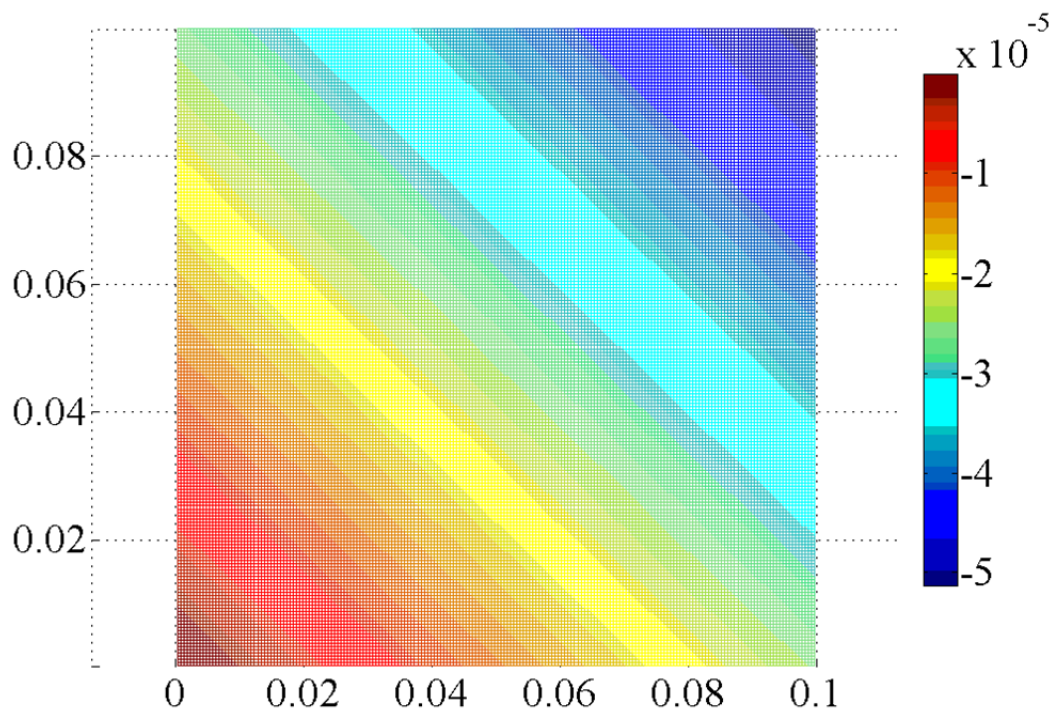


Figure 5.7 Comparison of u_x of 60° laminate calculated from peridynamics (top) and the composite theory (bottom).

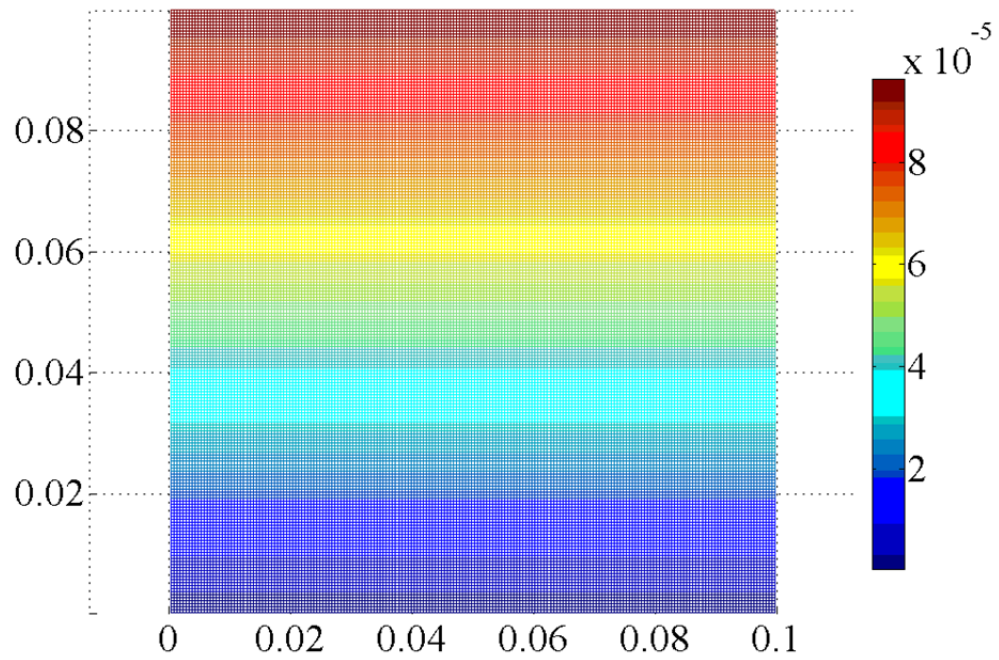
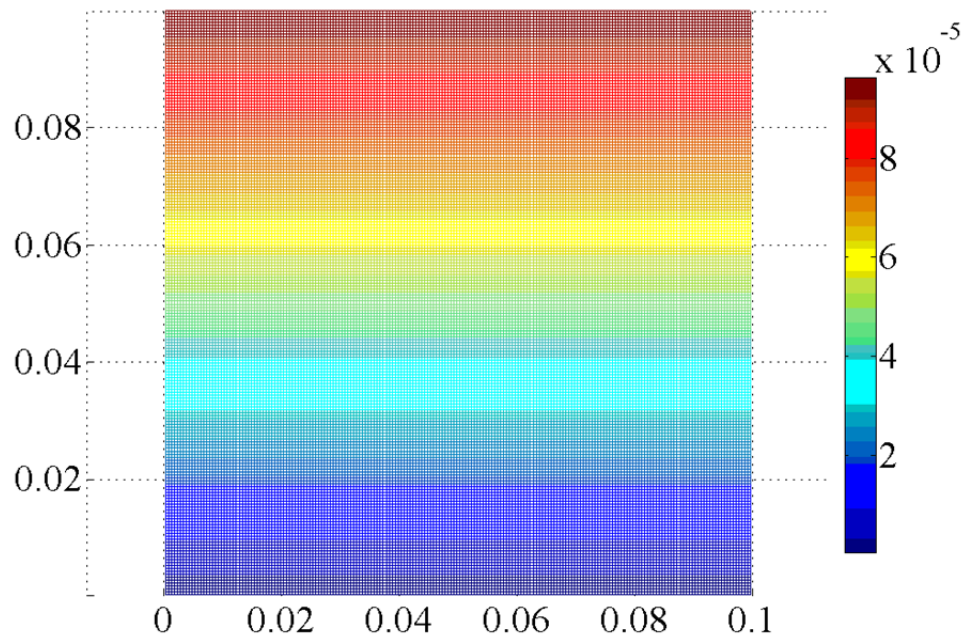


Figure 5.8 Comparison of u_y of 0° laminate calculated from peridynamics (top) and the composite theory (bottom).

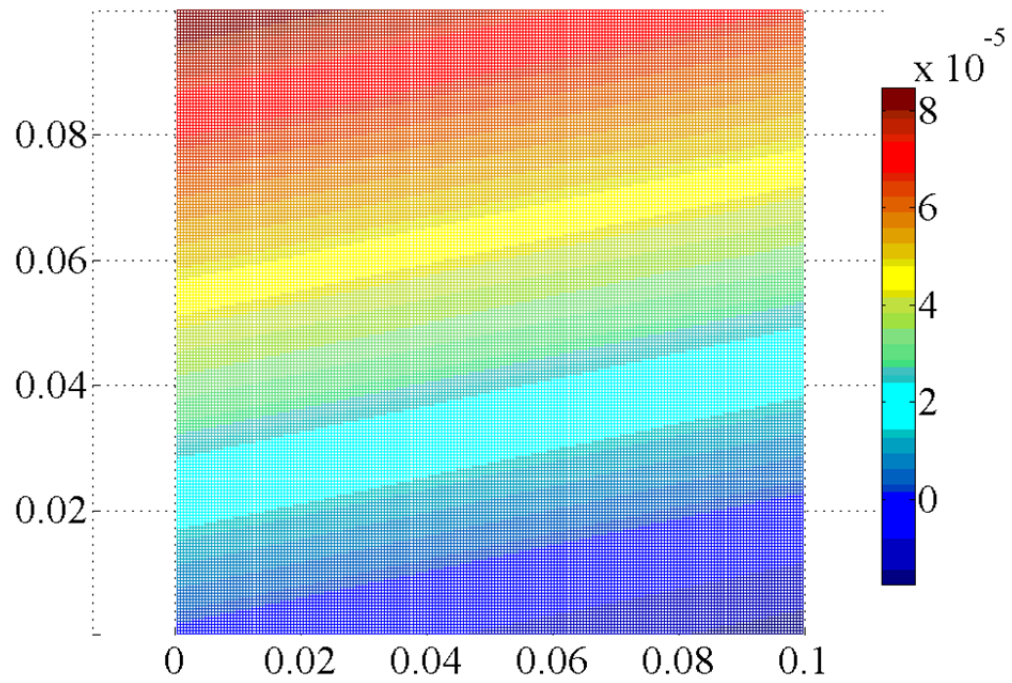
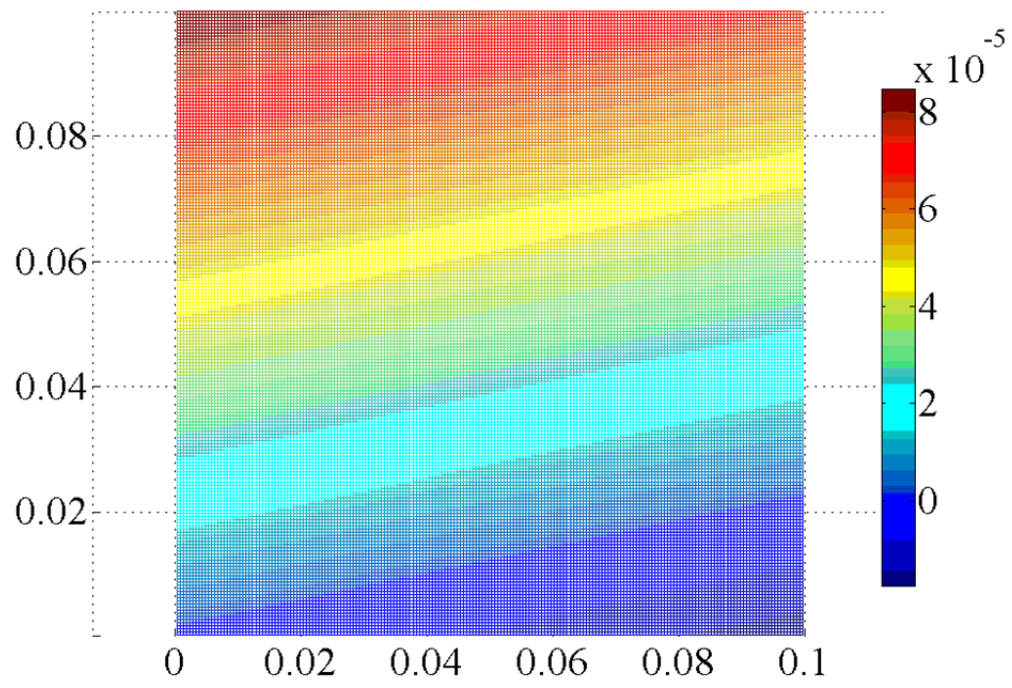


Figure 5.9 Comparison of u_y of 45° laminate calculated from peridynamics (top) and the composite theory (bottom).

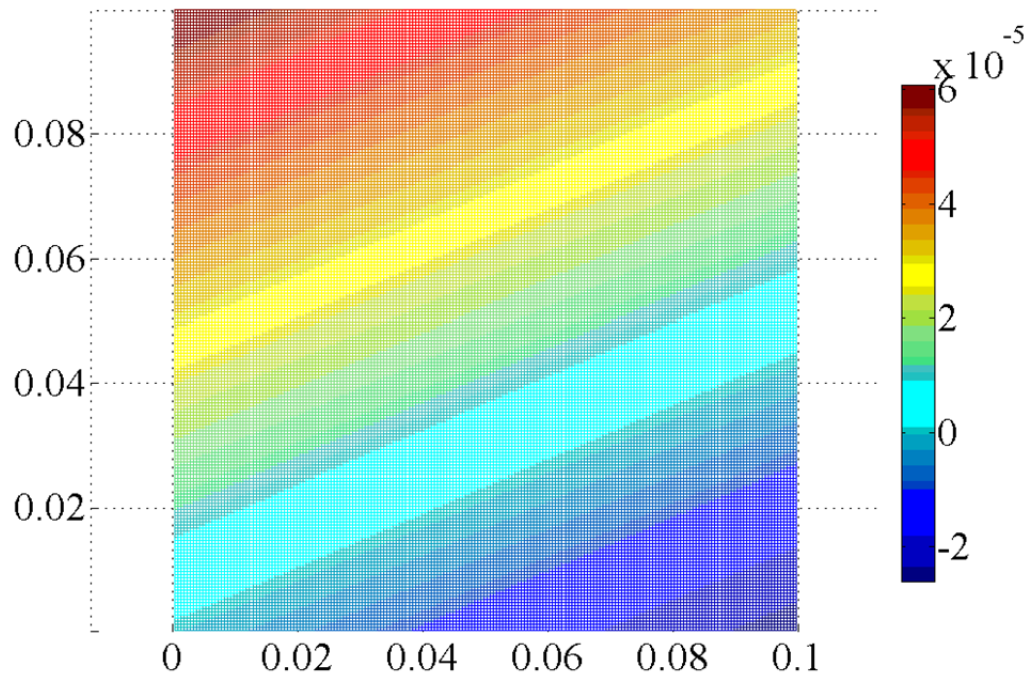
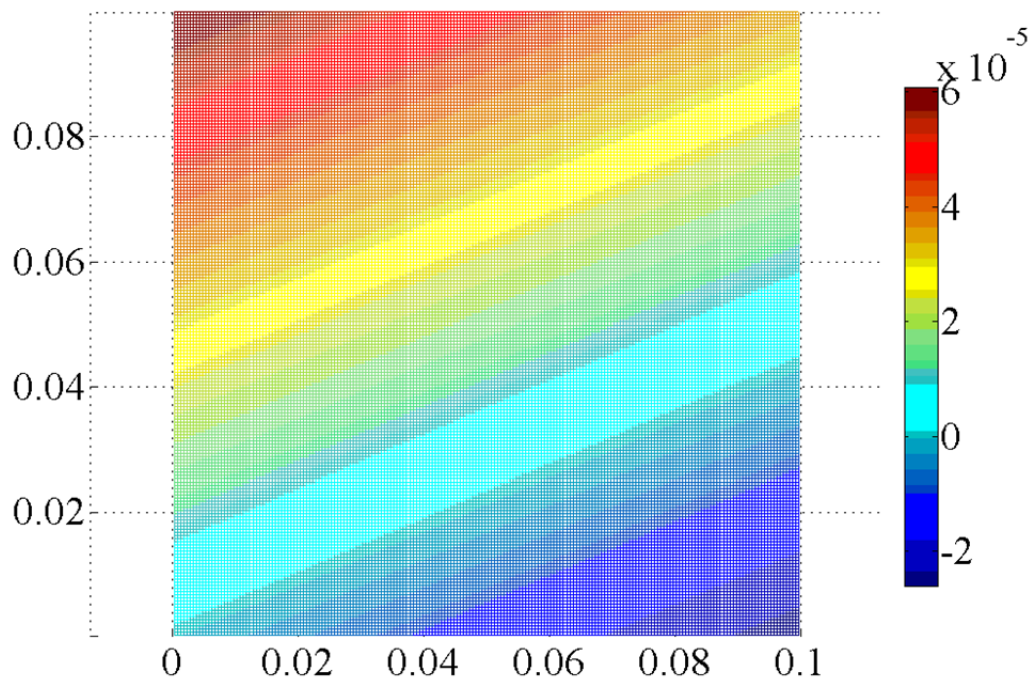


Figure 5.10 Comparison of u_y of 60° laminate calculated from peridynamics (top) and the composite theory (bottom).

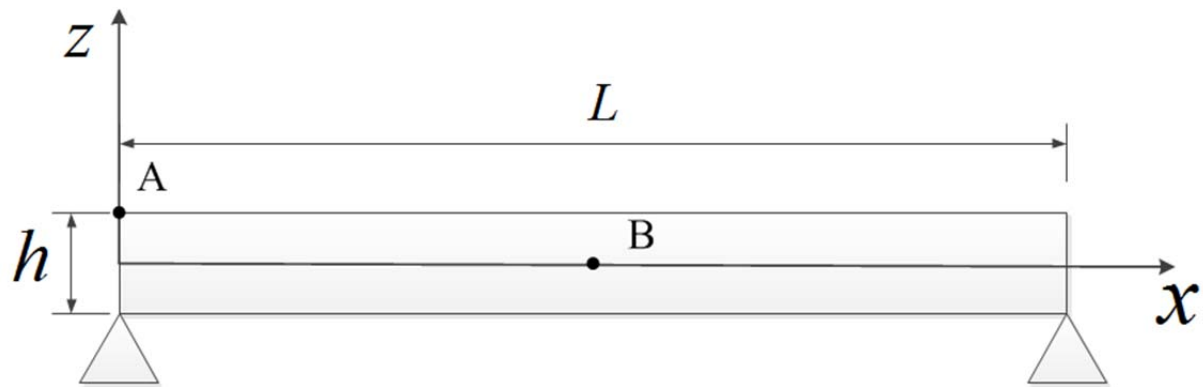


Figure 5.11 Free vibration of a laminated beam with fibers in x direction.

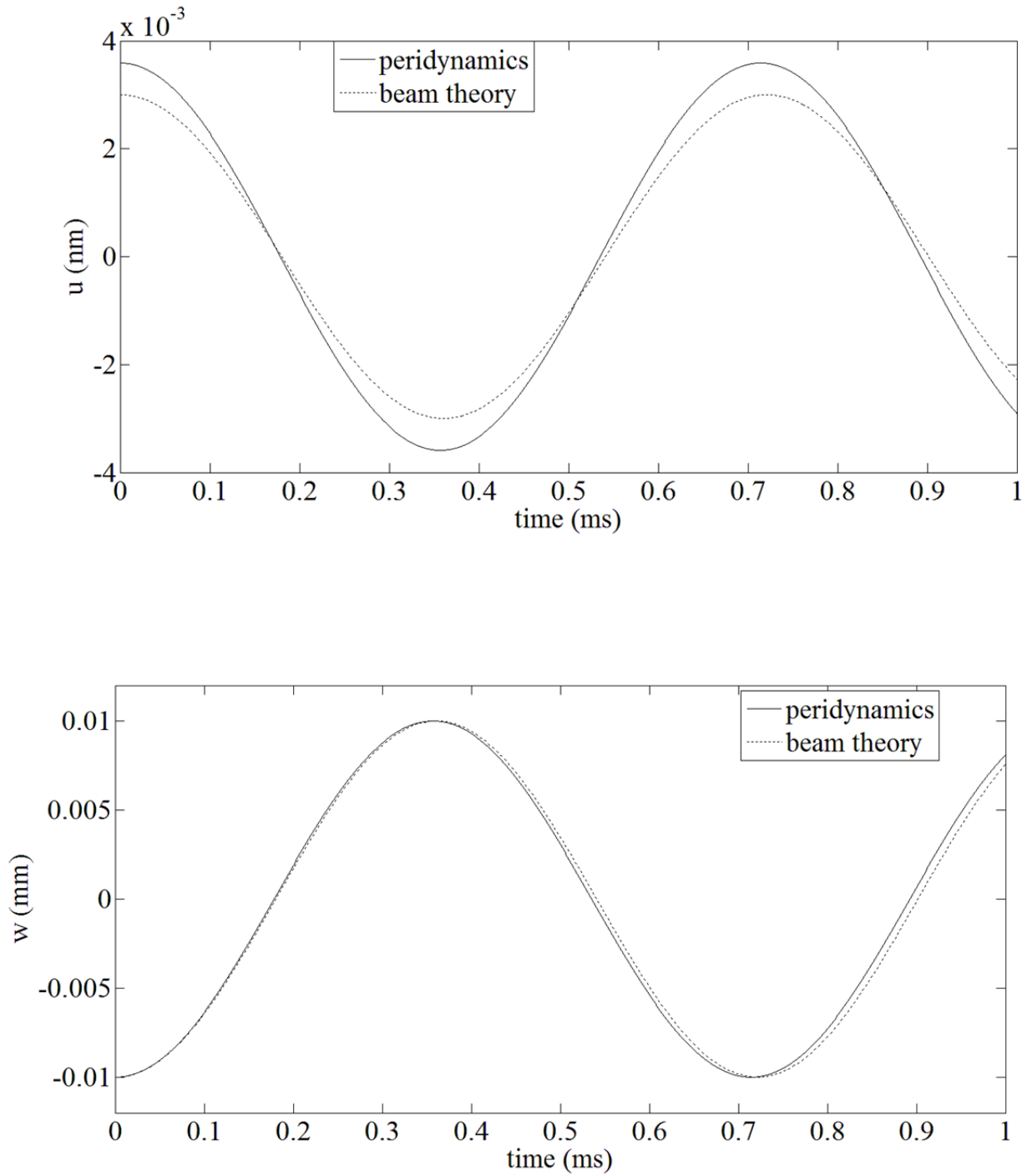


Figure 5.12 Peridynamic results compared with composite beam theory results with $a = 5$.

Top: horizontal displacement u of point A. Bottom: vertical displacement w of point B.

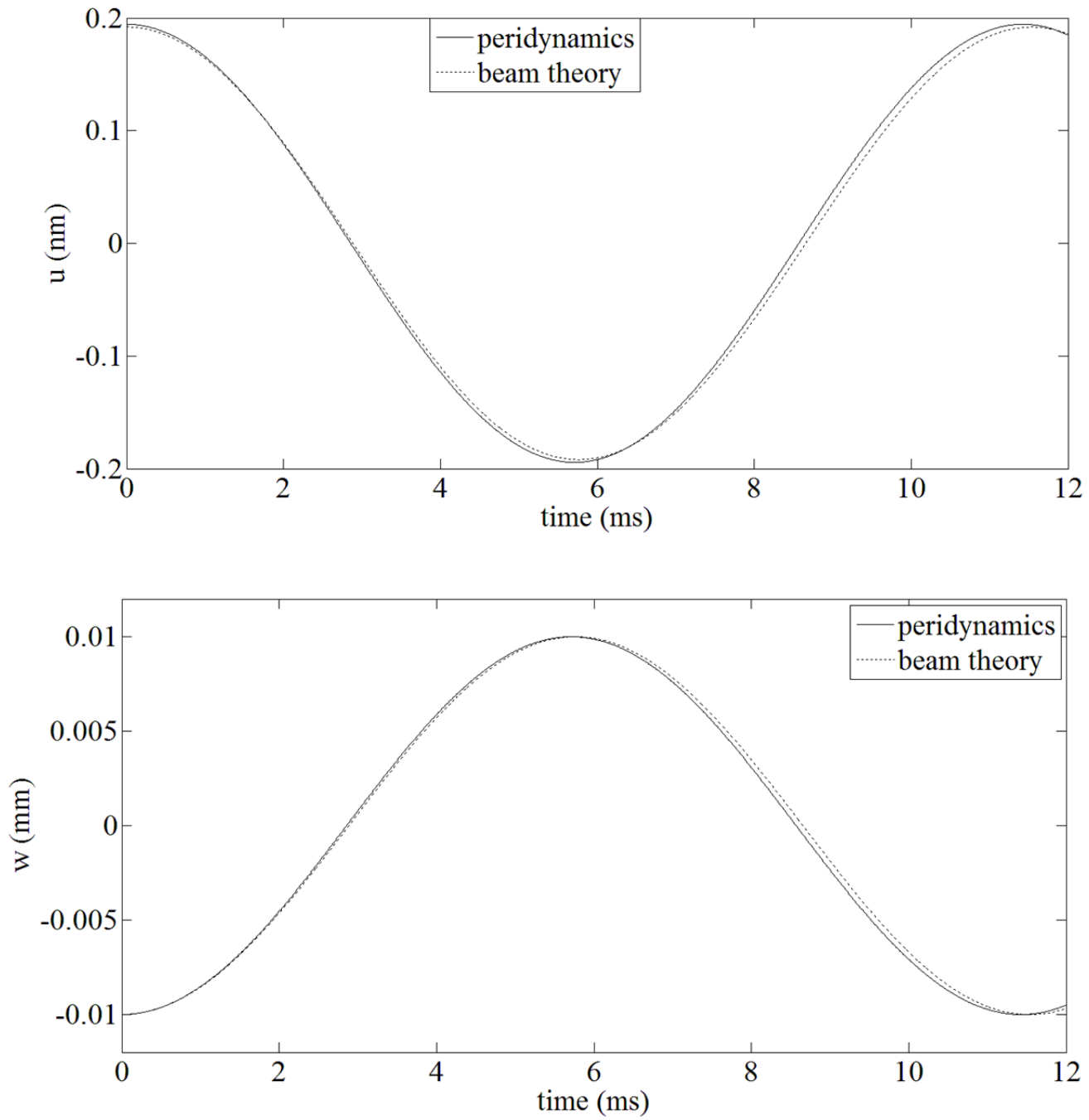


Figure 5.13 Peridynamic results compared with composite beam theory results with $a = 20$.

Top: horizontal displacement u of point A. Bottom: vertical displacement w of point B.

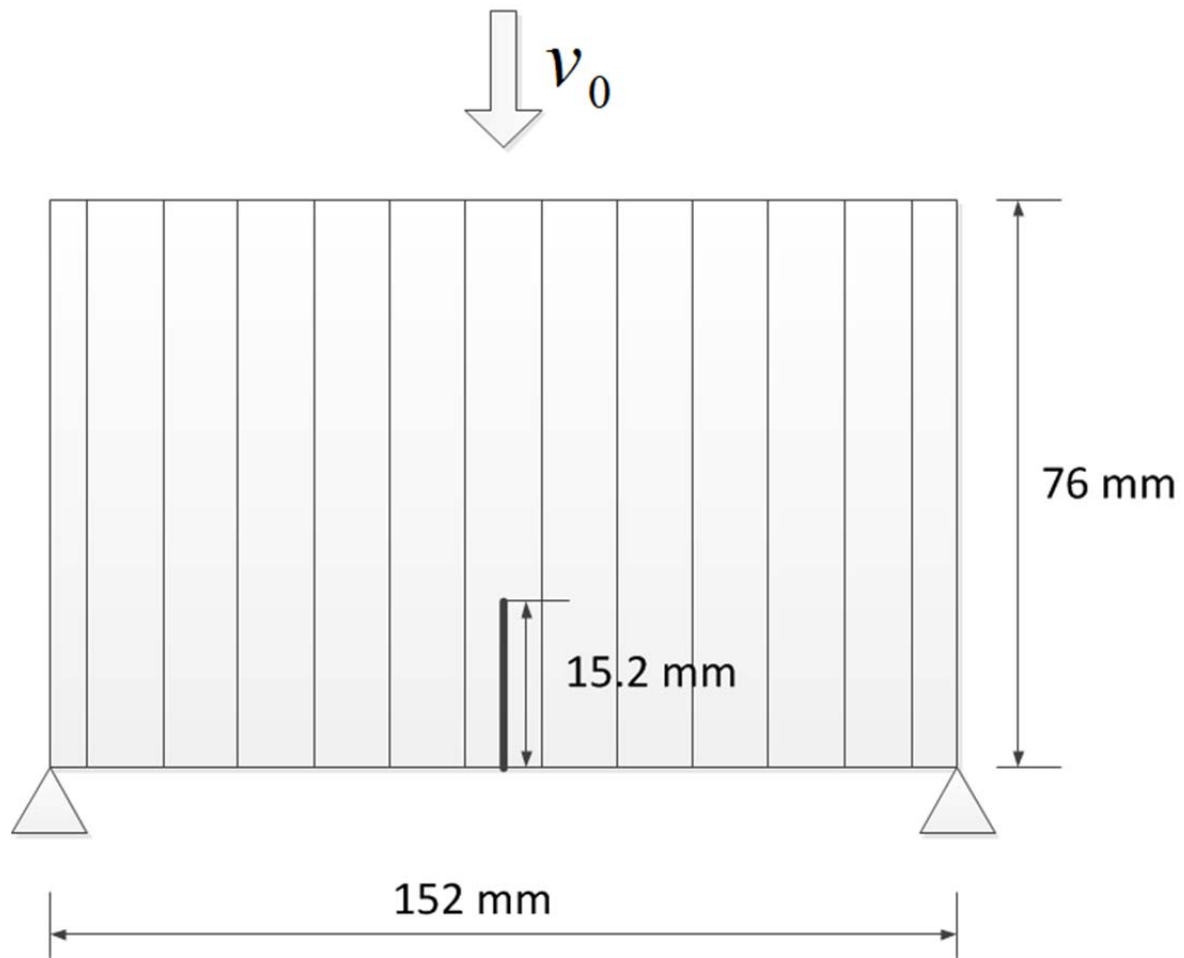


Figure 5.14 An unidirectional composite plate with single edge notch under three point bending.

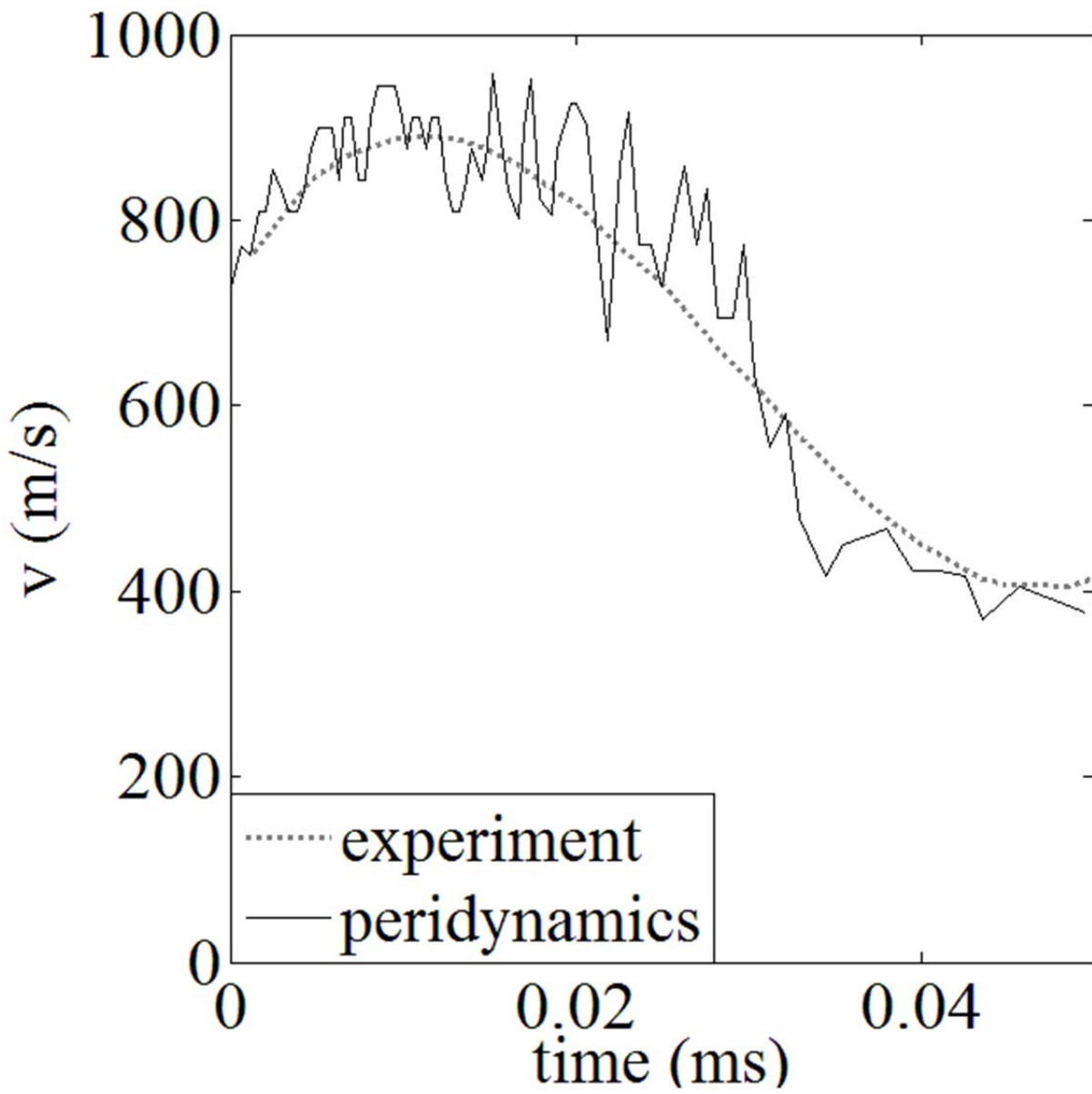


Figure 5.15 Comparison of crack propagation velocity between peridynamics and experiment.

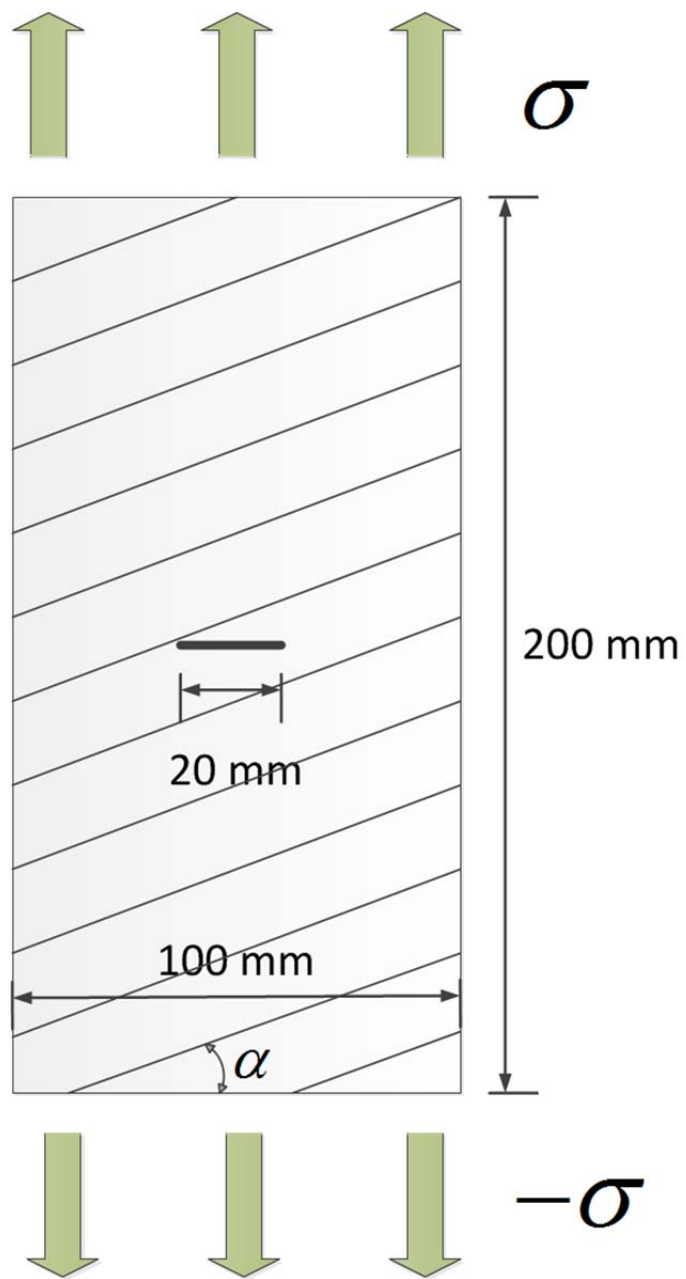
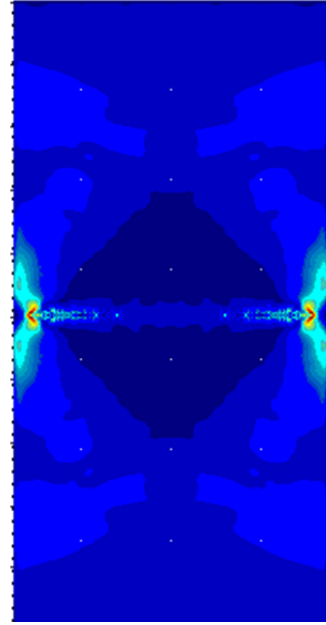


Figure 5.16 Compact tension test for a unidirectional composite plate.

(a)



(b)



(c)

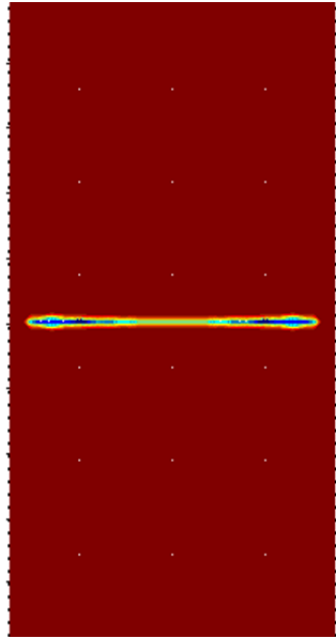


Figure 5.17 Simulation results for $t = 50 \mu s$ and $\alpha = 0^\circ$:

(a) vertical displacement, (b) strain energy density, (c) local damage.

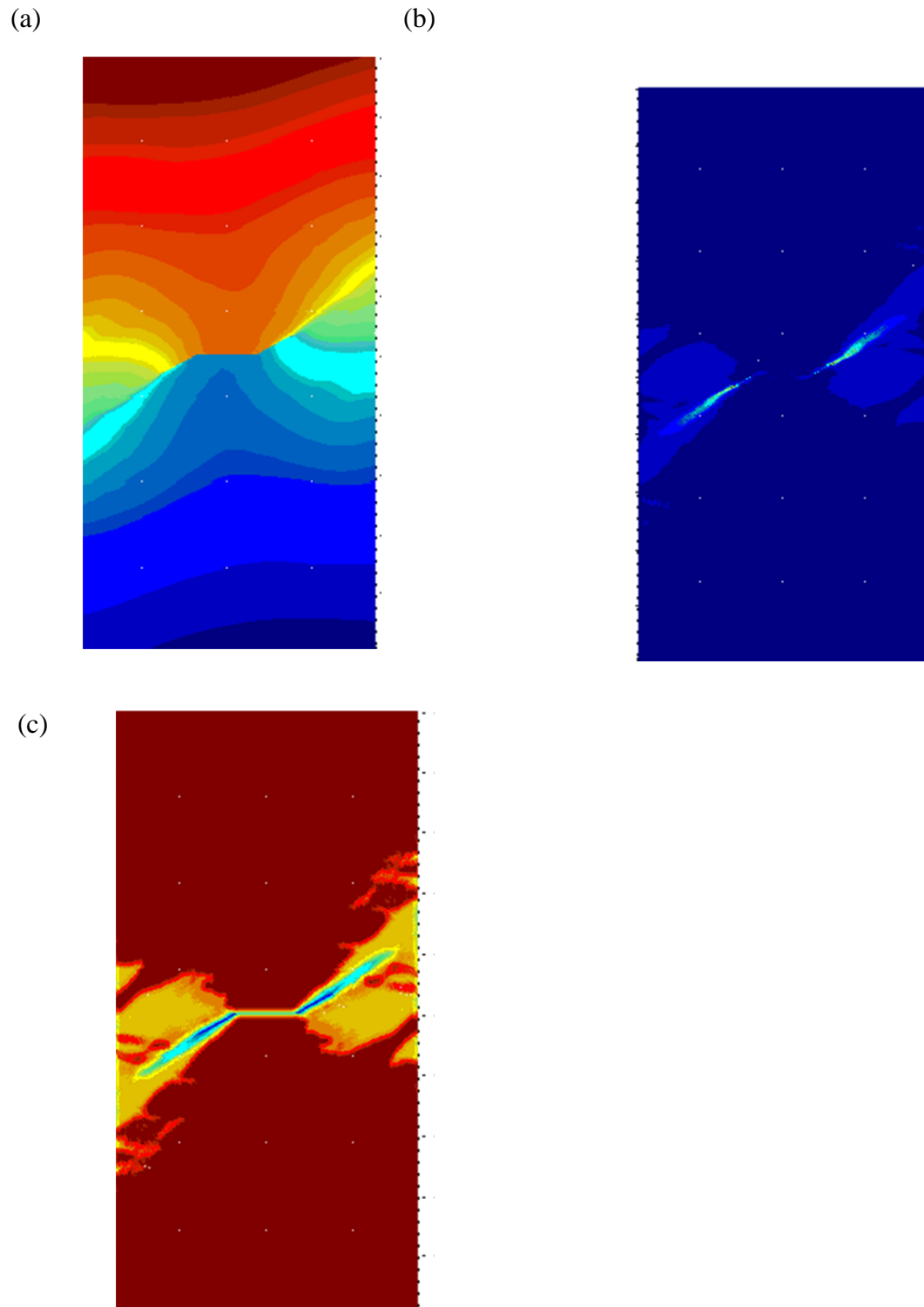


Figure 5.18 Simulation results for $t = 70 \mu s$ and $\alpha = 30^\circ$:

(a) vertical displacement, (b) strain energy density, (c) local damage.

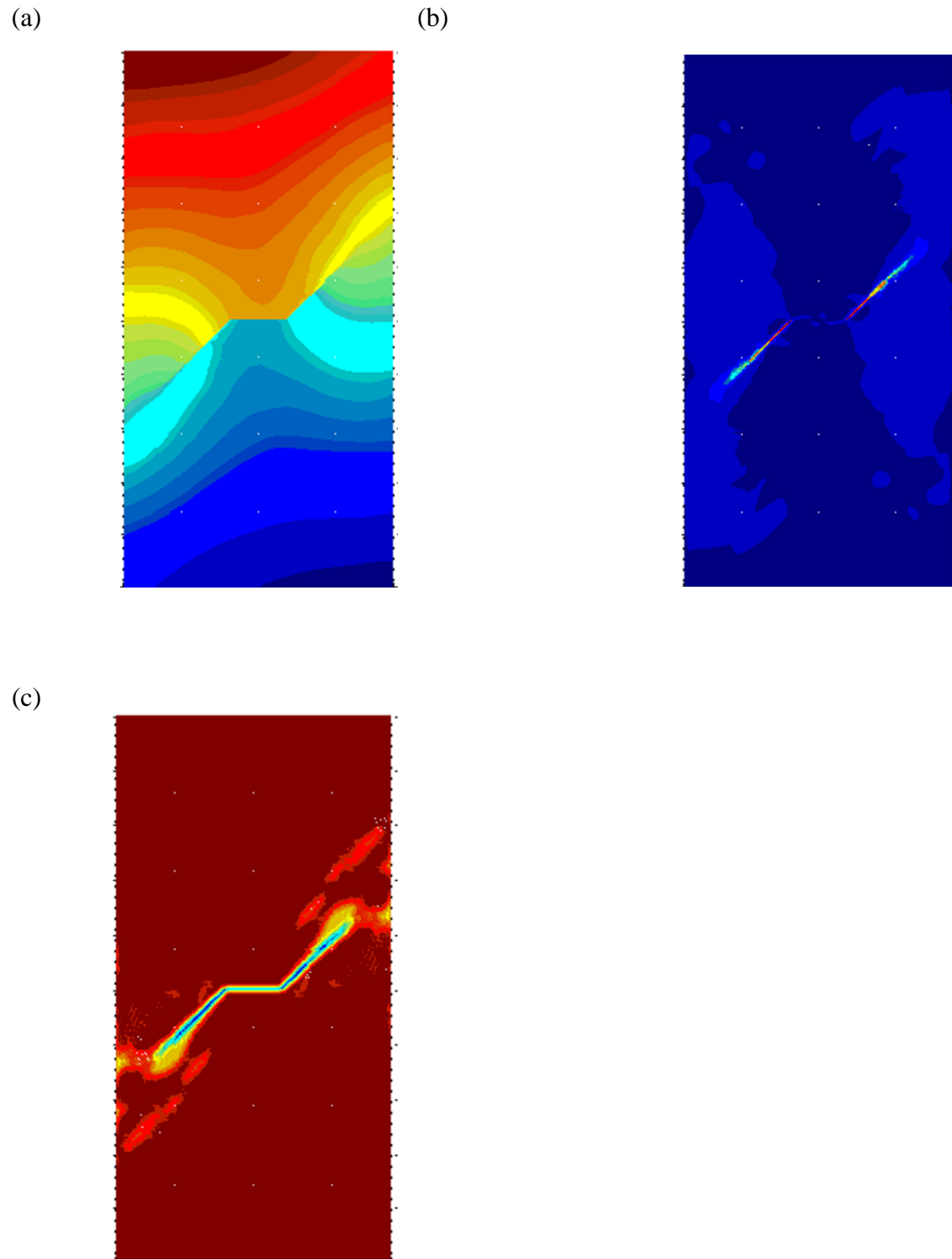


Figure 5.19 Simulation results for $t = 70 \mu s$ and $\alpha = 45^\circ$:

(a) vertical displacement, (b) strain energy density, (c) local damage.

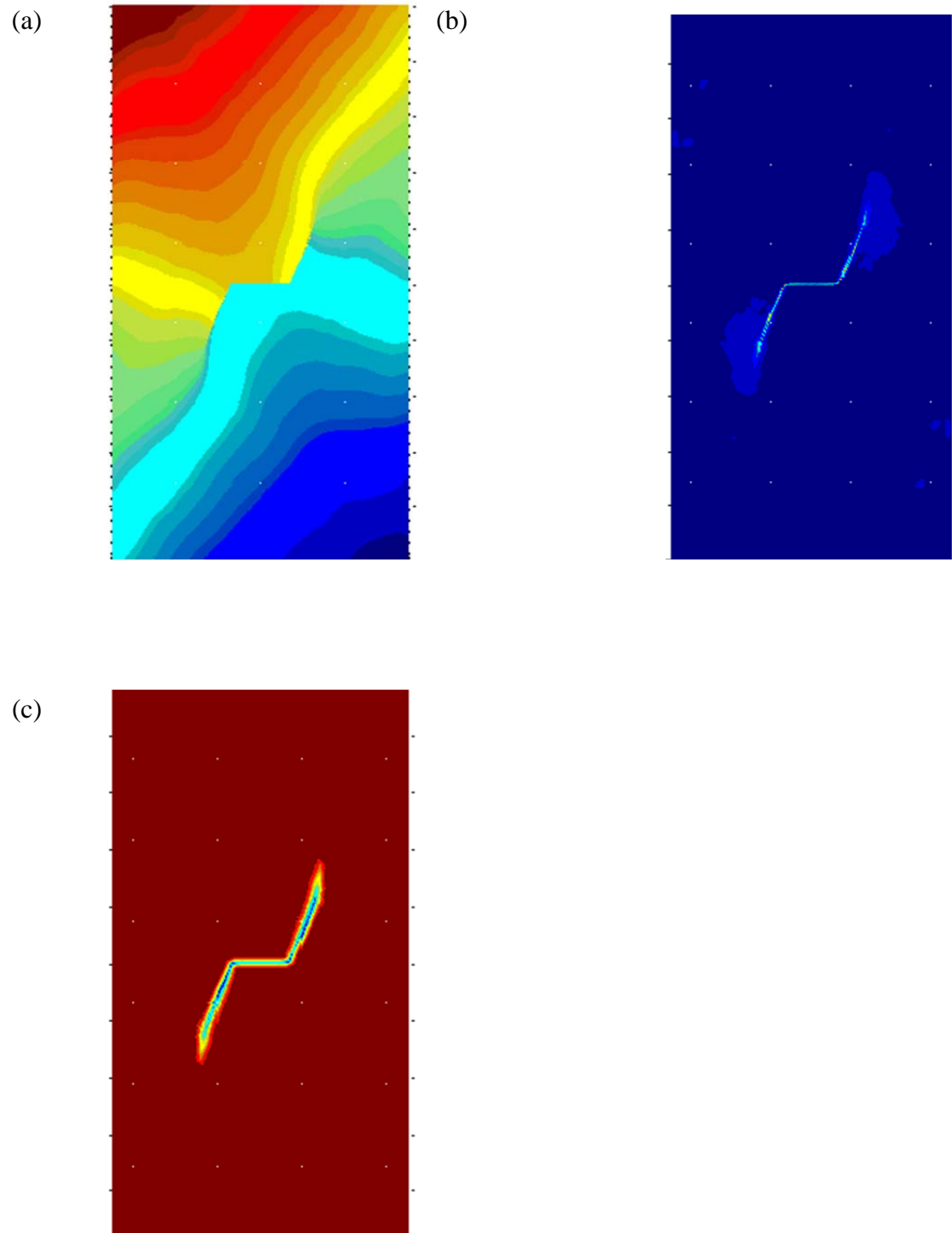


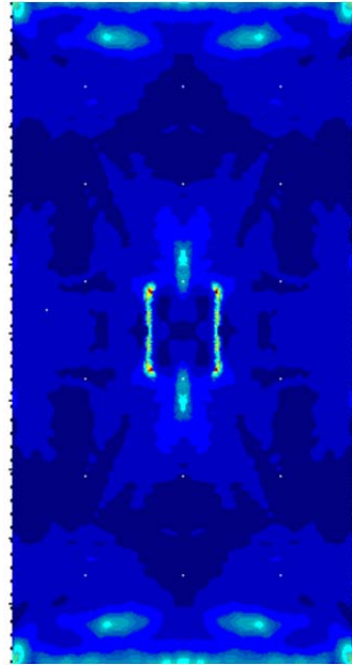
Figure 5.20 Simulation results for $t = 90 \mu s$ and $\alpha = 60^\circ$:

(a) vertical displacement, (b) strain energy density, (c) local damage.

(a)



(b)



(c)

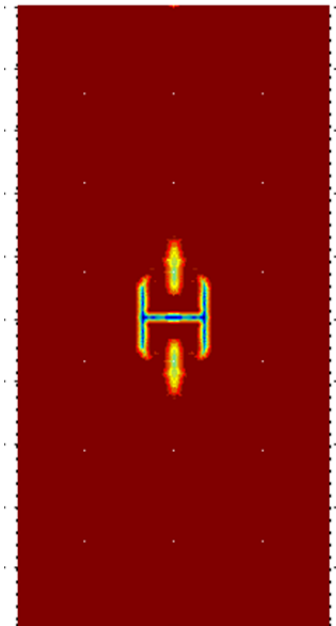


Figure 5.21 Simulation results for $t = 100.5 \mu s$ and $\alpha = 90^\circ$:

(a) vertical displacement, (b) strain energy density, (c) local damage.

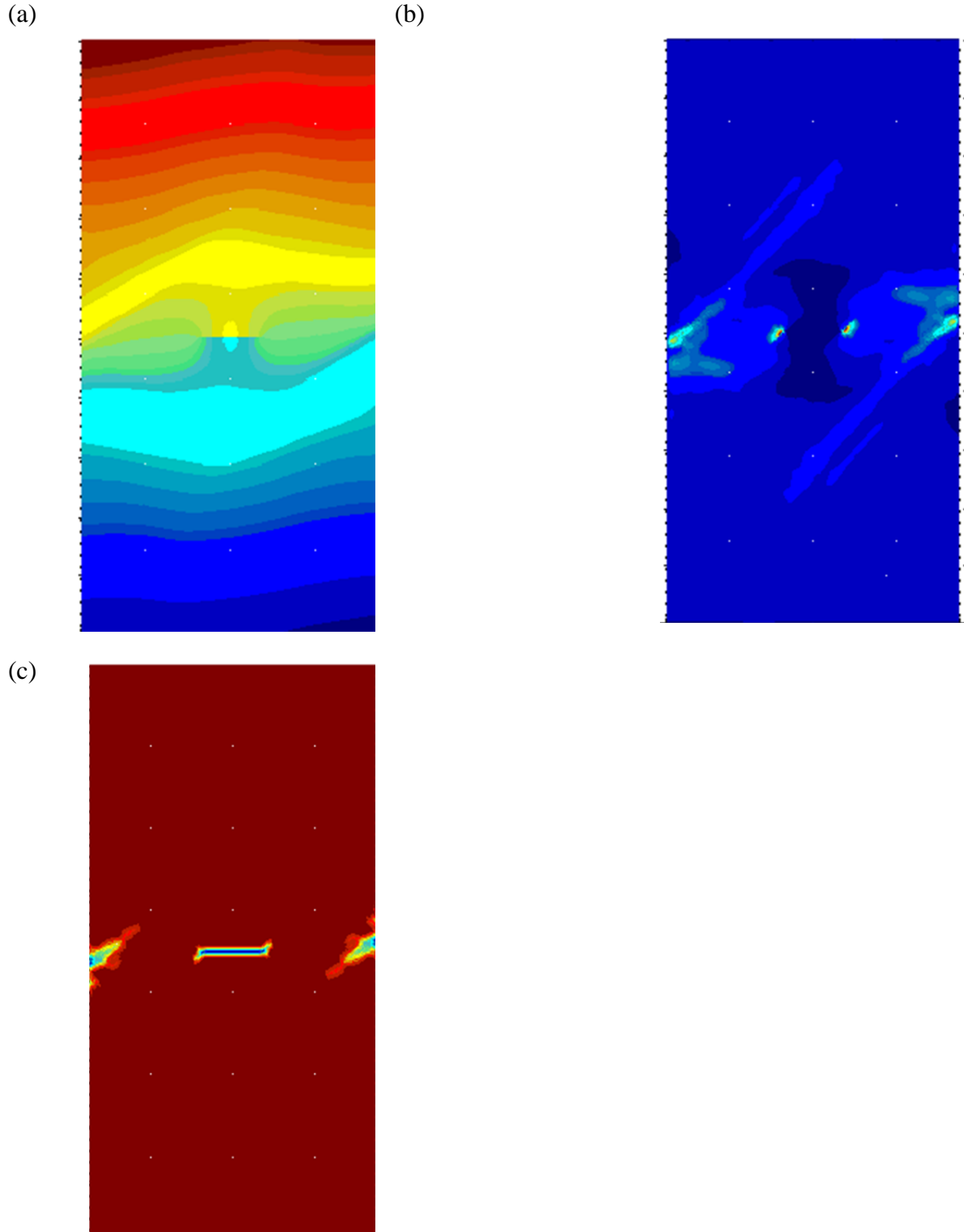


Figure 5.22 Simulation results for $t = 40 \mu s$ and $\alpha = 30^\circ$:

(a) vertical displacement, (b) strain energy density, (c) local damage.

REFERENCES

References

- [1] Dwivedi, S. K., Espinosa, Modeling dynamic crack propagation in fiber reinforced composites including frictional effects, *Mechanics of Materials*, **35**, 481-509 (2003)
- [2] Xu, J., Askari, A., Wechner, O., Damage and Failure Analysis of Composite Laminates under Biaxial Loads, 48th AIAA/ASME/ASCE/AHS/ASC Structures, Structural Dynamics, and Materials Conference, April 23-26, 2007, Honolulu, Hawaii
- [3] Hu, W., Ha, Y.D., Bobaru, F., Peridynamic model for dynamic fracture in unidirectional fiber-reinforced composites, *Comput. Methods Appl. Mech. Engrg.*, 217-220 (2012)
- [4] Silling, S. A., Reformulation of elasticity theory for discontinuities and long-range forces, *J. Mech. Phys. Solids*, **48**, 175-209 (2000)
- [5] <http://www.wolfram.com/mathematica/>
- [6] Daniel, I. M., Ishai, O., Engineering mechanics of composite materials, the Second Edition, Oxford University Press, Inc. (2006)
- [7] Whitney, J. M., Structural Analysis Of Laminated Anisotropic Plates, Technomic Publishing Company, Inc. (1987)
- [8] Lambros, J., Rosakis, A. J., Dynamic crack initiation and growth in thick unidirectional graphite/epoxy plates, *Composite Science and Technology*, **57**, 55-65 (1997)
- [9] Zheng, S., Sun, C.T., A double-plate finite-element model for the impact-induced delamination problem, *Composite Science and Technology*, **53**, 111-118 (1995)
- [10] Stout, M.G., Liu, C., Ellis, R.W., Haberman, K.S., Bennet, J.G., Williams, Addesio, F.L., Rosakis, A.J., Mechanics analysis and simulation of a graphite/epoxy composite plate, *Experimental Mechanics*, 187-192 (1998)
- [11] Coker, D., Rosakis, A.J., Experimental observations of intersonic crack growth in asymmetrically loaded unidirectional composite plates, GALCIT-SM Reports 98-16. CALTECH, Pasadena, CA (1998)
- [12] Coker, D., Rosakis, A.J., Experimental observations of intersonic crack growth in asymmetrically loaded unidirectional composite plates, *Philosophical Magazine*, **81**, 571-595 (2001)
- [13] Huang, Y., Wang, W., Liu, C., Rosakis, A.J., Analysis of intersonic crack growth in unidirectional fiber-reinforced composites, *Journal of the Mechanics and Physics of Solids*, **47**, 1893-1916 (1999)

- [14] Hwang, C., Geubelle, P., A spectral scheme to simulate dynamic fracture problems in composite, *Computer Modeling in Engineering and Science*, **4**, 45-56 (2000)
- [15] Kumar, P., Kishore, N.N., Initiation and propagation toughness of delamination crack under an impact load, *Journal of the Mechanics and Physics of Solids*, **46**, 1773-1787 (1998)
- [16] Lo, C. Y., Nakamura T., Kushner, A.S., Dynamic failure analysis along interfaces in composite materials, *Advanced Computational Methods for Material Modeling*, AMD-vol.180, ASME, 115-124 (1993)
- [17] Sun, C. T., Qian, W., The use of finite extension strain energy release rates in fracture of interfacial cracks, *International Journal of Solids and Structures*, **34**, 2595-2609 (1997)
- [18] Pandey, R.K., Sun, C.T., Calculating strain energy release rate in cracked orthotropic beams, *Journal of Thermoplastic Composite Materials*, **9**, 381-395 (1996)
- [19] Tippur, H.K., Krishnaswamy, S., Rosakis, A. J., Optical mapping of crack tip deformations using the method of transmission and reflection Coherent Gradient Sensing: A study of crack tip K-dominance, *Int. J. Fract.*, **52**, 91-117 (1991)
- [20] Tippur, H. V., Krishnaswamy, S., Rosakis, A. J., A coherent gradient sensor for crack tip measurements: Analysis and experimental results, *Int. J. Fract.*, **48**, 193-204 (1991)
- [21] Rosakis, A. J., Two optical techniques sensitive to gradients of optical path difference: The method of caustics and the coherent gradient sensor (CGS), *Experimental Techniques in Fracture*, J. Epstein, VCH, New York, 327-425 (1993)
- [22] Donaldson, S. L., Fracture toughness testing of graphite/epoxy and graphite/PEEK composites, *Composites*, **16**, 103-112 (1985)
- [23] Jose, S., Kumar, R. R., Jana, M. K., Venkateswara, R., Intralaminar fracture toughness of a cross -ply laminate and its constituent sub-laminates, *Composites Science and Technology*, **61**, 1115-1122 (2001)
- [24] Wu, E. M., *Fracture mechanics of anisotropic plates*, Composite material workshop, Lancaster, PA, Technomic Publishing Co. Inc, 20-43 (1968)
- [25] Boger, P. B., Satyanarayana, A., Chunchu, P. B., Comparison of damage path prediction for composite laminates by explicit and standard finite element analysis tools, 47th AIAA/ASME/ASCE/AHS/ASC structures, structural dynamics, and materials conference, Newport, RI, May 1-4, 2006
- [26] Satyanarayana, A., Bogert, P. B., Chunchu, P. B., The effect of delamination on damage path and failure load prediction for notched composite laminates, 48th AIAA/ASME/ASCE/AHS/ASC structures, structural dynamics, and materials conference, Honolulu, HI, April 23-26, 2007

Chapter 6

Conclusions and Recommendations

6.1 Conclusions

The governing equations of commonly used continuum mechanics are of differential equations. In simulating damage process, special techniques and updated boundary conditions must be applied on the crack surfaces. Since the differential governing equations require displacement continuity in the domain of study, they become troublesome when damage takes place. In modeling dynamic crack propagation, knowledge of crack positions and propagation directions are also required. It then is difficult and often times impossible for studying dynamic crack propagation of fiber-reinforced composite materials based on the traditional continuum mechanics. The following conclusions can be drawn from this dissertation research.

1. Instead of differential equations, peridynamics uses integral equations. Similar to molecular dynamics, peridynamics assumes that the domain of interest is organized by points. Each point interacts with every other point within the horizon through a bond. Damage at a point takes place when a critical number of bonds associated with the point are broken. There is no need to impose a separate damage theory such as fracture mechanics used in continuum mechanics. Chapter 2 introduced the governing equation of peridynamics and some basic properties of the peridynamics.

2. Being a novel method, peridynamic theory is still in its infant stage. New models are needed and require analytical verifications and experiment validations. In Chapter 3, the governing

equation and a bond function for one-dimensional problems were proposed. The model was verified by the analytical solution of a wave propagation problem. The analytical solution was also used to study the convergence of numerical method and a balanced set of parameters were identified. Split Hopkinson's pressure bar (SHPB) tests were conducted and the experiment results were used to validate the one-dimensional peridynamic model. Cross-interface bond models were proposed to study the interface related issues and contact problems of peridynamics. Both elastic model and plastic model were proposed so the peridynamic theory could be used to simulate SHPB tests in validating both elastic and plastic deformations. Several issues involved in the experiments were discussed and it was shown that peridynamic results matched well with the experiment results. Finally, using the plastic model, the shaping effects in the SHPB tests were simulated and the results suggested that the peridynamic model could be used for designing the shaper. The one-dimensional model was validated in this chapter and it was concluded that the impact process could be successfully simulated by peridynamics with its long range forces without involving contact mechanics.

3. In Chapter 4, a bar model and a beam model were proposed for two-dimensional problems. The two-parameter beam model was capable of presenting two independent material properties required by isotropic materials. The proposed model was verified by a two-dimensional vibration analysis. Compared with the solutions from classical mechanics, numerical parameters were studied to show the convergence of peridynamic solutions to classical mechanics solutions. Two computational techniques were also proposed and implemented. The computational efficiency was greatly improved using these techniques. The ability for executing two-dimensional analysis was thus proved feasible. Three dynamic damage propagation experiments from the literature

were also used to validate the peridynamic model and its damage theory. In the first experiment, the crack velocity in the single edge notch (SEN) test was simulated by peridynamics and the results matched well with those from experiment given in the literature. In the second experiment, peridynamics was shown to be capable of producing crack branching as reported in literature. In the third experiment, an impulse loading was simulated and peridynamic results showed the same crack propagation direction as given in the experiment. It was shown that the damage propagated in peridynamic simulation without any additional damage theory. There was no need of tracking individual crack paths or using special elements.

4. The orthotropic material models and their applications were studied in Chapter 5. A four-parameter peridynamic model for orthotropic materials was proposed to coincide with the four independent material properties required for orthotropic materials. This four-parameter model was different from the previous developed ones as it had four parameters and was mesh independent. The model was verified by a static tensile test and a vibration excitation of a laminated beam. An SEN (single edge notch) test of a 0° laminated plate was simulated by peridynamics and the computational results matched with published experiment results. Fracture initiation and crack path of laminated plates with different fiber orientations were also studied using peridynamics. The mesh-free peridynamic model was convenient and efficient since there was no need to have different meshes for different fiber orientations. Without using special meshes and requiring prior knowledge of fracture paths, a general peridynamic code was able to predict fracture velocity and crack path successfully.

In conclusion, a peridynamic code was generalized in this work using Matlab. Two computational techniques were proposed and implemented to improve the computational efficiency dramatically. This rendered simulations of large domains feasible and paved a way for peridynamics in simulating even larger structures in the future. Besides, material models for one-dimensional problems, two-dimensional problems and orthotropic materials were proposed and they matched well with the two material properties in isotropic materials and the four material properties in orthotropic materials, respectively. Elastic models, plastic models and damage theories of peridynamics were proposed and studied in this thesis work. These models were compared with either analytical solutions or experiment results. All the comparisons showed good matches. Finally, it is worth noting that the integral governing equation of peridynamics covers the entire domain regardless the continuity or discontinuity of the displacement. Therefore, as shown in this work, there is no need to apply special techniques or models on displacement discontinuity. Cracks or material weakening can grow automatically whenever and wherever they have to grow.

6.2 Recommendations

1. A three-dimensional peridynamic model can be developed in the future to simulate three-dimensional problems. Silling's bar model [1] is only able to model materials with Poisson's ratio of $\frac{1}{4}$. The three-dimensional model can be developed from the beam model in Chapter 4 to accommodate two material properties for isotropic materials. With the help of this three-dimensional model, a three-dimensional axisymmetric peridynamic model can be developed from the axisymmetric model in Chapter 4. The experiment data in Chapter 3 can be conveniently used to validate this model.

2. More complex constitutive functions can be proposed to accommodate material nonlinearity.

It has been shown that experiment based stress-strain data can be used as the computational input for the peridynamic code. More experiments can be performed to study material properties and the experiment data can help refining peridynamic models. Strain-rate dependent materials can also be modeled by peridynamics. Besides the spring model, elastic or plastic, a dash pot can be added to the constitutive bond function. Since a dash pot is velocity dependent, a material model with a dash pot can be strain rate dependent.

3. Multi-physical loads can be modeled using peridynamics. Currently, peridynamics is only used in solid mechanics. Gas and liquid can be modeled using similar governing equations as the peridynamics for solid mechanics. The constitutive functions of gas and liquid, however, will be greatly different from those for solids. Other than the mechanical loads, thermal loads, acoustic loads and electromagnetic loads can also be modeled in peridynamics. In peridynamics, all external loads are applied as body forces. The effects of all non-mechanical loads need to be studied and can be applied as mechanical effects in the peridynamic domain.

4. Once a three-dimensional peridynamic model is developed, a three-dimensional orthotropic materials can be modeled similar to the two-dimensional orthotropic material models in Chapter

5. This model can be conveniently used to model woven composite, which is a difficult subjects in commonly used finite element analysis. When modeling woven composite, the weaving structures of the woven composite need to be known to set up the material properties of bonds in

different directions. Deformations and damages of each bond are independent and crack can grow in any directions.

5. Currently, the peridynamics code is developed using Matlab. The domain grid is generalized manually. It will be better to use commercial mesh generalizers to define problem domains and generalize mesh in any size. Moreover, it will be better to embed the peridynamics code in a commercial software because commercial software are robust and likely more efficient.

6. Validations of new developed theories and models are necessary. Problems requiring peridynamic analysis are likely complex and it is almost impossible to find analytical solutions for these problems. To develop more complex peridynamic models, more experiments specifically designed for validating the peridynamic models are necessary.

REFERENCES

References

- [1] Silling, S. A., Reformulation of elasticity theory for discontinuities and long-range forces, *J. Mech. Phys. Solids*, **48**, 175-209 (2000)